

Mechanics and Dynamics of Nanosized Protein Cages

*A Thesis submitted in partial fulfillment
of the requirements for the degree of
Doctor of Philosophy*

Aida Llauro-Portell



**FACULTAD DE
CIENCIAS**
UNIVERSIDAD AUTÓNOMA DE MADRID

Departamento de Física de la Materia Condensada
Universidad Autónoma de Madrid, Madrid, Spain

Thesis supervisor:
Pedro José de Pablo Gómez

January 2015

*A ma mare, per ser una heroïna,
com tantes d'altres dones.*

Table of contents

Preface	7
Abbreviations	13
Chapter1:	
<i>Study of Nanosized Protein Cages with Atomic Force Microscopy</i>	15
Chapter2:	
<i>Mechanical Stability and Reversible Fracture of Vault Particles</i>	39
Chapter3:	
<i>Decrease in pH Destabilizes Individual Vault Nanocages by Weakening the Interprotein Lateral Interactions</i>	61
Chapter 4:	
<i>Influence of Calcium Ions and Swelling on the Mechanical Properties of Tomato Bushy Stunt Viruses</i>	83
Chapter 5:	
<i>Cargo-shell Coupling Governs the Mechanics of Virus-Derived Protein Cages.</i>	103
Chapter 6:	
<i>Mechanical Effects of Symmetry Specific Destabilization and Restabilization of the Bacteriophage P22 Virus-Like Particle.</i>	125
Chatper7:	
<i>Structural Dissection of a Temperature-Induced Structural Transition of a Viral Capsid by Hydrogen-Deuterium Exchange.</i>	147
Chatper8:	
Future Outlook and General Conclusions, Summarized Conclusions, List of Publications and Acknowledgements.	168
Appendix:	
Supporting Information	186

Preface

Virus particles represent a class of nanomaterial with outstanding mechanical capabilities.¹ They are robust cages capable of withstanding internal pressures of tens of atmospheres,² but yet tremendously plastic, as they have to modulate their mechanical properties in order to adapt to the different physicochemical conditions encountered during their life cycle.^{3,4} Although the most important impact of viruses in our society is related to their role as disease carriers, causing millions of deaths per year,⁵ over the last two decades the extraordinary features displayed by these structures have been exploited to human benefit.^{6,7} Virus-like particles (VLPs) have been engineered to work as vectors for drug delivery,⁸ nanoreactors for catalysis and synthesis,⁹⁻¹¹ imaging agents,¹² nanobatteries,^{13,14} or as building blocks for a new class of nanomaterials.^{15,16} However, despite all these advances, many aspects need still to be addressed to optimize these protein-based nanodevices. Studying the impact that the confinement of extrinsic agents have on the stability of their structures might contribute to the design of more robust and durable cages. Modulating the mechanical properties of VLPs by mutagenesis, pH change, or addition of external proteins, might improve the mechanical performance of virus-based nanomaterials or gene therapy vectors. Understanding the relationship between the structure and mechanics of natural viral particles might direct the design of *in novo* nanocages.¹⁷ These are only a few examples that illustrate the importance of investigating these systems from different perspectives, which requires the synergy of scientist coming from areas as diverse as biochemistry, medicine, physics or material science. This thesis is focused on studying the dynamics and mechanics of hybrid virus-like particles, or similar protein cages, that are of interest because of their potential role in biotechnology, biomedicine or material science.

Chapter 1 intends to be both an introduction and practical guide to the experimental study of protein nanocages by Atomic Force Microscopy (AFM). It introduces the unfamiliar reader to the field, with especial emphasis on some technical aspects that should be considered during an experiment. Chapter 2 to 7 contain the research papers, all based on the corresponding publication (either published or submitted). Chapter 2 is a study of the

mechanical properties of vault-like particle. Chapter 3 discusses the pH-dependent dynamics of individual vault-particles. Chapter 4 discusses the effect that pH and ions have on the mechanics of Tomato Bushy Stunt Virus. Chapter 5 discusses the role that a different cargo and a cargo-shell interaction have on the stability of P22 virus-like particles. Chapter 6 discusses the impact that introducing defects, and reinforcing the shell by an additional protein, have on the mechanical and chemical stability of P22 nanocages. Chapter 7 discusses a biologically relevant structural transition of the Minute Virus of Mice capsids. This last chapter does not contain AFM results but is based on Hydrogen-Deuterium Exchange Mass Spectrometry. This data was obtained during a two month internship that I got the opportunity to do in the lab of Prof. Albert Heck, at the University of Utrecht. In chapter 8 I present the general conclusions and a future outlook for the field; a summarized version of the conclusions are also included at the end of this chapter in both, English and Spanish. The appendixes at the end of the manuscript contain the supplemental information.

References

- 1 Roos, W. H., Bruinsma, R. & Wuite, G. J. L. Physical virology. *Nat Phys* **6**, 733-743, (2010).
- 2 Gelbart, W. M. & Knobler, C. M. Pressurized Viruses. *Science* **323**, 1682-1683, (2009).
- 3 Hernando-Perez, M., Lambert, S., Nakatani-Webster, E., Catalano, C. E. & de Pablo, P. J. Cementing proteins provide extra mechanical stabilization to viral cages. *Nat Commun* **5**, (2014).
- 4 Roos, W. H. *et al.* Mechanics of bacteriophage maturation. *Proceedings of the National Academy of Sciences* **109**, 2342-2347, (2012).
- 5 World Health Organization. *WHO Mortality Database*, <www.who.int/healthinfo/mortality_data> (2014).
- 6 Douglas, T. & Young, M. Viruses: Making friends with old foes. *Science* **312**, 873-875, (2006).
- 7 Aniygyei, S. E., DuFort, C., Kao, C. C. & Dragnea, B. Self-assembly approaches to nanomaterial encapsulation in viral protein cages. *J Mater Chem* **18**, 3763-3774, (2008).
- 8 Daya, S. & Berns, K. I. Gene Therapy Using Adeno-Associated Virus Vectors. *Clinical Microbiology Reviews* **21**, 583-593, (2008).
- 9 Patterson, D. P., Prevelige, P. E. & Douglas, T. Nanoreactors by Programmed Enzyme Encapsulation Inside the Capsid of the Bacteriophage P22. *Acs Nano* **6**, 5000-5009, (2012).
- 10 Comellas-Aragones, M. *et al.* A virus-based single-enzyme nanoreactor. *Nat Nano* **2**, 635-639, (2007).
- 11 Lucon, J. *et al.* Use of the interior cavity of the P22 capsid for site-specific initiation of atom-transfer radical polymerization with high-density cargo loading. *Nat Chem* **4**, 781-788, (2012).

- 12 Uchida, M. *et al.* Protein Cage Nanoparticles Bearing the LyP-1 Peptide for Enhanced Imaging of Macrophage-Rich Vascular Lesions. *Acs Nano* **5**, 2493-2502, (2011).
- 13 Lee, Y. J. *et al.* Fabricating Genetically Engineered High-Power Lithium-Ion Batteries Using Multiple Virus Genes. *Science* **324**, 1051-1055, (2009).
- 14 Jordan, P. C. *et al.* Self-assembling biomolecular catalysts for hydrogen production. *Nat Chem advance online publication*, (2015).
- 15 Sun, J. *et al.* Core-controlled polymorphism in virus-like particles. *Proc Natl Acad Sci U S A* **104**, 1354-1359, (2007).
- 16 Uchida, M., LaFrance, B., Broomell, C. C., Prevelige, P. E. & Douglas, T. Higher Order Assembly of Virus-like Particles (VLPs) Mediated by Multi-valent Protein Linkers. *Small* **11**, 1562-1570, (2015).
- 17 King, N. P. *et al.* Accurate design of co-assembling multi-component protein nanomaterials. *Nature* **510**, 103-108, (2014).

Prefacio

Las partículas víricas representan un tipo de nanomaterial con propiedades mecánicas extraordinarias.¹ Son estructuras robustas, capaces de aguantar presiones internas de decenas de atmósferas,² y a la vez extraordinariamente plásticas, ya que a lo largo de la evolución se han proveído de los mecanismos moleculares necesarios para poder adaptarse a las distintas necesidades del medio.^{3,4} A pesar de que el mayor impacto social de los virus sigue siendo su papel como portadores de enfermedad, causando millones de muertes humanas al año,⁵ sus exquisitas estructuras han propiciado que durante las dos últimas décadas derivados de partículas víricas (*virus-like particles*; *VLPs*) se investiguen para ser utilizados en beneficio de la sociedad.^{6,7} Este nuevo horizonte abarca áreas tan variopintas como la terapia génica,⁸ la catálisis de reacciones,^{9,10} la producción de energía a la nanoescala,^{13,14} o la síntesis de nuevos materiales.^{15,16} Siendo como es ya un campo tan multidisciplinar, la unión de científicos provenientes de distintas ramas es requisito imprescindible para la optimización y desarrollo de estas nuevas nanoestructuras. Entender el impacto que tienen introducir un agente foráneo en el interior de una cápsida vírica puede contribuir al diseño de nanoestructuras más robustas y duraderas. Modular las propiedades mecánicas de estos derivados proteicos vía mutagénesis, cambios de pH o anclaje de proteínas “cemento” puede mejorar el rendimiento de nanomateriales basados en ellos o su uso como agentes terapéuticos. Estudiar la relación que hay entre estructura y mecánica de virus infecciosos, optimizados durante el proceso evolutivo, puede inspirar y dirigir el diseño de nuevas nanoestructuras.¹⁷ Éstos son sólo algunos ejemplos de la importancia que tienen estudiar estos sistemas desde distintos puntos de vista. Esta tesis se centra en el estudio de la dinámica y propiedades mecánicas de cuatro derivados de nanoestructuras proteicas que han despertado el interés de la comunidad científica no por su papel como agentes infecciosos, sino por su potencial uso en biotecnología, biomedicina o ciencia de materiales.

El capítulo uno pretende ser una introducción y guía práctica al estudio experimental de nanoestructuras mediante la Microscopía de Fuerzas Atómica (AFM). Introduce al lector no familiarizado al campo, con especial hincapié en los aspectos técnicos que deberían de tenerse en cuenta a la hora de diseñar un experimento. Los trabajos científicos se exponen del capítulo 2 al 7, todos basados en la correspondiente publicación (o bien publicada, o pendiente de publicación). El capítulo 2 presenta un estudio de las propiedades mecánicas de

las partículas vaults. El capítulo 3 discute el papel que juega el pH en la dinámica de ensamblaje-desensamblaje de estas nanopartículas. El capítulo 4 discute el impacto que el pH y los iones calcio tienen en la estabilidad del virus del tomate (TBSV). El capítulo 5 discute la influencia que la interacción carga-carga y carga-cápsida tienen en la estabilidad de nanoestructuras proteicas derivadas del bacteriófago P22. El capítulo 6 discute el efecto que tiene, en estas nanoestructuras, introducir defectos y reforzar la cápsida mediante una proteína cemento. El capítulo 7 identifica estructuralmente la transición dependiente de temperatura que el virus diminuto del ratón (MVM) sufre durante su proceso de infección. Este último capítulo no contiene resultados de AFM sino que de Intercambio Hidrógeno-Deuterio mediante Espectrometría de Masas (HDX-MS). Los datos presentados en él fueron obtenidos durante un estancia de dos meses que tuve la oportunidad de hacer en el laboratorio del Prof. Albert Heck, de la Universidad de Utrecht. El capítulo 8 contiene las conclusiones generales y mi visión actual del estado del campo; además, al final del capítulo una versión resumida de las conclusiones se expone tanto en inglés como en español. Finalmente, los apéndices contienen la información suplementaria de los trabajos científicos.

References

- 1 Roos, W. H., Bruinsma, R. & Wuite, G. J. L. Physical virology. *Nat Phys* **6**, 733-743, (2010).
- 2 Gelbart, W. M. & Knobler, C. M. Pressurized Viruses. *Science* **323**, 1682-1683, (2009).
- 3 Hernando-Perez, M., Lambert, S., Nakatani-Webster, E., Catalano, C. E. & de Pablo, P. J. Cementing proteins provide extra mechanical stabilization to viral cages. *Nat Commun* **5**, (2014).
- 4 Roos, W. H. *et al.* Mechanics of bacteriophage maturation. *Proceedings of the National Academy of Sciences* **109**, 2342-2347, (2012).
- 5 World Health Organization. *WHO Mortality Database*, <www.who.int/healthinfo/mortality_data> (2014).
- 6 Douglas, T. & Young, M. Viruses: Making friends with old foes. *Science* **312**, 873-875, (2006).
- 7 Aniagyei, S. E., DuFort, C., Kao, C. C. & Dragnea, B. Self-assembly approaches to nanomaterial encapsulation in viral protein cages. *J Mater Chem* **18**, 3763-3774, (2008).
- 8 Daya, S. & Berns, K. I. Gene Therapy Using Adeno-Associated Virus Vectors. *Clinical Microbiology Reviews* **21**, 583-593, (2008).
- 9 Patterson, D. P., Prevelige, P. E. & Douglas, T. Nanoreactors by Programmed Enzyme Encapsulation Inside the Capsid of the Bacteriophage P22. *Acs Nano* **6**, 5000-5009, (2012).
- 10 Comellas-Aragones, M. *et al.* A virus-based single-enzyme nanoreactor. *Nat Nano* **2**, 635-639, (2007).

- 11 Lucon, J. *et al.* Use of the interior cavity of the P22 capsid for site-specific initiation of atom-transfer radical polymerization with high-density cargo loading. *Nat Chem* **4**, 781-788, (2012).
- 12 Uchida, M. *et al.* Protein Cage Nanoparticles Bearing the LyP-1 Peptide for Enhanced Imaging of Macrophage-Rich Vascular Lesions. *Acs Nano* **5**, 2493-2502, (2011).
- 13 Lee, Y. J. *et al.* Fabricating Genetically Engineered High-Power Lithium-Ion Batteries Using Multiple Virus Genes. *Science* **324**, 1051-1055, (2009).
- 14 Jordan, P. C. *et al.* Self-assembling biomolecular catalysts for hydrogen production. *Nat Chem* **advance online publication**, (2015).
- 15 Sun, J. *et al.* Core-controlled polymorphism in virus-like particles. *Proc Natl Acad Sci U S A* **104**, 1354-1359, (2007).
- 16 Uchida, M., LaFrance, B., Broomell, C. C., Prevelige, P. E. & Douglas, T. Higher Order Assembly of Virus-like Particles (VLPs) Mediated by Multi-valent Protein Linkers. *Small* **11**, 1562-1570, (2015).
- 17 King, N. P. *et al.* Accurate design of co-assembling multi-component protein nanomaterials. *Nature* **510**, 103-108, (2014).

Abbreviations

Introductory chapter

AFM	Atomic Force Microscopy
JM	Jumping mode
JM+	Jumping mode plus
HOPG	Highly Ordered Pyrolytic Graphite
HDMS	Hexamethyldisilazane
APTES	Aminopropyltriethoxysilane
FZC	Force-distance curve
FIC	Force-indentation curve
EDL	Electrostatic Debye Layer
VLP	Virus-like particle (or Vault-like particle)
MVM	Minute Virus of Mice
TBSV	Tomato Bushy Stunt Virus
P22 VLP	P22 virus-like particles

Chapters 2

VLP	Vault-like particle
MVM	Major vault protein
HOPG	Highly Ordered Pyrolytic Graphite
RT	Recovery time

Chapters 3

VLP	Vault-like particle
MVM	Major vault protein
QCM-D	Quartz Crystal Microbalance with Dissipation
DSF	Differential Scanning Fluorimetry

Chapter 4

TBSV	Tomato Bushy Stunt Virus
VNP	Virus-derived Nanoparticle
TBSV-NP	TBSV Nanoparticle (native virus)
ssRNA	single-stranded RNA
CP	coat protein
wt	wildtype
cVNP	compact TBSV-NP
sVNP	swollen TBSV-NP
rVNP	re-compacted TBSV-NP
ifVNP	ion-free TBSV-NPs

Chapter 5

VLP	Virus-like particles
SP	Scaffolding domain
CP	Coat protein
PC	Procapsid
EX	Expanded capsid (mature)
EGFP	Enhanced green fluorescence protein
CelB	β -glucosidase from the hyperthermophile <i>Pyrococcus furiosus</i>
Cryo-EM	cryo Electron Microscopy
3DR	3D reconstruction
HPLC	High-performance liquid chromatography
SEC	Size-exclusion chromatography
MALS	Multi-angle light scattering

Chapter 6

VLP	Virus-like particles
CP	Coat protein
SP	Scaffold protein
PC	Procapsid
EX	Expanded capsid (mature)
WB	Wiffle ball
SDS	Sodium dodecyl sulfate
SEC	Size-exclusion chromatography
MALS	Multi-angle light scattering
QELS	Quasi-elastic light scattering
TEM	Transmission Electron Microscopy
S5	5-fold symmetry axes
S3	3-fold symmetry axes
S2	2-fold symmetry axes

Chapter 7

MVM	Minute Virus of mice
ssDNA	single stranded DNA
HDX-MS	Hydrogen-deuterium exchange mass spectrometry
Nt	N-terminal
VP2	Capsid protein 2
ΔH	Enthalpy change

Study of Nanosized Protein Cages with Atomic Force Microscopy

The work presented in this chapter has been possible thanks to the collaboration of Prof. M. García-Mateu and Dra. M. Castellanos (MVM); Prof. Trevor Douglas, E. Edwards and B. Schwartz (P22 Bacteriophage); Prof. N. Verdaguer and P. Guerra (Vault particles); Prof. S. Cannistraro, Prof. L. Santi and E. Coppari (TBSV); and Prof. M. Manso and Dra. M. Hernando-Pérez (contact angle measurements).

Abstract

Stable imaging and manipulation of proteinaceous nanoparticles by Atomic Force Microscopy (AFM) have to overcome the challenge of scanning large and soft biological samples that can be easily damaged or detached during the imaging process. The success of this process requires a delicate balance between tip-sample and substrate-sample interaction. There are many reviews focused on the imaging modes or sample preparation procedures in the context of biological samples, here I illustrate some of these aspects using four different nanocages. Firstly, the imaging mode and substrates used during this thesis are presented. In this section it is shown, for example, that the choice of the substrate and electrolyte concentration modify the apparent height and percentage of adsorption of the minute virus of mice (MVM), which might be due to a conformational change that involves the reorganization of the capsid pore region. Secondly, the resolution and some technical aspects that should be considered during nanoindentation assays are discussed. Finally, the most relevant mechanical concepts in physical virology are summarized in three tables. Overall, this chapter intends to be both an introduction and practical guide to the experimental study of macromolecular nanostructures by AFM, highlighting some of the practical aspects that should be considered during an experiment.

Atomic Force Microscopy in Liquids – Jumping Mode Plus

The principles of Atomic Force Microscopy (AFM) are relatively simple. A sharp tip at the end of a flexible cantilever scans over the surface during consecutive sweeps. The deflection of this cantilever, caused by the probe-surface interaction, is detected by a photodiode that registers the movement of a laser beam focalized at the end of the cantilever.¹⁻³ This signal, in turn, is used as a feedback to reconstruct the sample surface and correct the position of the tip with a Z-piezo. There are different ways to correct for this position (termed as imaging modes) and they basically depend on which parameter is used for the feedback (*i.e.*, whether the normal force, the amplitude of oscillation, the frequency of oscillation, the amplitude of excitation, or a combination of the above, are the input parameters of the feedback).⁴ The mode employed during this thesis uses the normal forces as the input parameter, and it is based on jumping mode (JM).⁵ JM essentially operates by performing a force vs. Z-piezo distance curve (FZC) at each point of the image (Figure 1); the tip approaches the sample until the photodiode detects a normal deflection that corresponds to the set point selected by the user. To move between consecutive points, the tip displaces laterally when it is retracted from the sample, making it ideal to image biological sample because it minimizes the shear forces that you apply during the acquisition process.⁶

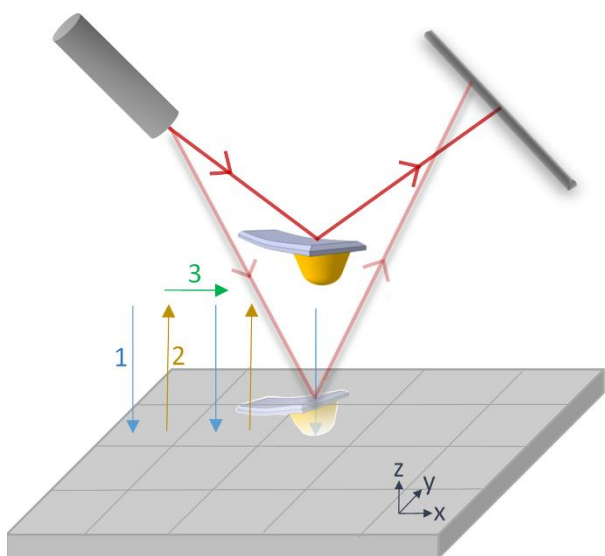


Figure 1. Schematic of jumping mode. At each point (pixel) of the image the tip perform a force vs. Z-displacement curve (FZC). It deflects up to a normal force (set point) set by the user. The image is acquired by sweeping each line with the x-scan and then moving to the next line with the y-scan. To move from point to point along the x-line the tip retracts and moves while is far from the substrate, minimizing shear forces and avoiding the damage of the sample. The retraction distance is also set by the user. Step 1 and 2 represent the approaching and retraction of the tip, step 3 represents the movement of the tip to another pixel.

Controlling tip-sample interaction forces is fundamental to achieve accurate imaging and manipulation of the sample. Soft biological specimens represent a challenge in this regard as they might be easily damaged during the imaging process. All the AFM experiments carried out in this thesis have been performed using jumping mode plus (JM+). JM+ represents an advantage in comparison with conventional JM as it confers a major control of the sample-tip interaction during the approach imaging cycle. This improvement was achieved by checking for the cantilever deflection as it approached to the surface, and stop it if the deflection was greater than the set point.⁷

Currently, the main technical drawback of JM+ (as it is for conventional JM) is the impossibility of acquiring high-speed images. For example, an image of 128x128 pixels (in the conditions required for measuring nanoparticles with an average height of 20-60 nm) typically last for 3 minutes. This hampers the possibility of exploring fast dynamics and might determine the choice of other imaging modes. However, for large macromolecular cages such as viruses, it is still one of the preferential choices. A comparison of the different AFM modes in the context of biological samples can be found in *Moreno-Herrero et al.*⁸

Adsorption of Nanoparticles on Substrates — HOPG, HDMS-coated Glass and Mica

In addition to an accurate control of the imaging parameters, substrate-sample interactions are also fundamental to have stable, high-resolution images of the probed specimen. Two main steps might be identified in the adsorption of nanoparticles. The first step involves the arrival of the particle at the surface, achieved by a diffusion process governed by the Brownian motion. The second step involves the binding of the particle to the substrate. The main driving forces responsible for this ‘physical’ attachment (*i.e.*, specimens are not covalently linked to a chemical modified support) are the van der Waals force, the electrostatic double layer (EDL) force, and the forces arising from the hydrophobic effect.⁹ The hydrophobicity of many proteins seems to play an important role in their adsorption on surfaces¹⁰ and several experimental AFM studies performed on viruses indicate that hydrophobic interactions represent also an efficient anchoring mechanism for these large macromolecular self-assemblies.¹¹ HOPG (chapter 1, 2 and 5), glass coverslips

functionalized with HDMS (chapter 4) and mica (chapter 3) were the substrates used for this thesis. HOPG and HDMS-coated glasses are two hydrophobic substrates, whereas mica becomes negatively charged when submerged in water.¹² To alter the surface density charge of the substrate different electrolytes might be incorporated to the buffer. Positively rather than negatively charged substrates are the preferential choice for AFM imaging of virus particles, as most of these proteinaceous self-assemblies display a net negative charge on the capsid exterior shell.¹³ Therefore, in order to create a positive layer of ions on top of the mica substrate, NiCl_2 was added to the buffer for the experiments of Tomato Bushy Stunt Virus (TBSV) (chapter 3). It should be mentioned that mica was the final choice for TBSV because these particles were usually displaced during nanoindentation experiments on HOPG. This weak HOPG-TBSV anchoring was also noticeable during the imaging process, where particles could be observed moving on the substrate likely due to the scanning process (Figure 2).

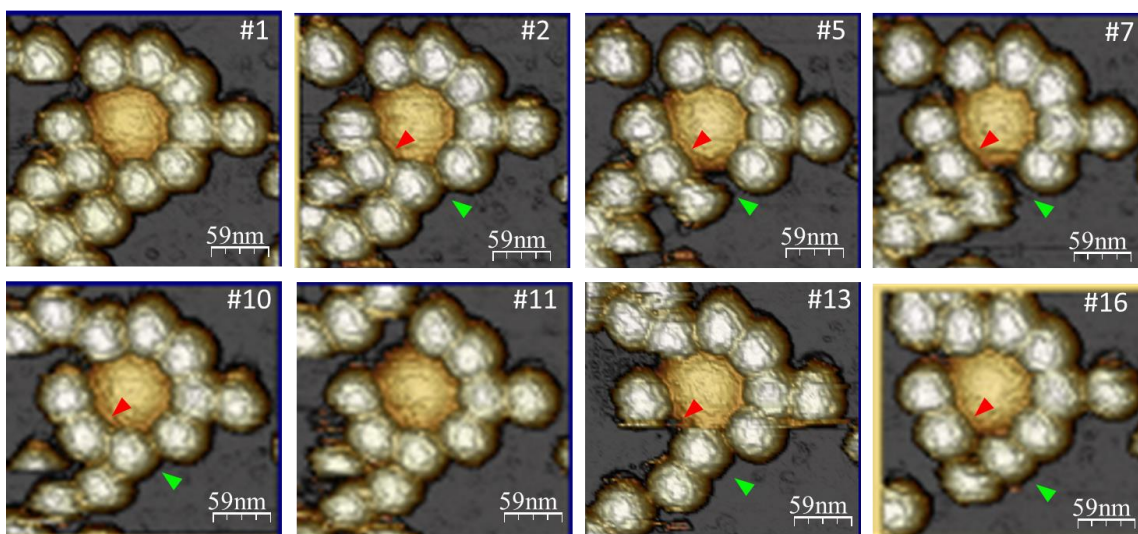


Figure 2. Diffusion of TBSV nanoparticles adsorbed on HOPG. Due to the weak interaction between the particles and the HOPG, the imaging process (performed with forces below 80 pN) induced the movement of the viruses. Different frames (#) of a movie acquired by scanning the same area consecutively are represented. Red and green arrowheads show positions presenting, alternatively, the presence and absence of particles.

The choice of the substrate for each specific nanoparticle was always made after testing the adsorption of the specimen on, at least, three different surfaces. The protein complexity of nanosized molecular cages makes very challenging to determine *a priori* what the most suitable substrate will be (even the adsorption of small proteins on surfaces is still a complex

and poorly understood process).¹⁴ Although hydrophobic surfaces were usually the preferential choice, a distinction between them should be made because different hydrophobic surfaces might have different effects on the adsorption process. In addition, the water molecules and salt ions present in solution are also an active component of the system. Changing the ionic strength (salts) or the pH of the solution might increase or reduce the electrostatic tip-sample interaction, which in turn might modify the height of the probed structures, their mechanical properties, or the adsorption configuration.^{15,16} Salts influence these outputs by screening electrical charges or modifying the hydrophobic effect. Low salt concentrations (<0.2mol/l) typically leads to the screening of surface charge-charge interaction (increase of the Debye length), while higher salt concentrations results in an increase of the hydrophobic effect.¹⁷ The stability, efficiency of attachment, and final configuration of a protein depends on both the specimen and the substrate, and with the current knowledge it is hard to predict in advance the final configuration of the system. An example of this is presented below, where the minute virus of mice (MVM) was studied for two different hydrophobic substrates (HOPG and HDMS-coated glass) under two different buffer solutions (PBS 1x and PBS 5x) (Figure 3). PBS 5x contained 5 times more salt concentration than PBS 1x (PBS 1x: 137 mmol/L NaCl, 2.7mmol/L KCl, 20.40mmol/l Na₂HPO₄, 1.8 mmol/L KH₂PO₄ pH=7.4).

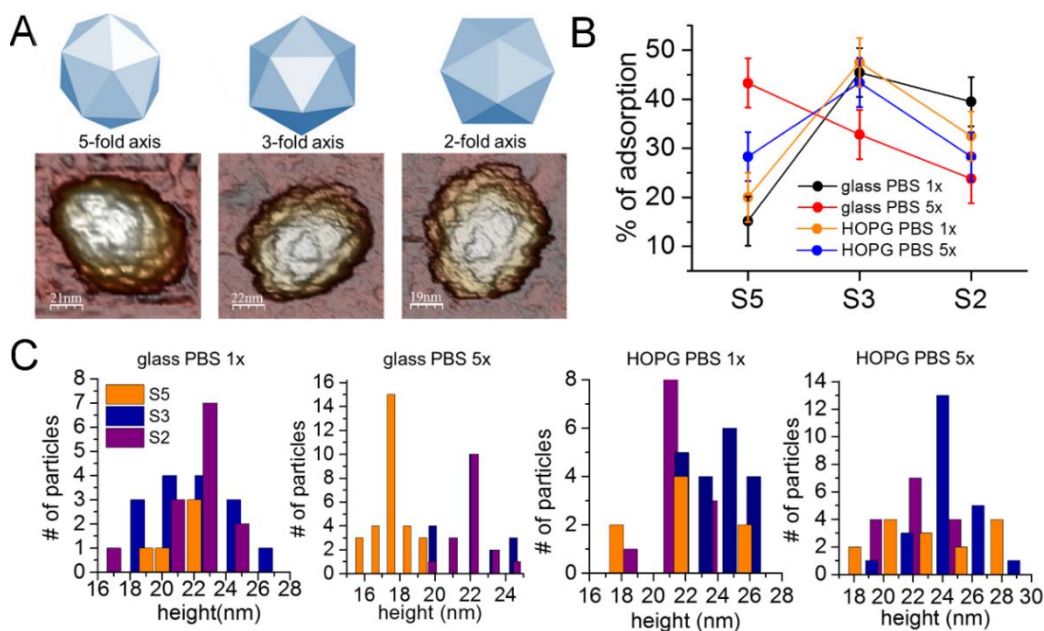


Figure 3. MVM adsorption of HDMS-coated glass and HOPG at two ionic strength. (A) AFM images of MVM capsids orientated along the 5-, 3- and 2-fold symmetry axes. An icosahedron is shown on top of each

High-resolution AFM images of MVM VLPs (150x150 nm²) could be easily classified according to their orientation as S5, S3 and S2, as previously done in several studies¹⁸⁻²² (Figure 3A). Our results revealed that the relative percentage of adsorption depended on both the substrate and the buffer (Figure 3B). The S5 orientation was the least frequently observed orientation for HOPG (at both salt concentration) or HDMS-coated glass at PBS 1x, but resulted the most frequent orientation for HDMS-coated glass under PBS 5x buffer. Noticeably, this increase in adsorption was accompanied by a significant decrease in height along the 5-fold axes, from ~21 nm to ~18 nm (Figure 3C and table 1). The S2 orientation did not present significant variation, whereas the S3 showed a slight decrease in height (~1.5 nm) between HOPG and HDMS-coated glass. Our results suggested that an increase in the electrostatic interaction (achieved at PBS 5x), together with the different nature of the substrate, promoted a conformational change that could only be trapped by the HDMS-coated glass. Analysis of the hydrophobicity of the different substrates performed with an optical water contact angle system (KSV CAM-101)²³ revealed that the HDMS-coated glass was the most hydrophobic substrate, with a surface angle of (83±5)° in comparison with the (66±5)° angle presented by HOPG (table 1). We might speculate that the ‘major hydrophobicity’ of the HDMS-coated glass can be the reason of the disagreement between both substrates, but the fact that HDMS is an organic compound that exposes methyl groups on the surface, with certain flexibility, in contrast to HOPG —composed of highly-ordered carbon conforming an hexagonal lattice— might also be the cause. It seems reasonable, though, to expect that the exposure of some residues around the pore, presumably hydrophobic, are the responsible for this capsid rearrangements that enhance the probability of anchoring the samples along the 5-fold symmetry axes. We mentioned above that the nature of the substrate and the electrolyte composition of the buffer determine the tip- and substrate-sample interaction, and thus the frequency of adsorption or the height of the particle, but the MVM example suggests

← (continued) AFM image for clarity. (B) Percentage of adsorption depending on the substrate and ionic strength for the three symmetry axes. The S5 orientation become the most frequent for HDMS-coated glass and PBS 5x (red line). (C) Histograms of height for the four different conditions. Particles adsorbed on HDMS-coated glass (PBS 5x) show a decrease in height for all orientation, with a more significant reduction along the 5-fold symmetry axes. It seems likely that under these conditions the particles had adopted a different configuration

that it can also trap (or promote) different structural configurations. Controlling and being aware of these limitations is fundamental not only to optimize the imaging process but also to properly drive conclusions of the AFM measurements. For example, in previous AFM studies it was assumed that the distribution of occurrence of the three symmetry sites could be based on the icosahedron structure of the virus (*i.e.*, the S3:S2:S5 ratio was expected to be 20:30:12, corresponding to 20 faces, 30 edge, and 12 vertices).²⁴ Our current data indicate that the assumption was probably mistaken, the frequency of adsorption is a buffer-, particle- and surface-specific process that have to be experimentally assessed case-by-case.

	contact angle (83±5)°						contact angle (66±5)°					
	Glass PBS 1x			Glass PBS 5x			HOPG PBS 1x			HOPG PBS 5x		
	#	mean	SE	#	mean	SE	#	mean	SE	#	mean	SE
S5	5	20.6	0.5	29	17.7	0.2	15	21	1	8	21.9	0.8
S3	15	22.5	0.6	22	22.0	0.3	23	23.9	0.4	19	23.9	0.4
S2	13	22.3	0.6	17	22.0	0.3	14	22.5	0.5	12	22.7	0.5

Table 1. Height of the particles sorted by symmetry, ionic strength and substrate. # indicates the number of particles and SE the standard error.

Finally, the substrate preparation or its cleanness are also important aspects to factor in before making the final substrate choice. HOPG and mica only require the cleavage of the upper layers, which can be easily achieved by peeling them with a piece of tape. It is a fast procedure that leads to very clean and flat surface. HDMS-coated glass coverslips have to be cleaned with a KOH solution mixed with ethanol and functionalized overnight in HDMS vapor.²⁵ It is a simple procedure that also leads to clean and flat surface, but it takes longer and substrates have to be replaced monthly. Other well-established methods for substrate preparation, such as the functionalization of mica with polylysine⁹ or APTES,²⁶ were generally discarded because the tip was easily contaminated during the imaging process.

For an overview of the most standardized biological sample preparation procedures for AFM imaging, beyond the three cases exposed here, see *El Kirat et al.*²⁷

Tip-Sample Interaction and Mechanical Properties of Virus Cages

AFM is not only suitable for imaging different samples but it can also manipulate them. By pushing on a particle with an AFM tip it is possible to apply forces and measure how the particles respond to them. The interaction between the AFM tip and the probed particle (or substrate) can be generally described with an intermolecular Lennard-Jones potential (Figure 4).

$$V_{LJP} = 4\epsilon \left[\left(\frac{\sigma}{r} \right)^{12} - \left(\frac{\sigma}{r} \right)^6 \right], \quad [1]$$

where ϵ is the depth of the potential well, σ is the distance at which the potential is zero, and r the distance between the two objects (i.e., between the tip and the sample or the tip and the substrate). The distance at which the potential reaches its minimum is defined as r_{eq} and corresponds to the point of zero force, at the border between the attractive and repulsive regimes (Figure 4).

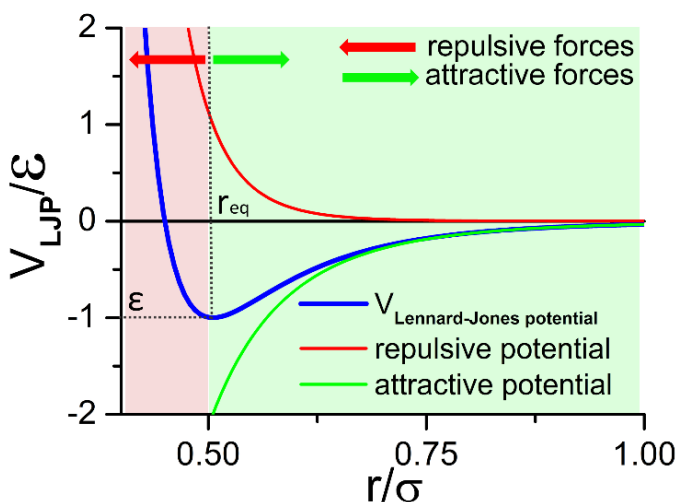


Figure 4. Lennard-Jones potential representing the tip-sample interaction.

Two regimes might be distinguished as a function of the distance: attractive forces dominate at large distance (green region), whereas at shorter differences the interaction is governed by repulsive forces (red region). It is important to notice that under liquid conditions the attractive region is significantly reduced and the tip might transition from no-interaction to repulsive interaction directly.

In liquid, these attractive and repulsive terms basically account for:¹²

- 1) Contact force.** It is a short-range repulsive force that arises from the overlapping electron orbitals. These contact force deform contacting objects by displacing their atoms and molecules.

2) Hydration force. It is a short-range repulsive interaction (~ 0.5 nm).²⁸ Its nature is attributed to the work required to remove water molecule from the vicinity of the interacting surfaces. In the field of physical virology, this force has been shown to increase the strength of lambda WT phages.²⁹

3) Van der Waals force (vdW). It is a long-range attractive force that arises from the interaction between permanent or induced dipoles of molecules. In liquids, the range of this force is of the order of 1-2 nm and, in comparison with vacuum conditions, its contribution is almost negligible.³⁰ It is particularly important to bear this last point in mind when one looks at the widely used Lennard-Jones potential to describe tip-sample interactions because, in most of our experiments (performed in aqueous solution), the attractive contribution might be so negligible that the tip transitions directly from no-interaction to repulsive interaction.

An example of this can be seen in the inset of [Figure 5A](#): whereas the FZC performed on the substrates displays a ‘jump’ to contact when approaching the sample due to the vdW attraction (blue curve), the FZC performed on the particle does not experience any attractive interaction before reaching the contact point (red curve).

4) Coulombic electrostatic force. It is a long-range attractive or repulsive force that is caused by the presence of charges on the tip and/or substrate. In aqueous medium, this force is almost always present and repulsive, even if the surfaces do not display a net surface charge.^{31,32}

The charging of surfaces in liquids can come about in two ways: by the dissociation of surface groups or by the adsorption of ions onto the surface. An electric double layer (EDL) formed by the electrolyte of the solution is formed in the vicinity of the surface due to the charged nature of the surfaces. This layer screens the surface charges and decays exponentially in a range set by the Debye screening length (λ_D), which depends on both the charge z_i and the concentration c_i of the electrolytes

$$\lambda_D \propto \frac{1}{\sum_i c_i z_i^2}$$

The modulation of this EDL repulsion between the sample and the tip might mitigate the local effect of undesired forces and allow for higher resolution.³³ In addition, the EDL forces have allowed to calculate with AFM the surface density charge of DNA molecules³⁴ and, more recently, of virus particles.³⁵

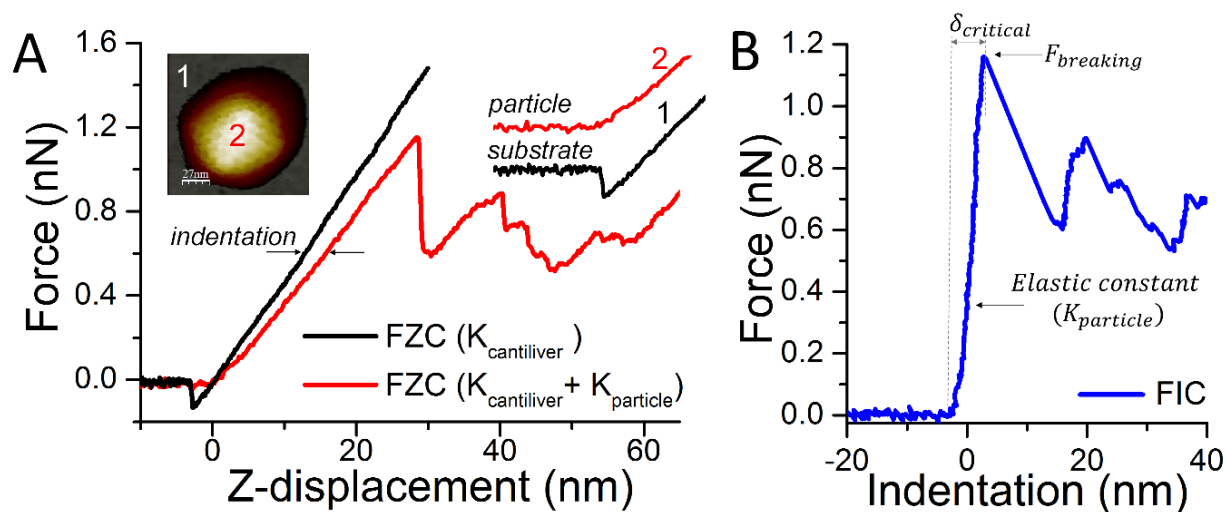


Figure 5. Nanoindentation experiment on an expanded P22 VLP particle. (A) Force-distance curves (FZC) performed on: substrate (black line) and particle (red line). The differences between both slopes accounts for the deformation of the particles (indentation). (inset) Zoom-in of the transition to contact for both the particle and the substrate. The tip did not experience any attractive force during its approach to the particle surface. (B) Force-indentation curve (FIC) of the particle. It was obtained by subtracting the contribution of the cantilever. Mechanical parameters such as critical indentation, breaking force or elastic constant can be obtained from this curve.

In the field of physical virology, the deformation of particles have been widely interpreted in the framework of continuum elasticity theory of thin elastic shells, where the cantilever and the particle are represented as two spring constants in series, both presenting a linear initial deformation.^{36,37} Figure 5A shows two force-distance curves (FZC) performed, respectively, on a substrate (black curve) and a particle (red curve). Whereas the FZC performed on the substrate only accounts for the deformation of the cantilever (the cantilever stiffness used in our experiments is so low that the substrate can be considered to a very good approximation as an undeformable object), the FZC performed on the particle contains the deformations of both the cantilever and the particle. Therefore, in order to obtain the mechanical properties of the particle alone, the contribution of the cantilever has to be eliminated. This is achieved

by subtracting the black curve (cantilever) from the red curve (cantilever and particle), a process that leads to the force-indentation curve (FIC) (Figure 5B). The FIC contains information about the critical deformation, the rigidity (elastic constant) and the breaking force of the particle.^{11,38}

From the force-indentation curve (FIC) we can extract information about the mechanical properties of the nanoparticles, such as the elastic constant or the breaking force (Figure 5B). The mechanical concepts and parameters used in AFM studies of nanoparticles are summarized in three tables at the end of the chapter (table 2, 3 and 4). These parameters permitted the comparison not only of different morphology of a given specie, but also between species. It is important to notice that the technical parameters of the FIC, such as the loading rate or the number of points acquired per curve, might also affect our results and thus have to be considered (Figure 6).

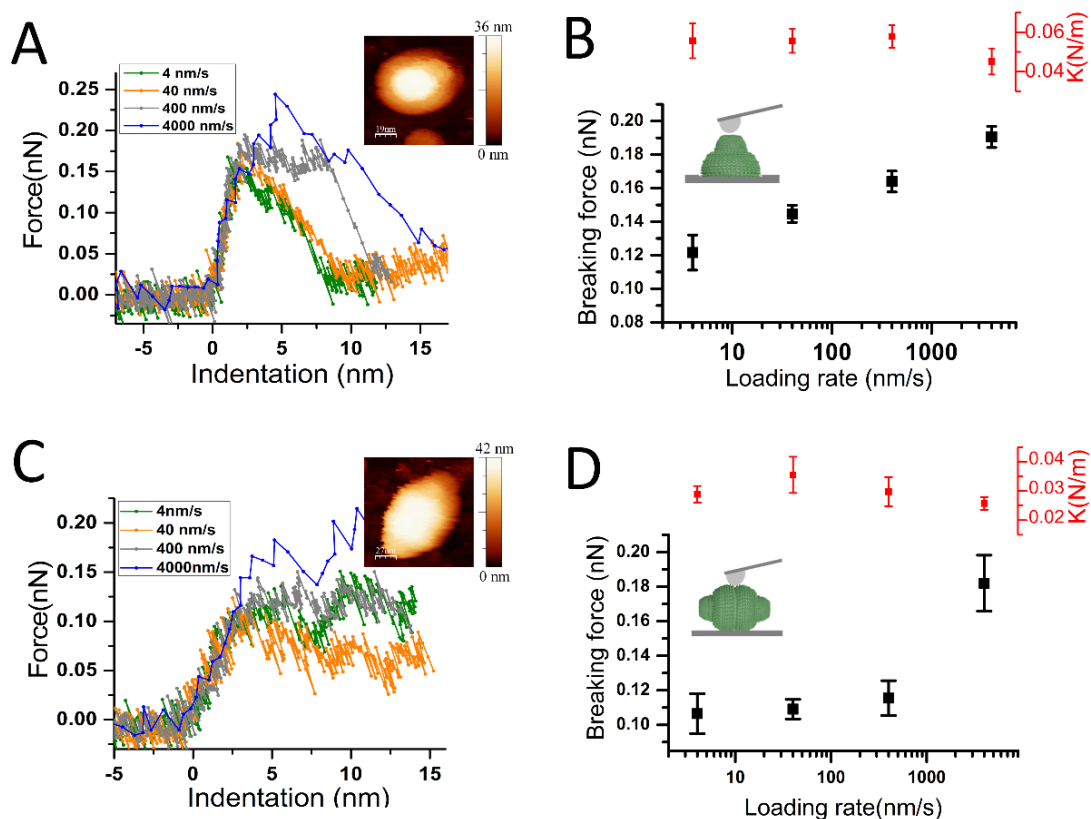


Figure 6: Dependence of the mechanical parameters on the loading rate (A) Force vs. indentation curves performed on a half-vault at different loading rates. The images of the half-vault is shown as an inset. Because of the self-healing capacity of the particle multiple FICs at different loading rates could be performed on the same particle. Nanoindentations were acquired at 40 nm/s, 34 FICs at 340 nm/s, and 29 FICs at 4000 nm/s. The FICs were obtained for 7 different particles. (B) Evolution of the elastic constant and the breaking force as a

Figure 6 shows the results of an experiment performed on vault particles to address this issue. Nanoindentations were acquired at four different loading rates and the elastic constant and breaking force were compared. The results indicated that there was an exponential dependence of the breaking force on the loading rate for half-vaults (Figure 6A and 6B), but this value was maintained for full-vaults up to loading rates of 400 nm/s (Figure 6C and 6D). This distinct behavior was already found in studies performed on CCMV, HK97 and phi29,³⁹ where different dependency of the breaking force and elastic constant on the loading rate were observed within each specie. Such considerations are especially relevant when comparing the experiments with molecular dynamics simulations, where the loading rates might be orders of magnitude faster⁴⁰ than the experimental ones (most of the AFM experimental studies performed on virus to date, including the ones in this thesis, have been performed at loading rates between 60-100 nm/s). In addition, further exploring of these dependencies might provide insights into the unbinding/rebinding mechanism of large macromolecular cages (in a way similar to that of smaller proteins^{41,42}) or might permit studying viscoelastic properties of viral cages.^{43,44}

Spatial Resolution —Intra-Capsomeric Details Revealed by AFM

The resolution of AFM depends mainly in three factors: the control of tip-sample interaction, the anchoring of the sample to the substrate and the tip geometry. In the late nineties, the proper adjustment of pH and concentration of electrolyte permitted to successfully image biological samples in contact mode with lateral resolutions of 0.5 nm and normal resolutions of 0.1 nm.⁴⁵ However, it was not until 2010 when acquiring images of biological systems with sub-nanometer resolution in liquids (lateral resolution of 0.5 nm) was possible with dynamic modes.^{28,46-49} The advantage of dynamic or jumping mode in comparison with contact modes is that they apply lower frictional (lateral) forces, thus enabling to image

← function of the loading rate (4 nm/s, 40 nm/s, 400 nm/s and 4000 nm/s). The values are obtained after averaging 26 FICs at 4 nm/s, 46 FICs at 40 nm/s, 34 FICs at 34 nm/s, and 29 FICs at 4000 nm/s. The FICs were obtained (continued) for 7 different particles. (C,D) Same than before but performed on a full-vault reclining on the barrel. The values of the graph were obtained for 7 different particles after averaging 16 FICs at 4 nm/s, 42 FICs at 40 nm/s, 19 FICs at 34 nm/s, and 15 FICs at 4000 nm/s.

isolated molecules weakly bound. These sub-nanometer, high-resolution images of biological systems, however, have been acquired in lipid layers or small molecules, such as DNA.

The maximum lateral resolution achieved by AFM in viruses is on the order of 5 nm.^{50,51} This resolution has permitted to resolve the trimers of adenovirus particles,⁵⁰ the intra-pentameric subunits of bacteriophage T7,⁵¹ or the capsomeric structure of herpes simplex virus⁵² or lambda phage.⁵³ All the previous examples were acquired using JM or JM+, although it must be mentioned that detailed structure of viruses has also been resolved with dynamic modes.^{54,55} Perhaps, an advantage of JM for measuring such large molecular cages, which likely explains why it has been so successfully used in the field, is that it provides a very accurate control of the imaging force, avoiding undesirable peak-forces that might damage or move the sample.⁵⁶ In addition, JM and JM+ offer a much simpler interpretation than dynamic modes, where the motion cantilever and forces exerted by the tip are always much harder to model.

In this thesis, JM+ has allowed us to acquire images of vault particles, whose delicate structure hampered their visualization with dynamic modes or conventional jumping mode (chapter 2 and 3); visualize the granular structure of TBSV, attributed to the protruding domains of the virus (chapter 4); and resolving the capsomeric structure of mature expanded P22 VLPs, with lateral resolutions of ~5 nm, which enabled us to identify the pentamers and hexamers that compose the capsid (chapter 5 and 6) (Figure 7).

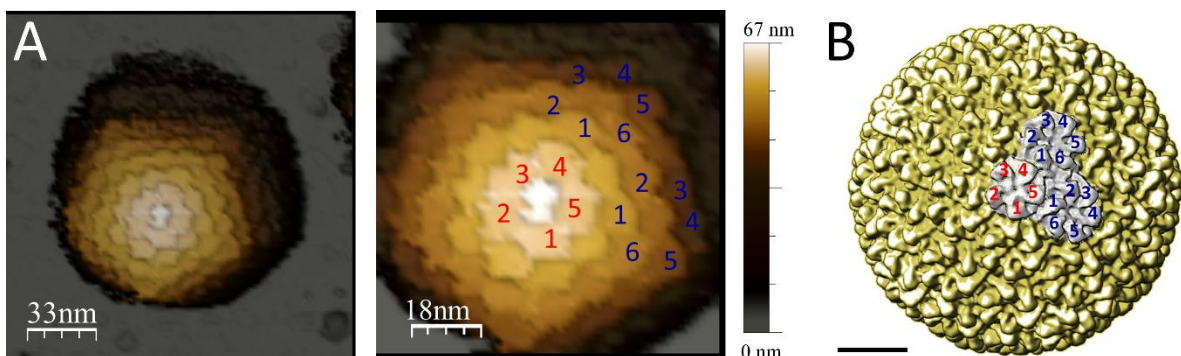


Figure 7. AFM images of expanded P22 VLP. (A) (left) 3D AFM topography of a P22 VLP adsorbed along the 5-fold symmetry axes. (right) A zoom-in of the same image with the position of intra-pentameric (red) and intra-hexameric (blue) subunits labelled on top. (B) Cartoon of an expanded P22 VLP based on the cryo-EM

We mentioned above that the physical size of the tip is one of the main bottlenecks that limits AFM resolution. The lateral resolution (l) between two objects imaged by a parabolic tip with a radius R_{tip} is

$$l = \sqrt{2R_{\text{tip}}} (\sqrt{\delta z + \Delta h}) \quad [2]$$

where δz is the vertical resolution and Δh is the height differences (Figure 8). Because the vertical resolution ($\sim 0.07 \text{ nm}$ for a cantilever with a spring constant of $K_c = 0.07 \text{ N/m}$)⁵⁷ is a factor 100 times lower than the lateral resolution, formula [1] is often expressed as

$$l = \sqrt{2\Delta h R_{\text{tip}}} \quad [3]$$

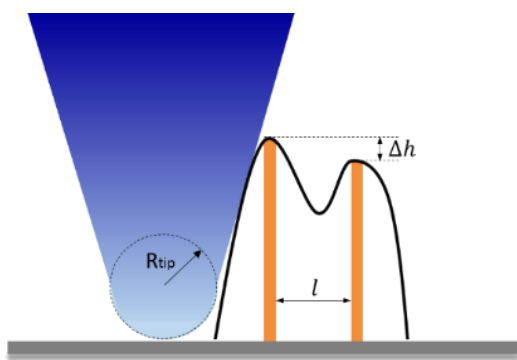


Figure 8. Schematic of the lateral resolution achieved by an AFM tip of radius R_{tip} . The distance (l) and height difference (Δh) between two objects limit the lateral resolution (equation 2). Adapted from *Biophysical determinants for adenovirus uncoating and infectivity*.¹²

A consequence of the finite size of the tip is that the probed objects appeared dilated (black line, figure 8). Note, however, that this dilation only affects the lateral resolution, not the vertical resolution (height).

The nominal radius of the AFM tip used during my experiments, and most of the mechanical experiments performed in viruses,¹¹ is 15 nm (Olympus cantilever, RC800PSA). Therefore, the fact that the resolution commonly achieved is of the order of 5 nm means that, for most of the cases, the “effective tip radius” is smaller than the nominal radius. A small apex attached to the end of the tip is likely the responsible for achieving such good resolution (inset, Figure 9). It is important to notice, however, that this apex is not the responsible for determining the lateral width of the particles, which typically present heights in the range of 30-100 nm and, therefore, is dilated with the nominal size of the tip (black line, Figure 9).

← (continued) data (chapter 5). A penton and two hexamers are highlighted in white and labelled correspondingly to the AFM image. Bar scale: 17 nm.

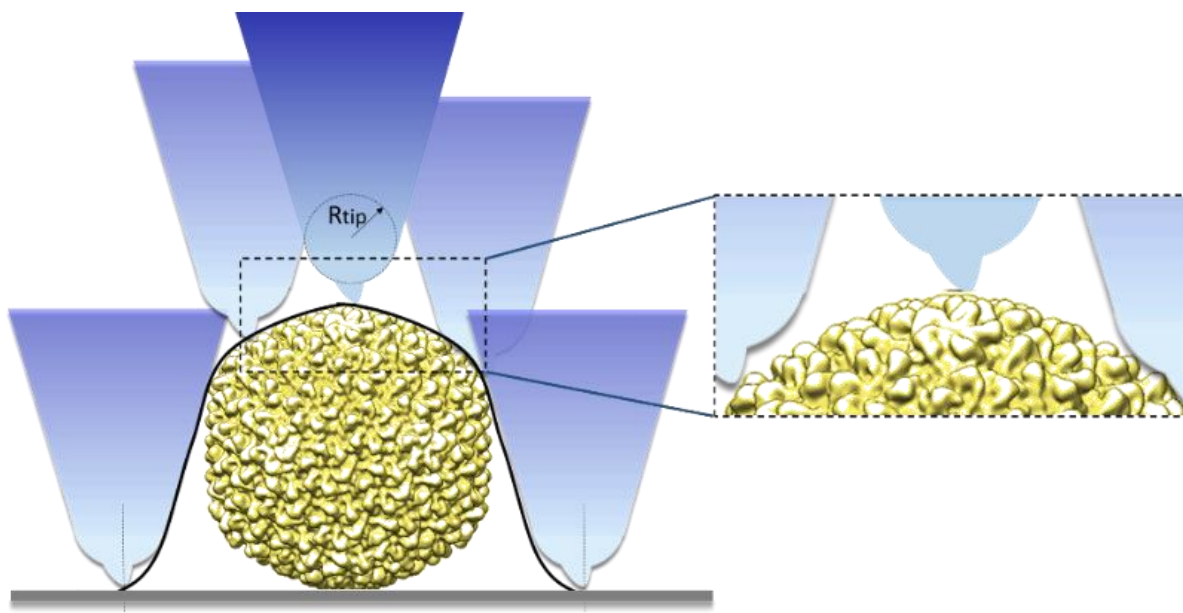


Figure 6. Schematic of the dilation process of a viral particle. The black line indicates the dilated profile of the particle. Due to the finite size of the AFM tip, the width appear wider. (Inset) Because the dilation on top of the particles is performed with a smaller object (apex), the resolution of the surface features is higher.

Concept	Description
Stiffness/rigidity	Ability of a material to resist deformation in response to an applied force. The opposite of a rigid material is a soft material (do not confuse with hard). Likewise, the complementary concept is flexibility: the more flexible an object is, the less stiff it is.
Mechanical strength	The ability to withstand an applied load without failure or plastic deformation.
Brittleness	A brittle material breaks without significant deformation.
Elastic deformation	Reversible deformation — upon unloading the object return to its original shape.
Plastic deformation	Irreversible deformation — upon unloading the object dos not return to its original shape.
Resilience	Ability of a material to absorb and release energy when it is deformed elastically.
Toughness	Ability of a material to absorb (elastic and plastic) energy without fracturing
Fatigue	The weakening of a material caused by repeated loading. The failure of the material is caused by the accumulation of cracks (broken bonds in a nanostructure). In physical virology the resistance to fatigue has been related to the probability of a virus to survive in crowded environments. ⁵³

Table 2. Mechanical concepts of material science.

Quantity	Abbreviation/Formula	Units	Definition	Related concept	
Height	height	nm	Height of the particle	Deformability	
Elastic constant	k	N/m	Resistance of a material to be deformed under a force	Stiffness/Rigidity	
Breaking Force	$F_{breaking}$	nN	Maximum force required to break a particle	Mechanical Strength	
Critical Deformation	$\delta_{critical}$	nm	Deformation at which the particle breaks	Brittleness	
Continuum Elastic Theory	Critical strain	$\varepsilon = \frac{\delta_{critical}}{height}$ [¶] $\left(\varepsilon \propto \frac{\delta_{critical}}{Radius}\right)$ [§]	-	Normalized critical deformation	Brittleness
	Elastic constant	$k = \frac{F_{breaking}}{\delta_{critical}}$ [¶]	nN/nm	Resistance of a material against a normal linear deformation.	
	2D Young's modulus	$Y = E_{3D}h$	MPa	Resistance of a material against normal linear deformation	Stiffness/rigidity
	3D Young's modulus	$E_{3D} = \frac{\sigma}{\varepsilon}$ $\left(E_{3D} \propto \frac{Rk_{shell}}{h^2}\right)$ [*]			
Elastic & Plastic behavior	Elastic limit (yield force)	$F_{elastic\ limit}$	nN	Force at which a material starts deform plastically	Related to resilience and toughness
Energy	For fracturing bonds	$E_{fract} = E_{before} - E_{after}$	K _B T	Energy to rupture a bond – subtracting the elastic energy before and after the fracture	Intermonomeric Energy
	Elastic	$E_{elastic} = \frac{F_{breaking} \cdot \delta_{critical}}{2}$ [¶]	K _B T	Elastic energy supplied to a particle to produce the breakage	Resilience
Cyclic loading with nanoindentations (FIC)	# of FICs	-	Number of FICs performed per particle	Mechanical fatigue	
Cyclic loading with imaging	# of images	-	Number of images acquired per particle – proportional to the number of FICs		

Table 3. Mechanical terms and nomenclature used in AFM studies of protein nanostructures. [¶]Linear behavior. [§]Very often the deformation capacity (brittleness) of a virus is expressed as a fraction of the capsid radius ^{*}Thin shell loaded with a point force (R is the radius of the shell and h the thickness).

Quantity	Abbreviation/Formula	Units	Definition	Virus mechanics' related concept
Shell thickness	h	nm	Average thickness of a shell	-
Shell Radius	R	nm	Average radius of the shell	-
Normal Stress	$\sigma = \frac{F_{normal}}{area}$	MPa	Force per unit area	-
Normal Strain	$\varepsilon = \frac{\Delta L}{L}$	-	Ratio of the total deformation to the initial dimension	-
Poisson ratio	$\nu = -\frac{d\varepsilon_{trans}}{d\varepsilon_{axial}}$	-	Relationship between the transverse and axial strain	-
Bending rigidity	$\kappa = \frac{Yh^2}{12(1-\nu^2)}$	K _{BT}	Resistance of a material against bending deformation	-
				Level of sphericity
Föppl-von Kármán number	$\gamma = \frac{YR^2}{\kappa} = 12(1-\nu^2)\left(\frac{R}{h}\right)^2$	-	Relationship between the stretching and bending energies	- $\gamma \leq 150$ (sph.) $\gamma \geq 300$ (ang.)

Table 4. Mechanical concepts used in physical virology.

References

- 1 Binning, T. & Miller, M. Approaches to the management of soft tissue defects of the malleolar region. *Clinics in podiatric medicine and surgery* **3**, 769-780, (1986).
- 2 Meyer, G. & Amer, N. M. Novel optical approach to atomic force microscopy. *Appl Phys Lett* **53**, 1045-1047, (1988).
- 3 Alexander, S. *et al.* An atomic-resolution atomic-force microscope implemented using an optical lever. *Journal of Applied Physics* **65**, 164-167, (1989).
- 4 Jaafar, M. *et al.* Drive-amplitude-modulation atomic force microscopy: From vacuum to liquids. *Beilstein journal of nanotechnology* **3**, 336-344, (2012).
- 5 de Pablo, P. J., Colchero, J., Gómez-Herrero, J. & Baró, A. M. Jumping mode scanning force microscopy. *Appl Phys Lett* **73**, 3300-3302, (1998).
- 6 Moreno-Herrero, F. *et al.* Jumping mode scanning force microscopy: a suitable technique for imaging DNA in liquids. *Appl Surf Sci* **210**, 22-26, (2003).
- 7 Ortega-Esteban, A. *et al.* Minimizing tip-sample forces in jumping mode atomic force microscopy in liquid. *Ultramicroscopy* **114**, 56-61, (2012).
- 8 Moreno-Herrero, F., Colchero, J., Gomez-Herrero, J. & Baro, A. M. Atomic force microscopy contact, tapping, and jumping modes for imaging biological samples in liquids. *Phys Rev E* **69**, (2004).
- 9 Muller, D. J., Amrein, M. & Engel, A. Adsorption of biological molecules to a solid support for scanning probe microscopy. *Journal of Structural Biology* **119**, 172-188, (1997).
- 10 Wang, D., Douma, M., Swift, B., Oleschuk, R. D. & Horton, J. H. The adsorption of globular proteins onto a fluorinated PDMS surface. *J Colloid Interf Sci* **331**, 90-97, (2009).
- 11 Mateu, M. G. Mechanical properties of viruses analyzed by atomic force microscopy: A virological perspective. *Virus Res* **168**, 1-22, (2012).
- 12 Ortega-Esteban, A. *Biophysical determinants for adenovirus uncoating and infectivity* Physics thesis, UAM, (2015).
- 13 Siber, A., Bozic, A. L. & Podgornik, R. Energies and pressures in viruses: contribution of nonspecific electrostatic interactions. *Phys Chem Chem Phys* **14**, 3746-3765, (2012).
- 14 Di Marco, M. *et al.* Overview of the main methods used to combine proteins with nanosystems: absorption, bioconjugation, and encapsulation. *Int J Nanomed* **5**, 37-49, (2010).
- 15 Medalsy, I. D. & Muller, D. J. Nanomechanical Properties of Proteins and Membranes Depend on Loading Rate and Electrostatic Interactions. *Acs Nano* **7**, 2642-2650, (2013).
- 16 Muller, D. J. & Engel, A. The height of biomolecules measured with the atomic force microscope depends on electrostatic interactions. *Biophys J* **73**, 1633-1644, (1997).
- 17 Date, M. S. & Dominy, B. N. Modeling the Influence of Salt on the Hydrophobic Effect and Protein Fold Stability. *Commun Comput Phys* **13**, 90-106, (2013).
- 18 Carrasco, C. *et al.* DNA-mediated anisotropic mechanical reinforcement of a virus. *Proceedings of the National Academy of Sciences* **103**, 13706-13711, (2006).

- 19 Carrasco, C., Castellanos, M., de Pablo, P. J. & Mateu, M. G. Manipulation of the mechanical properties of a virus by protein engineering. *P Natl Acad Sci USA* **105**, 4150-4155, (2008).
- 20 Castellanos, M. *et al.* Mechanical elasticity as a physical signature of conformational dynamics in a virus particle. *P Natl Acad Sci USA* **109**, 12028-12033, (2012).
- 21 Castellanos, M., Carrillo, P. J. P. & Mateu, M. G. Quantitatively probing propensity for structural transitions in engineered virus nanoparticles by single-molecule mechanical analysis. *Nanoscale* **7**, 5654-5664, (2015).
- 22 Castellanos, M., Perez, R., Carrillo, P. J. P., de Pablo, P. J. & Mateu, M. G. Mechanical Disassembly of Single Virus Particles Reveals Kinetic Intermediates Predicted by Theory. *Biophys J* **102**, 2615-2624, (2012).
- 23 Naveas, N. *et al.* Fabrication and characterization of a chemically oxidized-nanostructured porous silicon based biosensor implementing orienting protein A. *Colloids and surfaces. B, Biointerfaces* **115**, 310-316, (2014).
- 24 Roos, W. H. *et al.* Squeezing Protein Shells: How Continuum Elastic Models, Molecular Dynamics Simulations, and Experiments Coalesce at the Nanoscale. *Biophys J* **99**, 1175-1181, (2010).
- 25 Ivanovska, I. *et al.* Exploring the nano-mechanics of single virus shells using scanning force microscopy. *Biophys J* **86**, 153a-154a, (2004).
- 26 Crampton, N., Bonass, W. A., Kirkham, J. & Thomson, N. H. Formation of aminosilane-functionalized mica for atomic force microscopy imaging of DNA. *Langmuir* **21**, 7884-7891, (2005).
- 27 El Kirat, K., Burton, I., Dupres, V. & Dufrene, Y. F. Sample preparation procedures for biological atomic force microscopy. *J Microsc-Oxford* **218**, 199-207, (2005).
- 28 Herruzo, E. T., Asakawa, H., Fukuma, T. & Garcia, R. Three-dimensional quantitative force maps in liquid with 10 piconewton, angstrom and sub-minute resolutions. *Nanoscale* **5**, 2678-2685, (2013).
- 29 Ivanovska, I., Wuite, G., Jonsson, B. & Evilevitch, A. Internal DNA pressure modifies stability of WT phage. *P Natl Acad Sci USA* **104**, 9603-9608, (2007).
- 30 Garcia, N. & Binh, V. T. van der Waals forces in atomic force microscopy operating in liquids: A spherical-tip model. *Physical review. B, Condensed matter* **46**, 7946-7948, (1992).
- 31 Butt, H. J. Measuring electrostatic, van der Waals, and hydration forces in electrolyte solutions with an atomic force microscope. *Biophys J* **60**, 1438-1444, (1991).
- 32 Parsegian, V. A. & Gingell, D. On the electrostatic interaction across a salt solution between two bodies bearing unequal charges. *Biophys J* **12**, 1192-1204, (1972).
- 33 Fotiadis, D., Scheuring, S., Muller, S. A., Engel, A. & Muller, D. J. Imaging and manipulation of biological structures with the AFM. *Micron* **33**, 385-397, (2002).
- 34 Sotres, J. & Baro, A. M. AFM imaging and analysis of electrostatic double layer forces on single DNA molecules. *Biophys J* **98**, 1995-2004, (2010).
- 35 Hernando-Perez, M. *et al.* Quantitative nanoscale electrostatics of viruses. *Nanoscale* **7**, 17289-17298, (2015).
- 36 Landau, L. D. & Lifshitz, E. M. *Theory of Elasticity*. Vol. 7 (Pergamon Press, 1959).

- 37 Ivanovska, I. *et al.* Bacteriophage capsids: tough nanoshells with complex elastic properties. *P Natl Acad Sci USA* **101**, 7600-7605, (2004).
- 38 Roos, W. H., Bruinsma, R. & Wuite, G. J. L. Physical virology. *Nat Phys* **6**, 733-743, (2010).
- 39 Snijder, J., Ivanovska, I. L., Baclayon, M., Roos, W. H. & Wuite, G. J. Probing the impact of loading rate on the mechanical properties of viral nanoparticles. *Micron* **43**, 1343-1350, (2012).
- 40 May, E. R. Recent Developments in Molecular Simulation Approaches to Study Spherical Virus Capsids. *Molecular simulation* **40**, 878-888, (2014).
- 41 Evans, E. Probing the Relation Between Force—Lifetime—and Chemistry in Single Molecular Bonds. *Annu Rev Bioph Biom* **30**, 105-128, (2001).
- 42 Diezemann, G. & Janshoff, A. Dynamic force spectroscopy: Analysis of reversible bond-breaking dynamics. *The Journal of Chemical Physics* **129**, 084904, (2008).
- 43 Rayaprolu, V., Manning, B. M., Douglas, T. & Bothner, B. Virus particles as active nanomaterials that can rapidly change their viscoelastic properties in response to dilute solutions. *Soft Matter* **6**, 5286-5288, (2010).
- 44 Wang, H., Wang, X., Li, T. & Lee, B. Transient viscoelasticity study of tobacco mosaic virus/Ba(2+) superlattice. *Nanoscale research letters* **9**, 300, (2014).
- 45 Müller, D. J., Fotiadis, D., Scheuring, S., Müller, S. A. & Engel, A. Electrostatically Balanced Subnanometer Imaging of Biological Specimens by Atomic Force Microscope. *Biophys J* **76**, 1101-1111, (1999).
- 46 Ido, S. *et al.* Beyond the helix pitch: direct visualization of native DNA in aqueous solution. *Acs Nano* **7**, 1817-1822, (2013).
- 47 Leung, C. *et al.* Atomic Force Microscopy with Nanoscale Cantilevers Resolves Different Structural Conformations of the DNA Double Helix. *Nano Lett* **12**, 3846-3850, (2012).
- 48 Sheikh, K. H. & Jarvis, S. P. Crystalline Hydration Structure at the Membrane–Fluid Interface of Model Lipid Rafts Indicates a Highly Reactive Boundary Region. *J Am Chem Soc* **133**, 18296-18303, (2011).
- 49 Hernando-Pérez, M. *et al.* Nanoindentation of Isometric Viruses on Deterministically Corrugated Substrates. *The Journal of Physical Chemistry B*, (2015).
- 50 Ortega-Esteban, A. *et al.* Monitoring dynamics of human adenovirus disassembly induced by mechanical fatigue. *Sci Rep-Uk* **3**, (2013).
- 51 Hernando-Perez, M. *et al.* The interplay between mechanics and stability of viral cages. *Nanoscale* **6**, 2702-2709, (2014).
- 52 Roos, W. H. *et al.* Scaffold expulsion and genome packaging trigger stabilization of herpes simplex virus capsids. *P Natl Acad Sci USA* **106**, 9673-9678, (2009).
- 53 Hernando-Perez, M., Lambert, S., Nakatani-Webster, E., Catalano, C. E. & de Pablo, P. J. Cementing proteins provide extra mechanical stabilization to viral cages. *Nat Commun* **5**, (2014).
- 54 Martinez-Martin, D. *et al.* Resolving Structure and Mechanical Properties at the Nanoscale of Viruses with Frequency Modulation Atomic Force Microscopy. *Plos One* **7**, (2012).

- 55 Martinez-Martin, D. *et al.* Resolving structure and mechanical properties at the nanoscale of viruses with frequency modulation atomic force microscopy. *Plos One* **7**, e30204, (2012).
- 56 Xu, X., Carrasco, C., de Pablo, P. J., Gomez-Herrero, J. & Raman, A. Unmasking imaging forces on soft biological samples in liquids when using dynamic atomic force microscopy: a case study on viral capsids. *Biophys J* **95**, 2520-2528, (2008).
- 57 Ares, P. *et al.* High resolution Atomic Force Microscopy of double-stranded RNA.

Mechanical Stability and Reversible Fracture of Vault Particles

Based on:

A. Llauro, P. Guerra, N. Irigoyen, J. F. Rodríguez, N. Verdaguer, P. J. de Pablo “Mechanical stability and reversible fracture of vault particles”. *Biophys J.* (2014); 106:687-695.

Abstract

Vaults are the largest ribonucleoprotein particles found in eukaryotic cells, with an unclear cellular function and promising applications as drug delivery containers. In this chapter we study the local stiffness of individual vaults and probe their structural stability with Atomic Force Microscopy (AFM) under physiological conditions. Our data show that the barrel, the central part of the vault, governs both the stiffness and mechanical strength of these particles. In addition, we induce single protein fractures in the barrel shell and monitor their temporal evolution. Our high-resolution AFM topographies show that these fractures occur along the contacts between two major vault proteins and disappear over time. This unprecedented systematic self-healing mechanism, which enables these particles to reversibly adapt to certain geometric constraints, might help vaults safely pass through the nuclear pore complex and potentiate their role as self-reparable nanocontainers.

Introduction

Vault particles are naturally occurring nanoscale protein cages widely found in eukaryotes. Since their discovery in 1986,¹ diverse hypotheses have been developed as to the possible functions of vaults, based on their unique capsular structure, their mobility and the distinct subcellular localisation of the particles. Most of these hypotheses might implicate cargo transport, which suggests that they could act as a versatile regulatory platform for diverse cellular signal and transport processes.²

The X-ray structure of rat liver vaults revealed that their shell is organized into two identical moieties, each consisting of 39 copies of the major vault protein (MVP) (Figure 1A).³ The MVP monomer is organized in two well defined regions: the first half of the molecule folds into a series of small β -domains that assemble into a wide, thin barrel at the center of the particle, whereas the second half forms a long α -helix which assembles into the narrow cap at the C-terminal end. The N-terminal end of the MVP forms the particle's waist and accounts for the non-covalent interface at the vault's midsection. A combination of electrostatic and hydrophobic interactions governs the association of the two half-vault moieties.⁴ Natural vaults also enclose three minor components; two proteins, the vault poly-ADP-ribose polymerase (VPARP) and the telomerase associated protein 1 (TEP1), and several small non-coding RNA molecules (vRNA).⁵⁻⁷ Vault-like particles (VLPs), similar to purified endogenous vaults, are observed when rat MVP is expressed in insect cells, which indicates that MVP is sufficient to direct the formation of the vault shell.⁸ These VLPs, with overall dimensions of 40 x 40 x 70 nm³ and an average wall thickness of 1.5 nm, define an internal cavity (5x10⁴ nm³) that can store hundreds of molecules.

The peculiar structure and dynamics of vault particles,⁹ their large size and natural occurrence in humans, together with the reported presence of unidentified cargos,² have led to the idea that they could be exploited as natural nanocontainers for drug, nucleic acid, or protein delivery. In recent years recombinant vaults have gone through significant engineering, including cell-surface receptor targeting and the encapsulation of a wide variety of molecules^{10,11}. However, using vaults as functional containers requires a deep knowledge of their structural stability.

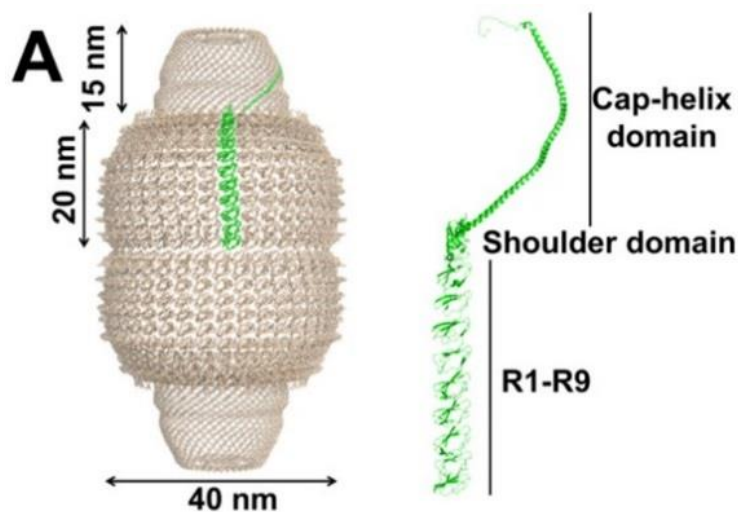
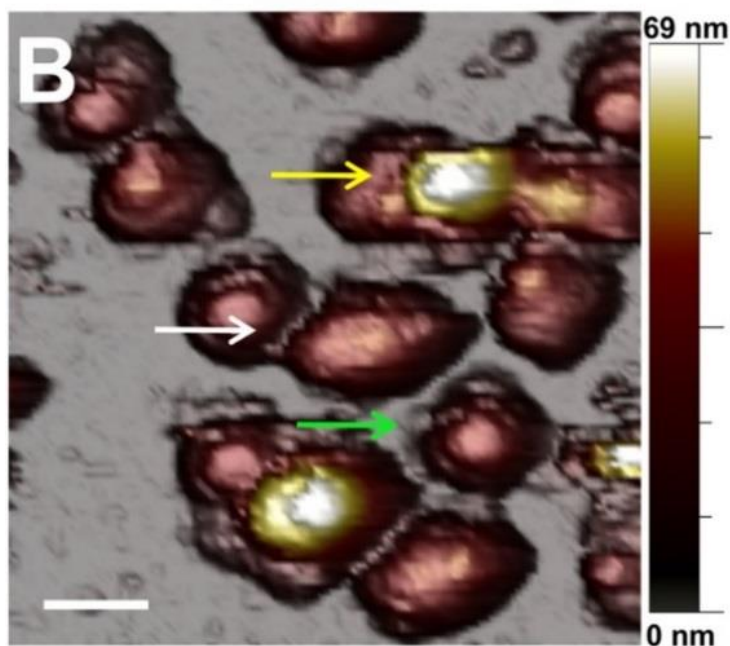


Figure 1. Vault structure and adsorption geometry. (A) Side view of a vault from X-ray data.³ The major vault protein (MVP) is colored in green on the structure and zoomed-in on the right side. MVP is composed of twelve domains: nine structural repeat domains at the N-terminus, an α/β shoulder domain, a cap-helix domain and a cap-ring domain at the C-terminus. (B) General topography image of vaults in buffer conditions. Particle orientations: full upright particle (yellow arrow), full reclining particle (white arrow) and half-vault (green arrow). Scale bar: 75 nm.



In this work, we studied the mechanical properties of vaults using Atomic Force Microscopy (AFM) under physiological conditions. We explored the stiffness of full- and half-vaults with single indentations, and probed the stability of these particles by exerting cyclic loading. Beyond the mechanical characterization of vault particles, our data monitored the first fracture/recuperation dynamics of a protein shell in which the particle repeatedly self-repairs over time.

Results and Discussion

Surface Attachment and AFM Imaging

Once vaults were attached to a freshly cleaved HOPG surface, AFM imaging in jumping mode¹² revealed a variety of adsorption geometries. [Figure 1B](#) shows a general topography where vaults present three different orientations: full particles lying on either the barrel (reclining) or cap, and half-vaults adsorbed through the waist with the cap facing up. AFM topographies revealed an excellent agreement between the height of the particles and the crystallographic structure³ ([Figure S1](#), in the Supporting Information), which excluded any effect of denaturation upon adsorption. Because the upright configuration was too unstable for AFM experiments, our study focused on full reclining particles and half-vaults.

AFM imaging at different feedback forces provided a first approach for testing the mechanical stability of vaults. [Figure 2A](#) presents a series of topographies where a reclining full particle and a half-vault were imaged under equal conditions. In that case, the imaging force was purposely changed back and forth from frame to frame ([Figure 2B](#), black crosses) causing variations in the height of the structures. Topographies revealed that the full-vault suffered some damage through the process. For instance, the inset of the seventh frame of [Figure 2A](#) shows the comparison between the topographies of frames 1 (*black*) and 7 (*green*), suggesting the partial collapse of the structure at the barrel. In addition, we observed a constant loss of height over time ([Figure 2B](#), red dots). Besides these disruptions, however, partial recovery of the average height of the structure was observed between frames as a consequence of lowering the imaging force ([Figure 2A](#) and [B](#); frames 4, 7 and 10).

On the other hand, the half-vault structure reduced its height abruptly from 36 nm to 15 nm when the imaging force was increased ([Figure 2B](#), *black squares*). Despite this large deformation, though, at lower imaging force the particle was capable of restoring its original height ([Figure 2A](#) and [B](#); frames 4 and 7). The ability to undergo such a large strain (around 60%) in a reversible manner, which was also reproducible for other half-vault structures (see [Figure S2](#) in the Supporting Information), demonstrated the remarkable structural stability of these particles under mechanical stress. In addition to this global phenomenon, self-recovery

capabilities were also observed at the local scale. The white arrow in the second frame of [Figure 2A](#) indicates a fracture on the barrel structure that disappeared over time.

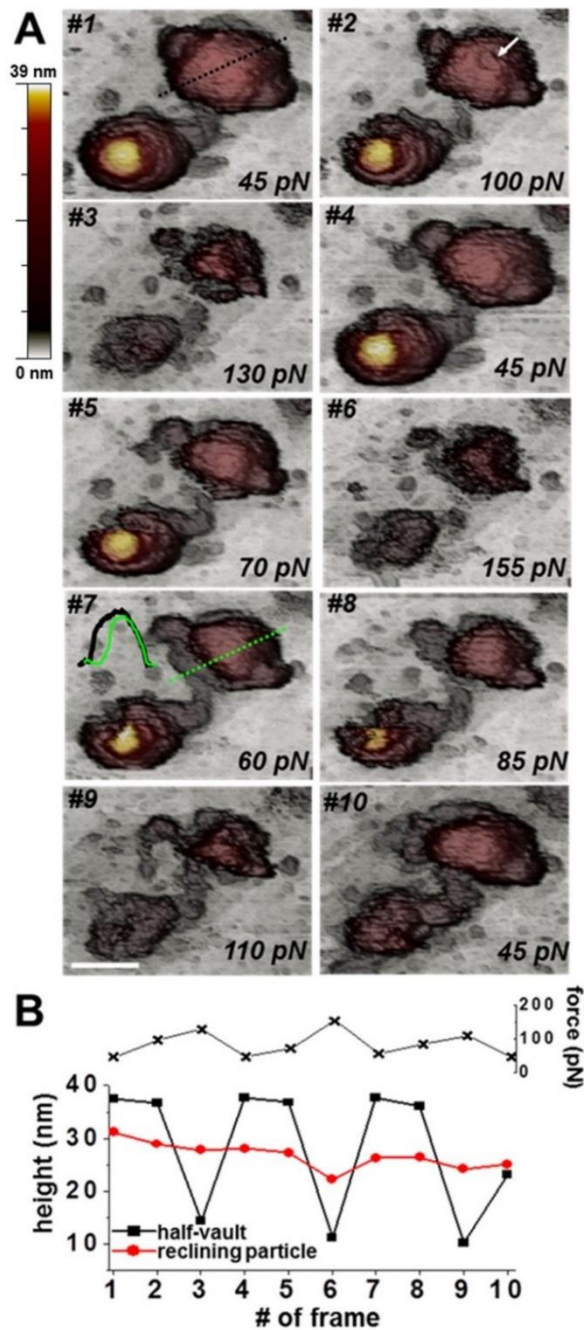


Figure 2. Vault stability depends on imaging force. (A) Topography images are time ordered and each frame is labeled with its corresponding imaging force. The elapsed time between images was 3 minutes. Scale bar: 50 nm. (Frame #7, inset) Comparison of the profiles taken along the dotted lines of frames #1 (black) and #7 (green). (B) (top) Imaging force evolution. (bottom) Maximal height evolution of the half-vault (black) and full reclining particle (red).

Stiffness and breaking force of individual particles

To investigate local phenomena rather than global deformations, we focused on performing individual nanoindentations both on full reclining particles and half-vaults ([Figure 3](#)). The resulting force vs. indentation curves (FIC) provided information about vault's mechanical

properties, such as stiffness (elastic constant, *green dashed line* in [Figure 3A-3](#) and [B-3](#)) and breaking force (*a* in [Figure 3A-3](#) and [B-3](#)). For reclining particles, our experiments provided average values for stiffness and breaking force of 0.03 ± 0.01 N/m and 122 ± 83 pN. For half-vaults these values rose to 0.06 ± 0.03 N/m and 165 ± 38 pN ([table 1](#)).

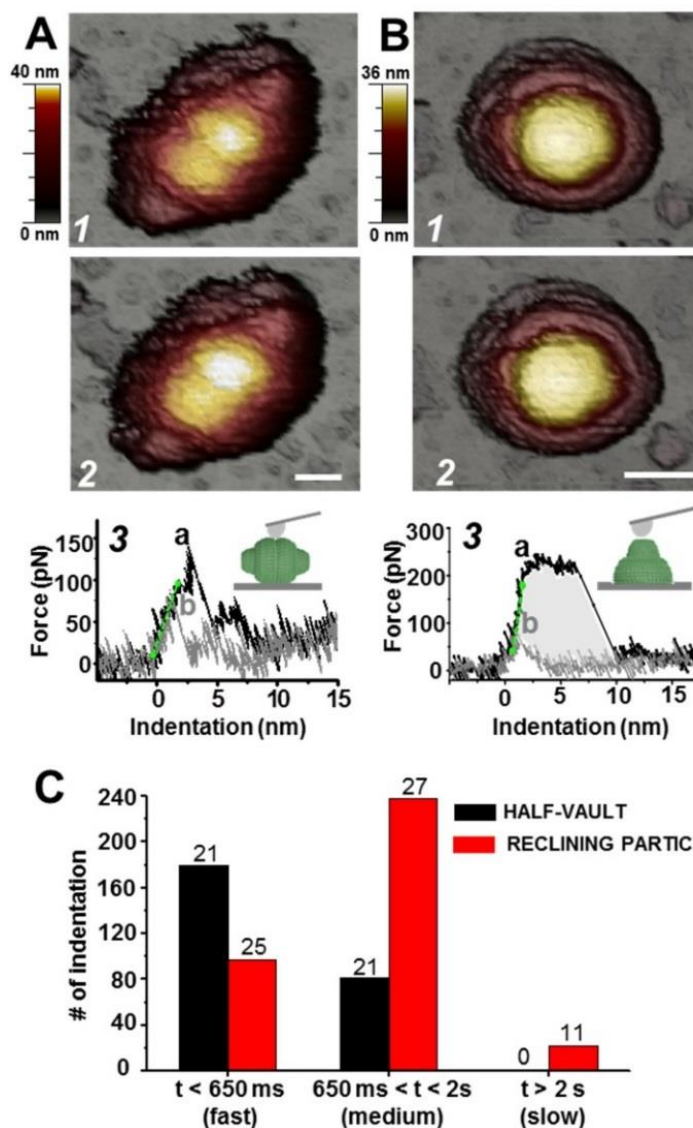


Figure 3. Indentation experiments on single vaults and histogram of the recovery time (A) Images of a reclining particle before (panel 1) and after (panels 2) the FIC of panel 3. From the forward curve (black) we calculated the elastic constant (dashed green line), breaking force (point *a*), and the critical indentation (indentation at point *a*). The backward curve (grey) shows a recovery during tip retraction. (B) The same experiment performed on a half-vault. The shadowed area represents the energy supplied to the vault during the nanoindentation. Scale bar: 25 nm. (C) Histogram of the recovery times (RT) for both orientations. The time criterion for classifying these curves was: fast recovery ($RT < 650$ ms), medium recovery ($650\text{ms} < RT < 2\text{s}$), and slow recovery ($RT > 2\text{s}$) (see Materials and Methods for criteria). The histogram contains information of 260 FICs (black) and 357 FICs (red). The number on top of each bar indicates the number of particles that we found presenting the corresponding time recover.

	$K(\text{N/m})$	$F_{\text{breaking}}(\text{pN})$	$\delta_{\text{critical}}(\text{nm})$	$\text{Energy}(\text{K}_B T)$	n
Half-vault	(0.06 ± 0.03)	(165 ± 38)	(4 ± 2)	(302 ± 34)	21
Reclining particle	(0.03 ± 0.01)	(122 ± 83)	(3.9 ± 1.5)	(220 ± 34)	13

Table 1. Elastic constant, breaking force and indentation at which shell ruptures, means \pm SD. n indicates the number of particles.

Our results showed that the stiffness value of half-vaults doubled the stiffness value of full reclining particles. To check if this result agreed with continuum mechanics, we constructed a Finite Element Model considering a shell with a geometry based on the X-ray structure of a vault (Figure S3). To reproduce the experimental curves with the simulation, the model was deformed with a sphere of 15 nm in diameter, which mimicked the AFM tip. The Young's modulus of the vault was estimated by tuning the Young's modulus of the model until the Finite Element simulation coincided with the experimental data (see Materials and Methods). The procedure led to a Young's modulus value of 0.7 GPa, which was on the order of magnitude of other protein nanoshells.¹³

Vault Particles Self-repair after Rupture

The breaking force is a sign of particle damage, commonly ascribed to the permanent fracture of the structure.¹⁴⁻¹⁶ However, the fact that particles looked intact after the nanoindentations (Figure 3A-2 and 3A-3) suggested that the process was reversible in our case. A recovery of the force during tip retraction also suggested this reversibility (*b* in Figure 3A-3 and 3B-3). Interestingly, the same behavior was found when we indented particles repeatedly, all the FICs presented drops ascribed to ruptures but the structures before and after the breakages were indistinguishable (Figure S4). In addition, study of the elastic constant of the particle through this repeated loading showed that the initial elastic behavior was completely restored (Figure S5). The average spring constant was maintained during, at least, the first five indentation, which probed the fast capacity of these particle to restore their elastic properties.

Vault particles were able to recover within a time span of ~650 ms, which roughly corresponded to half of the FIC time. Because those times were too short for acquiring a complete AFM image of the particle (~3 minutes), we decided to monitor the topography of the particles right after the nanoindentation took place. To do so we switched off the *y-scan* and enabled only the *x-scan* (Figure S6). In that way we obtained a kymograph that displayed the height of the particle immediately after each indentation (Figure S6, A-2 and D-2). With this method, we could image 22 topographic reversible damages in 11 different reclining particles corresponding to recovery times (RTs) longer than 2000 ms (the time of a single

FIC). During those experiments we also found that some backward curves do not exhibit force recovery, even though the vault structure remains unaltered (Figure S6-E, curves 1 and 7). We interpreted those cases as corresponding to vaults that recuperate from failure after the tip releases the vault surface but prior to imaging of the particle, which corresponded to recovery times (RT) between 650 ms and 2000 ms.

These distinctions allowed us to classify particles depending on the recovery time (RT). We defined fast-recovery as when force was restored during the backward curve ($RT < 650\text{ms}$); medium recovery as when, although no restoring force was observed, the subsequent topography showed an intact particle ($650\text{ms} < RT < 2\text{s}$); and slow recovery as when AFM imaging could monitor the reversible process ($RT > 2\text{s}$). The histogram in Figure 3C, which classifies 617 FIC for 26 half-vaults and 28 full reclining particles, shows that half-vaults restored faster than full reclining particles. Indeed, while a 70% of the FICs performed on half-vaults (179 of 260) show a recuperation occurring before 650 ms, only 22% of the FICs did so on full reclining vaults (97 of 357).

The role that the bending and stretching energies play after the fracture could explain these differences in RT. Thin-shell theory predicts that, due to the ability of a cylinder to bend without much in-plane stretching, more energy is needed to deform a spherical shell than a cylindrical one.¹⁷ If we approximate the geometry of a vault particle to that of a spherocylinder, its spherical (k_{sph}) and cylindrical (k_{cyl}) parts are related as $\frac{k_{\text{sph}}}{k_{\text{cyl}}} \sim \sqrt{R/h} \sim 3.65$, where R and h are, respectively, the radius of the cylinder ($R=20\text{nm}$) and the wall thickness ($h=1.5\text{ nm}$). By considering $k_{\text{half-vaults}}$ and $k_{\text{reclining}}$ as k_{sph} and k_{cyl} , our result $\frac{k_{\text{sph}}}{k_{\text{cyl}}} \sim 2$ coincides with the trend predicted by the theory. Therefore, we speculate that when the tip induced a fracture on half-vaults, the in-plane stress present in this structure (which lacked in the reclining particle) could trigger a faster recovery.

This hypothesis was supported by an estimation of the energy required to deform both configurations. The area enclosed by the forward and backward curves is a rough approximation of the energy supplied to a single vault to deform and, eventually, produce the rupture of the shell (*i.e.*, the shadowed area in Figure 3B -3). The average energy provided to reclining particles and half-vaults was, respectively, $220 \pm 34\text{ k}_B\text{T}$ and $302 \pm 34\text{ k}_B\text{T}$ (table

1). This result suggested that breaking vaults axially (“pushing on the spherical cap”; half-vaults) required more energy than breaking vaults radially (“pushing on the cylindrical barrel”, full reclining vaults).

Vault Fractures Occur along MVP-MVP Contacts

Although continuum elastic theory provided an understanding of particle elasticity, the discrete protein structure of vault particles had to be considered in order to investigate the fractures. Molecular dynamic simulations have shown that abrupt changes in the breaking force are due to the breakage of molecular bonds.¹⁸ Therefore, a correct interpretation of the fracture mechanism required a revision of all inter- and intra-subunit non-covalent contacts. The building block of the vault particle is the MVP molecule. The X-ray structure of the full vault reveals that the strongest MVP-MVP contacts are found between cap-helix domains, where hydrophobic interactions dominated the packing (29 of the 41 pairs of residues forming the interface between two adjacent helices are hydrophobic). The intermolecular interactions in the central barrel are weaker, mainly involving polar contacts (16 hydrogen bonds, 5 ionic bonds, and 10 hydrophobic contacts).^{3,19,20} To roughly estimate the difference of the interaction energy between these two regions we determined the non-covalent interactions of two consecutive MVP molecules using the program HBPLUS implemented in the package DIMPLOT.^{21,22} The energy values of -1.5 kcal/mol, -4.5 kcal/mol and -40 kcal/mol, associated to hydrophobic interaction, hydrogen bond, and ionic pair, respectively, were taken from *Brändén et al.*²³ Using these values we obtained that the bonding energy between two α -helices was about 4 times higher than the bonding energy between two β -sheets domains. From an energetic viewpoint, this calculation already suggests that the fractures should appear in the barrel.

To study in more detail these fractures we focused on the slow fracture-recovery cases ($RT > 2s$) (Figure 4 and S7). The AFM topographies in Figure 4A show the evolution of one reclining particle that restored its initial shape within 90 seconds (the time required to take a complete AFM image). Analysis of the pattern of fracture showed that the rupture was produced in the barrel (Figure 4 A-2). Lines ϵ and γ in Figure 4B are the profiles of the

fractured area along the transverse and longitudinal directions of the vault. The black and green curves, which are the height profiles before and after the fracture, provide direct evidence of recuperation. The red profiles depict the fractured zone: the ε -profile shows that the topographic outline is cut by a sharp fall; alternatively, the γ -profile shows a smooth decrease in height. To interpret these data we created a geometric model that simulated the rupture (Figure 4D, top). When the line of rupture was produced through the MVP-MVP contacts of the barrel, the profiles of the geometrical tip-dilated model (Figure 4D, bottom) showed a good agreement with the experimental data (Figure 4B, blue). This result confirmed that the transient breakages were produced in the direction in which MVPs align. The other slow recovery cases (Figure S7) also support the longitudinal fracture of the barrel. Independently of the orientation of the particle with respect to the scan direction, the lines of rupture were aligned with the MVP-MVP contacts.

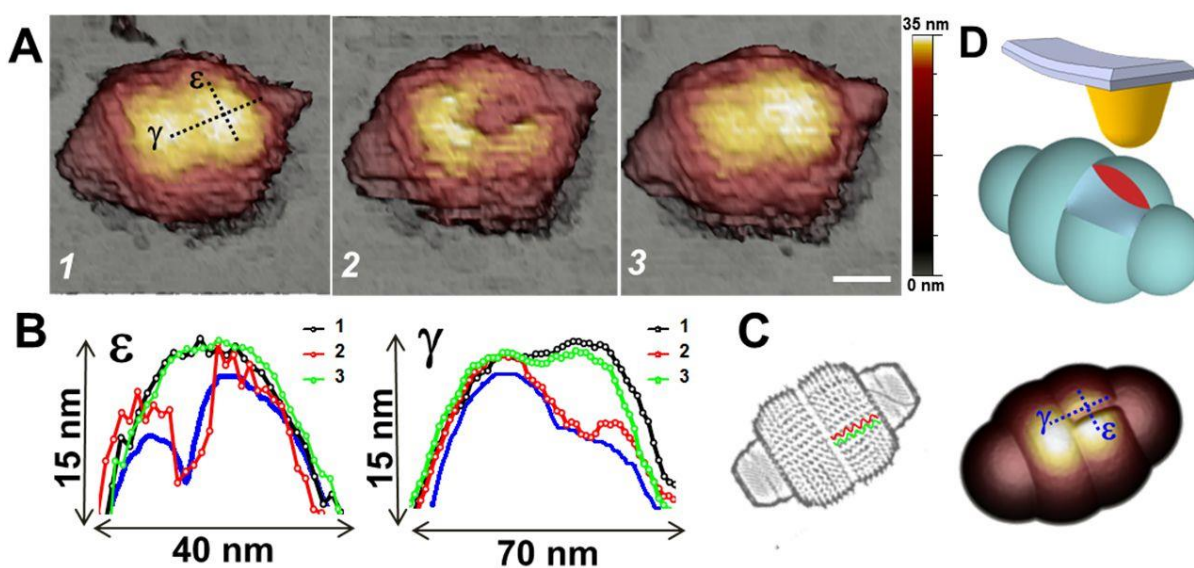


Figure 4. Reversible fracture. (A) Topographical images: -1- before fracturing, -2- after fracturing, and -3- after recovering. Scale bar: 35 nm. (B) Profiles ε and γ depicted with dotted black lines in Figure A-1: before the fracture (black), after the fracture (red), and after the recovery (green). (C) Fracture is produced between the β -sheet domains of two neighboring MVPs (green and red). (D) Dilation model: (top) sketch of a fractured vault; (bottom) tip-dilation simulation. The blue solid lines in Figure B correspond to the profiles obtained from this model.

While AFM images provide unequivocal information of the pattern of fracture, the interpretation of single FICs is not trivial because each case depends on several uncontrolled factors, such as the shape and dimension of the tip or the relative tip-particle orientation.

Despite that, our data systematically indicated that there were two patterns of FICs depending on the adsorption geometry (Figure 5). For reclining particles, the force after the rupture exhibited several peaks (Figure 5A). In contrast, half-vaults were always characterized by a single peak (Figure 5B). The zipper-like pattern observed in the reclining forms suggested a sequential unbinding of the β -sheets domains. Each of those unbinding events, characterized by a step distance, had a dissipated energy defined by the area under the curve (highlighted area in the *inset* of 5C). This area represented the difference in work between deforming a particle with and without the breakage.²⁴ By estimating those areas from the average distances and forces of the steps ($\Delta z = 1.3 \pm 0.95$ nm and 117 ± 50 pN), we obtained that each unbinding event had an average energy of ~ 20 k_BT. Comparison of this value with the strength of the non-covalent interactions that govern the assembly of the barrel domains, 2 k_BT for hydrophobic interactions and 8 k_BT for hydrogen bonds,²³ we estimated that every peak that we saw roughly corresponded to separating two of the structural repeat domains at the N-terminus (R1-R9) (Figure 1A).

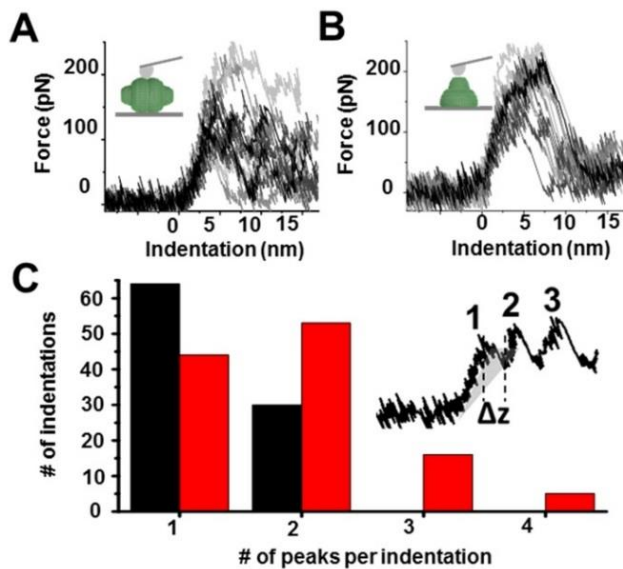


Figure 5. The pattern of FICs depends on the vault orientation. (A) 21 indentations performed on 21 reclining particles. (B) 13 indentations performed on 13 half-vaults. (C) Histogram of the number of peaks counted in each indentation for 21 half-vaults (black) and 13 reclining particles (red). (Inset) Example of an indentation performed on a reclining particle showing 3 peaks. The shadowed area indicates the work needed for a single fracture event. This area was calculated by the difference between the measured FIC and the backward-extrapolated from the curve after the step. The obtained average energy of these steps was about 20 k_BT.

The Barrel of the Vault Governs its Structural Strength

Consecutive AFM imaging at different forces provoked the disruption of some areas in the β -sheet region whereas the α -helix domains of the cap remain unaltered (*i.e.* Figure 2A,

frame 2). To determine if this also happened under constant force, we performed fatigue experiments on half-vaults²⁵ and confirmed that the barrel was the region where the breakage started (Figure 6 and S8, and movie in the Supporting Information).

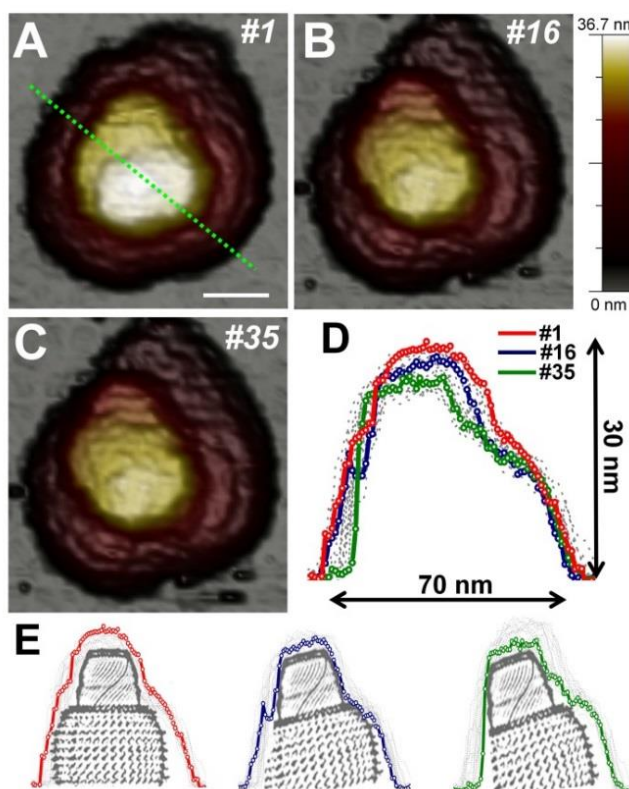


Figure 6. Mechanical fatigue of a half-vault.

This particle was imaged along 37 frames at an imaging force of 65 pN (movie, SI). (A, B, C) Topographical images corresponding to frames 1, 16, and 35, respectively. Scale bar: 25 nm. (D) Evolution of the profile taken along the dotted black line in frame #1. The profiles corresponding to frames 1, 16, and 35 are depicted in red, blue, and green, respectively. The rest of them are depicted with dotted grey lines. (E) Sketch of the disruption process suffered by the particle.

Figure 6 shows that, as a consequence of the disruption of barrel region, the cap tilted and the particle lost its axial symmetry. It is tempting to relate this behavior to the lower inter-bonding energy of β -sheets (barrel) compared to that of α -helices (caps). The tight and twisted-like geometry of the α -helices, in contrast with the aligned position of the β -sheet domains, also suggests a greater mechanical stability in the cap region. In the first section we showed that gentle variations in the imaging force caused striking differences between the relative deformations of both orientations (Figures 2 and S2). Whereas reclining particles deformed by about 10%, half-vaults underwent strains of around 60%. Interestingly, this impressive strain on half-vaults reduced the height of the particle to 15 nm, which corresponds to the size of a cap alone (Figure 1A). An increase in the imaging force provoked complete deformation of the barrels whereas the caps maintained their shape (an idea consistent with the ability of vaults to open into flower-like structures).²⁶ These evidences,

and the fact that we have only detected fractures on the barrel surface, prove that the barrel is the structure that governs the mechanical strength of both adsorption geometries.

Biological Implications and New Insights into Self-healing Dynamics

Several studies have reported that vault's exterior shell is a dynamic structure capable of "breathing" and exchanging material from the environment to its interior.²⁷ Although the precise function of vaults remains unclear, it is widely accepted that they act as cellular transporters.² Our experiments unveil new dynamics of this nanostructure induced by mechanical stress. We found that the bonds between MVPs were able to self-repair just by being in a liquid environment at room temperature. This feature indicates that these particles are highly adaptive to mechanical deformations, and transforms them into safe nanoplateforms capable of adapting to certain geometric constraints. Nonetheless, these particles are known to translocate material through the nuclear pore complex,^{28,29} which is a gate with a functional diameter of 39 nm,³⁰ right below vault's diameter.

Beyond their natural role, vaults are promising drug delivery systems due to their biocompatibility and recent success in the engineering of targeted vaults with controllable release.³¹ As a consequence, understanding vault dynamics is a necessary step towards their use in biomedicine. Fracture-recovery is likely related to the nature of the inter-domain interactions, the thermal shaking of these broken inter-MVPs bonds in a liquid milieu, and the geometry imposed by the vault. The inter-domain unions of β -sheets (which are mainly due to ionic and hydrogen bond interactions) are labile enough to allow particles to undergo reversible conformational changes at low energy inputs. In fact, the stress threshold that vaults must reach before breakage is lower compared with those of other molecular shells; the force at which vaults rupture is at least 5 times lower than the breaking forces of other nanoshells with similar Young's modulus.^{14-16,32,33} On the other hand, vault particles seem optimized to self-repair from fracture. Although it has been suggested that these self-healing capabilities may be present in other protein cages,^{24,34,35} our experiments reveal a systematic fracture-recovery mechanism that has been topographically monitored for the first time. Our results indicate that vaults may have evolved to facilitate low energy conformational changes

that reverse easily. The vault's rare self-healing dynamics, apart from being likely related to their function inside the cell, could inspire nanomaterial science in the creation of new engineered nanocontainers.

Conclusions

We have characterized the mechanical properties of individual vaults by performing indentations on full reclining particles and half-vaults adsorbed on their waists. Our results demonstrate that vaults exhibit striking self-healing capabilities that enable them to quickly recover from fracture. Also, we found that this rupture consists of separating two neighboring MVPs in the barrel structure. We believe that these novel insights into vault dynamics will add valuable information to understanding the role and function of these enigmatic particles and help to envision their use as nanocontainers.

Materials and Methods

Recombinant Baculoviruses

The generation of a recombinant baculovirus (rBV) containing the full length MVP was performed as follows: A DNA fragment containing the MVP sequence, flanked by NcoI and KpnI restriction sites, was generated by PCR. The DNA fragment was digested with NcoI and KpnI and inserted into the multiple cloning site of the baculovirus transfer vector pFastBacHta (Invitrogen), previously digested with the same restriction enzymes. The resulting plasmid, pFB_MVP, was subjected to nucleotide sequencing to assess the correctness of the inserted MVP sequence, and was then used to produce the corresponding rBV using the Bac-to-Bac system and following the manufacturer's instructions (Invitrogen)TM.

Production and Purification of Recombinant Vaults

HighFive cells (Invitrogen)TM were infected with rBVs at a multiplicity of infection of 5 PFU/cell. Cells were harvested at 48 hr postinfection, washed using Phosphate Buffered Saline and pelleted with a 5 minute centrifugation at 3000 r.p.m. This pellet was resuspended in 6 ml of buffer A (75 mM NaCl, 50 mM Tris pH 7.4, 1.5 mM MgCl₂, 1 mM DTT) plus 1% NP-40 and protease inhibitors (Protease inhibitor cocktail tablets; Roche) and maintained on ice for 30 min. The resuspended pellet was sonicated and cellular debris was removed by centrifugation at 10,000 rpm for 30 minutes. The supernatant was applied to 4 ml of buffer A with 25% sucrose and centrifuged at 37,000 rpm (using a SW41Ti rotor) for 2:30 hours. The resulting pellet was re-suspended in 600 µl of Buffer A and centrifuged for 1 minute at 13,000 rpm. The supernatant was applied to a 25–50% sucrose gradient in buffer A and centrifuged for 45 minutes at 40,000 rpm. The gradient was fractionated and then analyzed by SDS-PAGE and negative-stain electron microscopy. Finally, fractions enriched in recombinant vaults were concentrated to approximately ~5 mg/ml using a centrifugal filter device (Centricon YM-100; Millipore).

AFM

Measurements were performed with an AFM microscope (Nanotec Electrónica S.L., Madrid, Spain) operating in Jumping mode plus¹². In this mode, the tip displaces laterally when it is far from the sample and images are taken by performing force vs. Z-piezo displacement curves at all the points. Most images were taken with a maximal force of about 75 pN, which leads to average heights of (38±2) nm and (35.5±2) nm for reclining particles lying on the barrel and half-vaults, respectively. These values agree with the dimensions obtained by X-Ray EM, 33.5 nm for half-vaults and 40 nm for reclining particles.³ Rectangular silicon-nitride cantilevers (Olympus, RC800PSA) with a nominal spring constant of 0.05 N/m were used and calibrated using Sader's method³⁶. The experiments were carried out under physiological conditions; 1 20 µl drop of stock solution, consisting of vault particles under TMS buffer conditions, was incubated on a fresh HOPG surface (ZYA quality, NT-MDT) and, after 30 minutes, washed with buffer until a volume of 60 µl was reached. The tip was also pre-wetted with a 20 µl drop of buffer.

The elongation of the Z-piezo approached the top of the shell to the tip at a loading rate of 60 nm/s. The bending of the cantilever, which indicated the force, was recorded simultaneously with a four quadrant photodiode. These force vs. Z-piezo displacement curves included the contribution of the cantilever and the particle. Therefore, we had to subtract the bending of the cantilever on the substrate to obtain the deformation of the particle. This procedure has been well established by the study of microtubules²⁴ and virus particles^{32,37}. Recently, few reviews^{13,38,39} have recapitulated the techniques and advances of this research field. The elastic constant of the particle was obtained from the slope of the initial linear part of the force vs. indentation curve (FIC). The linear part of the indentation (regarding the elastic response of the shell) is sometimes preceded by a short-range non-linear region due to electrostatic, van der Waals, and hydration forces^{40,41}. Therefore, we excluded this initial curvature when calculating the elastic constant of the particle. All the FICs have been performed under identical experimental conditions, such as rate and kind of tip for providing comparable parameters. Particles were imaged before and after curve sets of ~ 5 FICs. The values presented in table 1 were obtained from 21 half-vaults and 13 reclining particles. The spring constant value is the slope of the first curve performed on each particle. The breaking force, critical indentation, and energy were obtained by averaging 95 curves and 120 curves for half-vaults and reclining particles, respectively. This population size ranges within the typical number of curves found in literature^{24,32,33,37,42-44}. To determine the energy supplied to the particle we calculated the area of the forward and backward curve (integrating each curve from the contact point to the maximum Z-piezo) and subtracted the areas from the forward and backward curves.

To check for any topographic change, AFM kept scanning between FICs (Figure S6). To classify particles depending on their recovery times, we increased the statistics to raise the number of slow recovery time cases. The histogram in Figure 3C contains data from 26 half-vaults (260 curves) and 28 reclining particles (357 curves).

The experiments of mechanical fatigue consisted of consecutively imaging the particle at a constant force that was far below the breaking force of its structure²⁵. The imaging force was calculated as: Imaging force (nN) = $K^{\text{cantilever}} (\text{nN}/\text{nm}) \cdot \text{Calibration} \left(\frac{\text{nm}}{\text{V}} \right) \cdot \text{Set point (V)}$.

Forces vs. Z-piezo displacement curves were performed on the substrate after each image to control the calibration of the system.

Finite Element Model and Tip-dilation Model

Finite Element simulations were performed with FEMLAB 3.1 (Comsol, Zoetermeer, The Netherlands). The thick shell model used in the simulation was designed to mimic the dimensions and geometry of the vault's X-ray structure (assuming a wall thickness of 1.5 nm). The capsid wall was made of a homogenous material with a Poisson ratio of 0.3 — similar to that used in other protein shells such as viruses^{13,33,39}, and was meshed over 30,000 tetrahedral elements. To match the experimental curves with the simulation, the particle was indented with a 15 nm radius sphere and Young's modulus was varied until the accordance between simulation and experiment was reached^{24,37,43}.

To create the model of a fractured vault we used *Sketchup* (www.sketchup.com). The dilation process⁴⁵ was performed by implementing the algorithm provided by WSxM⁴⁶ with a 10 nm diameter tip.

References

- 1 Kedersha, N. L. & Rome, L. H. Isolation and characterization of a novel ribonucleoprotein particle - large structures contain a single species of small rna. *Journal of Cell Biology* **103**, (1986).
- 2 Berger, W., Steiner, E., Grusch, M., Elbling, L. & Micksche, M. Vaults and the major vault protein: Novel roles in signal pathway regulation and immunity. *Cellular and Molecular Life Sciences* **66**, (2009).
- 3 Tanaka, H. *et al.* The Structure of Rat Liver Vault at 3.5 Angstrom Resolution. *Science* **323**, 384-388, (2009).
- 4 Querol-Audi, J. *et al.* The mechanism of vault opening from the high resolution structure of the N-terminal repeats of MVP. *EMBO J.* **28**, 3450-3457, (2009).
- 5 Kickhoefer, V. A. *et al.* The 193-kD vault protein, VPARP, is a novel Poly(ADP-ribose) polymerase. *J. Cell Biol.* **146**, 917-928, (1999).
- 6 Kickhoefer, V. A., Stephen, A. G., Harrington, L., Robinson, M. O. & Rome, L. H. Vaults and telomerase share a common subunit, TEP1. *J. Biol. Chem.* **274**, 32712-32717, (1999).
- 7 Kedersha, N. L. & Rome, L. H. Isolation and Characterization of a Novel Ribonucleoprotein Particle - Large Structures Contain a Single Species of Small Rna. *J. Cell Biol.* **103**, 699-709, (1986).
- 8 Stephen, A. G. *et al.* Assembly of vault-like particles in insect cells expressing only the major vault protein. *J Biol Chem* **276**, (2001).
- 9 Yang, J. *et al.* Vaults Are Dynamically Unconstrained Cytoplasmic Nanoparticles Capable of Half Vault Exchange. *Acs Nano* **4**, 7229-7240, (2010).
- 10 Casañas, A., Guerra, P., Fita, I. & Verdaguer, N. Vault particles: a new generation of delivery nanodevices. *Curr. Opin. Biotechnol.* **23**, 927-977, (2012).
- 11 Rome, L. & Kickhoefer, V. Development of the Vault Particle as a Platform Technology *Acs Nano* **7**, 889-902, (2013).
- 12 Ortega-Esteban, A. *et al.* Minimizing tip-sample forces in jumping mode atomic force microscopy in liquid. *Ultramicroscopy* **114**, 56-61, (2012).
- 13 Roos, W. H., Bruinsma, R. & Wuite, G. J. L. Physical virology. *Nat Phys* **6**, 733-743, (2010).
- 14 Roos, W. H. *et al.* Scaffold expulsion and genome packaging trigger stabilization of herpes simplex virus capsids. *Proc. Natl. Acad. Sci. U. S. A.* **106**, 9673-9678, (2009).
- 15 Ivanovska, I. L., Miranda, R., Carrascosa, J. L., Wuite, G. J. L. & Schmidt, C. F. Discrete fracture patterns of virus shells reveal mechanical building blocks. *Proc. Natl. Acad. Sci. U. S. A.* **108**, 12611-12616, (2011).
- 16 Castellanos, M., Perez, R., Carrillo, P. J. P., de Pablo, P. J. & Mateu, M. G. Mechanical Disassembly of Single Virus Particles Reveals Kinetic Intermediates Predicted by Theory. *Biophys J* **102**, 2615-2624, (2012).
- 17 Landau, L. D., Pitaevskii, L. P., Lifshitz, E. M. & Hosevich, A. M. *Theory of Elasticity*. 3rd edn, Vol. 7 195 (Elsevier 1984).

- 18 Cieplak, M. & Robbins, M. O. Nanoindentation of virus capsids in a molecular model. *J. Chem. Phys.* **132**, 015101, (2010).
- 19 Tanaka, H. & Tsukihara, T. Structural studies of large nucleoprotein particles, vaults. *P Jpn Acad B-Phys* **88**, 416-433, (2012).
- 20 Casañas, A. *et al.* New Features of Vault Architecture and Dynamics Revealed by Novel Refinement Using the Deformable Elastic Network approach. *Acta Crystallogr D Bioll Crystallogr* **69**, 1054-1061, (2013).
- 21 Laskowski, R. A. & Swindells, M. B. LigPlot+: Multiple Ligand-Protein Interaction Diagrams for Drug Discovery. *J. Chem. Inf. Model.* **51**, 2778-2786, (2011).
- 22 McDonald, I. K. & Thornton, J. M. Satisfying Hydrogen-Bonding Potential in Proteins. *J. Mol. Biol.* **238**, 777-793, (1994).
- 23 Brändén, C. I. & Tooze, J. *Introduction to Protein Structure.* 89 (Garland Pub., 1991).
- 24 Schaap, I. A. T., Carrasco, C., de Pablo, P. J., MacKintosh, F. C. & Schmidt, C. F. Elastic response, buckling, and instability of microtubules under radial indentation. *Biophys J* **91**, (2006).
- 25 Ortega-Esteban, A. *et al.* Monitoring dynamics of human adenovirus disassembly induced by mechanical fatigue. *Sci. Rep.* **3**, 1434, (2013).
- 26 Kedersha, N. L., Heuser, J. E., Chugani, D. C. & Rome, L. H. Vaults .3. Vault Ribonucleoprotein-Particles Open into Flower-Like Structures with Octagonal Symmetry. *J. Cell Biol.* **112**, 225-235, (1991).
- 27 Poderycki, M. J. *et al.* The vault exterior shell is a dynamic structure that allows incorporation of vault-associated proteins into its interior. *Biochemistry-Us* **45**, (2006).
- 28 Chugani, D. C., Rome, L. H. & Kedersha, N. L. Evidence That Vault Ribonucleoprotein-Particles Localize to the Nuclear-Pore Complex. *J. Cell Sci.* **106**, 23-29, (1993).
- 29 Dickenson, N. E., Moore, D., Suprenant, K. A. & Dunn, R. C. Vault ribonucleoprotein particles and the central mass of the nuclear pore complex. *Photochem. Photobiol.* **83**, 686-691, (2007).
- 30 Pante, N. & Kann, M. Nuclear pore complex is able to transport macromolecules with diameters of similar to 39 nm. *Mol. Biol. Cell* **13**, 425-434, (2002).
- 31 Han, M., Kickhoefer, V. A., Nemerow, G. R. & Rome, L. H. Targeted Vault Nanoparticles Engineered with an Endosomolytic Peptide Deliver Biomolecules to the Cytoplasm. *Acs Nano* **5**, 6128-6137, (2011).
- 32 Ivanovska, I. L. *et al.* Bacteriophage capsids: Tough nanoshells with complex elastic properties. *Proceedings of the National Academy of Sciences of the United States of America* **101**, 7600-7605, (2004).
- 33 Michel, J. P. *et al.* Nanoindentation studies of full and empty viral capsids and the effects of capsid protein mutations on elasticity and strength. *P Natl Acad Sci USA* **103**, (2006).
- 34 Rapaport, D. C. Role of Reversibility in Viral Capsid Growth: A Paradigm for Self-Assembly. *Physical Review Letters* **101**, 186101, (2008).

- 35 Cuellar, J. L., Meinhoefel, F., Hoehne, M. & Donath, E. Size and mechanical stability of norovirus capsids depend on pH: a nanoindentation study. *J Gen Virol* **91**, 2449-2456, (2010).
- 36 Sader, J. E., Chon, J. W. M. & Mulvaney, P. Calibration of rectangular atomic force microscope cantilevers. *Rev Sci Instrum* **70**, 3967-3969, (1999).
- 37 Carrasco, C. *et al.* DNA-mediated anisotropic mechanical reinforcement of a virus. *Proceedings of the National Academy of Sciences of the United States of America* **103**, 13706-13711, (2006).
- 38 Roos, W. H. & Wuite, G. L. Nanoindentation Studies Reveal Material Properties of Viruses. *Advanced Materials* **21**, (2009).
- 39 Mateu, M. G. Mechanical Properties of viruses analyzed by atomic force microscopy: A virological perspective. *Virus Res.* **168**, 1-22, (2012).
- 40 Butt, H. J. Measuring Electrostatic, Vanderwaals, and Hydration Forces in Electrolyte-Solutions with an Atomic Force Microscope. *Biophys. J.* **60**, 1438-1444, (1991).
- 41 Sotres, J. & Baro, A. M. AFM Imaging and Analysis of Electrostatic Double Layer Forces on Single DNA Molecules. *Biophysical journal* **98**, 1995-2004, (2010).
- 42 Carrasco, C. *et al.* Built-In Mechanical Stress in Viral Shells. *Biophys J* **100**, 1100-1108, (2011).
- 43 Hernando-Perez, M. *et al.* Direct Measurement of Phage phi29 Stiffness Provides Evidence of Internal Pressure. *Small* **8**, 2366-2370, (2012).
- 44 Castellanos, M. *et al.* Mechanical elasticity as a physical signature of conformational dynamics in a virus particle. *P Natl Acad Sci USA* **109**, 12028-12033, (2012).
- 45 Villarrubia, J. S. Algorithms for scanned probe microscope image simulation, surface reconstruction, and tip estimation. *Journal of Research of the National Institute of Standards and Technology* **102**, 425-454, (1997).
- 46 Horcas, I. *et al.* WSXM: A software for scanning probe microscopy and a tool for nanotechnology. *Review of Scientific Instruments* **78**, 013705, (2007).

Decrease in pH Destabilizes Individual Vault Nanocages by Weakening the Interprotein Lateral Interactions

Based on:

A. Llauro, P. Guerra, R. Chaudhary, B. Bothner, N. Verdaguer, P. J. de Pablo. Real-time experiments reveal new insights into the dynamics of individual vault nanocages upon pH variation. *Submitted*.

Abstract

Vault particles are naturally occurring proteinaceous nanocontainers with promising application as drug delivery vehicles. The role of vaults as functional transporters requires a profound understanding of their structural stability to guarantee the protection and controlled payload delivery. Previous results performed with bulk techniques at non-physiological conditions are interpreted such as pH mediates a dynamic exchange between half and full structures. Here we use Atomic Force Microscopy (AFM) to monitor the structural evolution of individual vault particles while changing the pH of the solution in real time. Our experiments show that decreasing the pH below 6.0, instead of opening vaults into halves, triggers the formation of holes and cracks in the barrel region, the central part of the vault. We suggest that this changes are caused by the disruption of four histidine-mediated polar bonds across lateral contacts between subunits, with an histidine- α -helix charge-dipole interaction at the shoulder of the cage playing a crucial role among them. Additional orthogonal bulk analyses using a second surface-based method, Quartz-Crystal Microbalance (QCM), as well as solution phase thermal denaturation by Differential Scanning Fluorimetry (DSF) are consistent with our single molecule AFM experiments. Our study unveil a new mechanism for the observed influence of pH on the stability and dynamics of vault particles and might suggest strategies to control the release of internalized payloads from these nanocages.

Introduction

Vault particles are nanosized protein cages implicated in numerous cellular processes, including multidrug resistance, innate immunity and cellular transport.^{1,2} However, the specific functions ascribed to this unique cellular organelle have not yet been irrevocably defined. Highly conserved and present in nearly all eukaryotes, vault particles consist of 78 copies of the major vault protein (MVP), which forms the MVP shell, plus three minor components. The less abundant species are the 193 kDa vault poly-ADP-ribose polymerase (VPARP), a 290 kDa telomerase associated protein 1 (TEP1), and several small non-coding RNA molecules (vRNA).³⁻⁵ A 3.5 Å resolution structural model for the rat vault assembly, based on X-ray crystallography, shows that the vault shell can be divided into identical halves, each consisting of 39 copies of MVP.⁶ Each MVP chain folds into 12 domains: a cap-helix domain, a shoulder domain and nine structural repeat domains that form the barrel (Figure 1A).^{6,7} The strongest MVP-MVP lateral contacts are found between cap-helix domains, where hydrophobic residues stabilize the interface between helices on adjacent proteins. A combination of hydrophobic and electrostatic interactions stabilizes the association of the two half-vault moieties. The entire particle forms an ovoid structure with overall dimensions of 40 x 40 x 67 nm³.

Recombinant vaults can be assembled *in vitro* after expression of MVP in insect cells. These vault-like structures are identical in size to natural vaults but have a hollow internal compartment that permits the storage of protein payloads.⁸ The ability to store hundreds of proteins, inherent biocompatibility and non-immunogenic cell response, make vault-like particles promising candidates as drug delivery vehicles for biomedical applications.¹ Indeed, the shell of recombinant vaults has been genetically modified by addition of an INT motif (the shortest C-terminal domain of VPARP that interacts with MVM) to target packaging of specific payloads;⁹⁻¹¹ cell specific targeting can be manipulated by modification of the C- and N-termini of MVP.¹²⁻¹⁴ Despite all these promising advances, though, little is known about the determinants that govern the dynamics of vaults, which is a fundamental step towards their use in biomedicine applications. Exogenous proteins are able to incorporate into vault interior even after the formation of vault particle shell, which proves that these particles are highly dynamic.¹⁵ In addition, studies using fluorescently labeled protein showed that recombinant vault particles are capable of half-vault exchange *in vivo*, and Small-Angle X-

ray Scattering (SAXS) experiments indicated that the percentage of half-vaults and full-vault was close to 50:50 in solution, suggesting that this opening mechanism could be a way whereby vaults could deliver their cargoes.¹⁶

To utilize vaults in drug delivery applications it would be convenient to find an external parameter to control the opening of the particles. During internalization of vault particles into cells through endocytosis, the acidic pH of the endosomal compartment might trigger vault dissociation. Vault particles engineered with adenovirus membrane lytic peptide (pVI) can escape the endosome and deliver molecules to the cytoplasm in about 10-30 minutes.^{13,14} Interestingly, previous studies have suggested that vault particles dissociate into halves at low pH.^{17,18} In another study the structural stability of vault particles was studied across a range of pHs (3 to 8) and temperatures (4 to 70°C).¹⁹ This characterization revealed a variety of structures; full assemblies, half-vaults, states of aggregation and losses of secondary and tertiary structure. The most stable forms of vaults were found at pH 7, below 40°C. However, some data seem contradictory (if lowering the pH triggers vault opening, why the percentage of half-vaults and full-vault at pH is 50:50) and the responsible for vault opening are yet to be determined. The majority of studies reporting the impact of pH on vault structures used biochemical techniques that average population from large numbers of particles and lack direct visualization at the single particle level. An exception was negative stain Transmission Electron Microscopy (TEM), but in that case the stain and sample drying could induce the damage of the structures,²⁰ precluding the possibility of visualizing the structure under physiological conditions.

To investigate the impact of pH on vault particle stability and dynamics, we carried out experiments using three different methods; Quartz Crystal Microbalance with Dissipation (QCM-D), Differential Scanning Fluorimetry (DSF) and Atomic Force Microscopy (AFM). Specifically, the environmental control of the buffer conditions at the AFM liquid chamber offered the possibility of studying structural changes of the vault protein *in situ*.²¹⁻²³ We monitored the structural changes of individual vault particles as pH transitioned from 7.5 to 4.0 in real time. Our results provide direct evidence that low pH weakens the interaction between adjacent MVPs in the barrel zone, in contrast to the previous results.^{17,18} In addition, based on the crystallographic structure, we propose a model of the structural determinants that would lead to this pH-dependent vault dissociation.

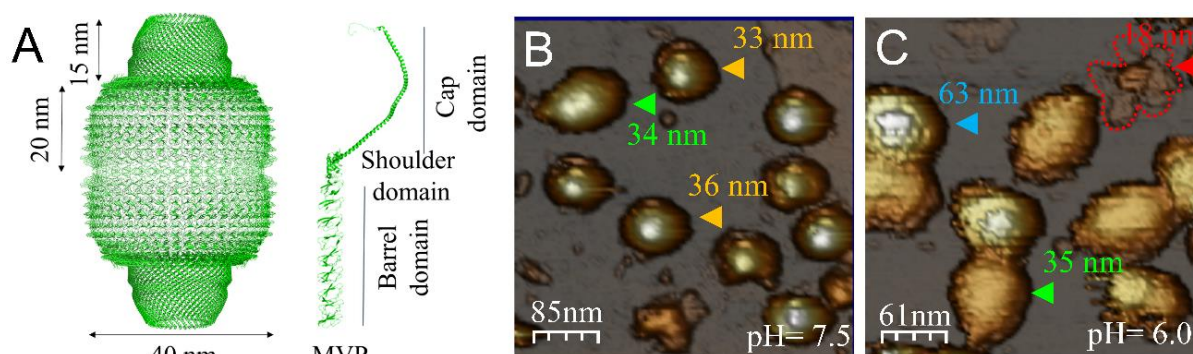


Figure 1. Vault structure and AFM adsorption geometry. (A) Side view of a full-vault particle (PDB: 4V60). Each full-vault consists of two identical moieties, each of one comprising 39 major vault proteins (MVP). MVP is composed of twelve domains: nine structural repeat domains at the N-terminus (barrel domain), an α/β shoulder domain, a cap-helix domain and a cap-ring domain at the C-terminus. (B) General AFM topography image of vaults at pH 7.5. The images show two different configuration: reclined full-vault (green arrowhead) and half-vaults (yellow arrowheads). (C) General AFM topography image showing upright full-vaults (blue arrowhead), reclining full-particle (green arrowhead) and flower-like structures (red arrowhead). To guide the eye the contour of the flower-like structure is shown with dotted red lines. Color scale bar: White-brown-grey, from the highest points to the substrate.

Results

In-solution Characterization of Vault Particles

AFM images of vaults adsorbed on HOPG showed that at pH 7.5 full and half configurations were present (Figure 1B). Likewise, if the solution pH was lowered from 7.5 to 6.0 before adsorbing the particles on the HOPG surface both configurations were found. Figure 1C shows an AFM area with full particles at pH 6.0: either reclining on the barrel (green arrow) or stand up (black arrow). Flower-like structure, consisting of a cap with the barrel domains open such as petals around it, could be also seen (red arrow).²⁴ Despite we found no differences in the percentage of half and full configuration as a function of pH, particles at pH 6 systematically decreased the height by 14% and 7% for both reclined full- and half-vaults, respectively (table 1). This result suggests that while the open/close mechanism remains the same at both 7.5 and 6.0 pH, the overall structure of the particle is weaker at lower pH. AFM images of particles incubated at pH 5.2 for 1 minute before the adsorption

on the substrate showed mostly empty areas and some clusters of protein, suggesting high levels of protein aggregation under these conditions (data not shown).

	Full-vault		Half-vault	
	<i>n</i>	<i>height</i> ±SD	<i>n</i>	<i>height</i> ±SD
pH=7.5	30	37±3	47	35±3
pH=6.0	9	35±3	6	30±2
pH=5.2	18	25±6	35	27±4

Table 1. Height of the particle as a function of pH (mean±standard deviation). Particles at pH 7.5 and 6.0 were incubated in-solution at the corresponding buffer before adsorption. Particles at pH=5.2 were adsorbed at pH 7.5 and then the pH was exchanged to 5.2.

Imaging of Adsorbed Vault Particles

Because protein aggregation hampers the identification of the structures at single particle level, vault particles were anchored to the HOPG substrate at pH 7.5 and then the pH was decreased to 5.2, reassembling previous experiments performed by TEM.¹⁹ In this situation particles are not freely diffusing in solution and cannot form clusters, which allowed us to identify single structures at pH 5.2 (Figure 2). Whereas at pH 7.5 particles were undamaged and could be easily classified as half- or full-vaults (Figure 2A). Structures at pH 5.2 showed marked damaged in the beta-sheet region of the barrel (Figure 2B). Flower-like structures were also observed under these conditions (Figure 2B, right bottom). Interestingly, the height of these flower-like structures (~13nm) correspond to the intact cap region size on native vaults, indicating that the twisted alpha-helices maintain their conformation even at acidic pHs. The cap stability is believed to arise from the alpha-helix domain which is a major contributor to interactions between MVPs⁶ proteins and remains stable at low pH, more so than the beta-sheet domains of the barrel. A systematic analysis revealed that the average height of particles decreased with pH as measured at 7.5, 6, and pH 5.2 (Figure 2C and table 1). This supports the hypothesis that exposure to low pH is responsible for an overall weakening of the barrel region.

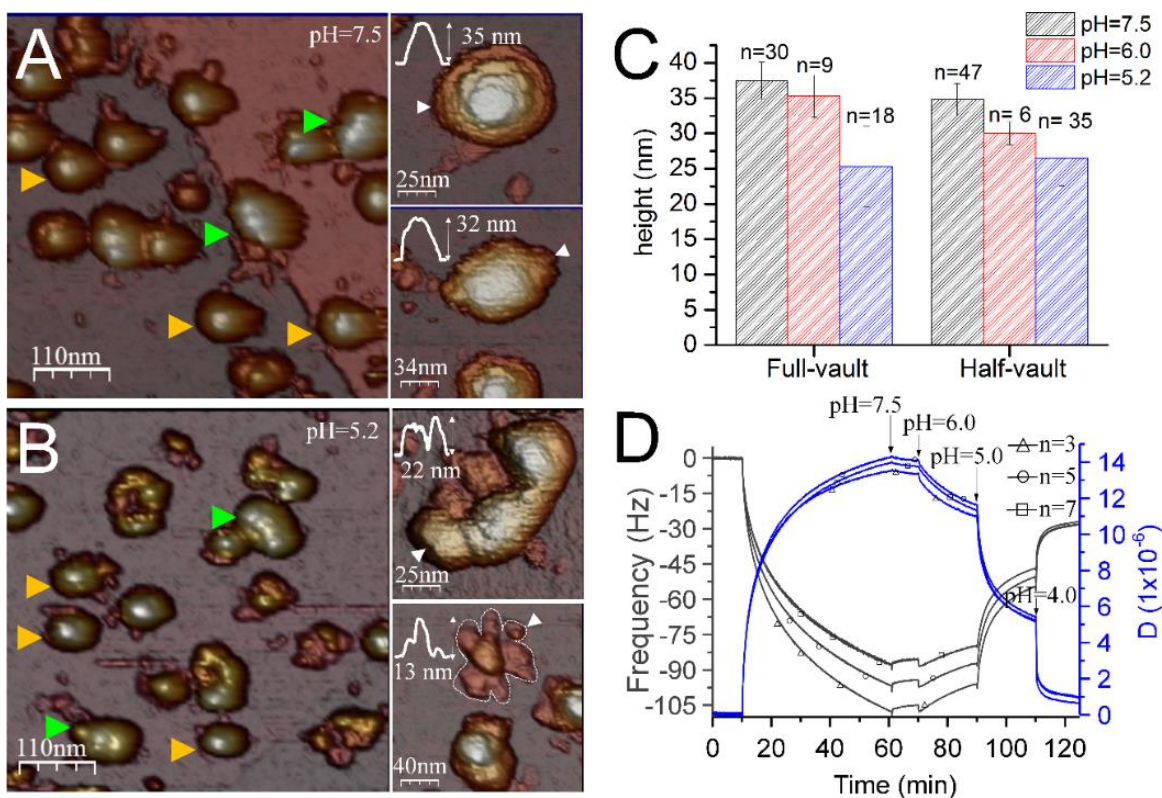


Figure 2. (A) General AFM topography of particles at pH 7.5. The Image shows vault with different configuration: reclined full-vault (green arrowheads) or half-vault (yellow arrowheads). A high-resolution AFM image of a typical particle at pH 7.5 is shown on the right: half vault (top) and reclined full-vault (bottom). The white arrowheads indicate the line along which the height profile was taken. (B) General AFM topography of particles at pH 5.2. Most the particles reveal some damaged: half-vaults (yellow arrowheads) and reclined full-vaults (green arrowheads). The images on the right show two typical configuration found at pH 5.2 reclining particles (top), and half-vault and flower-like structure (bottom). (C) Bar histogram of the average height of the particles at pH 7.5, 6.0 and 5.2. Both configurations (reclined full-vault and half-vault) show a progressive decrease in height as a consequence of lowering the pH. The n indicates the number of particles considered for calculating the mean (D) QCM-D analysis of vault particles. Traces show the frequency in black (Y1 axis) and dissipation in blue (Y2 axis) for three different overtones ($n=3, 5$ and 7 , corresponding to 15MHz, 25MHz and 35MHz). After loading the particles on the gold-coated crystal the buffer was exchanged three times, to 6.0, 5.0 and 4.0 (black arrows). Important changes in frequency and dissipation were observed after decreasing the pH from 6 to 5 and from 5 to 4. Color scale bar: white-brown-purple, from the highest points to the substrate.

Rigidity and Stability of Vaults

The structural transition as a consequence of decreasing the pH was also studied by QCM-D.²⁵⁻²⁷ QCM-D is a sensitive and straight-forward technique that measures viscoelastic

changes associated with proteins and protein complexes. We have used it to study the pH-dependent conformational change of the small RNA virus CCMV.²⁸ To measure and compare the rigidity of vault particles, they were loaded onto gold-coated quartz crystals simultaneously changes in frequency (Δf) and dissipation (ΔD) as a function of pH were recorded at three overtones ($n=3, 5, 7$) (Figure 2D). Vault particles were allowed to adsorb for 50 minutes which resulted in a decrease in frequency and an increase in dissipation. Loosely bound vault particles were removed by washing the sample at pH 7.5 for 10 minutes. The stable signal during the wash (60-70 mins.) indicates strong adsorption of vault particles to the surface. Introduction of pH 6.0 buffer led to a small increase in frequency (12%) and decrease in dissipation (15%). A more significant decrease in frequency (45%) and decrease in dissipation (52 %) was observed after adding the pH 5.0 buffer. This change in frequency is related to the mass change which could be due to a detachment of material from the surface, a partial disassociation/compression of vault nanocages or a reduction of the vault hydration shell. The decrease in dissipation indicates an increase in the rigidity. A soft material is easily deformed during oscillations which leads to high dissipation, while a rigid material has low dissipation because it strongly couples to the crystal. The increase in rigidity observed here is likely due to the collapse of the structure and the increase of contact area between the particles and the surface. Further decrease of pH (from 5.0 to 4.0) was accompanied by a sharp increase in frequency (30%) and decrease in dissipation (33%). These results show that lowering the pH has a progressive destabilizing effect on the structure of vaults. A previous QCM study used a single pH change, making it impossible to discern between a one-step transition (full-/half-vault) or a progressive disassembly process.¹⁷

Our QCM-D experiments suggest that at pH 6.0, the majority of vault particles maintain their quaternary structure, although the reduction in height measured by AFM indicates that some of the inter-monomeric contacts at the barrel may have weakened. Below pH 6, particles start to aggregate when they are in solution and our AFM and QCM-D experiments on adsorbed particles reveal major structural changes.

We performed thermal denaturation experiments with Differential Scanning Fluorimetry (DSF) to further investigate the effect of pHs on stability (Figure S1).^{29,30} When pH was changed from 7.5 to 6, the melting temperature (T_m) was reduced by 1.5°C. At pH 5, a significant difference of 13°C was observed in T_m . DSF at pH 4 showed that particles were

unstable even before heating. This result supports our hypothesis that below pH 6.0, particle integrity is compromised, but above that value, particles maintain quaternary structure.^{13,14}

***In singulo* Real-time Structural Dynamics as a Function of pH**

Up to this point, our analysis has either used population averages to assess the properties of vault particles or caught individual frames through the pH-dependent destabilization process. To unequivocally identify the structural rearrangements occurring in individual vault particles, we used continuous scanning AFM while lowering the pH from 7.5 to 5.2. To accomplish this, the AFM liquid chamber was coupled to a two-syringe pump system that permitted *in situ* pH exchange (Materials and Methods). Before initiating the pH change, an area ($\sim 700 \text{ nm}^2$) containing multiple vaults was selected. This allowed single particles to be imaged in parallel. [Figure 3A](#) shows 6 frames of the area that was imaged at different times. Vault particles were equilibrated in pH 7.5 buffer. At $t=0$ min (frame #3) we started a slow buffer exchange. The area was continuously imaged until the buffer was completely exchanged and the pH was 5.2 ($t=71$ min, frame #26). [Figure 3B](#) shows the evolution of height of individual particles through the pH-exchange process ([movie 1](#)). Curves correspond to the particles labelled in frame # 3. For example, F1 corresponds to the full-vault labeled as 1 and H1 to the half-vault labeled as 1 (see frame #3). Analysis of the intermediate states showed that the height of the particles started to decrease once the solution reached pH 5.7 ($t=56$ min, frame #24). From this point onward, a monotonic decrease in height was observed. After aligning the images we took profiles of the particles along the green dotted lines indicated in frame #3. Comparison of the profiles at four different times (0, 38, 71 and 95 min) indicated that the decrease in height was concomitant with the shrinkage of the barrel zone ([Figure 3C](#)). Interestingly, in a previous study cross-linked vaults appeared to shrink in size at low pH; however, the authors could not find an explanation for the observation of that shrinkage.¹⁸

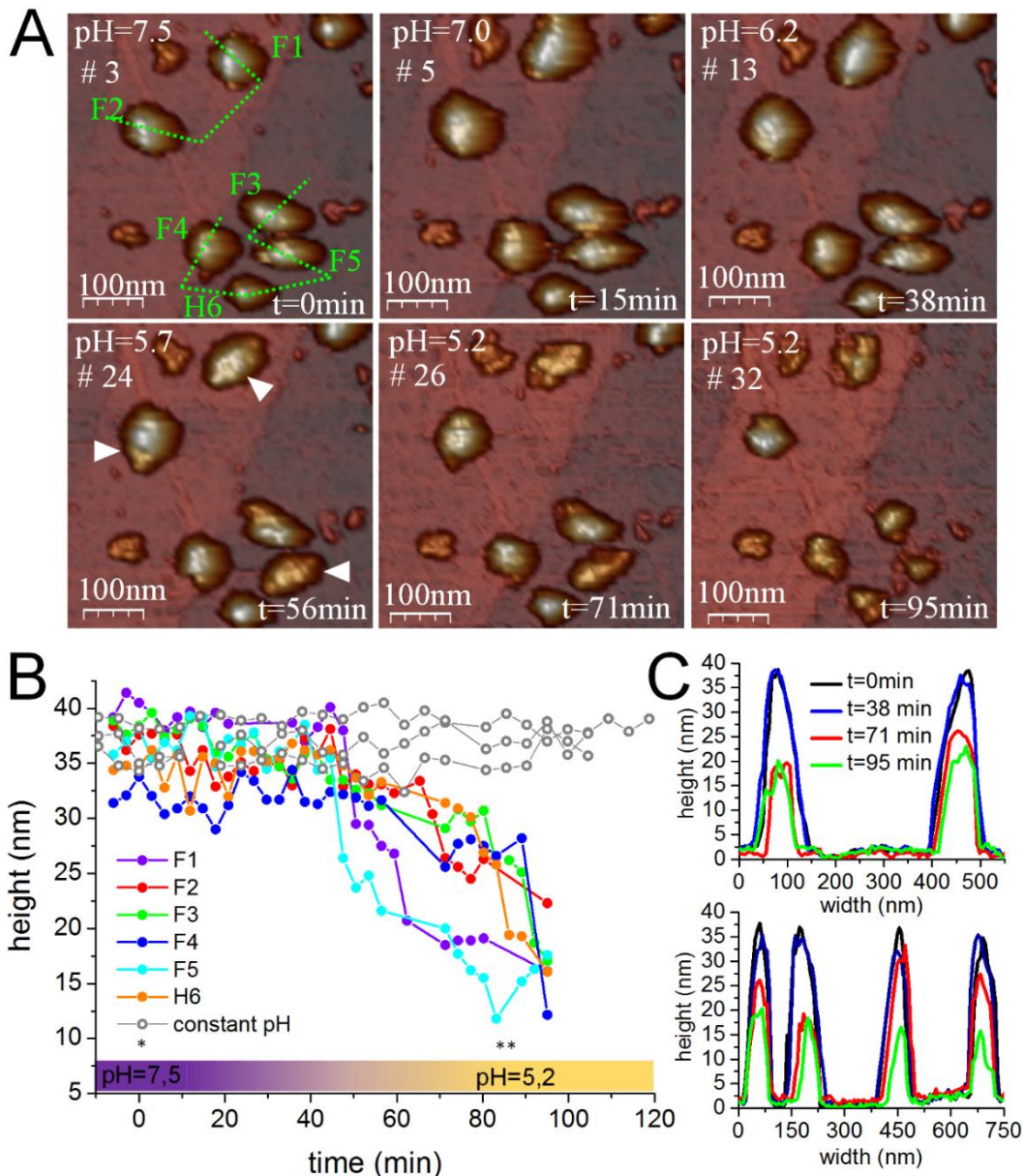


Figure 3. Real-time AFM images of vault particles while decreasing the pH from 7.5 to 5.2. (A) Different snapshots of the movie showing the structural transition caused by the pH lowering. Each frame is labeled with the time, the number of frame and the corresponding pH. Frame #3 (t=0 min) shows the initial configuration, with the particles labeled from 1 to 6: five reclined full-vault (F1-F5) and one half-vault (H6). White arrowheads (frame #24) indicate damage on the surface of the particles. At pH 5.2 (frame #32) the structure had aggregated. (B) Evolution of the height for each individual particles. From pH=5.7 (t=56 min) onwards a steady decrease in height was observed. The grey lines indicate that height of particles imaged while maintaining the pH constant. The color bar at the bottom indicates the pH, from 7.5 (purple) to 5.2 (yellow). The asterisks indicate the pumping settings: onset of infusion (*) and complete pH exchanged (**). (C) Profiles of the particles at different pHs (dotted green lines in frame #3 indicate the lines along which the profiles were taken). Particles decrease their height, shrink and aggregate as a consequence of the pH lowering. Color scale bar: white-brown-purple, from the highest points to the substrate.

Our AFM images show that loss of structural integrity including the formation of holes and cracks on the surface of the barrel became evident once the solution reached pH 5.7 (white arrowheads, frame # 24). Higher resolution images of F1 and F2 (Figure 3A, see frame #3) acquired at pH 5.2 confirmed that these fractures occurred at the barrel zone, with longitudinal cracks between MVPs leading to an overall reduction of the particle height (Figure 4). These data are incompatible with the opening of vault particles into halves as there is no evidence of fractures occurring along the waist. It could be argued that the substrate would impair such division of the vaults into halves while resting on the barrel zone. However, we also found that full-particles laying on their cap maintain their full structure at pH 5.2 (Figure S2). Noticeably, some of these structures decrease their height from 70 nm to 60nm, which agrees with a weakening of the overall structure but not with pH-mediated opening into halves.

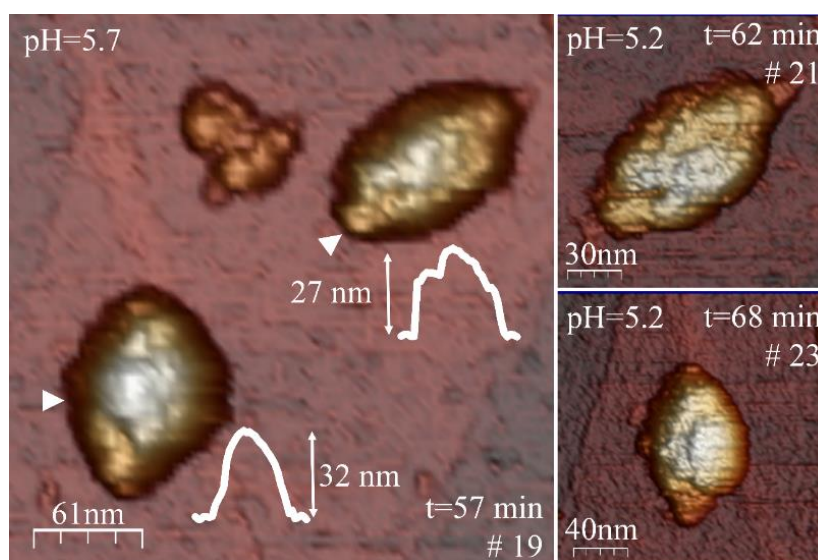


Figure 4. High-resolution AFM images of F1 and F2 (see Figure 3) at pH 5.7. The barrel zone present clear damage, suggesting the weakening of inter-monomeric contacts at the barrel.. (Inset) Height profiles of the particles taken along the lines indicated by the white arrowheads. Both cages present heights lower than the ones expected from the crystallographic structure (~ 40 nm).³¹ On the right panels, AFM images of the particles at pH 5.2 are shown. Major damaged is observed on the barrel zone as a consequence of the lower pH. The image at the bottom suggests that the lines of fracture occur along the MVP-MVP contacts, in agreement with our hypothesis that lowering the pH weaken lateral interactions instead of opening vaults into halves, as previously reported.^{7,17,18}. Color scale bar: white-brown-purple, from the highest points to the substrate.

Because the AFM probe establishes mechanical contact with vault particles during imaging,³² it was important to rule out physical contact of the probe as a source of damage or weakening. To address this we performed control experiments by imaging vaults at neutral pH under the same AFM conditions: image area, set-point force and number of pixels. For example, we scanned vault particles during 33 times during 110 minutes at constant pH 7.5 (Figure S3) and did not observe a significant decrease in height (grey lines, Figure 3 and S3). In addition, we performed experiments with a faster pH exchange rate than the 71 mins used above (see Figure 3). At the faster exchange rate conditions pH 5.2 was reached after 20 mins (Figure S3). In that case, the height of the particle started to decrease at t=18 min, which corresponds to pH 5.5. From that point onwards a decrease in height was observed until particles were completely aggregated after 60 minutes. Therefore, our control experiments probed that the pH, and not the AFM imaging, was responsible for vaults destabilization.

Structural Determinants of the Observed pH-dependent Dissociation

The experiments presented here provide direct evidence that the low pH destabilized the MVP-MVP interactions. Surprisingly and in contrast to what has previously been described,^{17,18} the destabilization occurs between adjacent MVP monomers causing the formation of cracks in the vault barrel but not the opening of the two vault halves. The analysis of the X-ray structure of the vault particle revealed a combination of electrostatic and hydrophobic interactions, mediated by R1 repeats, governing the association of the two half-vault moieties^{6,33} (Figure 5). The presence of the electrostatic bonds in the half-vault interface prompted us to suggest a reversible mechanism of dissociation of the vault particle induced at acidic pH.⁷ However, data obtained in this work indicate that the hydrophobic cluster composed of residues Ala6, Ile7 and Ile36, also in the R1-R1 interface, would form the key interaction (Figure 5). To provide a further structural explanation for the effect of the pH in the destabilization of the MVP-MVP lateral contacts, we re-examined here these contacts, using the refined structure of the particle (PDB id: 4HL8),³³ paying special attention to residues easily protonable at middle acidic pH. The analysis showed the interactions of four histidines with polar residues across the MVP-MVP lateral interfaces in the shoulder and barrel zones [His85 (R2), His464 (R9) and, His534 and His592 shoulder]. Among them,

His534 of one MVP monomer appears to play a crucial role, participating in a histidine- α -helix charge-dipole interaction, with the cap α -helix N-terminus of the neighboring MVP (Figure 5). In light of these interactions is tentative to speculate that the stability of the vault barrel and shoulder would be mainly governed by these histidine residues and that its protonation would explain the weakening of the lateral MVP-MVP interactions at low pH due to local charge repulsion. Comparable interactions governing the stability of a viral capsid were previously described.³⁴

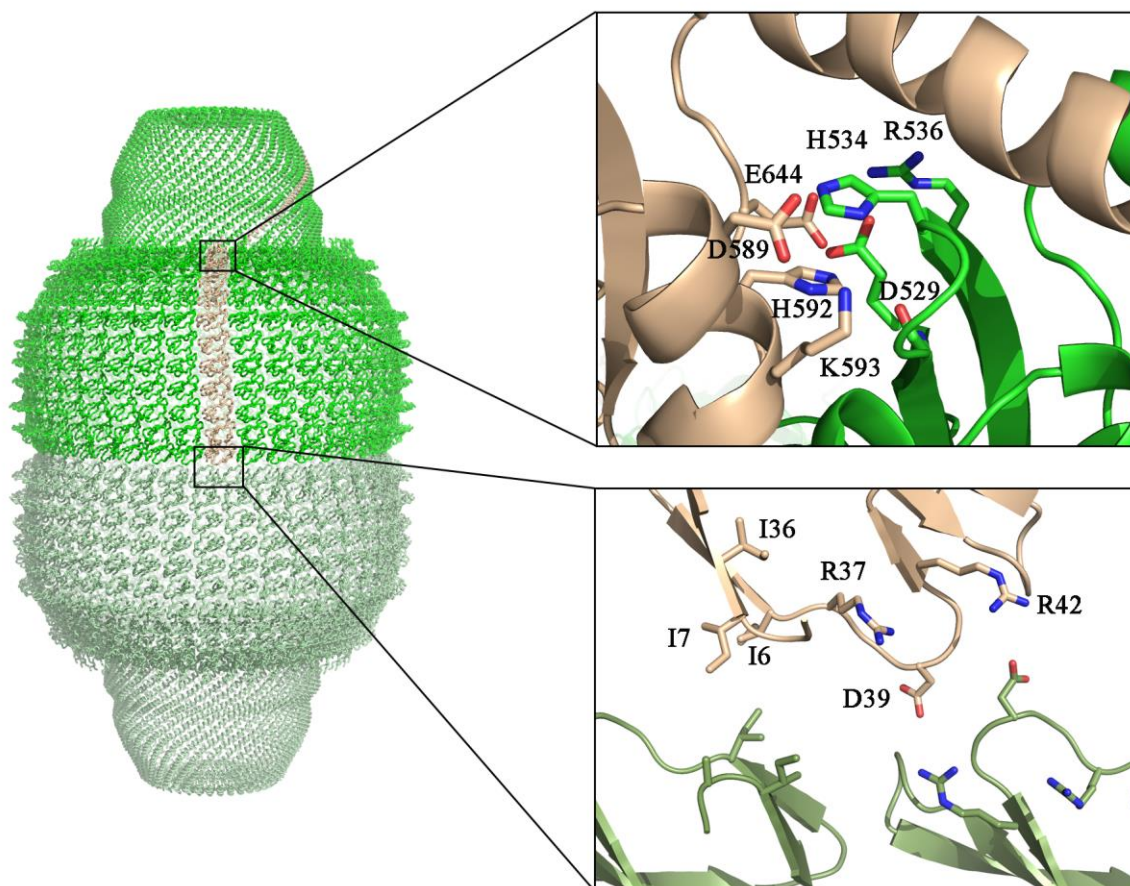


Figure 5. Structure of the vault shell, colored in green and pale green for the top and bottom half-vault moieties respectively, with one of the 78 MVP copies forming the particle shown in wheat (PDB id: 4JL8). The top inset shows a close up of the MVM-MVP lateral electrostatic interactions in the shoulder domain. The bottom inset shows the R1-R1 interactions established at the half-vault interface.

Biophysical Implications and Future Outlook for Controlled Payload Delivery

Our data show that the pH lowering triggers the weakening of lateral intermonomeric interactions rather than opening vaults into halves. These results agree with our previous mechanical study showing that AFM tip-induced mechanical fractures occur along lateral MVP-MVP contacts.³⁵ Interestingly, those fracture were found to be capable of self-healing.³⁵ Another protein assembly that also displays longitudinal fractures and self-healing capabilities are microtubules (MT).^{36,37} In MT, this high reversibility of lateral bonds has been suggested to repair the cracks between shortening protofilaments in the MT wall and serve as means of inhibiting de-polymerization. It seems interesting that the spatial distribution of tubulin protofilaments conforming MT reassembles that of MVP monomers in the barrel zone, which also bundle parallel to one another and form a cylindrical structure. In our case, decreasing the pH from 7.5 to 6.0 leads to the formation holes and cracks on the vault barrel that might permit the escape of different payloads with sizes smaller than the vault diameter (~35 nm). This pH-dependent dynamics might be exploited during vault cellular uptake upon endocytosis, where the pH of the environment suffers mild acidification.^{13,14}

Conclusions

In this paper we have combined single particle techniques with bulk techniques to study the structural dynamics of individual vault particles as a function of pH. Our results showed that at pH 7.5 and 6.0 the quaternary structure of vaults (observed as full- or half-particles) was maintained. Despite the overall structure was preserved, though, our AFM experiments indicated that at pH 6.0 the height of the particles was reduced a 15%. The adsorption of individual vaults on substrates allowed us to monitor the pH-dependent dynamics of single particle in real time. Our experiments showed that pH lowering destabilized the interaction between adjacent MVP monomers, which resulted in the formation of cracks on the barrel zone. Those cracks were observed in vault particles maintaining their quaternary structure if the pH was maintained above 5.7 but lower values of pH led to protein aggregations. Lowering the pH does not open vaults into halves, as previously described in literature,^{7,17,18}

but promote a global destabilization of the particle that is governed by the weakening of the inter-monomeric contacts at the barrel. Based on the crystallographic structure, we propose that the interactions of four histidines with polar residues across the MVP-MVP lateral interfaces in the shoulder and barrel zones, are the determinants of the pH-dependent disassembly of the structure. In particular, His534 of one MVP monomer appears to play a crucial role, participating in a histidine- α -helix charge-dipole interaction, with the cap α -helix N-terminus of the neighboring MVP. In summary, our results reveal new insights into the pH-dependent dynamics of vault particles and might offer a means of controlling artificial cargo delivery upon cell endocytosis, where the pH of the environment gradually decreases.

Materials and methods

Production and Purification of Recombinant Vaults

Recombinant vaults were produced and purified as previously described (22). Briefly, H5 cells (Invitrogen)™ were infected with the MVP recombinant baculovirus, harvested at 48 hours post-infection, washed with Phosphate Buffered Saline, resuspended in buffer A (75 mM NaCl, 50 mM Tris pH 7.4, 1.5 mM MgCl₂, 1mM DTT) plus 1% NP-40 and protease inhibitors (Protease inhibitor cocktail tablets; Roche) and maintained on ice for 30 min. The resuspended pellet was sonicated and cellular debris was removed by centrifugation. Vault particles were pelleted through a 25% (w/w) sucrose cushion in buffer A (37,000 rpm, using a SW41Ti rotor for 2:30 hours at 4°C). The resulting pellet was re-suspended in 600 μ l of Buffer A and applied to a 25–50% sucrose gradient in buffer A and centrifuged for 45 minutes at 40,000 rpm. Fractions containing vaults were dialyzed against buffer A and concentrated to ~5mg/ml using a centrifugal filter device (centricon YM100; Millipore).

AFM

AFM measurements were performed with a Nanotec microscope (Nanotect Electrónica S.L., Madrid, Spain) operating in Jumping mode plus.³² In this mode, the feedback is done in normal force by performing a force-vs.-distance curve at all point of the images. For moving from point to point, the tip retracts and moves laterally while being far from the surface, thus

reducing the lateral forces that might damage the sample. For all the images, imaging force was kept below ~ 70 pN. Rectangular silicon-nitride cantilevers (Olympus, RC800PSA) with a nominal spring constant of 0.05N/m were used.

All the experiments were performed in liquid environment, with buffers at three different pHs: 7.5 (50 mM Tris), 6.0 (50mM Hepes), 5.2 (50 mM NaOAc). All the buffers also contained 75mM NaCl and 0.75 MgCl. To perform the AFM experiments three different adsorptions strategies were tested: (1) pre-incubation of the sample on the Eppendorf under a specific pH conditions for 5 minutes prior to adsorption, (2) adsorption of the sample at pH=7.5 for 30 minutes and posterior pH exchange before imaging, and (3) adsorption of the sample at pH=7.5 followed by real-time imaging of the sample while lowering the pH. For all the cases 1 μ l of stock solution was diluted into 19 μ l of the considered buffer. This 20 μ l drop of diluted solution was incubated on a fresh highly ordered pyrolytic graphite (HOPG) surface (ZYA quality NT-MDT) and, after 30 minutes, washed with the desired buffer until a volume of 70 μ l was reached. The tip as also pre-wetted with a 20 μ l drop of buffer.

To exchange the buffer in-real time imaging a home-made system composed of two syringe pumps (NE-1000, New Era Pump Systems, Inc.) was coupled to the AFM.³⁸ Two experiments at different infuse and withdraw rates were performed (Figure 3 and S3). For both experiments the initial conditions were the same (pH=7.5) and pH was exchanged by infusing buffer at pH=5.2. Slow exchange (Figure 4): at t=0min infusing was set at 30 μ l/min and increased to 40 μ l/min at t=18 min (it was maintained at this rate for the rest of the experiment). Withdrawing, while still infusing, started at t=39min and it was set at a rate of 50 μ l/min. The total volume was exchanged at a time of ~ 72 min. Fast exchange (Figure S3) was accomplished within ~ 21 min. At t=0 min, infusing started at 20 μ l/min and increased to 25 μ l/min at t=15 min. Withdrawing started at t=15 min at 25 μ l/min. The control experiment was performed by imaging an image of similar size (600x600 nm²) at constant pH. After 24 images (t=105min) the height of the particle was only reduced a 2% —for fast exchange after 15 images (t=64 min) the height was reduced 37% and for slow exchange after 24 images it was reduced to 25%.

All the images were acquired and processed with WSxM software.³⁹ The height of the particles was considered as the maximum value obtained in the topographical profile, also determined by WSxM.

QCM-D Experiment

The viscoelastic changes associated with vault particles at different pHs (7.0, 6.0, 5.0, and 4.0) were studied by QCM-D (Q-Sense D300 system, Q-Sense AB, Goteborg, Sweden). For these measurements, gold quartz crystals (AT cut) with a fundamental resonant frequency of 5 MHz were used. Before loading of vault particles, control experiments using buffer changes (7.0, 6.0, 5.0, and 4.0) were conducted to quantitate the effect of buffers on frequency and dissipation. For the measurements, a baseline was established with 10mM sodium acetate buffer (pH 7.0) and recorded for 10 minutes. After observing a stable baseline, vault particles (50µg in 600ul acetate buffer, pH=7.0) were gradually deposited on the crystal and allowed it to stabilize for 50 minutes. To remove loosely bound material, the surface was washed with 0.6 ml of buffer at pH=7 for 10 minutes. Buffer was then exchanged, consecutively, to lower the pH to 6.0, 5.0 and 4.0. Time between exchanging buffers was 20 minutes. The same experiment was also conducted with 10 µg of sample to ensure that there was no artifact to signal coming from particle aggregation or the formation of particle multilayers. After each run, gold surface was cleaned and regenerated by soaking the crystal in a 1:1:5 mixture of H₂O₂ (30%), NH₃ (25%), and distilled water at 60°C for 15 min followed by exposure to UV light for 10 min. Frequency and dissipation values were recorded at fundamental frequency 5MHz and three overtones (15MHz, 25MHz and 35MHz); temperature was 24.5°C.

Thermal Denaturation

Thermal stability of vault particles was studied using four pHs (pH=7.5, 50 mM Tris; pH=6.0, 50 mM CaCO₃; 50 mM, pH=5.0, NaOAc 50 mM; pH=4.0, NaOAc). These buffers also contained 50 mM MgCl₂ and 75mM NaCl. Vault particles were diluted in each buffer to a final concentration of 0.2mg/ml. To each sample, 2.5 µL of 1% Sypro-Orange dye (Invitrogen 140 Inc. S6651) was added to obtain the final reaction volume to 25 µL. The assays were conducted in a qPCR instrument (Corbett Research, RG-3000). A temperature

ramp from 25 to 99°C, increasing 1 degree per minute was used. Lysozyme was run as a positive control at concentrations of 0.3 and 0.5mg/ml. Melting temperature of samples was determined using the first derivative (dF/dT) of the raw fluorescence data. All these experiments were conducted in three technical replicates.

References

- 1 Rome, L. H. & Kickhoefer, V. A. Development of the Vault Particle as a Platform Technology. *Acs Nano* **7**, 889-902, (2013).
- 2 Casanas, A., Guerra, P., Fita, I. & Verdaguer, N. Vault particles: a new generation of delivery nanodevices. *Curr Opin Biotech* **23**, 972-977, (2012).
- 3 Kedersha, N. L. & Rome, L. H. Isolation and Characterization of a Novel Ribonucleoprotein Particle - Large Structures Contain a Single Species of Small RNA. *J Cell Biol* **103**, (1986).
- 4 Kickhoefer, V. A., Stephen, A. G., Harrington, L., Robinson, M. O. & Rome, L. H. Vaults and telomerase share a common subunit, TEP1. *J Biol Chem* **274**, (1999).
- 5 Vilalta, A., Kickhoefer, V. A., Rome, L. H. & Johnson, D. L. The rat Vault RNA Gene Contains a Unique RNA-Polymerase-III Promoter Composed of both External and Internal Elements that Function Synergistically. *J Biol Chem* **269**, (1994).
- 6 Tanaka, H. *et al.* The Structure of Rat Liver Vault at 3.5 Angstrom Resolution. *Science* **323**, 384-388, (2009).
- 7 Querol-Audi, J. *et al.* The mechanism of vault opening from the high resolution structure of the N-terminal repeats of MVP. *Embo J* **28**, 3450-3457, (2009).
- 8 Stephen, A. G. *et al.* Assembly of vault-like particles in insect cells expressing only the major vault protein. *J Biol Chem* **276**, 23217-23220, (2001).
- 9 Kickhoefer, V. A. *et al.* Engineering of vault nanocapsules with enzymatic and fluorescent properties. *P Natl Acad Sci USA* **102**, (2005).
- 10 Goldsmith, L. E., Pupols, M., Kickhoefer, V. A., Rome, L. H. & Monbouquette, H. G. Utilization of a Protein "Shuttle" To Load Vault Nanocapsules with Gold Probes and Proteins. *Acs Nano* **3**, (2009).
- 11 Buehler, D. C., Toso, D. B., Kickhoefer, V. A., Zhou, Z. H. & Rome, L. H. Vaults Engineered for Hydrophobic Drug Delivery. *Small* **7**, 1432-1439, (2011).
- 12 Kickhoefer, V. A. *et al.* Targeting Vault Nanoparticles to Specific Cell Surface Receptors. *Acs Nano* **3**, 27-36, (2009).
- 13 Lai, C. Y., Wiethoff, C. M., Kickhoefer, V. A., Rome, L. H. & Nemerow, G. R. Vault Nanoparticles Containing an Adenovirus-Derived Membrane Lytic Protein Facilitate Toxin and Gene Transfer. *Acs Nano* **3**, 691-699, (2009).
- 14 Han, M., Kickhoefer, V. A., Nemerow, G. R. & Rome, L. H. Targeted Vault Nanoparticles Engineered with an Endosomolytic Peptide Deliver Biomolecules to the Cytoplasm. *Acs Nano* **5**, 6128-6137, (2011).
- 15 Poderycki, M. J. *et al.* The vault exterior shell is a dynamic structure that allows incorporation of vault-associated proteins into its interior. *Biochemistry-Us* **45**, 12184-12193, (2006).
- 16 Yang, J. A. *et al.* Vaults Are Dynamically Unconstrained Cytoplasmic Nanoparticles Capable of Half Vault Exchange. *Acs Nano* **4**, 7229-7240, (2010).

- 17 Goldsmith, L. E., Yu, M., Rome, L. H. & Monbouquette, H. G. Vault nanocapsule dissociation into halves triggered at low pH. *Biochemistry-US* **46**, 2865-2875, (2007).
- 18 Yu, M., Ng, B. C., Rome, L. H., Tolbert, S. H. & Monbouquette, H. G. Reversible pH Lability of Cross-linked Vault Nanocapsules. *Nano Lett* **8**, 3510-3515, (2008).
- 19 Esfandiary, R., Kickhoefer, V. A., Rome, L. H., Joshi, S. B. & Middaugh, C. R. Structural Stability of Vault Particles. *Journal of Pharmaceutical Sciences* **98**, (2009).
- 20 Carrasco, C. *et al.* The capillarity of nanometric water menisci confined inside closed-geometry viral cages. *P Natl Acad Sci USA* **106**, 5475-5480, (2009).
- 21 Muller, D. J. & Engel, A. Voltage and pH-induced channel closure of porin OmpF visualized by atomic force microscopy. *J Mol Biol* **285**, 1347-1351, (1999).
- 22 Bayburt, T. H. & Sligar, S. G. Single-molecule height measurements on microsomal cytochrome P450 in nanometer-scale phospholipid bilayer disks. *P Natl Acad Sci USA* **99**, 6725-6730, (2002).
- 23 De Yoreo, J. J., Chung, S. & Friddle, R. W. In Situ Atomic Force Microscopy as a Tool for Investigating Interactions and Assembly Dynamics in Biomolecular and Biomineral Systems. *Adv Funct Mater* **23**, 2525-2538, (2013).
- 24 Kedersha, N. L., Heuser, J. E., Chugani, D. C. & Rome, L. H. Vaults .3. Vault Ribonucleoprotein-Particles Open into Flower-Like Structures with Octagonal Symmetry. *J Cell Biol* **112**, 225-235, (1991).
- 25 Dixon, M. C. Quartz Crystal Microbalance with Dissipation Monitoring: Enabling Real-Time Characterization of Biological Materials and Their Interactions. *Journal of Biomolecular Techniques : JBT* **19**, 151-158, (2008).
- 26 Dutta, A. K. & Belfort, G. Adsorbed gels versus brushes: Viscoelastic differences. *Langmuir* **23**, 3088-3094, (2007).
- 27 Voinova, M. V., Rodahl, M., Jonson, M. & Kasemo, B. Viscoelastic acoustic response of layered polymer films at fluid-solid interfaces: Continuum mechanics approach. *Phys Scripta* **59**, 391-396, (1999).
- 28 Rayaprolu, V., Manning, B. M., Douglas, T. & Bothner, B. Virus particles as active nanomaterials that can rapidly change their viscoelastic properties in response to dilute solutions. *Soft Matter* **6**, 5286-5288, (2010).
- 29 Niesen, F. H., Berglund, H. & Vedadi, M. The use of differential scanning fluorimetry to detect ligand interactions that promote protein stability. *Nat. Protocols* **2**, 2212-2221, (2007).
- 30 Ablinger, E., Leitgeb, S. & Zimmer, A. Differential scanning fluorescence approach using a fluorescent molecular rotor to detect thermostability of proteins in surfactant-containing formulations. *International Journal of Pharmaceutics* **441**, 255-260, (2013).
- 31 Tanaka, H. & Tsukihara, T. Structural studies of large nucleoprotein particles, vaults. *P Jpn Acad B-Phys* **88**, 416-433, (2012).
- 32 Ortega-Esteban, A. *et al.* Minimizing tip-sample forces in jumping mode atomic force microscopy in liquid. *Ultramicroscopy* **114**, 56-61, (2012).

- 33 Casanas, A. *et al.* New features of vault architecture and dynamics revealed by novel refinement using the deformable elastic network approach. *Acta Crystallogr D* **69**, 1054-1061, (2013).
- 34 van Vlijmen, H. W. T., Curry, S., Schaefer, M. & Karplus, M. Titration calculations of foot-and-mouth disease virus capsids and their stabilities as a function of pH1. *J Mol Biol* **275**, 295-308, (1998).
- 35 Llauro, A. *et al.* Mechanical Stability and Reversible Fracture of Vault Particles. *Biophys J* **106**, 687-695, (2014).
- 36 Schaap, I. A. T., Carrasco, C., de Pablo, P. J., MacKintosh, F. C. & Schmidt, C. F. Elastic response, buckling, and instability of microtubules under radial indentation. *Biophys J* **91**, (2006).
- 37 Kononova, O. *et al.* Tubulin Bond Energies and Microtubule Biomechanics Determined from Nanoindentation in Silico. *J Am Chem Soc* **136**, 17036-17045, (2014).
- 38 Hernando-Perez, M. *et al.* Direct Measurement of Phage phi29 Stiffness Provides Evidence of Internal Pressure. *Small* **8**, 2366-2370, (2012).
- 39 Horcas, I. *et al.* WSXM: A software for scanning probe microscopy and a tool for nanotechnology. *Rev Sci Instrum* **78**, (2007).

Calcium Ions Modulate the Mechanics of Tomato Bushy Stunt Virus

Based on

A. Llauró*, E. Coppari*, F. Imperatori, A. R. Bizzarri, J.R.Castón, L. Santi, S. Cannistraro, P. J. de Pablo, Elastic-plastic switch of tomato bushy stunt virus particles”, Biophys J. (2015);109:390-7. **these authors contributed equally to the work*

Abstract

Viral particles are endowed with physicochemical properties whose modulation confers certain metastability to their structures, to fulfill each task of the viral cycle. Here we investigate the effects of swelling and ions depletion on the mechanical stability of individual Tomato Bushy Stunt Virus nanoparticles (TBSV-NPs). Our experiments show that calcium ions modulate the mechanics of the capsid. The sequestration of calcium ions from the intracapsid binding sites reduces the rigidity and resilience of TBSV-NPs in about 24% and 40%, respectively. Interestingly, mechanical deformations performed on native TBSV-NPs induce an analogous result. An analysis of the pattern of fracture revealed that TBSV-NPs do not show capsomeric vacancies after surpassing the elastic limit. We hypothesize that, despite there are breakages among neighboring capsomers, RNA-capsid protein interaction is the responsible for preventing the release of capsid subunits. This work shows the mechanical role of calcium ions in viral shells stability and identify TBSV-NPs as malleable protein-based platforms based on protein cages for cargo transportation at the nanoscale.

Introduction

Viral capsids are self-assembled macromolecular shells that naturally protect, shuttle and release the enclosed genetic material upon the proper physicochemical conditions.¹ The stability of viral shells has been tuned by evolution to respond to a variety of environments encountered along their biological cycle. This enormous adaptability to the environment, together with the possibility of genetically engineering their coat protein (CP) coding sequence, have made viruses attractive systems to construct virus-derived nanoparticles (VNPs) for applications in bionanotechnology.² Among them, plant virus capsids display a variety of properties particularly appropriate for their applications in nanotechnology, such as their controllable genetic manipulation, their inability to infect and replicate in vertebrate hosts, or their ease of production.³ Tomato Bushy Stunt Virus nanoparticles (TBSV-NPs) are robust, stable, highly modifiable and easy to manufacture using *Nicotiana benthamiana* as the production host.⁴ In addition, the intrinsic tendency of these viruses to form ordered aggregates has already been used to build homogeneous monolayers, which probes the possibility of using these VNPs as building blocks for applications in material science.⁵

TBSV is a small non-enveloped virus with an outer diameter of 33 nm and an icosahedral symmetry with a triangulation number of $T=3$ (Figure 1A, left). The viral capsid is formed by the assembly of 180 subunits of a single CP and its genome consists of a monopartite ssRNA.⁶ An attractive feature of TBSV-NPs is the possibility to access their inner cavity using a swelling process that mediates the reversible opening of pores on the VNPs' surface. (Figure 1A, right).⁷ This process, which likely occurs during the first stages of the infection cycle, increases the virus dimension through a Ca^{2+} -dependent transition, and it is required for the release of the RNA during uncoating.⁸ The subunits of TBSV are arranged in three packing environments: A-, B-, and C-subunits (Figure 1A and 1B). A-subunits (blue) pack around the 5-fold symmetry axes, whereas B- and C-subunits (white and green) pack alternatively around the 3-fold symmetry axes. Each capsomeric subunit is divided in three regions: the P-domain, that protrudes outwards giving the virus a granular appearance; the S-domain, that forms the shell; and the R-domain, an inner tail protein that is inserted into the viral RNA.^{7,9}

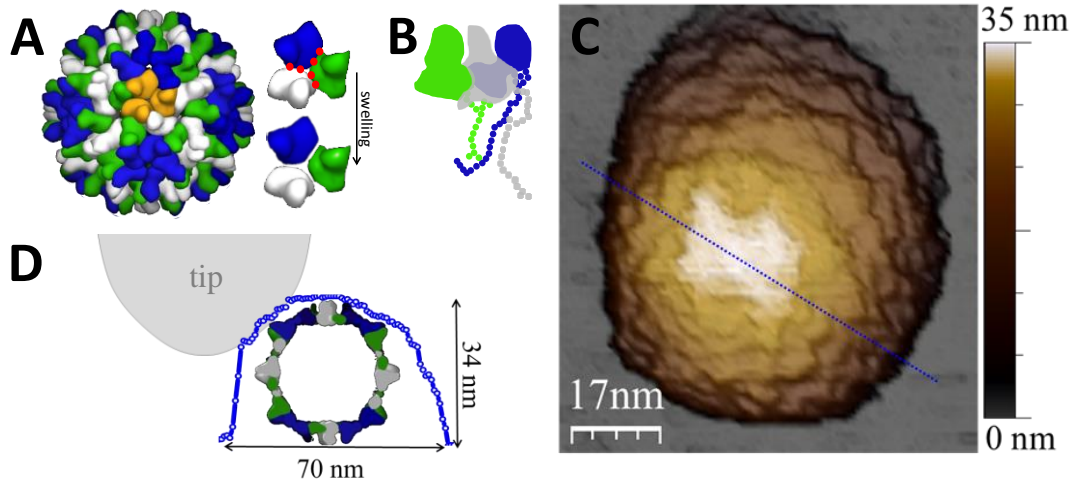


Figure 1. TBSV structure. (A) (*Left*) Side view derived from X-ray diffraction data (*pdb 2TBV*).⁹ One of the protein trimers at the quasi-threefold axes is highlighted in orange. (*Right*) Schematic of the conformational change associated with the swelling process. (*Top*) The subunits of the trimer before expansion are tightly packed and Ca²⁺ are present (red dots). (*Bottom*) After the expansion the Ca²⁺ ions are removed and the electrostatic repulsion between subunits opens pores at the quasi-threefold axes. (B) Illustration of the trimer. Each trimer is composed of A-, B- and C-type protein subunits: the A-type are packed around the 5-fold axes (blue), and the B- and C-types alternate around the three-fold axes (gray and green). The inner tail proteins (dots) would interact with the ssRNA.⁵ (C) JM-AFM image of compacted wild-type VNPs in liquid conditions. The dotted blue line shows the profile along which the height was determined. The minimum resolved feature on the virus was ~5 nm. (D) Profile of the particle (dotted blue line in B). The tip geometrically dilates¹⁰ the lateral dimension of the particle.

Investigating virus physicochemical properties under different conditions is important for the application of these nanostructures in biotechnology. In particular, the study of virus mechanics by Atomic Force Microscopy (AFM)¹¹ has emerged as a powerful technique to unravel the structural role of nucleic acids^{12,13} or capsid mutations.^{14,15} In addition, AFM has contributed to understanding the influence of environmental conditions on the stability of viruses, including pH variations¹⁶⁻¹⁸ and humidity.¹⁹ The study of the mechanical properties of viral shells pivots on the measurement of the stiffness and the breaking force of the particle, which are both determined by recording indentation curves that result from squeezing the particles with an AFM tip. The stiffness (directly linked to the spring constant of the viral particle) is obtained from the linear regime of the deformation and provides information about the rigidity of the capsid. On the other hand, the breaking force, which is

ascribed to the force needed to disrupt the capsids, typically corresponds to the end of the elastic regime and provides information about the mechanical strength of the capsid.²⁰

In this chapter we present a twofold study based on the topographic and mechanical analysis of individual TBSV-NPs varying two conditions, the pH and the chelation of calcium ions. Our results show that the intra-capsid calcium ions are inextricably linked to both virus rigidity and breaking force (termed here as elastic limit). In addition, we show that viral particles keep their capsomers after irreversible deformation. This property might represent a valuable feature to utilize these systems as malleable nanocarriers for drug delivery.

Results

Four different forms of TBSV-NPs have been studied in this work: compact wt TBSV-NPs (cVNPs), swollen TBSV-NPs (sVNPs), recompacted TBSVs-NPs (rVNPs), and Ca²⁺-free TBSV-NPs (ifVNPs) (see [Table S1](#) in the Supporting Information and [Figure 2A](#)). cVNPs are the native compact viruses and sVNPs are the expanded forms. These expanded forms were subjected to two different procedures: we studied the reversibility of the process by decreasing the pH of the solution in the presence of calcium ions (rVNPs) and we studied the role of the ions by decreasing the pH of the solution in the absence of calcium ions (ifVNPs). All the AFM measurements were conducted at pH 5.3, except for the case of sVNPs, where the measurements were at pH 8.5 (see Materials and Methods for details in sample preparation).

Topographic Characterization

High-resolution AFM image of single wt cVNP on mica presented particles with a diameter (height) fully compatible with the X-ray structure⁹ ([Figure 1C](#)). Despite tip-particle lateral dilation¹⁰ (see [Figure 1D](#)), we were able to resolve features of ~5 nm, which corresponded to the size of individual capsomers. The granular structure obtained in our images was attributed

to the protruding domains (P-domains) present on the outer shell of TBSV NPs.⁹ This resolution was routinely obtained with different tips (Figure S1).

We studied the stability of the four different forms of TBSV-NPs using TEM and AFM (Figure 2). TEM images of wt cVNPs and rVNPS showed stable structures that were indistinguishable. However, the structural integrity of sVNP particles was less preserved, some particles appeared broken and the negative staining agent could penetrate inside some shells (Figure 2B, arrows). Similarly, AFM images of cVNPs and rVNPs showed structures with an average height that corresponded to intact particles, but sVNPs appeared as collapsed structures with an average height of only 10 nm (Figure 2B and 2C). These results suggested the sVNPs were less stable than wt cVNPs.

Interestingly, the ion-free nanoparticles (ifVNPs) gave rise to an intermediate state that laid between the compact and the swollen forms. AFM images of these ifVNPs showed that the particles maintained their structure, but the average height was decreased to 30 nm (Figure 2B and 2C). In addition, the existence of debris and genome on the mica substrate suggested that some particles were broken during the process. The higher dispersion of the height distribution also indicated that ifVNPs were less homogeneous than the native forms (Figure S2). In agreement with the AFM results, TEM images of ifVNPs showed close particles (no staining agent penetrated inside the shell) and the presence of some debris on the grid (Figure 2B). This confirmed, with another technique, that the adsorption process (and perhaps the drying in TEM) was the responsible for the loss of stability of the swollen forms.

Mechanics

To further investigate the stability of the particles we performed nanoindentation experiments. Multiple force-indentation curves (FIC) were performed on the same particle in order to study the evolution of the mechanical properties and topography at the single particle level. Figure 3 shows a wt cVNP and an ifVNP subjected, respectively, to two cyclic

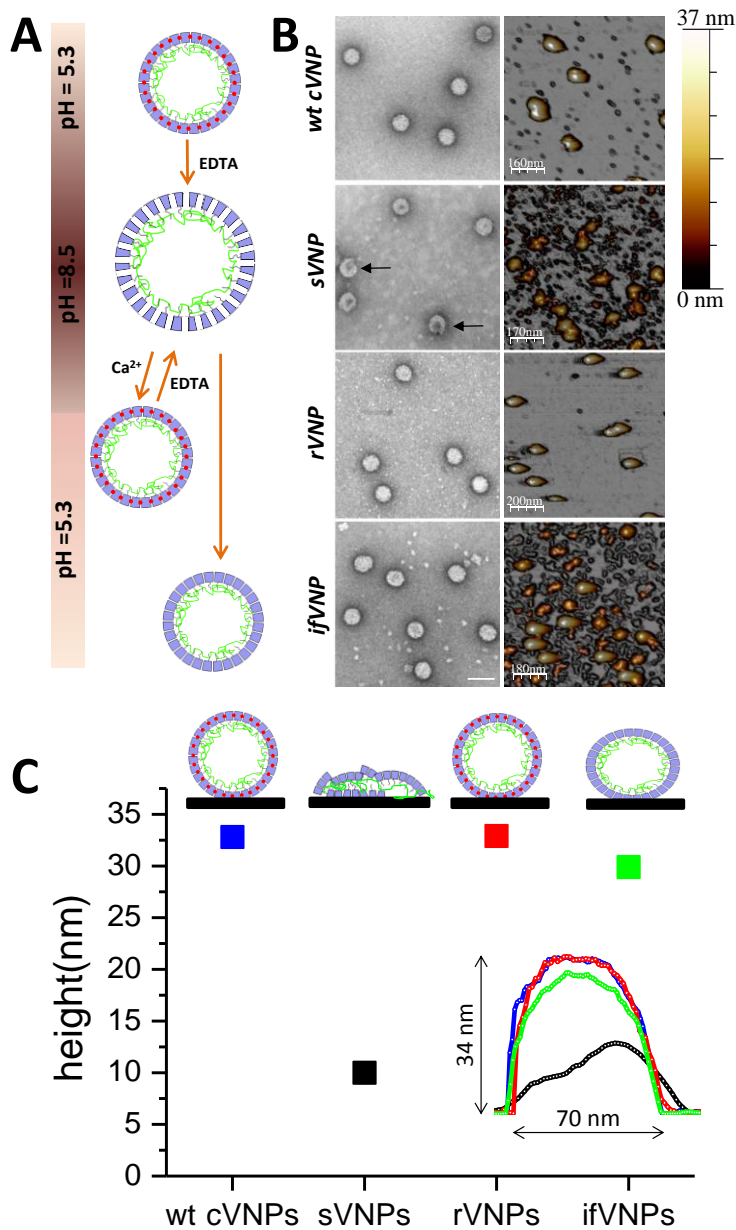


Figure 2. Schematic of the swelling process and images of the particles by AFM and TEM (A) Representation of the pH-induced expanding/compacting process. Under acidic conditions (pH 5.3) the Ca²⁺ ions are located at specific binding sites (red dots) contributing with an attractive component to the protein-protein interaction. The swelling of the particle was achieved by increasing the pH in the presence of a chelation agent.^{7,8,21} This procedure promoted the expansion of the capsid as a consequence of the deprotonation of the aspartate residues at the calcium binding sites and the subsequent sequestration of these ions. The swollen forms were either (1) recompactated by lowering the pH in the presence of calcium (rVNPs) or (2) compacted by lowering the pH in the absence calcium ions (ifVNPs). (B) (left) TEM images of the different forms of the particles. Scale bar: of 50 nm. (right) AFM images. Images of wt cVNPs, rVNPs and ifVNPs were taken at pH 5.3. Images of sVNPs were taken at pH=8.5. (C) Graph comparing the AFM heights of the different forms. (*inset*) Typical profiles of the four different forms.

loading assays. In order to investigate the changes in height and topography induced by the deformations, AFM image were acquired between nanoindentations (Figure 3C and 3F). The consecutive FICs performed on the wt cVNP transitioned from a linear deformation (FIC #1) to a Hertzian-like behavior (FIC #10) (Figure 3A). In addition, significant differences were observed between the first (FIC #1) and second (FIC#2) nanoindentation. FIC #1 presented a linear response up to 4.8 nN, where a sharp drop in force was registered. This maximum

force is typically ascribed to the breakage of the particle and the loss of capsid subunits.^{18,22-25} However, immediate imaging of the particle after the nanoindentation demonstrated the absence of capsomeric vacancies and a height decrease of less than 2 nm (Figure 3B-C). Because nanoindentations below that point were totally reversible, we decided to term this maximum force as 'elastic limit'. The backward curve of FIC#1 (blue line) defined a hysteresis loop characteristic of non-equilibrium processes such as breakage or buckling.^{26,27} Whether breakage, buckling, or a combination of both took place in our case was difficult to assess, but the change in mechanical properties observed during the second nanoindentation (FIC#2) indicated that the particle had suffered some irreversible damage. FIC#2 presented lower values of elastic limit and elastic constant, which had to be the consequence of a change in the virus structure. Indeed, the slight decrease in height (~2 nm) suggested a rearrangement that could be compatible with the alteration of some intercapsomeric contacts without loss of capsomers. This argument was further supported by the topographies obtained through the entire loading cycle. Up to FIC #5, structural damages were limited to the progressive reduction of the particle height without loss of capsomers (Figures 3B-C and S3). This progressive reduction in height occurred in parallel with the transition from a linear to a Hertzian-like behavior (FIC #10), which is typical of solid objects.²⁸ The absence of capsomeric vacancies and this Hertzian-like behavior suggested that the capsid and the genome were compressed through the process and, the fact that the final height of the structure (~20 nm) was larger than only two capsid walls (~10 nm) demonstrated the inextricable link between the capsid and the genome.

Moreover, comparison of the mechanical properties between wt cVNPs and ifVNPs revealed that the former presented a higher elastic limit and rigidity at the beginning (FIC#1) (Figure 3A and 3D). Besides that, the evolution of the mechanical properties of ifVNPs and wt cVNPs were very similar: a progressive decrease in height and a transition from a linear to a Hertzian-like behavior (Figure 3D-F).

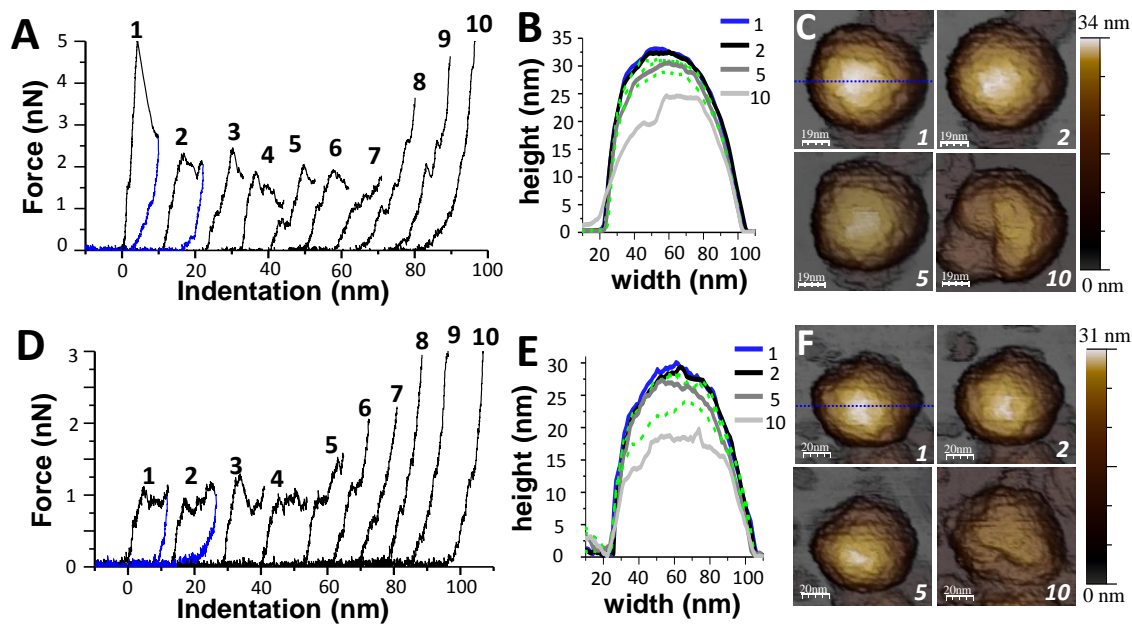


Figure 3. Cyclic loading with single indentation assay. (A) Cyclic loading performed on a wt cVNP. (B, C) Profile and topographic evolution of the wt cVNP through the loading process. Profiles were taken on top of the VNP structures (marked with a dotted blue line in the AFM images). Labels indicates the number of FIC (*i.e.*, the profile labeled as 1 shows the topography in which the FIC-1 was performed). (D, E, F) The same experiment performed on an ifVNP. All the images were acquired in JM-AFM under acidic buffer conditions (pH 5.3). Nanoindentation curves of (A) and (D) are laterally shifted for clarity.

An ensemble analysis allowed us to compare the differences between the two forms statistically. [Figures 4A](#) and [4B](#) show the initial 3 FICs performed on 11 wt cVNPs and 16 ifVNPs, respectively. Comparison of the elastic limit between both forms ([Figure 4C](#)) showed that whereas wt cVNPs presented a higher value at the beginning (FIC #1), no significant differences were found in the consecutive loads (FIC #2 and FIC #3). The evolution of the spring constant between wt cVNPs and ifVNPs presented a similar behavior ([Figure 4D](#)). Although the stiffness decreased monotonically for both kinds of particles, wt cVNPs started with a higher value of elastic constant. Likewise, a progressive decrease in height was found for both wt cVNPs and ifVNPs, but wt cVNPs presented an initial higher height ([Figure 4E](#)).

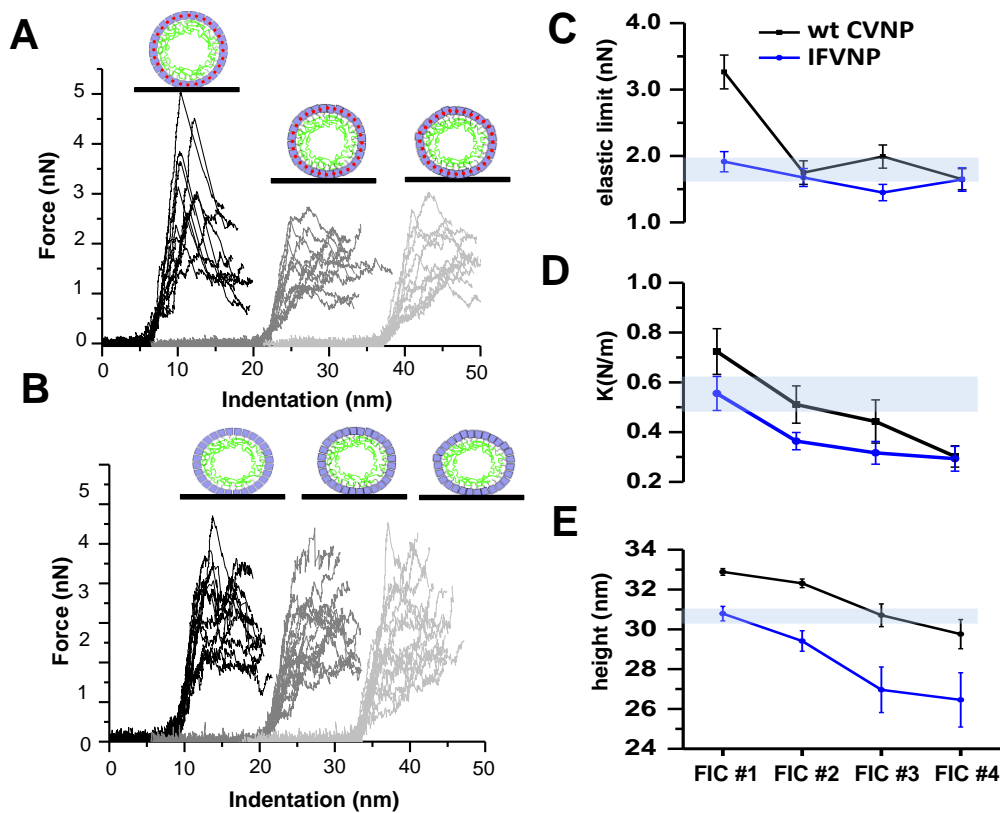


Figure 4. Comparison between the mechanical properties of wt cVNP and ifVNPs. (A) The graph shows the overlap of the first three FICs performed on 11 wt cVNPs: first curve (black), second curve (dark grey), and third curve (light grey). Curves are laterally shifted for clarity. (B) Nanoindentations performed on 15 ifVNPs (displayed as in A). The insets represent the progressive deformation of the particles through the loading process. The observed irreversible decrease in height is likely caused by the rearrangements of inter-capsomeric interactions that do not entail the release of individual protein subunits. (C) Comparison of the evolution of the elastic limit between wt cVNPs (black line) and ifVNPs (blue line). (D) Comparison of the evolution of the elastic constant, obtained by fitting the initial linear, for wt cVNPs (black line) and ifVNPs (blue line). (E) Comparison of the evolution of the height between wt cVNPs (black line) and ifVNPs (blue line). It indicates the average height of the particles before performing the corresponding FIC.

Discussion

Our results can be discussed from a twofold perspective, including the topographical aspects of the viral particles adsorption and the mechanical characterization addressed by the nanoindentation experiments. The high heterogeneity of charge density and hydrophobic

patches within a virus shell permits the anchorage of particles to substrates through a combination of van der Waals, electrostatic and hydrophobic forces.²⁹ AFM imaging of adsorbed particles provides valuable parameters that reveal subtle details about VNP stability. Note, however, that this information is only valid for comparing particles of the same type, as the complexity of the structure could make the comparison between different specimens misleading.

Our experiments showed that wt cVNPs and rVNPs presented heights (~34 nm) compatible with the crystallographic structure,⁹ which in turn proved the well-known reversibility of the swelling process (Figure 2).^{5,7} However, topographical AFM images of sVNPs showed collapsed structures characterized by heights around 10 nm. TEM images complemented the AFM results; whereas wt cVNPs and rVNPs were stable and indistinguishable, sVNPs appeared broken after the adsorption and drying on the TEM grid. This result allowed us to conclude that the expanded forms were less stable. Viral structures have to be labile enough to provide the convenient meta-stability for the virus particle to accomplish its infectivity cycle. Some viruses, belonging to families other than TBSV, do not need virion swelling for the co-translational disassembly.³⁰ TBSV and many other plant viruses, however, require swelling-induced structural changes for making RNA accessible to the cellular machinery.^{7,21,31} Our results reflect this situation by showing that the swollen forms of the virus, where the internal genome is still packed but reachable by the cellular proteins, are mechanically less stable than the native forms.

The ion-free form (ifVNPs) appeared to be an intermediate state between the native and swollen structures. The decrease in height observed by AFM (~5 nm, Figure 2C) suggested that the structure might have undergone some structural rearrangement due to the lack of ions. The ion chelation, though, did not preclude that most of the viruses maintained the assembled shape. Comparison of the mechanical properties between the native and ion-free particles supported these results. If we assume the spring constant as a measurement of virus deformability (which can not only be induced by the AFM tip, but also by the substrate during adsorption), the fact that ifVNPs were softer than cVNPs by about 0.2 N/m suggested that they were more malleable structure, thus explaining why the height was lower. In this regard, our high-resolution AFM images present the first experimental evidence of virus plasticity,

which has been previously suggested for other viruses.^{32,33} This results was also support by the lack of capsomeric vacancies observed during the consecutive loading.

Previous mechanical studies of VNPs have shown that the AFM tip usually removes individual structural components after the elastic limit (breaking force) is reached.^{18,22,24,25} In contrast, our data showed that consecutive FICs induced an irreversible deformation of the structure that was not accompanied by the removal of capsid subunits. Since AFM imaging is able to resolve individual capsomers,^{25,34} we assumed that the mechanical variation of TBSV-NPs after indentations was likely related to structural alterations consisting of inter-capsomeric cracks that fell beyond the limit of our AFM. We hypothesize that the resistance of individual capsomers to be removed originates from the presence of the inner capsid proteins tails interacting with ssRNA.^{5,9} These domains would maintain the viral subunits joined to the viral core and avoid the disassembly of the capsid. Supporting this hypothesis, the Hertzian-like behavior and height of the structure observed at the end of the loading cycle indicated the existence of a tight and stabilizing interaction between the genome and the capsid shell in the native form. In contrast, this interaction disappear in the expanded form due to the increase in electrostatic repulsion. At pH 8.5 the genome is able to escape the capsid and the structure collapse. Indeed, the average height of the sVNPs structures was 10 nm, which roughly corresponds to the width of two collapsed capsid walls.⁶

Our AFM results also suggested that the decrease in spring constant and elastic limit obtained after the chelation of calcium ions could be mimicked by deforming the virus with the AFM tip (Figures 4C and 4D). This observation does not imply that the structural changes induced by the deformation are the same as those induced by the ion sequestration, but it indicates that both effects have similar mechanical consequences. We suggest that the first indentation might disrupt some of the inter-capsomeric interactions mediated by calcium ions, which consequently reduce the resilience and rigidity of the particles. Subsequent deformations would then be probing a softer and more malleable structure that is held together, despite the alteration of these inter-capsomeric bonds, due to the complex amalgam of coat protein (presumably inner tail domains) and ssRNA. From a biophysical viewpoint, calcium ions could act as ‘elastic staples’ inserted between capsomers and their sequestration would leave the main mechanical clamp for maintaining viral subunits together to the inner CP-RNA binding domain.

Conclusions

In this paper we report the first experimental evidence of the mechanical role of calcium ions bound to intracapsid sites. The sequestration of these ions reduces capsid resilience and rigidity. We found that an analogous decrease could also be induced by the first indentation on wt TBSV-NP, which produced a permanent deformation of the particle without removing capsomers. Additionally, our mechanical data is consistent with the required meta-stability that TBSV-NP needs to accomplish its infection cycle. Calcium ions appear as molecular determinants for virus strength and their removal causes a mechanical instability that reduces virus resilience, which we hypothesize is governed by intercapsomeric interactions. In summary, our results highlight the crucial structural role of calcium ions on the viral shell stability. Also, TBSV ability of deforming without losing capsomers and avoiding cargo release suggests that these particle might represent suitable protein cages for payload transportation at the nanoscale.

Materials and Methods

TBSV-wt

Infectious cDNA clones were assembled using standard recombinant DNA techniques as described in details in Grasso et al. ⁴

Plant Infection

Six to eight weeks old *Nicotiana benthamiana* plants were inoculated with two different TBSV constructs ⁴. Briefly, cDNA templates of TBSV-wt constructs were digested with the restriction enzyme XmaI. One μ g of completely linearized cDNA was used for *in vitro* transcription reaction following the manufacturer's instructions (MEGAscript®T7 High Yield Transcription kit, Ambion Applied Biosystems). Plants were mechanically inoculated abrading the adaxial side of two leaves per plant using the carborundum powder (VWR International) mixed with the TBSV infectious RNAs, previously checked for integrity by TBE denaturing agarose gel electrophoresis.

Virus Purification

Virus purification was carried out as described in Grasso *et al.* 2012⁴. Briefly, infected tissue was ground in liquid nitrogen and homogenized with 3 ml/g of ice-cold extraction buffer [50 mM sodium acetate, 1% (w/v) ascorbic acid, pH 4.5, supplemented with a cocktail of protease inhibitors (P9599, Sigma)]. Homogenate was immediately filtered through Miracloth and, after low-speed centrifugation, the supernatant was adjusted to pH 5.0 with NaOH and ultracentrifuged for 1 h at 90000 x g at 4 °C, using a Sorvall-Thermo Scientific, WX ULTRA 100 ultracentrifuge with an AH629 rotor. The pellet was gently suspended in ice-cold acetate buffer (50 mM sodium acetate, pH 5.3) and then centrifuged at low speed for further clarification. Quality of the preparations was verified by a silver stained 13.5% SDS-PAGE (Figure S4). Viral particles concentration was quantified using Bradford Reagent (Bio-Rad) and Bovine Serum Albumin (BSA) as reference standards.

Sample Preparation for AFM Measurements

i) compact wt VNPs (cVNPs): stock VNPs solution (3µg/µl in 50 mM sodium acetate, pH 5.3) was diluted 1:100 into the acidic buffer (5 mM NiCl₂, 50 mM sodium acetate, pH 5.3). A 20 µl drop of this diluted solution was incubated in a freshly cleaved mica surface for 30 minutes and then gently rinsed with the same buffer. The tip was also prewetted with a drop of 20 µl of the acidic buffer before starting AFM measurements.

ii) swollen wt VNPs (sVNPs): stock wt cVNPs solution was diluted 1:10 in swelling buffer (TRIS-HCl 0.1M, pH 8.5, EDTA 50 mM) and incubated for 2 hours at 4° C. Then, the solution was diluted 1:10 in swelling buffer in the presence of NiCl₂ (TRIS-HCl 0.1 M, pH 8.5, EDTA 50 mM, NiCl₂ 5 mM) before incubating a 20 µl drop of this solution on the mica surface. After 30 minutes the sample was washed with swelling buffer, maintaining always an aqueous environment. The tip was prewetted with a 20 µl drop of swelling buffer.

iii) recompacted wt VNPs (rVNPs): the swollen VNPs (stock wt cVNPs diluted 1:10 in swelling buffer during 2 hours at 4° C) were diluted 1:10 into compacting buffer (200 mM CaCl₂, 50 mM Na-acetate, pH 5.3) and incubated for 2 hours at 4° C. Afterwards, the solution was diluted 1:2 into acidic buffer and a 20 µl drop of this solution placed on a cleaved mica surface. After 30 minutes the sample was washed with the acidic buffer.

iv) Ca²⁺-free wt VNPs (ifVNPs): stock wt cVNP solution was diluted 1:10 in the swelling buffer (TRIS-HCl 0.1 M, pH 8.5, EDTA 50 mM) and incubated for 2 hours at 4°C. Afterwards, the solution was 1:10 diluted into acidic buffer. A 20 µl drop of this diluted solution was deposited on a freshly cleaved mica surface and washed with acidic buffer after 30 minutes. The swelling buffer promoted the deprotonation of the aspartate residues of the calcium binding sites (pH 8.5) and the consecutive sequestration of the Ca²⁺ ions by the EDTA which, in this case, were not added when lowering the pH conditions.

AFM Experiments

All measurements were conducted with an AFM (Nanotec Electrónica S.L., Madrid, Spain) operated in jumping mode (JM) plus for imaging in liquid³⁵. The relevant feature of this mode is that the lateral displacement of the tip occurs when it is not in contact with the sample so that shear forces are mostly avoided during scanning. We used rectangular cantilevers (Olympus, RC800PSA) with a nominal spring constant of 0.7 N/m and a tip radius of about 15 nm. These cantilevers were chosen because their spring constant was similar to the spring constant of the virus. Sader's Method was used to calibrate the spring constant of the cantilever.³⁶ Typical imaging force was set to 200 pN.

In order to carry out the nanoindentation experiments we followed well-established procedures on virus mechanics^{20,37}. In brief, they consist of performing a single force vs. distance curve (FDC) at the very top of a single virus while recording the force as a function of the Z-piezo motion²⁰. All FDCs were performed at the same z-piezo displacement (~17 nm) with a loading rate of about 60 nm/s. These FDCs can be converted into force vs. indentation curves (FICs) by recording a calibration FDC of the cantilever deflection on the substrate next to the virus¹¹. From fitting the slope of the linear part of the FIC it is possible to calculate the spring constant (rigidity) of the virus (k_v). The steps in the indentation curve that follow the linear region after the elastic limit²² are interpreted as rupture events^{27,38}, ranging from big cracks²³ to removing single capsomers²⁵. The linear part of the FICs is sometimes preceded by a short-range non-linear region due to electrostatic, van der Waals, and hydration forces^{39,40} that was excluded from the fitting.

During the first 5 deformations, the VNP was imaged before and after each FIC. From there on, the particle was cyclically *loaded* and images were taken after sets of 5 FICs. We stopped the loading experiments when the particle responded with an Hertzian-like behavior ⁴¹. All the images were analyzed using the program WSxM (Nanotec Electrónica S.L., Madrid, Spain) ⁴²; and the profile along the top of the VNP was determined by averaging the height of a 5-pixel radius of influence.

Transmission Electron Microscopy (TEM)

For conventional TEM, 5 μ l samples were applied to glow-discharged carbon-coated grids and negatively stained with 2% aqueous uranyl acetate. Samples were applied on carbon-coated grids under the same conditions in which they were adsorbed on mica substrates for AFM measurements. Images were acquired on a JEOL JEM-1011 electron

References

- 1 Flint, S. J., Enquist, L. W., Racaniello, V. R. & Skalka, A. M. *Principles of virology*. (ASM Press, 2004).
- 2 Douglas, T. & Young, M. Host-guest encapsulation of materials by assembled virus protein cages. *Nature* **393**, 152-155, (1998).
- 3 Young, M., Willits, D., Uchida, M. & Douglas, T. Plant Viruses as Biotemplates for Materials and Their Use in Nanotechnology. *Annual Review of Phytopathology* **46**, 361-384, (2008).
- 4 Grasso, S., Lico, C., Imperatori, F. & Santi, L. A plant derived multifunctional tool for nanobiotechnology based on Tomato bushy stunt virus. *Transgenic Research* **22**, 519-535, (2012).
- 5 Luders, A., Muller, C., Boonrod, K., Krczal, G. & Ziegler, C. Tomato bushy stunt viruses (TBSV) in nanotechnology investigated by scanning force and scanning electron microscopy. *Colloids and Surfaces B-Biointerfaces* **91**, 154-161, (2012).
- 6 Olson, A. J., Bricogne, G. & Harrison, S. C. Structure of Tomato Bushy Stunt Virus .4. The Virus Particle at 2.9 Å Resolution. *Journal of molecular biology* **171**, 61-93, (1983).
- 7 Robinson, I. K. & Harrison, S. C. Structure of the Expanded State of Tomato Bushy Stunt Virus. *Nature* **297**, 563-568, (1982).
- 8 Kruse, J. *et al.* Divalent Ion-Dependent Reversible Swelling of Tomato Bushy Stunt Virus and Organization of the Expanded Virion. *Journal of molecular biology* **162**, 393-414, (1982).
- 9 Hopper, P., Harrison, S. C. & Sauer, R. T. Structure of Tomato Bushy Stunt Virus. Coat Protein-Sequence Determination and Its Structural Implications. *Journal of molecular biology* **177**, 701-713, (1984).
- 10 Villarrubia, J. S. Algorithms for scanned probe microscope image simulation, surface reconstruction, and tip estimation. *Journal of Research of the National Institute of Standards and Technology* **102**, 425-454, (1997).
- 11 Ivanovska, I. L. *et al.* Bacteriophage capsids: Tough nanoshells with complex elastic properties. *Proceedings of the National Academy of Sciences of the United States of America* **101**, 7600-7605, (2004).
- 12 Carrasco, C. *et al.* DNA-mediated anisotropic mechanical reinforcement of a virus. *Proceedings of the National Academy of Sciences of the United States of America* **103**, 13706-13711, (2006).
- 13 Hernando-Pérez, M. *et al.* Direct Measurement of Phage phi29 Stiffness Provides Evidence of Internal Pressure. *Small* **8**, 2365, (2012).
- 14 Carrasco, C., Castellanos, M., de Pablo, P. J. & Mateu, M. G. Manipulation of the mechanical properties of a virus by protein engineering. *Proceedings of the National Academy of Sciences of the United States of America* **105**, 4150-4155, (2008).
- 15 Castellanos, M. *et al.* Mechanical elasticity as a physical signature of conformational dynamics in a virus particle. *Proceedings of the National Academy of Sciences of the United States of America* **109**, 12028-12033, (2012).

- 16 Cuellar, J. L., Meinhoevel, F., Hoehne, M. & Donath, E. Size and mechanical stability of norovirus capsids depend on pH: a nanoindentation study. *Journal of General Virology* **91**, 2449-2456, (2010).
- 17 Rayaprolu, V., Manning, B. M., Douglas, T. & Bothner, B. Virus particles as active nanomaterials that can rapidly change their viscoelastic properties in response to dilute solutions. *Soft Matter* **6**, 5286-5288, (2010).
- 18 Snijder, J. *et al.* Probing the biophysical interplay between a viral genome and its capsid. *Nature Chemistry* **5**, 502-509, (2013).
- 19 Carrasco, C. *et al.* The capillarity of nanometric water menisci confined inside closed-geometry viral cages. *Proceedings of the National Academy of Sciences of the United States of America* **106**, 5475-5480, (2009).
- 20 Roos, W. H., Bruinsma, R. & Wuite, G. J. L. Physical virology. *Nature Physics* **6**, 733-743, (2010).
- 21 Aramayo, R. *et al.* Divalent ion-dependent swelling of tomato bushy stunt virus: A multi-approach study. *Biochimica Et Biophysica Acta-General Subjects* **1724**, 345-354, (2005).
- 22 Ivanovska, I. L., Miranda, R., Carrascosa, J. L., Wuite, G. J. L. & Schmidt, C. F. Discrete fracture patterns of virus shells reveal mechanical building blocks. *Proceedings of the National Academy of Sciences of the United States of America* **108**, 12611-12616, (2011).
- 23 Perez-Berna, A. J. *et al.* The Role of Capsid Maturation on Adenovirus Priming for Sequential Uncoating. *Journal of Biological Chemistry* **287**, 31582-31595, (2012).
- 24 Castellanos, M., Perez, R., Carrillo, P. J. P., de Pablo, P. J. & Mateu, M. G. Mechanical Disassembly of Single Virus Particles Reveals Kinetic Intermediates Predicted by Theory. *Biophysical journal* **102**, 2615-2624, (2012).
- 25 Hernando-Perez, M. *et al.* The interplay between mechanics and stability of viral cages. *Nanoscale* **6**, 2702-2709, (2014).
- 26 Cieplak, M. & Robbins, M. O. Nanoindentation of 35 virus capsids in a molecular model: relating mechanical properties to structure. *PloS one* **8**, e63640, (2013).
- 27 Klug, W. S. *et al.* Failure of viral shells. *Physical Review Letters* **97**, (2006).
- 28 Landau, L. D. & Lifshitz, E. M. *Theory of Elasticity*. Vol. 7 (Pergamon Press, 1959).
- 29 Muller, D. J., Amrein, M. & Engel, A. Adsorption of biological molecules to a solid support for scanning probe microscopy. *Journal of Structural Biology* **119**, 172-188, (1997).
- 30 Albert, F. G., Fox, J. M. & Young, M. J. Virion swelling is not required for cotranslational disassembly of cowpea chlorotic mottle virus in vitro. *Journal of Virology* **71**, 4296-4299, (1997).
- 31 Bakker, S. E. *et al.* Isolation of an asymmetric RNA uncoating intermediate for a single-stranded RNA plant virus. *Journal of molecular biology* **417**, 65-78, (2012).
- 32 Arkhipov, A., Roos, W. H., Wuite, G. J. & Schulten, K. Elucidating the mechanism behind irreversible deformation of viral capsids. *Biophysical journal* **97**, 2061-2069, (2009).
- 33 Baclayon, M. *et al.* Prestress strengthens the shell of Norwalk virus nanoparticles. *Nano letters* **11**, 4865-4869, (2011).

- 34 Ortega-Esteban, A. *et al.* Monitoring disassembly of individual adenovirus particles shows stepwise dismantling and core uncoating in real time. *Scientific Reports* **3**, 1434, (2013).
- 35 Ortega-Esteban, A. *et al.* Minimizing tip-sample forces in jumping mode atomic force microscopy in liquid. *Ultramicroscopy* **114**, 56-61, (2012).
- 36 Sader, J. E., Chon, J. W. M. & Mulvaney, P. Calibration of rectangular atomic force microscope cantilevers. *Review of Scientific Instruments* **70**, 3967-3969, (1999).
- 37 Mateu, M. G. in *Subcellular Biochemistry* Vol. 68 (Springer, London, 2013).
- 38 Vliegthart, G. A. & Gompper, G. Mechanical deformation of spherical viruses with icosahedral symmetry. *Biophysical journal* **91**, 834-841, (2006).
- 39 Butt, H. J. Electrostatic Interaction in Atomic Force Microscopy. *Biophysical journal* **60**, 777-785, (1991).
- 40 Sotres, J. & Baro, A. M. AFM Imaging and Analysis of Electrostatic Double Layer Forces on Single DNA Molecules. *Biophysical journal* **98**, 1995-2004, (2010).
- 41 Sneddon, I. N. The relation between load and penetration in the axisymmetric boussinesq problem for a punch of arbitrary profile. *International Journal of Engineering Science* **3**, 47-57, (1965).
- 42 Horcas, I. *et al.* WSXM: A software for scanning probe microscopy and a tool for nanotechnology. *Review of Scientific Instruments* **78**, 013705, (2007).

Cargo-Shell Coupling Governs the Mechanics of Virus-derived Protein Cages

Based on:

A. Llauró, D. Luque, E. Edwards, B. L. Trus, J. Avera, D. Reguera, T. Douglas, P. J. de Pablo, J. R. Castón. Cargo-shell coupling governs the stability of individual virus-derived protein cages. Submitted.

Abstract

Nucleic acids are the natural cargo of viruses and key determinants that affect viral shell stability. In some cases the genome structurally reinforces the shell, whereas in others genome packaging causes internal pressure that can induce destabilization. Although it is possible to pack heterologous cargoes inside virus-derived shells, little is known about the physical determinants of these hybrid nanocantainers stability. Using atomic force and cryo-electron microscopies, we determined the physical mechanisms that govern the mechanical strength of protein-loaded P22 bacteriophage shells. We analyzed the effects of cargo-shell and cargo-cargo interactions on shell stability after encapsulating two types of proteinaceous payloads. While bound cargo to the inner capsid surface mechanically reinforced the capsid in a structural manner, unbound cargo diffusing freely within the shell cavity pressurized the cages up to ~30 atm due to steric effects. Understanding the stability of artificially loaded nanocages will help to design more robust and durable synthetic nanocontainers.

Introduction

Synthetic biomimetic nanostructures are revolutionizing materials design at the nanoscale. Inspired by nature, where intracellular structures act as optimized nanocompartments, new self-assembling biological systems have been generated with growing interest in biology, chemistry, and materials science.¹⁻⁷ Virus-like particles (VLP) show a controlled hierarchical assembly, are easy to produce, and their structure can accommodate modifications of their inner and/or outer surfaces. *These attributes enable the incorporation of artificial cargos in the VLP, such as small molecules,⁷⁻⁹ metal nanoparticles¹⁰⁻¹² or proteins,⁸ to produce hybrid materials that can be used for a broad range of applications.* The confinement of proteins inside VLP permits the modulation, spatial control and protection of their enzymatic activity in a variety of environments, and has evident interest for pharmaceutical and nanotechnological disciplines.¹³⁻¹⁵

The development of robust nanocages able to maintain their structure is crucial for their durability in harsh environmental conditions. To accomplish so, some successful strategies can be adopted from nature. Genetic material can reinforce natural viral shells after packing via structural interaction with the viral shell, similar to the way beams buttress the structure of a building.^{16,17} However, the genome might also destabilize the viral shell by inducing outward pressurization that stiffens the viral particles.¹⁸⁻²⁰ In the light of these results, it seems reasonable to expect that the stability of protein-derived cages loaded with heterologous proteins not only on the presence of its internal cargo, but also on the mutual cargo-shell and cargo-cargo interplay, as in the case of their natural counterparts.

Virus-like particles (VLP) derived from the *Salmonella typhimurium* bacteriophage P22 are suitable models to address some of these questions, as it is a versatile and well-characterized system in virology and nanomaterials synthesis.^{21,22} The P22 VLP capsid is built of 420 copies of a coat protein (CP) that assembles into a T=7 icosahedral shell with the aid of 100-300 copies of scaffolding proteins (SP), whose C-terminal helix-loop-helix motif interacts with the CP. In contrast to authentic phages, these VLPs have 12 identical pentons with no portal.²³ P22 VLP procapsids (PC) undergo a series of well-defined structural transitions after heating that generate mature viral shells (EX particles), emulating bacteriophage P22 maturation.^{21,22,24} This capsid transition (PC→EX) involves an increase in internal volume of ~35%, as well as a capsid shell thinning and decrease in its porosity.

Heterologous expression of CP and N-terminal-truncated SP fused to other gene products results in self-assembly of the PC (59.6 nm outer diameter, 46,450 nm³ internal volume); heating at 65°C for 20 min yields the EX (64.8 nm, 71,900 nm³) (Figure 1A). We used the SP fusion strategy to incorporate enhanced green fluorescence protein (EGFP) or β -glucosidase from the hyperthermophile *Pyrococcus furiosus* (CelB) into the VLP interior when expressed in *Escherichia coli* together with CP (Figure 1B). Because the interaction between EGFP monomers is anticipated to be weaker than that between CelB monomers, which form spontaneous tetramers inside the shell,²⁵ we used these two proteins to study the effects of cargo-cargo coupling. On the other hand, the ability of PC structure to mature into the EX morphology allowed us to address the effects of cargo-shell coupling. During maturation, the SP C-terminal segment of the SP-cargo protein is unbound from the interior surface shell, resulting in soluble cargo molecules inside the EX.^{21,24,26-32}

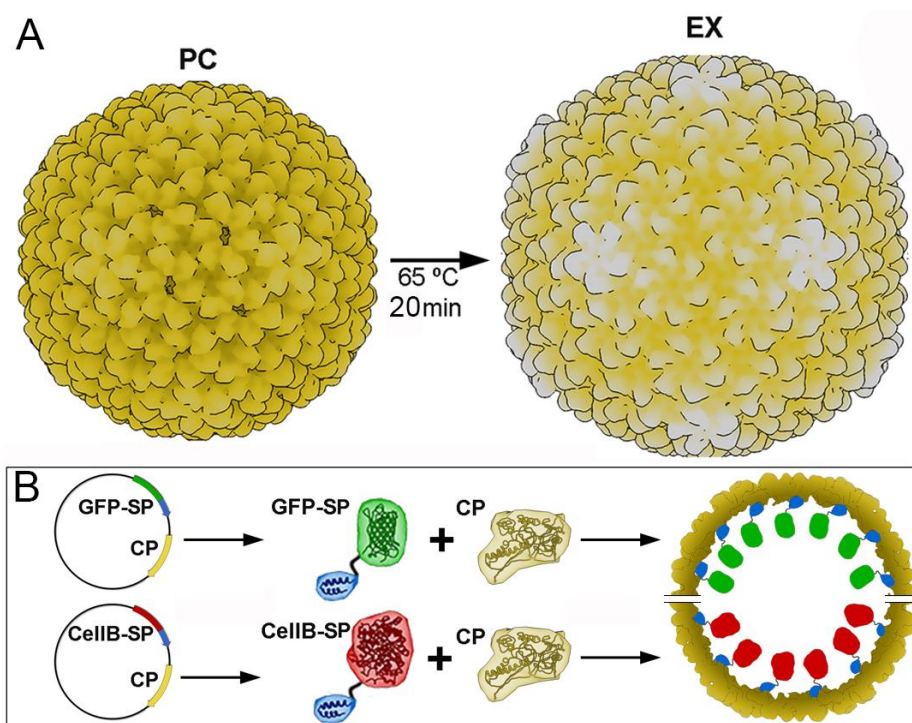


Figure 1. Synthesis of P22 nanocages and the expanded morphology of the P22 capsid. (A) P22 capsid maturation. P22 viral-like particles (VLP) are produced as procapsids (PC), which are transformed to an expanded shell form (EX) by heating at 65°C for 20 min. (B) Assembly of P22 VLP with different cargos. Co-expression of coat protein (CP, yellow) with N-terminal truncated scaffold protein (SP, blue) fused to EGFP (green) or CelB monomers (red) leads to VLP assembly as PC with encapsulated cargo. VLP assembly is facilitated by interaction of the essential SP C-terminal domain and CP subunits, which leads to encapsulation of SP-fused proteins. For clarity, EGFP and CelB are shown as monomers.

In this work we combine mechanical and structural information obtained from Atomic Force Microscopy (AFM) and three-dimensional cryo-Electron Microscopy (3D cryo-EM) to describe physico-chemical mechanisms that influence the stability of synthetic P22 protein cages. Our results show that the interplay between the cargo and the shell determines whether the mechanical reinforcement is structure- or pressure-induced, as happens in natural viral cages. The cargo bound to the shell provides structural reinforcement to the P22 procapsid, although a strong cargo-cargo interaction (*i.e.*, CelB) renders particles more brittle. In the expanded form, the SP-associated cargo proteins that remains inside the shell in a “free” soluble state pressurizes the expanded structure up to 30 atmospheres.

Results and Discussion

Three-Dimensional Structure of Cargo-loaded P22 VLP

We used 3D cryo-EM to analyze the structures of two morphologies of heterologous bacteriophage P22 T=7 VLP, termed PC and EX, loaded with a cargo of EGFP or CelB. Empty PC and EX were included as controls (Figure 2). We used HPLC size exclusion chromatography with multi-angle light scattering (MALS) to determine the number of cargo copies per particle, and found 128 ± 1 CelB monomers and 220 ± 5 EGFP. Figure 2A shows cryo-EM images of these purified P22 VLP with different morphologies, imaged at -170°C in a 200 kV cryo-electron microscope.

A 3D reconstruction (3DR) was calculated for each of the six sets of particle types (Figure 2B-D). Based on a Fourier shell correlation (FSC) coefficient, the resolutions achieved were between 12-16 Å (Figure S1). Particle diameters were determined from radial density profiles from the 3DR (Figure 2E). Whereas spherical PC (empty, EGFP- or CelB-loaded) had a 298 Å outer radius, EX form measured 324 Å. This capsid expansion range is similar in bacteriophages P22, λ and HK97.³³

Cargo-loaded PC and EX had the same size and general morphology as empty PC and EX. The P22 PC were T=7 isometric structures formed by 72 capsomers, 60 of which are skewed CP hexamers and 12 are CP pentamers, as they lack the portal structure (Figure 2B, top).²² Empty PC showed densities at the inner surfaces of the hexamers due to SP C-terminal

residues that cannot be accounted for by the CP (Figure 2C, arrows), as previously reported.^{21,22,24}

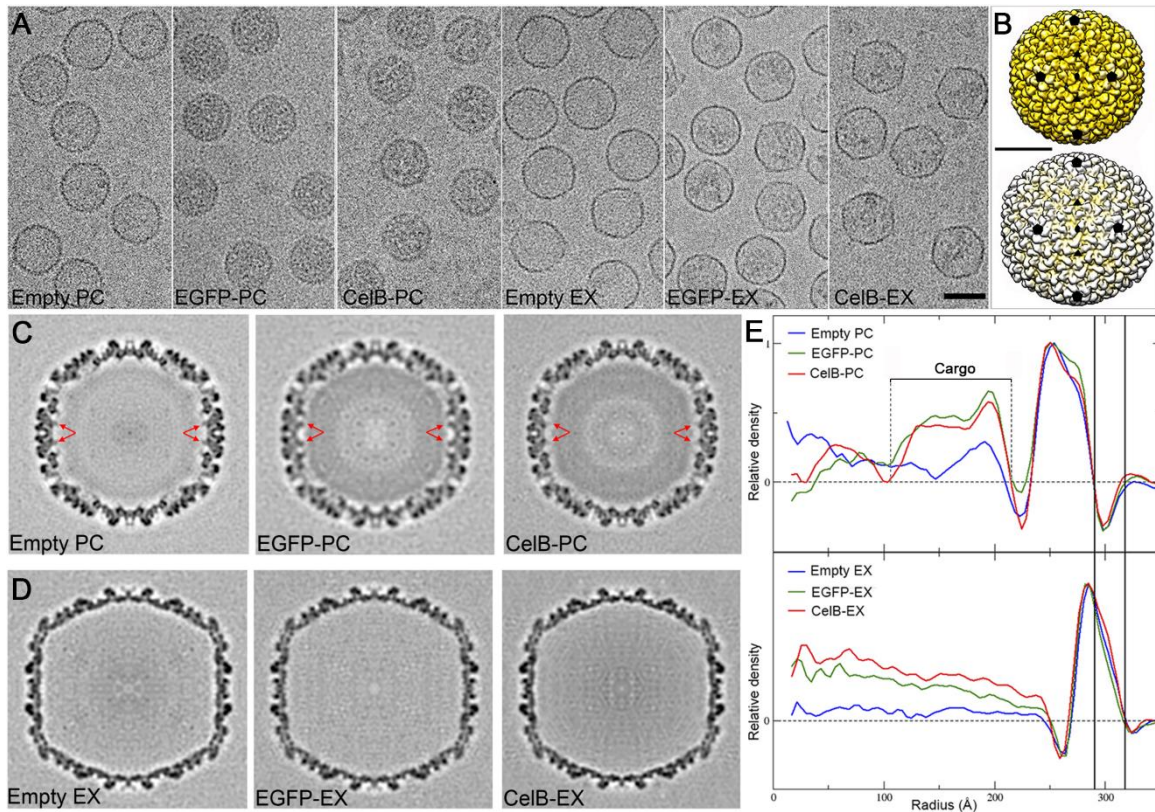


Figure 2. Three-dimensional cryo-EM reconstructions of empty, EGFP- and CelB-loaded P22 capsids.

(A) Cryo-EM of (left to right) empty PC, EGFP-loaded PC (EGFP-PC), CelB-loaded PC (CelB-PC), empty EX, EGFP-loaded EX (EGFP-EX) and CelB-loaded EX (CelB-EX). Bar: 50 nm. (B) Surface-shaded representations of the outer surfaces, viewed along an icosahedral twofold axis, of P22 PC (top) and EX (bottom). Outer surfaces of empty and loaded PC and EX are similar at this resolution. Symbols indicate icosahedral symmetry axes. Bar, 25 nm. (C) Central sections from the 3DR viewed along a twofold axis of T=7 empty PC (left), EGFP- (center) and CelB-PC (right). Darker shading indicates higher density. Arrows indicate some densities due to the SP C-terminal region in the PC internal surface (note that these densities are reduced in the CelB-PC central section). (D) Central sections from the 3DR viewed along a twofold axis of T=7 empty EX (left), EGFP- (center) and CelB-EX (right). (E) Radial density profiles of 3DR of empty PC, EGFP- and CelB-PC, empty EX, and EGFP- and CelB-EX. PC (top) and EX shells (bottom) are essentially superimposable. In PC, a cargo shell spans radii from 107 to 216 Å. Vertical lines indicate PC (298 Å) and EX radii (324 Å).

Images of EGFP- or CelB-loaded PC (EGFP-PC or CelB-PC) presented an interior darker than that of the empty forms (Figure 2A), which indicated the presence of packed cargos.

After imposing icosahedral symmetry, the 3DR showed that cargo density (within a 220 Å radius) was organized as a thick shell beneath the PC shell, with numerous connections to the PC inner surface (Figure 2C middle [EGFP-] and right [CelB-PC]). As in *in vivo*-matured virions, P22 EX were more angular than PC, and the hexons became symmetrical hexamers (Figure 2D). Heat-induced capsid maturation untethered EGFP- or CelB-fused SP from the EX interior surface and cargos were observed as free densities in the capsid interior (Figure 2A), in concordance with the wild-type P22 procapsid release of SP after heating.³⁴

AFM Topographical Analysis of Empty and Cargo-loaded P22 VLP *in vitro*

Fixation of the protein shells to a flat substrate via hydrophobic and/or electrostatic interactions is a requisite for AFM imaging. Each protein shell has individual features, such as hydrophobic patches or local charge densities, that result in distinct attachment forces. For a specific shell, these forces can even reduce the height of the softest virus-like morphologies.³⁵ The precise combination of factors that leads to this partial collapse remains undefined, but so far a decrease in height has been always accompanied with a decrease in the mechanical stiffness of the specimen. Representative AFM images of each VLP type adsorbed on glass showed partial collapse of the empty forms (Figure 3A), which allowed us to carry out a comparative mechanical study of particle deformability. Whereas empty VLP showed a height decrease of ~10% compared with their native size in cryo-EM, cargo-loaded VLP maintained heights near 100% of the cryo-EM value (Figure 3B). Therefore, the limited shell deformation of cargo-loaded VLP suggested that these particles were more rigid than their empty counterparts.

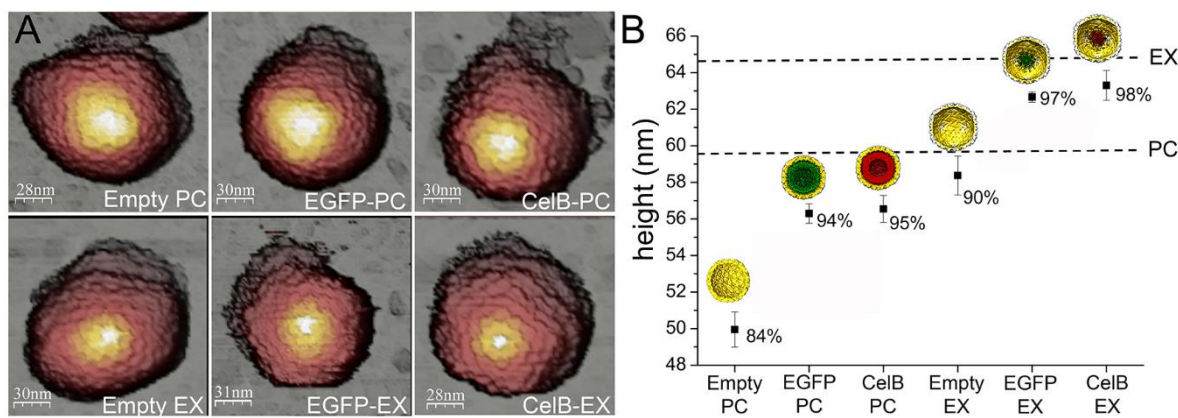


Figure 3. AFM topographies of P22 particles. (A) AFM images of empty PC, EGFP-PC, CelB-PC, empty

Cargo-Cargo and Cargo-Shell Interactions Determine P22 PC Mechanics

VLP mechanical stability was assessed systematically using single nanoindentation assays. The force vs. indentation curves (FIC) obtained in those experiments provided two mechanical parameters that were linked to the rigidity and brittleness of the probed particles.^{36,37} The slope of the curve (also termed as spring constant, k) was related to particle rigidity. The ratio between the critical deformation ($\delta_{critical}$) and the particle height (h), which defines the critical strain $\epsilon_{critical} = \frac{\delta_{critical}}{h}$ (Figure 4A, inset), was used to establish differences in brittleness.³⁸

Figure 4A shows a characteristic FIC performed on an intact EGFP-PC. AFM images taken before and after the FIC demonstrated the rupture of the shell, which in this case caused a crack associated with a reduction in height from 57 to 47 nm (Figure 4A, right). Other examples of this sort of experiments can be found in Figure S2; in all the cases, a clear disruption of the shell was observed. In addition, our AFM data showed that EGFP- and CelB-PC were more rigid than empty PC (Figure 4B top, Table S1), in agreement with the initial topographical analysis (Figure 3). To determine the cause of this difference in stiffness we analyzed the cryo-EM maps in detail. Comparison of the average radial densities of empty and full PC particles indicated that most cargo localized in a shell beneath the capsid wall within a 216-107 Å radius (Figure 2E). Whereas the empty PC structure showed a single spherical layer corresponding to the capsid shell, full PC presented an extra concentric layer corresponding to cargos. These data suggested that the stiffening was caused by a structural reinforcement that could be evaluated by continuous elasticity modeling. Simplification of these complex structures to homogeneous shells³⁹⁻⁴² permits estimation of the ratio of Young's modulus of the capsid (E_s) and the cargo (E_c). The radial density derived from the cryo-EM data indicated that empty- and loaded-PC had effective thicknesses of ~7.5 and ~17.5 nm, respectively (Figure 2E). Finite element modeling based on the experimental spring constant estimated E_s/E_c of 7 and 10 for EGFP and CelB cargos, respectively (Figure S3A). This result indicates that the capsid shell is approximately ten times more rigid than the

(continued) EX, EGFP-EX and CelB-EX. (B) Height of empty PC, EGFP-PC, CelB-PC, empty EX, EGFP-EX and CelB-EX after adsorption. Percentages indicate the ratio between average height as measured by AFM and nominal height based on 3D cryo-EM reconstructions. Dashed lines indicate nominal PC and EX outer diameters.

cargo “shell”, suggesting that from a mechanical viewpoint viral nanocontainers might represent an effective way to offer protection to highly-packed proteins (packing factors of 35-45%, [table 1](#)).

Study of the brittleness of the shells, though, revealed some interesting distinctions. While both packed cargos has similar influence on the rigidity of the particles, there was a difference in brittleness between EGFP- and CelB-loaded PC compared to empty shells ([Figure 4B](#), bottom; and [Table S1](#)). EGFP-PC and empty PC presented a critical strain ($\epsilon_{\text{critical}} = 0.17$) slightly higher than that of CelB-PC ($\epsilon_{\text{critical}} = 0.14$). To evaluate this difference in brittleness, we performed docking analysis of the P22 CP model [$C\alpha$ model, Protein Data Bank (PDB) ID 2XYY,²¹ and the SP C-terminal region (residues 238-303, PDB ID 2GP8)⁴³] in the empty and loaded PC cryo-EM density maps. The SP C-terminus fitted well in the triangular density at the internal surface of the PC skewed hexamers ([Figure 4C](#), left; blue). This SP-related density was also well preserved in the EGFP-PC at the same radial position, and showed the connections between CP shell and cargo ([Figure 4C](#), middle; green). However, CelB-PC were more disordered in this region than empty and EGFP-PC, and SP-mediated connections were irregular and less defined ([Figure 4C](#), right; red). This scenario is compatible with the existence of fewer (or less intense) SP-mediated connections for CelB-PC than for EGFP-PC. Because CelB monomers form tetramers inside the shell,²⁵ it seems reasonable to expect that the SP-CP interaction becomes affected as a consequence of it. CelB monomers are connected to CP by a 123 amino acid linker that joins the cargo with the SP-CP binding domain. We propose that the formation of CelB tetramers inside the PC shell tighten some of these SP-mediated connections, and leads to an additional geometrical constraint that reduce capsid subunit mobility upon deformation ([Figure 4D](#), top). In contrast, the monomeric condition of EGFP does not impose any constraint on the SP linkers and thus, there is no difference between these capsids and empty shells ([Figure 4D](#), bottom). Supporting this data we performed single nanoindentation studies in empty shells (which are scaffolding-lacking procapsids)⁴⁴ and saw that the removal of the SP, by its own, could not explain the difference in brittleness ([table S1](#)).

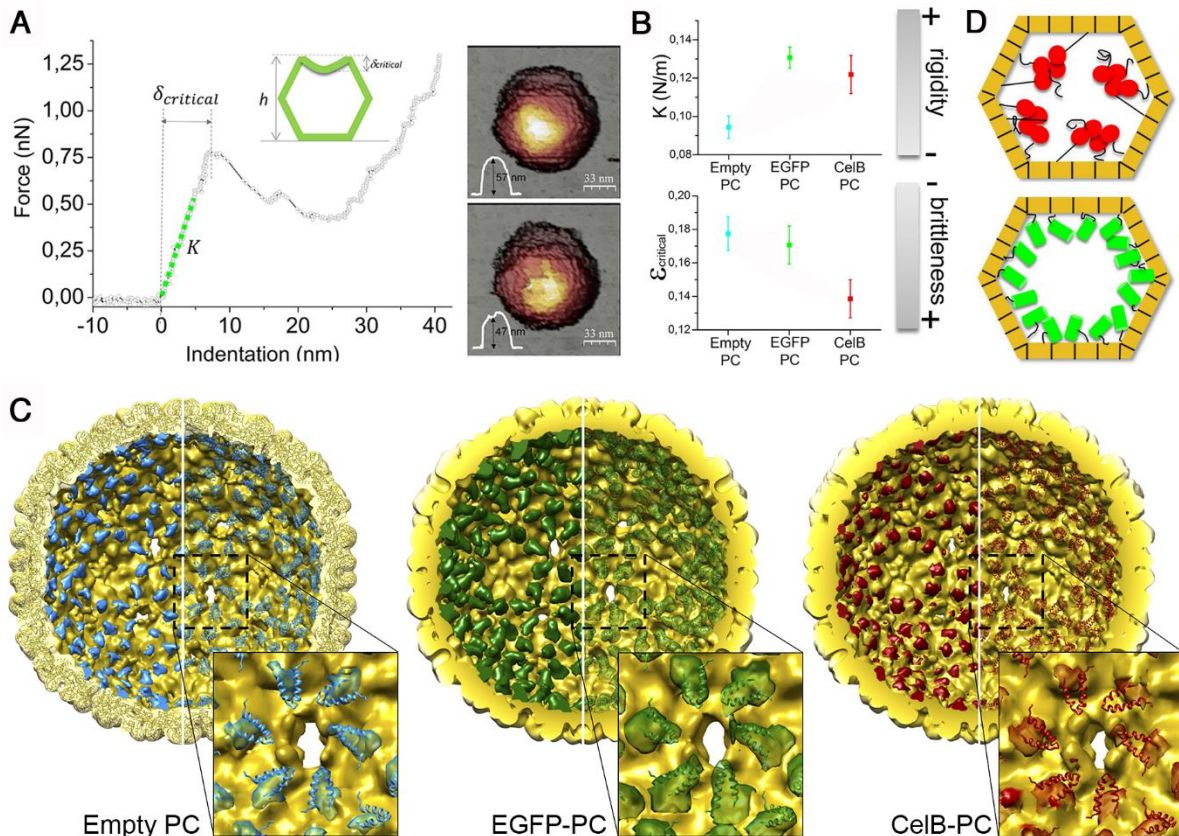


Figure 4. Structure and mechanical properties of P22 PC. (A) (Left) Typical force-*vs*-indentation curve (FIC) of an EGFP-PC. Particle rigidity (k) and critical deformation ($\delta_{critical}$) can be calculated from the nanoindentation. Critical strain ($\epsilon_{critical}$), which provides information about particle deformation before breakage, is defined as the ratio between the critical indentation and particle height (inset). (Right) AFM topographies of the PC before (top) and after nanoindentation (bottom). A profile of the particle along its center is inset in each image (bottom left). (B) Comparison of the average rigidity (top) and fragility (bottom) of empty and loaded PC. (C) Analysis of CP-SP interactions in empty and EGFP- and CelB-PC. PC viewed down a twofold axis from inside, with docked SP helix-loop-helix motif (right half). Empty PC shows the CP atomic model (yellow) in the shell and the SP motif in the SP density (blue; inset); the SP density is shown in EGFP-PC (green; center) and in CelB-PC (red; right). (D) Scheme of PC showing the organization of CelB tetramers (red, top) and EGFP monomers (green, bottom) fused to SP (black lines).

Mechanics of Empty and Cargo-loaded EX Structures

During the transition from PC to EX, the SP domains release the CP and escape from the capsid, resulting in empty EX particles.²⁴ However, in the case of loaded particles the SP fused to EGFP or CelB structures cannot escape and become free inside the EX after detaching of the capsid wall. We analyzed the mechanics of three expanded protein cages

(empty, CelB- and EGFP-EX) to establish differences between them. [Figure 5A](#) shows a representative nanoindentation curve performed on a CelB-EX, with the AFM images before and after the tip-induced breakage represented on the right ([Figure 5A](#)). Statistical analysis of the mechanical properties of the three EX types showed that cargo-loaded shells increased their rigidity but $\epsilon_{\text{critical}}$ did not vary ([Figure 5B](#)). The lack of influence of this cargo on EX brittleness is likely related to the detachment of SP domains; both EGFP monomers and CelB tetramers remained unanchored, free to diffuse within the EX cage ([Figure 5C](#)). On the other hand, because no permanent structural contacts exist between the cargo and the capsid shell, the increased rigidity seemed to be caused by an internal pressure. A possibility would be that the different concentration of protein between the inner shell and the surroundings would drive water molecules into the shell, thus causing an osmotic pressure. Alternatively, the electrostatic repulsion between cargo molecules retained within the capsid might originate this pressure. To determine which of these mechanisms, or if a combination of both, was responsible for the capsid reinforcement we modeled our system and performed new AFM experiments.

Pressurization of EX VLP

Regardless of its physical origin, we can estimate the magnitude of the internal pressure in loaded EX using the continuous elastic prediction for rigidity of a pressurized thin spherical shell indented by a point force.⁴⁵

$$k_1 = \frac{\pi}{2} k_0 \frac{(1-\tau^{-2})^{\frac{1}{2}}}{\operatorname{arctanh} \left[(1-\tau^{-2})^{\frac{1}{2}} \right]} \quad (1)$$

Here, $\tau = pR_1/k_0$ is a dimensionless parameter that compares the relative relevance of pressure p against the elastic constant of the unpressurized shell, k_0 , and R_1 the internal radius of the P22 EX, considered effectively as a sphere ($R_1 = 29.1$ nm). Taking $k_0 = k_{\text{EX}} = 0.21$ N/m, $k_1 = k_{\text{EGFP-EX}} = k_{\text{CelB-EX}} = 0.27$ N/m, and solving [Eq. \(1\)](#) for p , an estimate of 3 ± 1 MPa (30 atm) is obtained for the increase in internal pressure after cargo internalization, a value that was corroborated by Finite Element Simulations ([Figure S3B](#)).

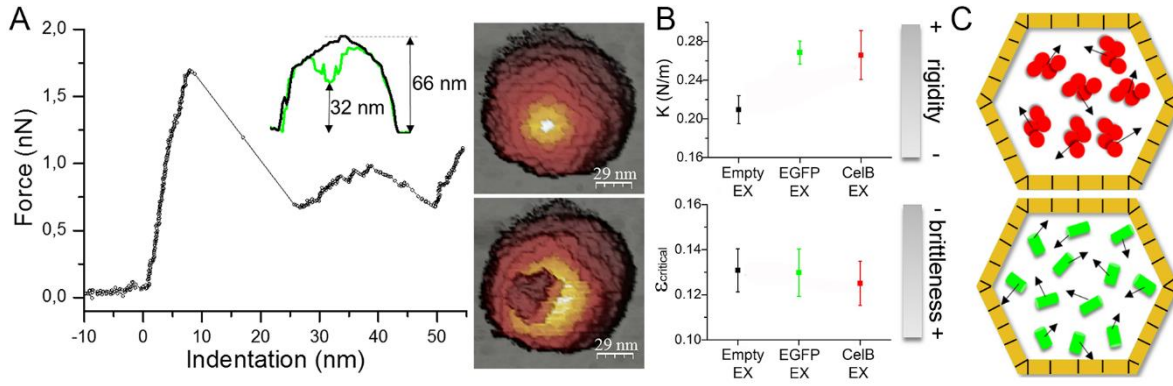


Figure 5. Mechanical characterization of EX capsids. (A) Typical FIC of a CelB-EX. Inset, Aligned profiles of particle topographies before (black) and after (green) breakage. Right, CelB-EX images before (top) and after breakage (bottom). (B) Comparison of the average rigidity (top) and fragility (bottom) of empty and loaded EX. (C) Scheme of EX showing cargo units as diffusing entities within the protein shell (colors as in Figure 5).

The osmotic pressure generated from a freely moving cargo constrained to the EX interior depends on the nature of the interactions between the cargo molecules and between the cargo and the inner capsid wall. The simplest influence stems from steric interactions between cargo molecules and the fact that they cannot escape from the capsid. The irregular geometry of the cargo, enhanced by the presence of the SP linker and the helix-loop-helix motif attached to it, makes accurate quantification difficult. Its magnitude can nonetheless be estimated by modeling the cargo molecules as uncharged hard spheres with an effective radius r_{HS} . In this approach, the expression for this “hard spheres” contribution to the osmotic pressure is^{46,47}

$$p_{HS} = k_B T \rho \frac{(1 + \eta + \eta^2 - \eta^3)}{(1 - \eta^3)^3} \quad (2)$$

where $k_B = 1.38 \times 10^{-23} \text{ m}^2 \text{ kg s}^{-2} \text{ K}_B$ is the Boltzmann constant, $T=300 \text{ K}$ is the temperature, ρ is the number density of the cargo inside the particle, and $\eta = \frac{V_{cargo}}{V_{EX}} = \frac{N^{4/3} \cdot \pi r_{HS}^3}{V_{EX}}$ is the packing fraction, defined as the volume occupied by the cargo divided by the available volume in the capsid (Tables 1 and S2). This assumption allowed us to evaluate the effective hard sphere radius (r_{HS}) needed to obtain the pressure values estimated in the experiments (Eq. 1).

In the case of CelB-EX, in which $N=128\pm 1$ monomers were encapsulated per capsid and the estimated pressure was $p=3\pm 1$ MPa, the effective radius was $R_{HS} = R_{CelB} = 7.8$ nm. For EGFP-EX, with $N = 220 \pm 5$ monomers encapsulated and the same pressure as CelB-EX, the effective radius was $R_{HS} = R_{EGFP} = 3.9$ nm. Although we approached the irregular geometry of the cargos as hard spheres, the model reasonably predicted an effective radius appropriate to the size of the CelB tetramer ($10.1 \times 10.1 \times 5.7$ nm³) and of the EGFP monomer ($4.8 \times 3.3 \times 3.5$ nm³) (Table S2).

	CelB-PC	EGFP-PC	CelB-EX	EGFP-EX
Physical origin	Structural reinforcement		Steric interactions	
Capsid volume (nm ³)	46,452		71,936	
# cargo/capsid	32	224	32	224
Packing factor	45.5	36.18	29.4	29.4
Pressure (MPa)	-	-	3 ± 1	3 ± 1

Table 1. Interactions that modulate P22 PC and EX mechanics. In PC, the cargo is constrained to the vicinity of the shell, whereas unattached cargo in EX moves freely inside the shell, creating osmotic pressure.

Note that the values that we used for calculating such pressures were based on the number of cargos internalized in PC shells, not in EX shells. Size exclusion chromatography coupled to multi-angle light scattering (SEC-MALS) indicated that, on average, the mass of loaded particles decreased slightly after expansion, as previously reported.³ In our case, loaded EX lost 20 CelB (16%) and 64 EGFP (30%) monomers in comparison with their PC forms. However, this loss of material was probably related to defective particles. Shell defects, such as missing pentamers, allow cargo molecules to leave the cavity. Because only particles flawed or broken during thermal expansion would be the responsible for this loss of average mass, and because AFM topographic characterization permits to select intact particles that have presumably not lost any cargo molecules, we assumed that PC and EX capsids contained the same amount of monomers and used the PC values to calculate the different packing factors and effective radii.

A second contribution to the pressure could arise from the electrostatic repulsion between the cargo molecules or/and the cargo and the shell. The magnitude of this influence could

be estimated in two ways, by considering a solution of N effective charged spheres in an electrolyte⁴⁸ or through the concept of Donnan equilibrium.⁴⁹ Both calculations led to theoretical pressure values that were negligible compared with the values obtained in our experiments (see Supporting Information for details). To confirm that result experimentally we carried out AFM nanoindentations on loaded EX. The electrostatic contribution of natural cargos, such as dsDNA, has been detected in natural viral cages by screening DNA-DNA repulsion with condensing agents or by lowering the ionic strength of the solution. This screening, which reduces the internal pressure, leads to a decrease in the rigidity of the cages.^{19,20,50} We performed nanoindentation experiments at lower ionic strength and in the presence of spermidine (Figure S5). Our results showed that there were no difference in stiffness, which confirmed the theoretical calculations predicting that the electric nature of the cargo plays no role in stiffening the shell.

Conclusions

The combination of cryo-EM and AFM has clarified the precise interplay between an artificial cargo and the protein shell in which it is confined, and could permit the rational design of more stable nanocontainers. Our data indicate that the presence of a cargo stiffens the cages in two different ways. In the case of PC, when the cargo is linked to the shell through the C-terminal SP motif, the capsid is reinforced structurally. For EX capsids, however, cargo-shell interaction are lost and the increase in rigidity arises from the different concentration of protein (CelB tetramers or EGFP monomers) between the inside of the capsid shell and the surroundings. This different concentration drives water molecules inside the particle creating an osmotic pressures of ~ 30 atm, a value comparable to the DNA-induced pressurization in natural viruses ($40-60$ atm for *phi29*^{19,51}, 20 atm for *lambda*⁵², 10 atm for P22 phages,^{53,54} and 30 atm for human adenovirus²⁰). In addition, we have seen that the formation of CelB tetramers inside procapsid represent a geometrical constraint that render particles more brittle. In summary, our results show that the mechanical stability of particles loaded with foreign proteins is governed by different physical mechanism. Understanding these mechanisms and their molecular determinants might permit designing

more robust cages and thus contribute to their development as protective shields towards their use in bionanotechnological applications.

Materials and methods

Biochemical and Genetic Analyses

Proteins were cloned, expressed and purified, and analyzed by size exclusion chromatography with multi-angle light scattering and refractive index detection was performed as described.^{3,4,7} Plasmids containing the genes for coat protein and cargo proteins of interest fused to scaffold protein (EGFP-SP³, CelB-SP²⁵) were transformed in BL21 (DE3) *Escherichia coli* (Novagen) for protein expression. The transformed *E. coli* cells were grown to an OD₆₀₀ = 0.6, induced with isopropyl β-D-thiogalactopyranoside (IPTG), and grown for an additional 4 h before cells were collected by centrifugation at 4,500 rpm. Cells were resuspended in PBS pH 7, lysed by sonication, centrifuged (at 12,000 rpm) to remove cell debris, and virus particles were isolated by ultracentrifugation through a sucrose cushion. The resuspended pellet was further purified on a Sephacryl (S-500; GE Healthcare) size exclusion column in PBS pH 7 (1 ml/min). For SEC-MALS analysis, samples were analyzed on a Dawn 8 instrument (Wyatt Technologies, Santa Barbara, CA). Samples were separated by Agilent 1200 HPLC on a WTC-0200S size exclusion column (Wyatt Technologies) and monitored with a UV-Vis detector (Agilent), a Wyatt HELEOS Multi Angle Laser Light Scattering (MALS) detector, a quasi-elastic light scattering detector (QELS), and an Optilab rEX differential refractometer (Wyatt Technologies). The Wyatt Astra 6 software determined average molecular weight (M_w) and radius of gyration (R_g) values.

Cryo-EM and Image Processing

Samples (5 μl) were applied to Quantifoil R 2/2 holey grids, blotted, and plunged into liquid ethane. Cryo-EM images were recorded in low-dose conditions with a FEI Eagle CCD camera in a Tecnai G2 electron microscope equipped with a field emission gun operating at 200 kV and at a detector magnification of 69,444X (2.16 Å/pixel sampling rate).

General image processing operations were performed using Xmipp⁵⁵, and graphics were produced using UCSF Chimera⁵⁶. The Xmipp automatic picking routine was used to select particles. Defocus was determined with CTFfind⁵⁷ and CTF phase oscillations were

corrected in images by flipping them in the required lobes. Homogeneous populations were selected by two-dimensional classification using the Xmipp CL2D reference-free clustering routine⁵⁸. Published structures of P22 PC and EX (PDB 2XYY and 2XYZ)²¹ were filtered to 30 Å, size-scaled and used as initial models for their respective samples. The Xmipp iterative projection matching routine⁵⁹ was used to determine and refine particle origin and orientation. For the CelB tetramer, an artificial noise model was used as starting reference for parallel iterative angular refinement using the EMAN program⁶⁰. Once converged, the resulting model was selected and refined using the Xmipp iterative projection matching routine. For PC, EX and CelB, 90% of the particles were included in the final 3DR, and resolution was assessed by FSC between independent half dataset maps (Figure S1). The final map of the CelB tetramer included 11,432 particles, and resolution for the 0.5 and 0.3 criteria was 16.4 and 14.5 Å, respectively. The UCSF Chimera fitting routine was used to dock the crystallographic models of PC, EX, SP and *Pyrococcus* β-glucosidase CelB (PDB 2XYY, 2XYZ, 2GP8 and 3APG, respectively) in the cryo-EM maps. The 3D reconstructions are deposited in the Electron Microscopy Data Bank (<http://www.ebi.ac.uk/pdbe/emdb>) with accession no. EMD-3171 (empty PC), EMD-3172 (EGFP-PC), EMD-3173 (CelB-PC), EMD-3174 (empty EX), EMD-3175 (EGFP-EX), EMD-3176 (CelB-EX) and EMD-3177 (CelB tetramer).

AFM

AFM experiments were performed as described⁴², using a Nanotec Electrónica microscope (Madrid, Spain) operating in jumping mode plus⁶¹. Imaging forces were maintained below 150 pN. Rectangular silicon-nitride cantilevers (RC800PSA, Olympus, Center Valley, PA) with a nominal spring constant of 0.05 N/m were calibrated before each measurement by Sader's method⁶². Experiments were carried out in standard buffer conditions (100 mM phosphate, 50 mM NaCl, pH 7) at a controlled temperature of 17°C. A 20 µl drop of diluted stock solution was incubated on previously silanized glass coverslips. Cleaning and functionalizing of glass surfaces was as described³⁹. After 30 min, the sample was washed with buffer solution to a volume of 90 µl. AFM images were processed with WSxM software. AFM control experiments were performed in two conditions, at low ionic strength (50 mM phosphate, 25 mM NaCl, pH 7) or with 1 mM spermidine (100 mM phosphate, 50 mM NaCl, 1 mM spermidine, pH 7). Details of the procedure are found in the SI.

Nanoindentation was done at a loading rate of 60 nm/s with forward elongation of 100 nm. Force-*vs*-indentation curves (FIC) were obtained from force-*vs*-Z-piezo curves as reported⁴². The elastic constant was obtained by fitting the initial linear part of each FIC. Breaking force and critical indentation were measured with WsxM⁶³. A summary of the number of particle and average values of the mechanical properties analyzed are detailed in the SI.

References

- 1 Yeates, T. O., Kerfeld, C. A., Heinhorst, S., Cannon, G. C. & Shively, J. M. Protein-based organelles in bacteria: carboxysomes and related microcompartments. *Nat Rev Micro* **6**, 681-691, (2008).
- 2 Cheng, S., Liu, Y., Crowley, C. S., Yeates, T. O. & Bobik, T. A. Bacterial microcompartments: their properties and paradoxes. *Bioessays* **30**, 1084-1095, (2008).
- 3 O'Neil, A., Reichhardt, C., Johnson, B., Prevelige, P. E. & Douglas, T. Genetically Programmed In Vivo Packaging of Protein Cargo and Its Controlled Release from Bacteriophage P22. *Angew Chem Int Edit* **50**, 7425-7428, (2011).
- 4 Patterson, D. P., Prevelige, P. E. & Douglas, T. Nanoreactors by Programmed Enzyme Encapsulation Inside the Capsid of the Bacteriophage P22. *Acs Nano* **6**, 5000-5009, (2012).
- 5 Tanaka, S. *et al.* Atomic-Level Models of the Bacterial Carboxysome Shell. *Science* **319**, 1083-1086, (2008).
- 6 Kerfeld, C. A. *et al.* Protein structures forming the shell of primitive bacterial organelles. *Science* **309**, 936-938, (2005).
- 7 Lucon, J. *et al.* Use of the interior cavity of the P22 capsid for site-specific initiation of atom-transfer radical polymerization with high-density cargo loading. *Nat Chem* **4**, 781-788, (2012).
- 8 Kang, S. *et al.* Implementation of p22 viral capsids as nanoplatfoms. *Biomacromolecules* **11**, 2804-2809, (2010).
- 9 Qazi, S. *et al.* P22 viral capsids as nanocomposite high-relaxivity MRI contrast agents. *Molecular pharmaceutics* **10**, 11-17, (2012).
- 10 Reichhardt, C. *et al.* Templated assembly of organic-inorganic materials using the core shell structure of the P22 bacteriophage. *Chem Commun* **47**, 6326-6328, (2011).
- 11 Uchida, M. *et al.* Protein Cage Nanoparticles Bearing the LyP-1 Peptide for Enhanced Imaging of Macrophage-Rich Vascular Lesions. *Acs Nano* **5**, 2493-2502, (2011).
- 12 Uchida, M., Kang, S., Reichhardt, C., Harlen, K. & Douglas, T. The ferritin superfamily: Supramolecular templates for materials synthesis. *Biochimica et Biophysica Acta (BBA)-General Subjects* **1800**, 834-845, (2010).
- 13 Patterson, D. P., Rynda-Apple, A., Harmsen, A. L., Harmsen, A. G. & Douglas, T. Biomimetic Antigenic Nanoparticles Elicit Controlled Protective Immune Response to Influenza. *Acs Nano* **7**, 3036-3044, (2013).
- 14 Schwarz, B. & Douglas, T. Development of virus-like particles for diagnostic and prophylactic biomedical applications. *Wiley Interdisciplinary Reviews: Nanomedicine and Nanobiotechnology*, (2015).
- 15 Manchester, M. & Steinmetz, N. F. *Viruses and nanotechnology*. (Springer, 2009).
- 16 Carrasco, C. *et al.* DNA-mediated anisotropic mechanical reinforcement of a virus. *Proceedings of the National Academy of Sciences* **103**, 13706-13711, (2006).

- 17 Carrasco, C., Castellanos, M., de Pablo, P. J. & Mateu, M. G. Manipulation of the mechanical properties of a virus by protein engineering. *P Natl Acad Sci USA* **105**, 4150-4155, (2008).
- 18 Gelbart, W. M. & Knobler, C. M. Pressurized Viruses. *Science* **323**, 1682-1683, (2009).
- 19 Hernando-Perez, M. *et al.* Direct Measurement of Phage phi29 Stiffness Provides Evidence of Internal Pressure. *Small* **8**, 2366-2370, (2012).
- 20 Ortega-Esteban, A. *et al.* Mechanics of Viral Chromatin Reveals the Pressurization of Human Adenovirus. *Acs Nano*, (2015).
- 21 Chen, D. H. *et al.* Structural basis for scaffolding-mediated assembly and maturation of a dsDNA virus. *Proc Natl Acad Sci U S A* **108**, 1355-1360, (2011).
- 22 Parent, K. N. *et al.* P22 Coat Protein Structures Reveal a Novel Mechanism for Capsid Maturation: Stability without Auxiliary Proteins or Chemical Crosslinks. *Structure* **18**, 390-401, (2010).
- 23 Bhardwaj, A., Olia, A. S. & Cingolani, G. Architecture of viral genome-delivery molecular machines. *Curr Opin Struc Biol* **25**, 1-8, (2014).
- 24 Prasad, B. V. V. *et al.* 3-Dimensional Transformation of Capsids Associated with Genome Packaging in a Bacterial-Virus. *J Mol Biol* **231**, 65-74, (1993).
- 25 Patterson, D. P. *et al.* Virus-like particle nanoreactors: programmed encapsulation of the thermostable CelB glycosidase inside the P22 capsid. *Soft Matter* **8**, 10158-10166, (2012).
- 26 Bazinet, C. & King, J. The DNA translocating vertex of dsDNA bacteriophage. *Annual Reviews in Microbiology* **39**, 109-129, (1985).
- 27 Kang, S. & Prevelige, P. E. Domain study of bacteriophage p22 coat protein and characterization of the capsid lattice transformation by hydrogen/deuterium exchange. *J Mol Biol* **347**, 935-948, (2005).
- 28 Jiang, W. *et al.* Coat protein fold and maturation transition of bacteriophage P22 seen at subnanometer resolutions. *Nature Structural & Molecular Biology* **10**, 131-135, (2003).
- 29 Prevelige Jr, P. E., Thomas, D., Aubrey, K. L., Towse, S. A. & Thomas Jr, G. J. Subunit conformational changes accompanying bacteriophage P22 capsid maturation. *Biochemistry* **32**, 537-543, (1993).
- 30 Earnshaw, W. C. & Casjens, S. R. DNA packaging by the double-stranded DNA bacteriophages. *Cell* **21**, 319-331, (1980).
- 31 Botstein, D., Waddell, C. H. & King, J. Mechanism of head assembly and DNA encapsulation in Salmonella phage P22: I. Genes, proteins, structures and DNA maturation. *J Mol Biol* **80**, 669-695, (1973).
- 32 Casjens, S. & Weigele, P. in *Viral Genome Packaging Machines: Genetics, Structure, and Mechanism* 80-88 (Springer, 2005).
- 33 Johnson, J. E. Virus particle maturation: insights into elegantly programmed nanomachines. *Curr Opin Struc Biol* **20**, 210-216, (2010).
- 34 Galisteo, M. L. & King, J. Conformational Transformations in the Protein Lattice of Phage-P22 Procapsids. *Biophys J* **65**, 227-235, (1993).

- 35 Llauro, A. *et al.* Calcium Ions Modulate the Mechanics of Tomato Bushy Stunt Virus. *Biophys J* **109**, 390-397, (2015).
- 36 Mateu, M. G. Mechanical properties of viruses analyzed by atomic force microscopy: A virological perspective. *Virus Res* **168**, 1-22, (2012).
- 37 Roos, W. H., Bruinsma, R. & Wuite, G. J. L. Physical virology. *Nature Physics* **6**, 733-743, (2010).
- 38 Rösler, J., Harders, H. & Bäker, M. *Mechanical behaviour of engineering materials : metals, ceramics, polymers, and composites.* (Springer, 2007).
- 39 Carrasco, C. *et al.* DNA-mediated anisotropic mechanical reinforcement of a virus. *P Natl Acad Sci USA* **103**, 13706-13711, (2006).
- 40 Klug, W. S. *et al.* Failure of viral shells. *Physical Review Letters* **97**, (2006).
- 41 Roos, W. H. *et al.* Squeezing Protein Shells: How Continuum Elastic Models, Molecular Dynamics Simulations, and Experiments Coalesce at the Nanoscale. *Biophys J* **99**, 1175-1181, (2010).
- 42 Llauro, A. *et al.* Mechanical Stability and Reversible Fracture of Vault Particles. *Biophys J* **106**, 687-695, (2014).
- 43 Sun, Y. H. *et al.* Structure of the coat protein-binding domain of the scaffolding protein from a double-stranded DNA virus. *J Mol Biol* **297**, 1195-1202, (2000).
- 44 Thuman-Commike, P. A. *et al.* Mechanism of scaffolding-directed virus assembly suggested by comparison of scaffolding-containing and scaffolding-lacking P22 procapsids. *Biophys J* **76**, 3267-3277, (1999).
- 45 Vella, D., Ajdari, A., Vaziri, A. & Boudaoud, A. The indentation of pressurized elastic shells: from polymeric capsules to yeast cells. *J R Soc Interface* **9**, 448-455, (2012).
- 46 Carnahan, N. F. & Starling, K. E. Equation of state for nonattracting rigid spheres. *The Journal of Chemical Physics* **51**, 635-636, (1969).
- 47 Wu, J. & Prausnitz, J. M. Osmotic pressures of aqueous bovine serum albumin solutions at high ionic strength. *Fluid Phase Equilibria* **155**, 139-154, (1999).
- 48 Hill, T. L. *An introduction to statistical thermodynamics.* (Courier Corporation, 2012).
- 49 Cordova, A., Deserno, M., Gelbart, W. M. & Ben-Shaul, A. Osmotic shock and the strength of viral capsids. *Biophys J* **85**, 70-74, (2003).
- 50 Snijder, J. *et al.* Probing the biophysical interplay between a viral genome and its capsid. *Nature Chemistry* **5**, 502-509, (2013).
- 51 Smith, D. E. *et al.* The bacteriophage phi 29 portal motor can package DNA against a large internal force. *Nature* **413**, 748-752, (2001).
- 52 Evilevitch, A., Lavelle, L., Knobler, C. M., Raspaud, E. & Gelbart, W. M. Osmotic pressure inhibition of DNA ejection from phage. *P Natl Acad Sci USA* **100**, 9292-9295, (2003).
- 53 Jin, Y. *et al.* Bacteriophage P22 ejects all of its internal proteins before its genome. *Virology* **485**, 128-134, (2015).
- 54 Lander, G. C. *et al.* The structure of an infectious P22 virion shows the signal for headful DNA packaging. *Science* **312**, 1791-1795, (2006).

- 55 Marabini, R. *et al.* Xmipp: An Image Processing Package for Electron Microscopy. *J Struct Biol* **116**, 237-240, (1996).
- 56 Pettersen, E. F. *et al.* UCSF Chimera--a visualization system for exploratory research and analysis. *J Comput Chem* **25**, 1605-1612, (2004).
- 57 Mindell, J. A. & Grigorieff, N. Accurate determination of local defocus and specimen tilt in electron microscopy. *J Struct Biol* **142**, 334-347, (2003).
- 58 Sorzano, C. O. *et al.* A clustering approach to multireference alignment of single-particle projections in electron microscopy. *J Struct Biol* **171**, 197-206, (2010).
- 59 Scheres, S. H., Nunez-Ramirez, R., Sorzano, C. O., Carazo, J. M. & Marabini, R. Image processing for electron microscopy single-particle analysis using XMIPP. *Nat Protoc* **3**, 977-990, (2008).
- 60 Ludtke, S. J., Baldwin, P. R. & Chiu, W. EMAN: semiautomated software for high-resolution single-particle reconstructions. *J Struct Biol* **128**, 82-97, (1999).
- 61 Ortega-Esteban, A. *et al.* Minimizing tip-sample forces in jumping mode atomic force microscopy in liquid. *Ultramicroscopy* **114**, 56-61, (2012).
- 62 Sader, J. E., Chon, J. W. M. & Mulvaney, P. Calibration of rectangular atomic force microscope cantilevers. *Review of Scientific Instruments* **70**, 3967-3969, (1999).
- 63 Horcas, I. *et al.* WSXM: A software for scanning probe microscopy and a tool for nanotechnology. *Rev Sci Instrum* **78**, (2007).

Mechanical Effects of Symmetry Specific Destabilization and Restabilization of the Bacteriophage P22 Virus-Like Particle

Based on:

A. Llauró*, B. Schwarz*, D. Reguera, P.J. de Pablo, T. Douglas, Mechanical effects of symmetry specific destabilization and restabilization of the bacteriophage P22 virus-like particle. In preparation. *These authors contributed equally to the work.

Abstract

Virus-like particles (VLP) are highly symmetric structures with outstanding mechanical properties. However, these nanosized protein assemblies might display defects that alter the local inter-monomeric interactions and change the overall performance of the capsid. Here we investigate the effects that the controllable introduction of defects have on the stability of P22 VLPs by using single-particle Atomic Force Microscopy and bulk biochemical techniques. We also use an accessory protein (Dec) as a means of restoring the stability of the cages. Our results show that the introduction of defects provokes a concomitant chemical and mechanical destabilization of the capsid and reveals that the lines between defects, corresponding to the capsid edges, are the mechanical determinants of the breakage. Consequent adhesion of Dec protein at these critical regions is capable of restoring the undermined chemical and mechanical stability. The surprising agreement between our single molecule and bulk techniques suggest that the same structural determinants govern both destabilizing process, and it offers the possibility of study symmetry-dependent effects in bulk biochemical studies. Overall, our results provide a systematic study of the effects of protein-specific destabilization and restabilization of a nanostructure and might serve as a model to understand the mechanical performance of other nanomaterials displaying high-levels of symmetry.

Introduction

Virus capsids represent a class of biological nanomaterials that exhibit impressive mechanical properties. These complex and highly regular structures are assembled from a limited number of subunits with the overall mechanical properties dependent on local subunit-subunit interactions.¹ Selective interruption or reinforcement of these interactions could lead to controllable changes in global mechanics.² To understand the effect of local interactions on the mechanics of the material it is necessary to probe the propagation of stabilizing and destabilizing perturbations with spatial resolution. These mechanical insights provide better structural understanding of biological nanomaterial systems as well as guidance for designing biomimetic assemblies with specific mechanical properties. Here we utilize a virus-like particle (VLP) as a controllable system for the examination of capsid mechanics after the introduction of destabilizing defects and subsequent reinforcement with accessory proteins.

VLPs are noninfectious cage architectures derived from viral or non-viral sources that provide nano-scale engineering platforms for the design of nanoparticles with functionalized exteriors and/or interiors.^{3,4} This potential for modification makes VLPs promising candidates for the design of a new class of nanomaterials with applications ranging from biomedicine to electronics.^{5,6} Self-assembly of many VLPs is remarkably robust but, as with any process, can generate structures with imperfect symmetry or defects that modify the overall performance of the material.⁷ Examination of the impact of these defects on the mechanical stability of the capsid allows for the design of strategies to avoid defect-promoting pathways and also offers insight into what elements of the capsid symmetry lead to their remarkable properties as robust nanostructures.

The VLP derived from bacteriophage P22 offers a controllable system for the introduction of structural defects and the potential recovery of structural integrity through the binding of accessory proteins. P22 procapsid VLPs consist of 415 copies of a coat protein (CP) that assemble into a T=7 icosahedral structures around 100-330 scaffolding proteins with a portal complex occupying one of the 5-fold vertices. DNA packaging triggers the expansion of the immature procapsid form of P22 into the more angular mature phage.⁸⁻¹⁴ A P22 VLP is assembled when CP and SP are coexpressed heterologously or recombined *in vitro*.¹⁵ The structural transition from PC to the mature phage can be mimicked in the VLP system by

either heating the sample at 65°C or by briefly incubating the sample with sodium dodecyl sulfate (SDS), which results in the expanded (EX) VLP morphology (Figure 1A).^{16,17} Further heating at 75°C leads to the release of the 12 pentons of the cage resulting in the porous and less angular wiffle ball (WB) VLP morphology (Figure 1B).¹⁸⁻²⁰ Because the mechanical stress of a polyhedron is concentrated at the pentons, expulsion of the pentons in the WB form relieves stress and introduces mechanical defects.²¹

The P22 VLP system additionally offers the possibility to reinforce the capsid with an exterior decoration protein. The Dec protein is a 15 kDa protein that binds to the surface of the Phage L capsid as trimers localized preferentially to the 60 quasi 3-fold sites.^{16,19,22} Phage L is highly similar to P22 with only 4 conserved amino acid differences in the coat protein sequences and it has been shown that mature P22 virus increase the heat stability of the infectious phage after Dec binding.¹⁶ Cryo-electron microscopy studies revealed that Dec also binds to the EX and WB P22 VLPs, localizing to the quasi 3-fold axes (nearest the icosahedral 2-fold axes) and with lower affinity to the true 3-fold axes (Figure 1C).^{19,22} Together, the heat-induced penton expulsion and addition of Dec allow for the potential controlled introduction and reinforcement of defect sites in the P22 VLP structures.

To understand the effect that defects and Dec protein have on the stability of these cages we studied the mechanical properties and chemical stability of four different forms of P22 (Figure 1D). We first focused on the effects of penton-release by comparing the mechanics and stability of EX vs. WB. Secondly, Dec protein was attached to both morphologies and the changes due to Dec addition were compared (*i.e.*, EX vs. EX+Dec and WB vs. WB+Dec). Our results showed that, as expected, stability was lost when EX transitioned to WB, but that stability could be recovered through the introduction of Dec. Symmetry dependent destabilization and restabilization also agreed well with the localization of Dec on either side of the 2-fold sites of the capsid. The addition of Dec at these sites increased the mechanical stability of the VLPs in a symmetric-dependent manner, showing that selective spatial reinforcement could be applied to enhance the overall stability of nanostructures displaying high levels of symmetry.

Results and Discussion

The Capsid is Destabilized by the Loss of Pentons

To assess the degree to which the loss of pentons destabilizes the P22 capsid the mechanics and chemical stability of WB was compared to EX. P22 VLPs were produced in *E. coli* and purified as SP containing procapsids. Capsid samples were heated to form either EX or WB from a common PC sample and expansion was monitored via non-denaturing agarose gel electrophoresis (Figure S1-A). Samples were also assessed by size-exclusion chromatography (SEC) monitored by multi-angle light scattering (MALS) and quasi-elastic light scattering (QELS). By SEC the EX and WB samples showed a shift in retention time suggesting larger particles (Figure S1-B). This was further supported by QELS, which reported a radius of hydration of 29.6 ± 1.4 nm for EX and 28.1 ± 1.1 nm for WB compared to 26.5 ± 0.8 nm for PC. By MALS the number average molecular weight of EX and WB was reduced compared to PC (Figure S1-C and S1-D). The molecular weight for EX of 20.3 ± 0.7 MDa was in good agreement with the expected weight of 19.7 MDa for a capsid completely devoid of SP. The molecular weight of WB of 18.3 ± 0.5 MDa indicated the loss of the majority of the pentons but was short of the expected 2.8 MDa reduction. This difference in mass was likely the consequence of having some intermediate state with only a few of the pentons released. Single molecule AFM experiments confirmed the existence of such intermediate forms in which only a few of the pentons were lacking (Figure S2).

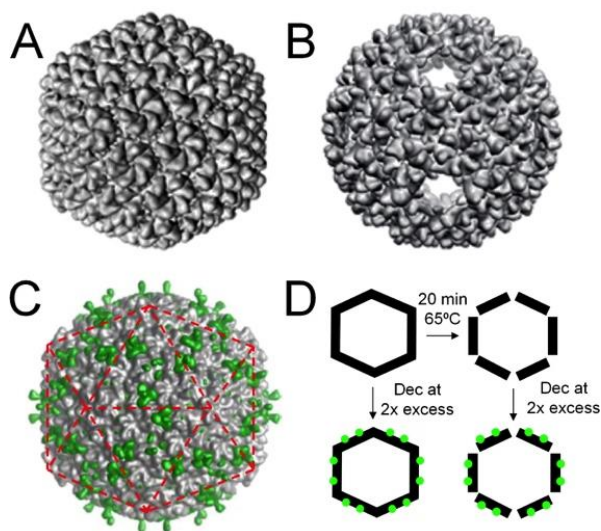


Figure 1. Structure of the particle. Cryo-EM reconstruction of (A) EX capsid (PDB: 3IYI)²⁰ and (B) WB (PDB: 3IYH)²⁰ (C) Dec protein bound to an EX capsid.²² An icosahedron is overlaid to the structure (red dashed lines). (C) Schematic of the transition of the particles in our study. EX VLPs were heated to expel pentons forming the WB morphology. Dec proteins were bound to either the EX capsids or the WB capsids at a ratio of 160 Dec proteins per capsids.

To compare the chemical stability of EX and WB samples were incubated with SDS. SDS is known to facilitate the expansion of the PC form of the capsid to the EX form presumably by providing more subunit flexibility allowing for transition of subunits to the EX structure.¹⁶ Extended incubation of the capsid in SDS or incubation in increasing concentrations of SDS leads to degradation of the capsid (Figure S3). When the normalized loss in light scattering for EX and WB was compared in 0.5% SDS, WB exhibited much lower stability with a 56% average reduction in scattering over 1 hour compared to only 31% for EX over the same time period (Figure 2A). By transmission electron microscopy WB samples exhibited a decrease of 63% in the percentage of well-formed particles after 20 minutes in 0.5% SDS. In contrast, EX samples remain largely intact with a decrease of 10% in the percentage of well-formed particles (Figure 2B and C).

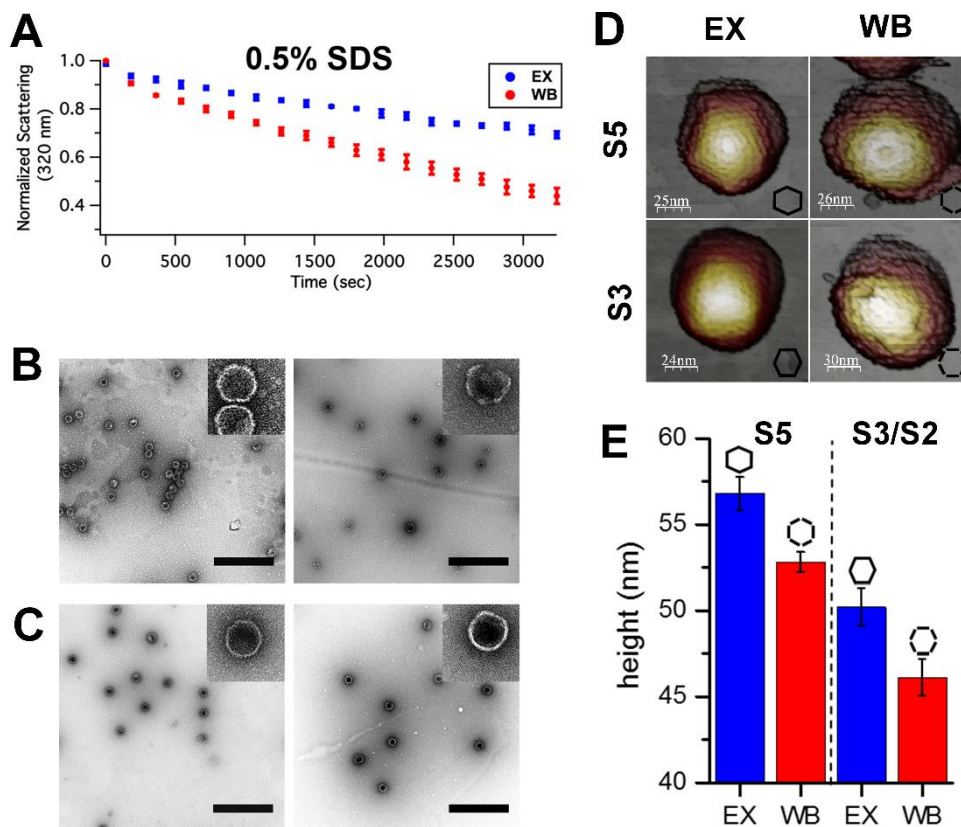


Figure 2. The P22 VLP is destabilized by the loss of pentons. (A) Normalized loss in light scattering at 320 nm due to degradation of either EX (blue) or WB (red) in 0.5% SDS. Error bars represent the standard error on the mean of the normalized scattering at each time point for 3 runs. Electron micrographs of (B) WB (left) and WB after 20 min in 0.5% SDS (right) or (C) EX (left) and EX after 20 min in 0.5% SDS (right). Insets in the upper right corner show an expanded view of a representative particle from the field. Scale bars: 500 nm.

To examine the degree and symmetry dependence of WB and EX destabilization samples were examined by AFM. Particles were adsorbed on freshly exfoliated graphite surfaces and their orientation was determined (Figure 2D). The 5-fold symmetry (S5) was the most frequent orientation, representing a 59% and 66% of EX and WB, respectively (Table S1). The other two orientations were classified together as 3- and 2-fold symmetries (S3/S2) because the precise position was difficult to distinguish. The average height of the particles measured by AFM depended on the orientation. Particles in the S5 orientation presented a higher height than particles showing a S3/S2 orientation (Figure 2E). These differences in height were in agreement with the fact that in an icosahedron the distance between two opposite vertices is larger than the distance between two opposite faces or edges. In both cases (S5 and S3/S2) WB particles presented a lower height compared to the corresponding orientation in the complete EX forms, which indicated that the loss of pentons had a significant effect on the deformability of the particles. Recent AFM experiments have shown that the mechanical properties of VLPs might be related to the measured height of the particles and that a lower height correlates with a softening of the overall structure.²³

To further investigate this change in the mechanical properties with penton loss we performed nanoindentation experiments at the single particle level. Nanoindentation assays have been extensively used to study the mechanical properties of viral and non-viral nanocages during the last decade.^{24,25} Briefly, the experiment consists of deforming individual particles with an AFM tip until the point of mechanical failure. The force vs. indentation curve (FIC) obtained during this irreversible deformation provides information about the rigidity (elastic constant) and the strength of the particle (breaking force and critical deformation).²⁴ A representative set of AFM images and model schematics is shown in Figure 3. The example displays an EX compressed along the S5 axis (Figure 3A and B) and a WB compressed along the S3 axis (Figure 3C and D) before and after breakage. The corresponding FICs for these particles are plotted together in Figure 3E, which demonstrates the strong impact of penton loss on the particle breaking force.

(continued) (D) AFM images of single particles. Top row: S5 oriented EX (left) and WB (right). Bottom row: S3/S2 oriented EX (left) and WB (right). (E) Average height measurements from AFM imaged particles of EX and WB with

either the 5- or 3/2-fold symmetry axes oriented upward. S3 and S2 axes were grouped because the orientations could not be reliably distinguished. Error bars represent standard error on the mean.

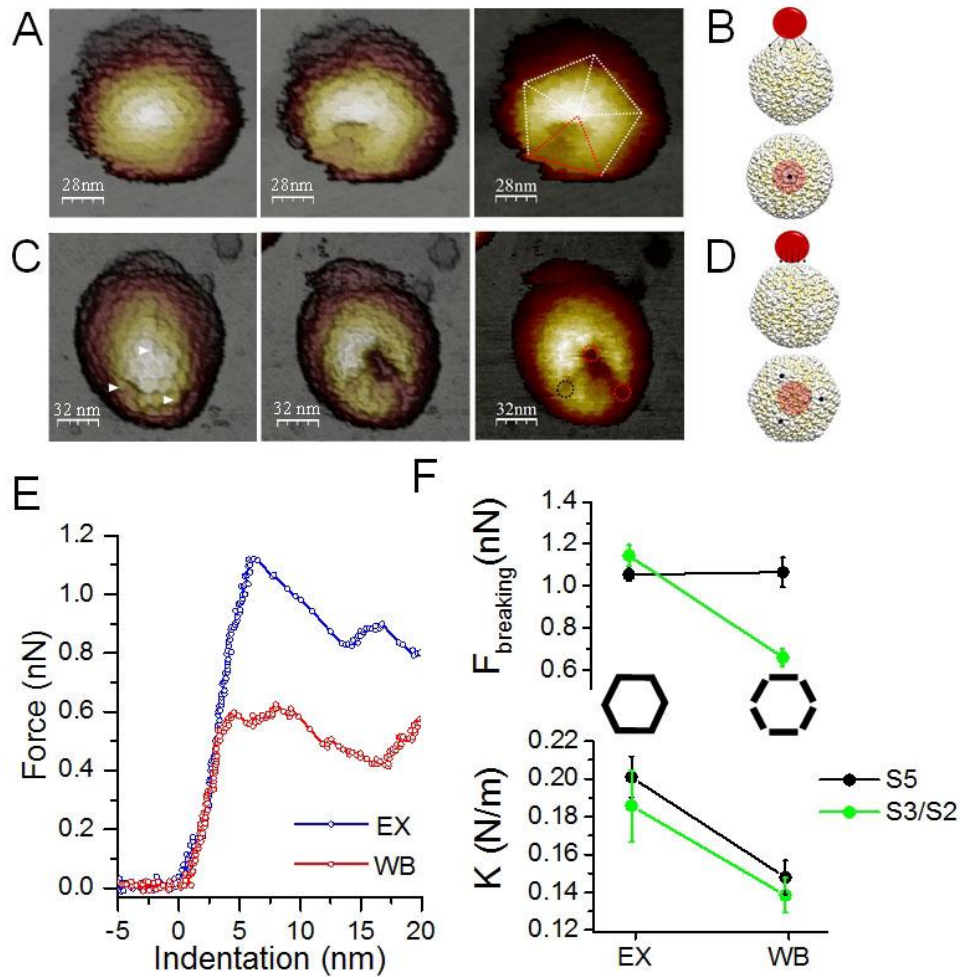


Figure 3. Individual AFM nanoindentation assay (A) AFM images of an EX capsid showing a S5 orientation before and after the nanoindentation. The particle is shown as a 3D representation before (left) and after (middle) breaking. The image at right shows a 2D representation after breakage. A pentagon with its 5 faces is overlapped to the image to guide the eye (dash lines). The red lines highlight the parts of the particle that were mostly affected by the nanoindentation. (B) Schematic at scale of an AFM tip indenting an EX capsid along the 5-fold symmetry axis. The size of the tip can be seen to extend past the edges of the penton at the capsid vertex. (C) AFM images of a WB showing a S3 orientation before and after a nanoindentation. The left and middle images are 3D representations (white arrowheads indicate the position of the missing pentons). The image at right shows a 2D representation of the particle after breakage. Dashed circles indicate the position of the missing pentons (in red are represented the pentameric sites that were connected after to the breakage). (D) Schematic at scale of an AFM tip indenting an EX²⁶ along the 3-fold symmetry axis. Black dots are located at the pentons. The contact of the AFM tip can be seen to be localized to the capsid face. (E) Nanoindentation curves that provoked the breakage in A (blue line) and C (red line). (F) Evolution of the elastic constant (k) and breaking force of 30 EX and 39 WB. The error bar represents the standard error.

The characterization of the pattern of breakage provided important information about the stability of the particles. Despite pentons are the regions subjected to the maximum stress,²¹ nanoindentations along the 5-fold symmetry axis were rarely accompanied by the release of the penton but, instead, resulted in damage to neighboring faces (Figure 3A, right, and Figure S4). This might be explained by the relative size and orientation between the particle and the AFM tip. Because the tip was much larger than a penton subunit, the area under pressure exceeded the size of the penton and spread over the entire structure provoking the collapse of one of the neighboring faces (Figure 3B). In contrast, deformations produced along the 2/3-fold symmetry axes typically involved the collapse (total or partial) of the top face (Figure 3C, right, and Figure S4). In those cases, the contact area of the AFM tip was confined within the top face of the capsid and deformations mainly affected the top three hexamers, which were radial indented (Figure 3D). These fractures usually occurred along the edges of the top face, connecting at least two penton sites (Figure 3C and S4). Note that the rupturing of these edges was especially notable in WB particles, where the cracks were usually constrained between two pentameric vacancies (Figure S3-D).

To quantify the mechanical parameters 30 EX particles and 39 WB particles were examined and the results separated by symmetry (Figure 3F). Measurements of stiffness suggested that the loss of pentons was accompanied by a loss of structural integrity. A decrease in particle stiffness of 25% was observed between EX and WB along both symmetry axes (Figure 3F, bottom). These results were in good agreement with continuum elastic theory and Montecarlo coarse-grained simulations predicting that pentons are the most stressed regions of the capsid and that their removal should make particles softer.^{21,27} Penton-less capsid forms exist across a wide size range of icosahedral viruses including adenovirus (T=25), HSV1 (T=16), HK97 and P22 bacteriophages (both T=7).^{18,28-30} It is worth noting that known penton-less forms seem to be localized to $T \geq 7$ particles, which agrees well with predictions that as the T number increases more stress is localized to the five-fold sites.²¹ This repeated occurrence of penton-less cages suggests that this state is a general consequence of the overall mechanics of icosahedral cage architecture. However, the symmetry-specific mechanical properties of a virus particle originate at residual level interactions.^{26,31-33} For example, single point mutations in MVM change the elastic response of the capsid more than twofold in a symmetry-dependent manner.² In a recent work by Cieplak et al., 35 virus capsids, with T

numbers from 1-7, were tested in a molecular model showing that the change in mechanical properties did not correlate with the virus size or the T number but with the mean number of interactions to neighboring amino acids.¹ This mechanical sensitivity to the molecular interactions was also captured in our work when we compared the presented P22 VLP experiments to previous studies examining bacteriophage T7, also a T=7 virus of similar size.³⁴ The expanded capsid form of P22 is isotropic (i.e, the same value of stiffness was obtained along the three different symmetry axes: $K_{EX-S5} \approx K_{EX-S3/S2} \approx 0,20$). In contrast, bacteriophage T7 capsids were found to be highly anisotropic (the 3-fold symmetry axis was two times stiffer than the 5-fold symmetry axis).²⁶

Our results on the breaking force supported the conclusion that the loss of pentons was accompanied by a loss of structural integrity ([Figure 3F](#), top). Note, however, that the impact of the breaking force was highly anisotropic. The loss of pentons had a huge impact on the S3/S2 symmetry (green line) but along the S5 remain the same (black line). This anisotropic decrease in breaking force with loss of pentons indicated that the removal of pentons had a very specific symmetry-dependent effect on capsid mechanics. The lack of pentons in WB reduced more dramatically the strength of the capsids along the S3/S2 most likely because the hexamers (of the top face or edge) involved in the deformation had lost their interaction with their neighboring pentons, which involves the reorganization of the N-arm of the hexameric subunit lying closest to the missing penton.²⁰ Analysis of the critical indentation distance supported this assertion and showed that along the S3/S2 WB particles could withstand shorter deformations than EX capsids ([table S2](#) and [Figure S5-A](#)). In addition to the connections lost due to penton removal, an analysis of the inter-capsomeric association energies based on the buried surface areas (obtained from *Carrilo-Tripp et al.*)³⁵ showed that three connections involving inter-hexameric interactions were also lost during the transition from EX to WB (see [table S3](#) and [Figure S6](#)). Two connecting hexamers along the edge and one connecting hexamers in the face (see blue dots in [Figure S6](#)). Those were all indication of the decrease in mechanical strength observed for the WB forms along the 2/3-fold symmetry axes.

Dec Protein Reinforces Pentonless Particles

Dec protein from bacteriophage L has been previously shown to enhance the heat tolerance of infectious P22.¹⁶ Though not part of the P22 viral genome, Dec binds to both the EX and WB VLP preferentially at the quasi 3-fold sites, which straddles the 2-fold axes of the capsid.¹⁹ We found that the destabilization of WB VLPs was most evident for the S3/S2 orientation, with fractures occurring along the edges of the cage (Figure S4-D). Binding of Dec directly adjacent to these points of destabilization in the WB may lead to recovery of stability. To examine this possibility, the SDS degradation of EX and WB were compared to Dec bound samples of both VLP morphologies. While Dec reinforcement had little effect on the degradation of EX in 0.5% SDS, the degradation of WB was significantly reduced. WB+Dec showed a 20% reduction in 0.5% SDS over 1 hr compared to 56% for WB alone (Figure 4A).

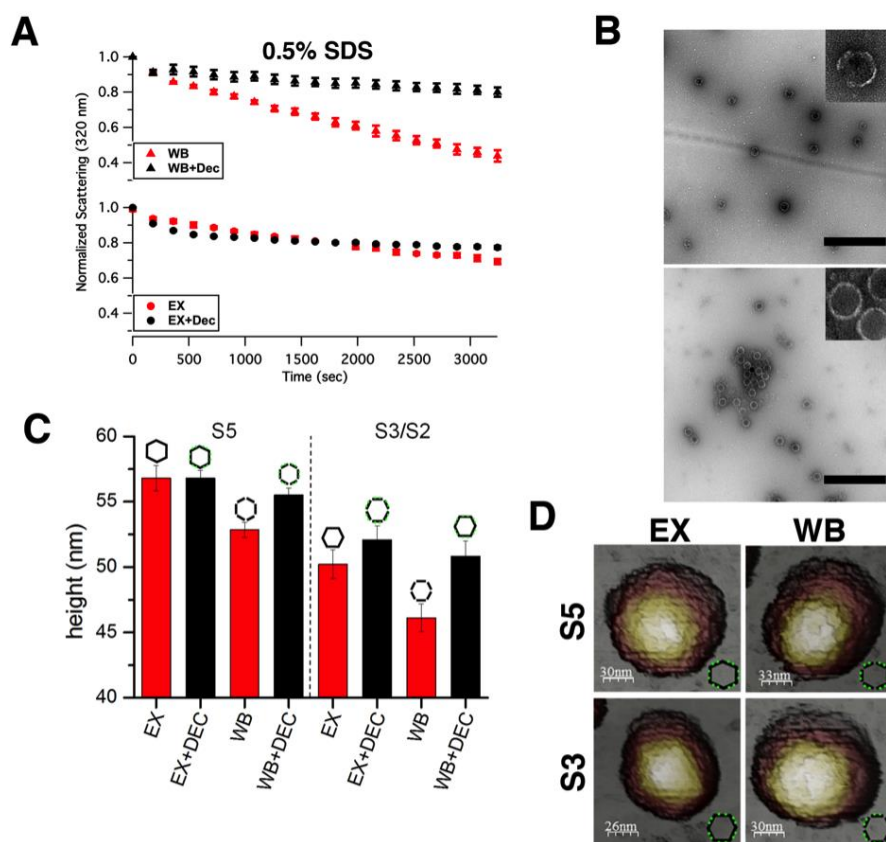


Figure 4. Dec selectively reinforces WB VLPs. (A) Normalized loss in light scattering at 320 nm due to degradation of (top) WB (red) or WB+Dec (black) and (bottom) EX (red) or EX+Dec (black) in 0.5% SDS. Error bars represent the standard error on the mean of the normalized scattering at each time point for 3 runs. (B) Electron micrographs of WB (top) or WB+Dec (bottom) after 20 min in 0.5% SDS. Insets in the upper right corner show an expanded view of a representative particle from the field. Scale bars are 500 nm. (C) Height of

This recovery in stability was supported by TEM. Micrographs of WB treated with 0.5% SDS for 20 min displayed 62% reduction in the ratio of formed to incomplete particles compared to untreated WB. With Dec bound, an 11% reduction in the ratio of formed to incomplete particles was observed (Figure 4B and S7). In agreement with these results, AFM images showed that Dec bound WB particles increased in average height 3% along the S5 axes and 5% along the S3/S2, whereas the height of EX capsid was only increased by 0.2% and 2%, respectively (Figure 4C). The presence of Dec attached to the particle surface could not be observed by our AFM due to limitations in lateral resolution (~ 5 nm),^{26,36} but we systematically observed that after Dec binding the capsomeric appearance of the structures was less defined (Figure 4D).

The effect of Dec binding was also explored by single nanoindentation assays (Figure 5A and 5B). No significant changes in the elastic constant were observed after Dec binding (only a slight increase of 13% for EX+DEC along the S5 axes), but important differences were observed in the breaking force. The binding of Dec to EX VLPs was accompanied by a moderate 15% and 12% increase in the breaking force for the the S5 and S3/S2 symmetries axes, respectively (Figure 5A). In contrast, WB VLPs showed a recovery of stability that highly depended on the orientation. With Dec binding the breaking force only increase a 6% along the S5 symmetry axes, but a rise of 31% was observed for the S3/S symmetry axes (Figure 5B). Remarkably, this symmetry-dependent reinforcement seemed to compensate for the observed loss of stability after the expulsion of pentons (Figure 3). Supporting this idea of a selective recuperation of stability, we observed that WB VLPs with Dec recovered the deformation capacity loss during the removal of pentons along the S3/S2 axes (table S2 and Figure S4). Naked WB VLPs resisted deformations of 9 nm, but after Dec binding WB VLPs extended this distance to 12 nm (the same value obtained for EX VLPs with and without Dec).



(continued) particles with either the S5 axis or the S3/S2 axes oriented upward. S3 and S2 were grouped because the orientations could not be reliably distinguished. Error bars represent standard error on the mean. (D) Single particle AFM images of either the S5 (top row) or S3 (bottom row) orientations or EX+Dec (left) or WB+Dec (right).

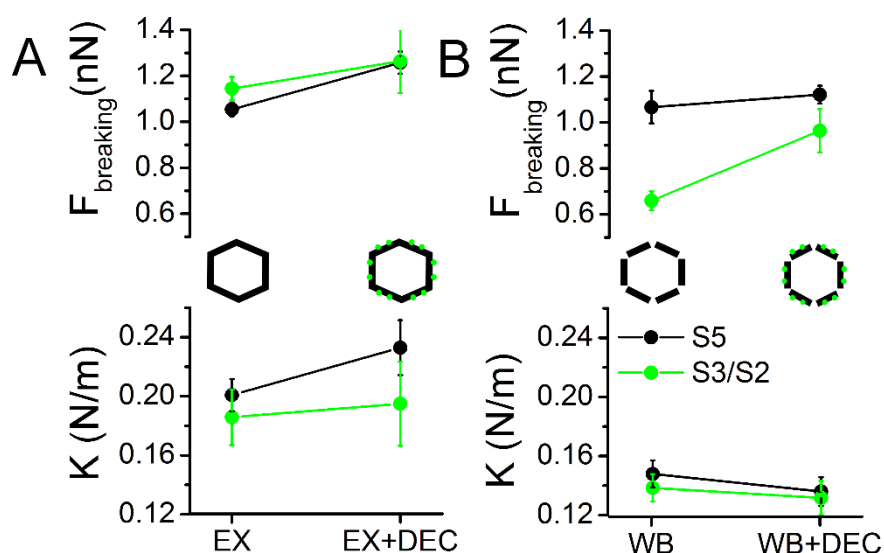


Figure 5. Mechanical changes due to Dec binding. (A) Evolution of the breaking force and elastic constant (k) for the transition EX \rightarrow EX+Dec along the S5 axes (black curve) and S3/S2 axes (green curve). (B) Evolution of the breaking force and elastic constant (k) for the transition WB \rightarrow WB+Dec along the S5 axes (black curve) and S3/S2 axes (green curve).

To collectively compare the multiple contributing mechanical parameters, the net elastic energy transferred to the system to produce the breakage was analyzed (Figure 6A). The energy required to break EX VLPs was similar to that of WB VLPs along the S5 axes, but this value dropped by 50% along the S3/S2 axes. As expected, after Dec binding the required elastic energy increased for both morphologies, but the effect was not proportional. Whereas along the S5 axes the effect of Dec was similar (25% vs. 30%), along the S3/S2 axes it was more significant for the WB morphology (10% vs. 50%). In summary, our energetic study demonstrated two things: (1) the insertion of defects had a symmetry-dependent effect, being more important for the S3/S2 orientation (see one asterisk in Figure 6A), and (2) it was precisely this orientation the one that show the major effect after Dec binding (see two asterisks in Figure 6A). An analysis of the position of Dec protein in the structures shed some light on these results (Figure S6). Dec proteins locate nearest the icosahedral 2-fold axes, reinforcing the edges of the capsid (see trimers in Figure S3).^{19,22} It binds precisely at the positions where the inter-capsomeric interactions were lost after the transition from EX to WB (blue dots, Figure S6). It seems reasonable to suggest that, in the same way that those interactions seemed the responsible for the symmetry-dependent loss of stability, the

reestablishment of those same connections by Dec result in the restoring of the mechanical strength.

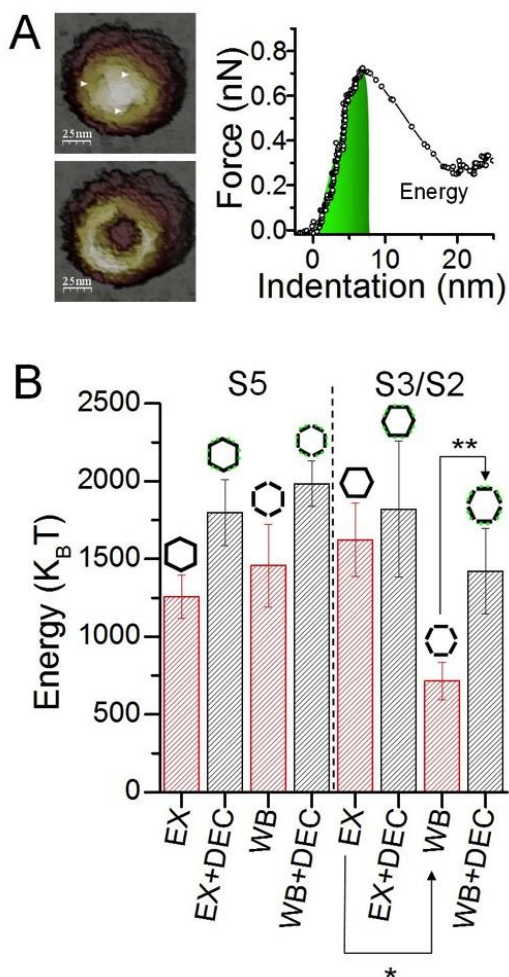


Figure 6. AFM elastic energy required to break each configuration. (A) Example of a nanoindentation experiment performed on a WB+Dec along the S3 axes. The AFM images before (top) and after (bottom) the rupture show that the top face was completely removed (white arrows indicate the penton-less vacancies). The area below the elastic FIC (green area) represents the energy provided to the system to produce the breakage. (B) Statistical analysis of the different energies of rupture: along the S5 axes (left side) and S3/S2 axes (right side). The most significant decrease in energy was observed for the S3/S2 orientation after penton removal (one asterisk). Likewise, the most significant increase in energy was observed for the S3/S2 orientation after Dec binding (two asterisks).

Chemical and Structural Determinants of the Stability

Despite the stark differences in the means of perturbation, our bulk chemical and single-particle mechanical stability experiments reflected the same trends between capsid morphologies. The agreement in these trends likely originates from similar structural elements of the capsid being interrupted. Due to the difficulty in observing chemical destabilization in a non-bulk, symmetry-specific manner there remains a gap in the understanding of this process. However, single-particle, symmetry-specific mechanical perturbation results may provide some insights into the similar trends seen in the chemical experiments.

Chemical destabilization and degradation of the particle with SDS likely functions by interrupting both intra- and inter-subunit hydrophobic contacts. This effect, although it will likely be isotropic about the capsid, may be more effective acting between subunits that are held under greater mechanical stress or interacting with a lower number of bonds. The observed initial expansion of the capsid in SDS suggests that intra-subunit contacts are initially disrupted allowing for adoption of the EX morphology without losing capsid integrity. Further degradation of the capsid suggests interruption of inter-subunit interactions and/or intra-subunit contact, resulting in eventual loss of capsid integrity.

Our AFM results showed that fractures occurred along the edges, the second most stressed regions of the capsid after the pentons.²¹ This feature was especially evident for the WB morphology, where deformation led to cracks that connected two pentameric sites. An inspection of the inter-capsomeric energies between subunits revealed that along those edges interactions were lost after the transition, which explained the symmetry-dependent destabilization observed in our single molecule experiments. Subsequent Dec binding at those critical points was able to restore the stability of the capsid in a symmetry-dependent way. The significant recovery of chemical stability with Dec binding to WB may indicate that capsid rupture under these conditions also occurs at the inter-capsomeric contacts along the edges, exposed during the transition from EX to WB, which would allow for more ready intercalation of SDS and faster degradation of the capsids.

Symmetry-dependent effects of auxiliary proteins

Auxiliary proteins are a common strategy used by different viruses to stabilize their structures against remarkable mechanical forces involved in the viral lifecycle.^{20,37} Recent publications have shown that binding to the shells enhances the mechanical stability of the viral cages. However, contradictory data has been published concerning the effect of gpD on lambda phage.^{37,38} A possible explanation of this disparity may be the absence of symmetry-specific examination of the effect of gpD binding. An anisotropic reinforcement is observed for P22 after the Dec binding and a similar effect could explain the disagreement observed for lambda phage, where symmetry was not considered. In fact, the difference in decoration protein binding site location for HSV1, which only binds adjacent to the pentons, and lambda phage, which binds similarly to Dec at the quasi and true 3-fold sites, has been justified by a

changing distribution of the stress with an increase in capsid size.^{37 20,37,38} If this is the case, it should be expectable that that the reinforcement mediated by auxiliary proteins would have a symmetry-dependent effect to compensate for the anisotropic stress contribution of the capsid.

Conclusions

We have shown that the controlled, symmetrical introduction of defects into a viral cage leads to a symmetry-dependent destabilization of the capsid. In addition, we have shown that symmetry-dependent binding of an accessory protein might be employed to restore the loss of stability.

The symmetric inclusion of defects in P22 VLPs modifies the chemical and mechanical properties of the capsid in a striking way. Our light scattering and TEM analysis showed that, under 0.5% SDS, WB VLPs exhibited much lower stability than EX VLPs. This transition was also explored by AFM, which showed that the stability loss was dependent on the orientation of the capsid. While along the S5 axes the breaking force was maintained for both VLPs morphologies, along the S3/S2 axes the breaking force dramatically dropped after the transition. An inspection of the patterns of breakage and interaction energies between capsid subunits allowed us to conclude that the edges of the cage were the main responsible for the loss of stability.

By adhering a decoration protein that bound directly over those edges the decrease in mechanical strength was restored. We found that the adhesion of Dec enhanced the overall mechanical properties of the VLPs but, notably, had a more significant effect on the mechanical variables most weakened after the removal of pentons. In agreement with these AFM results, our light scattering and TEM experiments showed that Dec binding had a greater stabilizing effect toward WB VLPs than toward EX VLPs. The coupling of single molecule and bulk techniques permitted the in depth examination of contributing factors to these symmetry-specific phenomenon, allowing for a deeper understanding of chemical bulk destabilization, and for the potential future examination of both infectious viral systems and synthesized nanomaterials.

Materials and methods

Materials

Chemically competent BL21 (DE3) *E. coli*, cells were purchased from Lucigen. TEM grids were purchased from Electron Microscopy Sciences. All other chemical reagents were purchased from Fisher Scientific.

Protein Production

E. coli strains transformed with a pET Duet plasmid containing either the CP and SP genes or an N-terminal 6x his-tag Dec gene were grown in LB medium at 37 °C in the presence of ampicillin. Expression was induced at mid-log phase ($OD_{600}=0.6$) with isopropyl β -D-thiogalactopyranoside (IPTG) added to a final concentration of 0.5 mM. 4 hours post-induction cells were harvested by centrifugation and cell pellets stored at -80 °C overnight.

Cell pellets were resuspended in PBS (100 mM sodium phosphate, 50 mM sodium chloride, pH 7) and lysozyme and RNase were added. Protease inhibitor, cOmplete™minitabs (Roche), were added to Dec cultures. Cell suspensions were incubated for 30 minutes at room temperature. Suspensions were lysed by sonication and cell debris was removed by centrifugation at 12,000 *g* for 45 min at 4 °C.

P22 VLPs were purified from the supernatant by ultracentrifugation through a 35% (w/v) sucrose cushion and the resulting pellet was resuspended in PBS. VLPs were purified using a S-500 Sephadex size exclusion column and a Biorad Biologic Duoflow FLPC. Flow rate for SEC purification was 1 mL/min. Fractions containing P22 were concentrated by ultracentrifugation.

Dec was purified via his-tag affinity chromatography using a 5 mL cOmplete™ his-tag column (Roche) and a Biorad Biologic Duoflow FLPC. Samples were initially eluted using a 60mL gradient from 20-250 mM imidazole. Fractions were dialyzed against PBS and reloaded onto the column. Samples were concentrated and further purified using a short 10 mL 20-250 mM gradient and subsequently redialyzed against PBS.

Expansion

P22 PC VLPs were diluted to ~1.5 mg/mL total protein in PBS and heated at either 65 °C or 75 °C for 25 minutes. Samples were at 16,000 *xg* for 5 minutes to remove any aggregates and

the supernatant analyzed for expansion. Samples were analyzed by non-denaturing gel electrophoresis as previously described.³⁹

SDS Destabilization

For TEM and initial concentration screening experiments, samples were incubated at room temperature in varying concentration of SDS in PBS and quenched at the point of analysis by either loading on a non-denaturing agarose gel or by deposition on a TEM grid.

For light scattering experiments samples were diluted to ~1 mg/mL CP. Dec-bound samples were made by mixing Dec with P22 VLP samples at a ratio of 160 Dec trimers per capsid prior to dilution. The intensity of light scattering was monitored through the optical density (OD) at 320 nm with a background subtraction of the OD at 800 nm to account for any baseline fluctuations. Data was normalized to the starting OD₃₂₀ value and all runs were performed n=3. Runs were plotted using IGOR Pro 6.3.

TEM

Samples (5 μ L, 0.1 mg/mL protein) were incubated for 30 s on carbon-coated copper grids. Grids were then washed with 5 μ L of distilled water and stained with 5 μ L 2% Uranyl acetate. Images were captured at an accelerating voltage of 80 kV on a JEOL 1010 transmission electron microscope.

AFM

AFM experiments were performed as described previously in chapter 2.⁴⁰ Experiments were done with a *Nanotec Electrónica* microscope (Madrid, Spain) operating in jumping mode plus.⁴¹ Imaging forces were kept between 60-150 pN. Rectangular silicon-nitride cantilevers (RC800PSA, Olympus, Center Valley, PA) with a nominal spring constant of 0.05 N/m were used. Before every measurement cantilevers were calibrated by Sader's method.⁴² Experiments were carried out in buffer conditions (100 mM phosphate, 50 mM NaCl, pH=7) at a controlled temperature of 17°C. A 20 μ L drop of diluted stock solution was incubated on a freshly exfoliated highly ordered pyrolytic graphite (HOPG) surface (ZYA quality; NT-MDT, Tempe, AZ). After 30 min, sample was washed with buffer solution until a volume of 90 μ L was reached. AFM images were processed with the WSxM software.⁴³ For the binding of Dec (50 mM HEPES, 100 mM NaCl) sample was mixed at 160 Dec trimers per capsid

(i.e., 2x excess Dec per binding site) and allow to bind for an hour at room temperature prior to the adsorption.

Nanoindentation were done at a loading rate of 60 nm/s with forward elongation of 100 nm. Force-vs.-indentation curves (FICs) were obtained from Force-vs.-Z piezo (FZ) curves as previously explained in chapter 2. In brief, to obtain the FIC one has to subtract from the FZ (which includes the deformation of the tip cantilever and the particle) the compliance of the tip cantilever. The elastic constant was obtained by fitting the initial linear part of each FIC; the breaking force and critical indentation were measured using the WsxM software.⁴³ To calculate the energy we assumed a linear deformation and integrated the area below the FIC, considering the elastic constant and the critical indentation.

References

- 1 Cieplak, M. & Robbins, M. O. Nanoindentation of 35 Virus Capsids in a Molecular Model: Relating Mechanical Properties to Structure. *Plos One* **8**, (2013).
- 2 Castellanos, M. *et al.* Mechanical elasticity as a physical signature of conformational dynamics in a virus particle. *P Natl Acad Sci USA* **109**, 12028-12033, (2012).
- 3 Uchida, M. *et al.* Biological containers: Protein cages as multifunctional nanoplatforms. *Adv Mater* **19**, 1025-1042, (2007).
- 4 Douglas, T. & Young, M. Viruses: Making friends with old foes. *Science* **312**, 873-875, (2006).
- 5 Schwarz, B. & Douglas, T. Development of virus-like particles for diagnostic and prophylactic biomedical applications. *Wiley Interdisciplinary Reviews: Nanomedicine and Nanobiotechnology*, (2015).
- 6 Lee, Y. J. *et al.* Fabricating Genetically Engineered High-Power Lithium-Ion Batteries Using Multiple Virus Genes. *Science* **324**, 1051-1055, (2009).
- 7 Wang, J. C.-Y., Chen, C., Rayaprolu, V., Mukhopadhyay, S. & Zlotnick, A. Self-Assembly of an Alphavirus Core-like Particle Is Distinguished by Strong Intersubunit Association Energy and Structural Defects. *Acs Nano*, (2015).
- 8 Earnshaw, W., Casjens, S. & Harrison, S. C. Assembly of Head of Bacteriophage P22 - X-Ray-Diffraction from Heads, Proheads and Related Structures. *J Mol Biol* **104**, 387-410, (1976).
- 9 Parker, M. H., Casjens, S. & Prevelige, P. E. Functional domains of bacteriophage P22 scaffolding protein. *J Mol Biol* **281**, 69-79, (1998).
- 10 Jiang, W. *et al.* Coat protein fold and maturation transition of bacteriophage P22 seen at subnanometer resolutions. *Nature Structural & Molecular Biology* **10**, 131-135, (2003).
- 11 Weigele, P. R., Sampson, L., Winn-Stapley, D. & Casjens, S. R. Molecular genetics of bacteriophage P22 scaffolding protein's functional domains. *J Mol Biol* **348**, 831-844, (2005).
- 12 Chen, D. H. *et al.* Structural basis for scaffolding-mediated assembly and maturation of a dsDNA virus. *Proc Natl Acad Sci U S A* **108**, 1355-1360, (2011).
- 13 Casjens, S., Adams, M. B., Hall, C. & King, J. Assembly-Controlled Autogenous Modulation of Bacteriophage-P22 Scaffolding Protein Gene-Expression. *J Virol* **53**, 174-179, (1985).
- 14 Zhang, Z. *et al.* Visualization of the maturation transition in bacteriophage P22 by electron cryomicroscopy1. *J Mol Biol* **297**, 615-626, (2000).
- 15 Prevelige, P. E., Thomas, D. & King, J. Scaffolding Protein Regulates the Polymerization of P22 Coat Subunits into Icosahedral Shells In vitro. *J Mol Biol* **202**, 743-757, (1988).
- 16 Gilcrease, E. B., Winn-Stapley, D. A., Hewitt, F. C., Joss, L. & Casjens, S. R. Nucleotide sequence of the head assembly gene cluster of bacteriophage L and decoration protein characterization. *J Bacteriol* **187**, 2050-2057, (2005).
- 17 O'Neil, A., Prevelige, P. E., Basu, G. & Douglas, T. Coconfinement of Fluorescent Proteins: Spatially Enforced Communication of GFP and mCherry Encapsulated within the P22 Capsid. *Biomacromolecules* **13**, 3902-3907, (2012).

- 18 Teschke, C. M., McGough, A. & Thuman-Commike, P. A. Penton release from p22 heat-expanded capsids suggests importance of stabilizing penton-hexon interactions during capsid maturation. *Biophys J* **84**, 2585-2592, (2003).
- 19 Parent, K. N. *et al.* Stepwise molecular display utilizing icosahedral and helical complexes of phage coat and decoration proteins in the development of robust nanoscale display vehicles. *Biomaterials* **33**, 5628-5637, (2012).
- 20 Parent, K. N. *et al.* P22 Coat Protein Structures Reveal a Novel Mechanism for Capsid Maturation: Stability without Auxiliary Proteins or Chemical Crosslinks. *Structure* **18**, 390-401, (2010).
- 21 Zandi, R. & Reguera, D. Mechanical properties of viral capsids. *Phys Rev E* **72**, (2005).
- 22 Tang, L., Gilcrease, E. B., Casjens, S. R. & Johnson, J. E. Highly discriminatory binding of capsid-cementing proteins in bacteriophage L. *Structure* **14**, 837-845, (2006).
- 23 Llauro, A. *et al.* Calcium Ions Modulate the Mechanics of Tomato Bushy Stunt Virus. *Biophys J* **109**, 390-397, (2015).
- 24 Roos, W. H., Bruinsma, R. & Wuite, G. J. L. Physical virology. *Nat Phys* **6**, 733-743, (2010).
- 25 Mateu, M. G. Mechanical properties of viruses analyzed by atomic force microscopy: A virological perspective. *Virus Res* **168**, 1-22, (2012).
- 26 Hernando-Perez, M. *et al.* The interplay between mechanics and stability of viral cages. *Nanoscale* **6**, 2702-2709, (2014).
- 27 Klug, W. S., Roos, W. H. & Wuite, G. J. L. Unlocking Internal Prestress from Protein Nanoshells. *Phys Rev Lett* **109**, (2012).
- 28 Perez-Berna, A. J. *et al.* The Role of Capsid Maturation on Adenovirus Priming for Sequential Uncoating. *J Biol Chem* **287**, 31582-31595, (2012).
- 29 Li, Y. Y. *et al.* Control of virus assembly: HK97 "Whiffleball" mutant capsids without pentons. *Journal of Molecular Biology* **348**, 167-182, (2005).
- 30 Newcomb, W. W. *et al.* Structure of the Herpes-Simplex Virus Capsid - Molecular Composition of the Pentons and the Triplexes. *Journal of Molecular Biology* **232**, 499-511, (1993).
- 31 Carrasco, C. *et al.* DNA-mediated anisotropic mechanical reinforcement of a virus. *P Natl Acad Sci USA* **103**, 13706-13711, (2006).
- 32 Carrasco, C., Castellanos, M., de Pablo, P. J. & Mateu, M. G. Manipulation of the mechanical properties of a virus by protein engineering. *P Natl Acad Sci USA* **105**, 4150-4155, (2008).
- 33 Snijder, J. *et al.* Probing the biophysical interplay between a viral genome and its capsid. *Nat Chem* **5**, 502-509, (2013).
- 34 Ionel, A. *et al.* Molecular Rearrangements Involved in the Capsid Shell Maturation of Bacteriophage. *J Biol Chem* **286**, 234-242, (2011).
- 35 Carrillo-Tripp, M. *et al.* VIPERdb2: an enhanced and web API enabled relational database for structural virology. *Nucleic Acids Res* **37**, D436-442, (2009).
- 36 Ortega-Esteban, A. *et al.* Monitoring dynamics of human adenovirus disassembly induced by mechanical fatigue. *Sci Rep-Uk* **3**, (2013).

- 37 Sae-Ueng, U. *et al.* Major capsid reinforcement by a minor protein in herpesviruses and phage. *Nucleic Acids Res* **42**, 9096-9107, (2014).
- 38 Hernando-Perez, M., Lambert, S., Nakatani-Webster, E., Catalano, C. E. & de Pablo, P. J. Cementing proteins provide extra mechanical stabilization to viral cages. *Nat Commun* **5**, (2014).
- 39 Kang, S., Hawkrige, A. M., Johnson, K. L., Muddiman, D. C. & Prevelige, P. E., Jr. Identification of subunit-subunit interactions in bacteriophage P22 procapsids by chemical cross-linking and mass spectrometry. *Journal of proteome research* **5**, 370-377, (2006).
- 40 Llauro, A. *et al.* Mechanical Stability and Reversible Fracture of Vault Particles. *Biophys J* **106**, 687-695, (2014).
- 41 Ortega-Esteban, A. *et al.* Minimizing tip-sample forces in jumping mode atomic force microscopy in liquid. *Ultramicroscopy* **114**, 56-61, (2012).
- 42 Sader, J. E., Chon, J. W. M. & Mulvaney, P. Calibration of rectangular atomic force microscope cantilevers. *Rev Sci Instrum* **70**, 3967-3969, (1999).
- 43 Horcas, I. *et al.* WSXM: A software for scanning probe microscopy and a tool for nanotechnology. *Rev Sci Instrum* **78**, (2007).

Structural Dissection of a Temperature-Induced Transition of a Viral Capsid by Hydrogen-Deuterium Exchange Mass Spectrometry

Based on:

M. van de Waterbeemd*, **A. Llauro***, J. Snijder, A. Valbuena, A. Rodríguez-Huete, M. A. Fuertes, P. J. de Pablo, M. G. Mateu, A. J.R. Heck. Monitoring a temperature-induced structural transition of a viral capsid by hydrogen-deuterium exchange. Submitted. *These authors contributed equally to the work.

Abstract

Protein assemblies, including viruses and virus capsids, are highly dynamic structures. Not only do they undergo concerted structural reorganizations in response to changes in the environment, they are also constantly subjected to thermally driven conformational fluctuations. Icosahedral viral capsids are made of a large number of symmetrically organized protein subunits whose local movements cause global structural reorganizations that are known to play an essential role in viral infection. In the capsid of the minute virus of mice, a conformational rearrangement is associated with molecular translocation events required for viral infection. *In vitro*, this transition can be reversibly induced by mild heating of the capsid, but little is known about the capsid regions involved. We used a modified form of hydrogen-deuterium exchange coupled to mass spectrometry (HDX-MS) at varying temperatures to structurally dissect the dynamics of the MVM capsid. Our data revealed that capsid pores through which the viral genome is packaged and peptide signals are externalized during viral infection, are among the most dynamic capsid regions at equilibrium at any temperature. Remarkably, the results also indicate that the transition associated with peptide translocation involves a global conformational change of the capsid leading to structural alterations in regions distant from the pores. These alterations are reflected in both an increased dynamics of some secondary structure elements in the capsid shell from which the spikes protrude, and a decreased dynamics of long intertwined loops that form large capsid spikes. More generally, this study demonstrates the potential of HDX-MS to explore in detail temperature-dependent structural dynamics in large macromolecular protein assemblies.

Introduction

Non-enveloped virus particles include multiple copies of one or a small set of proteins organized in a highly symmetrical capsid that encloses the viral genome. The structures of these large macromolecular assemblies at the atomic level, obtained mainly by X-ray crystallography or cryo-electron microscopy, have contributed enormously to the understanding of these complex, hierarchical biological systems.¹⁻³ However, the structures depicted by these techniques may be somewhat deceptive. Viruses are not a static ensemble of atoms with a fixed position over time, but highly dynamic structures that constantly fluctuate around an average conformation at equilibrium as a result of thermal energy. These fluctuations are commonly termed ‘breathing’, and represent an important feature in virus dynamics, playing a role in the infection process.⁴ In addition, changes in physicochemical conditions or the action of specific biomolecules *in vivo* can modify the energy landscape, leading to structural transitions between different states separated by an energy barrier.⁴⁻⁷ Characterization of these and other biologically relevant structural transitions (typically characterized by longer time scales) require specific physicochemical conditions, such as a particular range of temperatures, that frequently fall beyond the technical limits of current high-resolution structural methods.

The minute virus of mice (MVM) represents an excellent model system for studying functionally relevant motions and rearrangements in large protein complexes. MVM is a non-enveloped single-stranded DNA (ssDNA) parvovirus with a T=1 icosahedral capsid made of 60 equivalent subunits which share a same sequence and fold, except for the length of their structurally disordered N-terminal segments (Nt) (Figure 1A).⁸ VP2 is the most abundant capsid protein. VP1 is an extended form of VP2 and has a longer Nt, whereas in VP3 the Nt of VP2 has been shortened by proteolytic cleavage during virus entry into a host cell. The Nts of VP2 and VP1, initially buried in the capsid, contain molecular signals that are required during various stages of the infection cycle. They are then externalized through capsid pores located at the 5-fold symmetry axes (Figure 1B).⁹⁻¹⁵ These pores are also involved in packaging and ejection of the viral ssDNA.^{16,17} Recombinant VP2 capsid proteins are able to assemble into DNA-free virus-like particles (VLPs) that are structurally nearly indistinguishable from natural empty MVM capsids, except for the absence of the disordered VP1 Nts.¹⁸ These VLPs have been used as a model system to explore the structural

determinants of MVM capsid assembly, its physical properties and function.¹⁷⁻²⁷ The biologically required externalization of VP2 Nts, triggered *in vivo* by DNA encapsidation,¹³ can be mimicked *in vitro* by mild heating of the VLPs above approximately 45°C.^{19,20} The temperature-dependent transition causes a subtle, reversible cooperative conformational rearrangement that involves slight changes in the degree of solvent exposure of some tryptophan residues which can be measured by spectrofluorometry.²⁰ Previous attempts to characterize this conformational rearrangement by conventional methods has been hampered by the required heating conditions. In this work we use the MVM system to show the value of a modified form of hydrogen-deuterium exchange coupled to mass spectrometry (HDX-MS).²⁸⁻³³ to structurally dissect a viral conformational rearrangement by probing local variations in capsid dynamics with temperature.

HDX-MS has been previously used to study equilibrium dynamics, (un)folding, structural transitions and protein-protein and protein ligand interactions of numerous soluble and membrane embedded small proteins and protein complexes.³⁴⁻⁴⁰ It has proven most valuable to obtain information on the structure and dynamics of virus capsids, complementing and expanding the more static pictures obtained by X-ray crystallography or cryo-EM.⁴¹⁻⁴⁴ The potential of HDX-MS to distinguish not only the dynamic behavior of different regions of a protein, but also between multiple subpopulations of the protein ensemble provides complementary information to other dynamic techniques like nuclear magnetic resonance (NMR) spectroscopy.⁴⁵ Added to this, the reduced sample consumption and tolerance (mainly the absence of an upper size limit) make HDX-MS a popular and powerful tool in structural biology.

In this study we have performed HDX-MS experiments over a range of temperatures to study local variations in dynamics of the MVM capsid along its heat-induced structural rearrangement. First, we studied capsid dynamics in the basal state (at 0°C) and show that structural elements important for virus infectivity, such as the pore region or the Nts, present the fastest exchange. Second, we monitored the deuterium uptake at increasing temperature to determine region-specific temperature-dependent changes in capsid dynamics. Our results show that the cooperative transition required for viral infection and associated to

translocation events to the capsid pores is not constrained to the vicinity of the pores, but involves a global rearrangement of the capsid.

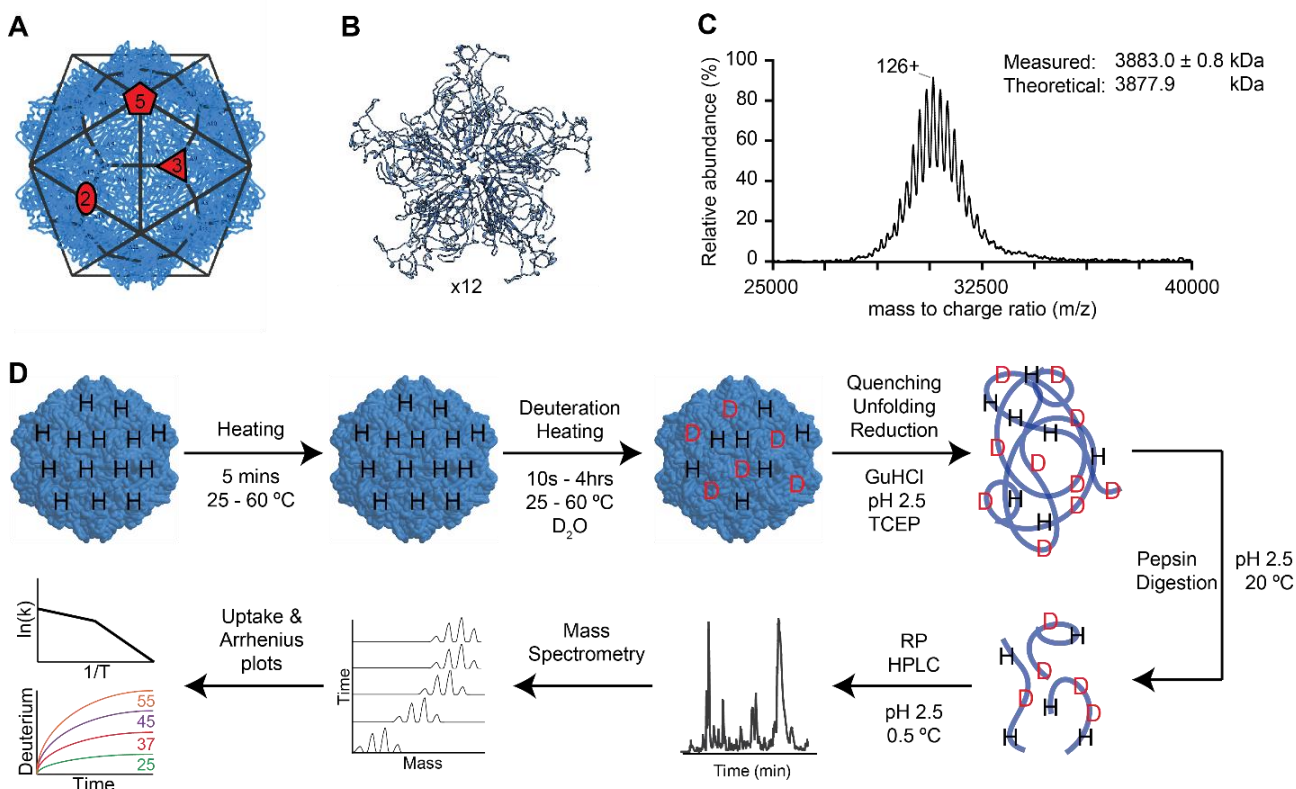


Figure 1. The MVM capsid and HDX-MS experimental setup. a) The MVM capsid structure (PDB ID 1Z14¹⁸) exhibits a icosahedral $T = 1$ symmetry. The black lines delimit the 60 VP2 subunits. The icosahedral symmetry axis (5-fold, 3-fold, 2-fold) are labeled. b) Five VP2 subunits (shown as ribbon models surround a 5-fold axis pore (center) through which translocation of peptide segments and viral DNA occurs during viral infection. The capsid contains 12 such pores. c) Native mass spectrum of the intact MVM VLPs. A well-resolved series of charge states reveals a mass of 3883 kDa, confirming that the capsid consists of 60 copies of the 64 kilo-Dalton VP2 capsid protein. d) Schematic representation of the modified HDX approach used. The uptake of deuterium by the capsid protein backbone is monitored as a function of time at varying incubation temperatures around the transition temperature.

Materials and Methods

Expression and Purification of VLPs of MVM

Bacmid BM-VP2²⁰ was used for the production of VLPs of MVM in H-5 insect cells. VLPs were purified as previously described¹⁹ with minor modifications. VLP preparations were

extensively dialyzed against phosphate-buffered saline. Capsid purity and integrity were assessed by electrophoresis and electron microscopy.

Spectrofluorometry of VLPs

The heat-induced conformational transition of the VLP associated to Nt externalization was initially probed by following the variation in intrinsic Trp fluorescence in thermal gradients as previously described.²⁰ Reversibility of the conformational rearrangement was ascertained by repeated fluorescence analysis after heating to a controlled maximum temperature (60°C) and cooling. Capsid dissociation was observed only at high (75°C) temperatures.²⁰

Native MS

Native MS samples were prepared by exchanging the buffer in which purified VLPs were obtained for aqueous ammonium acetate using multiple concentration and dilution steps with a centrifuge filter (Millipore). For the experiments shown in [Figure 1](#), samples were prepared in 100 mM Ammonium acetate pH 7.4 and kept on ice. For control experiments under HDX conditions, samples were heated at 60°C and spectra were acquired at multiple time points. Before injection into the mass spectrometer, low amounts of triethylammonium acetate were added. Mass spectrometry experiments were performed on a modified QToF II (MS Vision; Waters, U.K.)⁴⁶, operating at 10 mbar source pressure, 1300–1500 V capillary voltage, 100 V cone voltage, 300 V collision energy with 2×10^{-2} mbar pressure in the collision cell using xenon as collision gas.⁴⁷ Tandem mass spectrometry experiments were acquired by full envelope selection and fragmentation using a 400 V potential over the collision cell. Aliquots of the samples were introduced in the mass spectrometer through nano-electrospray ionization using gold coated boro-silicate capillaries produced in-house. All data was analyzed using Masslynx 4.1 software (Waters).

Hydrogen-Deuterium Exchange MS

Fluorometry studies showed that the structural transition is complete for most of the particles within a time of 5 minutes at $>50^\circ\text{C}$.²⁰ Aliquots of MVM VLPs of 3 $\mu\text{g}/\text{ml}$ and D_2O (99.99% deuterium content) were heated separately at different temperatures (25, 37, 45, 50, 55, 60

°C) for 5 minutes prior to the start of the exchange reaction. The exchange reaction was initiated by addition of the D₂O (98% of deuteration) and during the reaction heating was maintained. Reactions were quenched at set time points (10, 30, 60, 600, 1800, 3600 and 14400 seconds) by rapid addition of ice-cold quench solution (100 mM TCEP and 2M Guanidine HCl at pH 2.5). Immediately after quenching, the samples were injected into a Waters HDX / nanoAcquity system for digestion on an online pepsin column operating at 100 µL/min and 25°C, followed by separation on a 10 minute reverse phase UPLC gradient at 0.5°C and MS on a Waters Xevo QToF G2. Acquisition of HDX of MVM without heating was performed identically but samples were incubated on ice (at 0°C). All experiments at all temperatures were performed in triplicate. Identification of peptides was performed by dilution in H₂O and using MS^E data acquisition. 83 peptides covering 80% of the sequence were identified for the experiments performed at 0°C. For VP2 regions covered by more than one peptide the criteria were that the shortest peptides would be selected for the analysis, always ensuring that redundant information was consistent. This led to a subset of 51 peptides, representing the same 80% sequence coverage. For the experiments performed at increasing temperature 69 different peptides could be identified (over the entire temperature range) with a sequence coverage of 70%. From those, a subset of 35 peptides were used for the analysis. The criteria for selecting them was the same than before. Data for peptide identification was processed with ProteinLynx Global Server 2.5 software. Deuterium uptake was calculated compared with the control samples in H₂O using Waters DynamX 3.0 software.

MS under Denaturing Conditions

To acquire spectra of denatured VP2, samples were introduced in the Waters HDX / nanoAcquity system without pepsin digestion. Spectra were deconvoluted using MaxEnt algorithm in Masslynx 4.1 software (Waters).

Data Analysis

Uptake plots. Time courses of the number of deuterons incorporated at each temperature were plotted for the different peptides and, following procedures described earlier ³¹, fitted to two exponential equation

$$D = N - A_1 e^{-k_1 t} - A_2 e^{-k_2 t} \quad [1]$$

where D is the number of deuterons observed at time t, N equals the maximal deuteration that exchange within the time range of the experiment, A₁ is the number of amide Hs exchanging with fast kinetic rate constant (k₁~10min⁻¹) and A₂ the number of amide Hs exchanging with a slow rate constant (k₂~0.001min⁻¹). To determine the non-exchange amides the total number of exchangeable sites was subtracted from the sum of the detected exchangeable sites (i.e., A₁ + A₂). The total number of exchangeable sites was calculated by subtracting the N terminus and the number of prolines from the peptide length and multiplying it by 0.98 (% deuterium in the solvent). Profiles were fitted without considering back exchange or artifactual in-exchange (burst phase), as previously done by Monroe *et al.*⁴³ Due to rapidity of the exchange values from the fitting (k₁, k₂, A₁, A₂) for some of the peptides did not converge, and significant data could not be obtained from those fits. Therefore, we decided to base our analysis on the different deuteration levels that were reached over time at increasing temperature. To estimate the average enthalpy change (ΔH) for local rearrangement, ΔH_{avg}^o, we followed the procedure described in Oyeyemi *et al.*⁴⁸ The number of exchanged amide hydrogens at 4h was normalized to the total exchangeable amides (N_T, $\sqrt{N_{4h}}$). Plots of ln(N_T, $\sqrt{N_{4h}}$) as a function of 1/T for each peptide were linearly fitted to determine the average using Origin Pro 8.5.1. The same protocol was used for all the peptides despite the fact some of them did not reach a steady plateau at 4h (for example, peptide 248-255). We had to limit our analysis at 4 hours because data at 18 hours timepoints (not shown) showed great variation within the technical replicates. Nonetheless, native MS at 60°C for >5h confirmed the stability of the particles under HDX-MS conditions. Capsid dissociation occurs only at a temperature of 70-80°C.^{19,20} We should mention that defining an average enthalpy (ΔH_{avg}^o) for peptides not presenting a steady plateau is not accurate, as the equilibrium state might have not been reached. However, for simplicity we used the same thermodynamic protocol for all the peptides, which allowed us to systematically compare the energetic barriers of the different regions of the capsid.

Data fitting to a two-state transition. The transition temperature was determined by fitting the data to a two-state transition.²⁰ Thermodynamics parameters ($T_M, \Delta H_{T_M}^\ddagger$) were obtained

by nonlinear fitting of the experimental number of deuterons or fluorescence intensity, as previously done by Carreira et al.²⁰ For HDX-MS experiments, all peptides showing a linear increase in uptake were fitted, and the ones showing square r values of 0.99 or higher (11 peptides) were used for the calculation of the average T_m . The values of the transition enthalpy, ΔH^{TM} , were subjected to large errors hampering an accurate estimation.

Results and Discussion

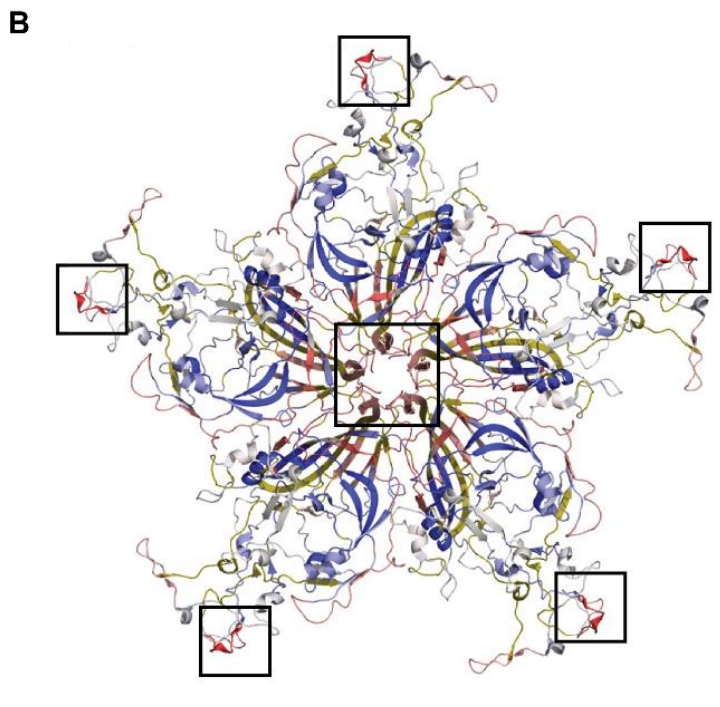
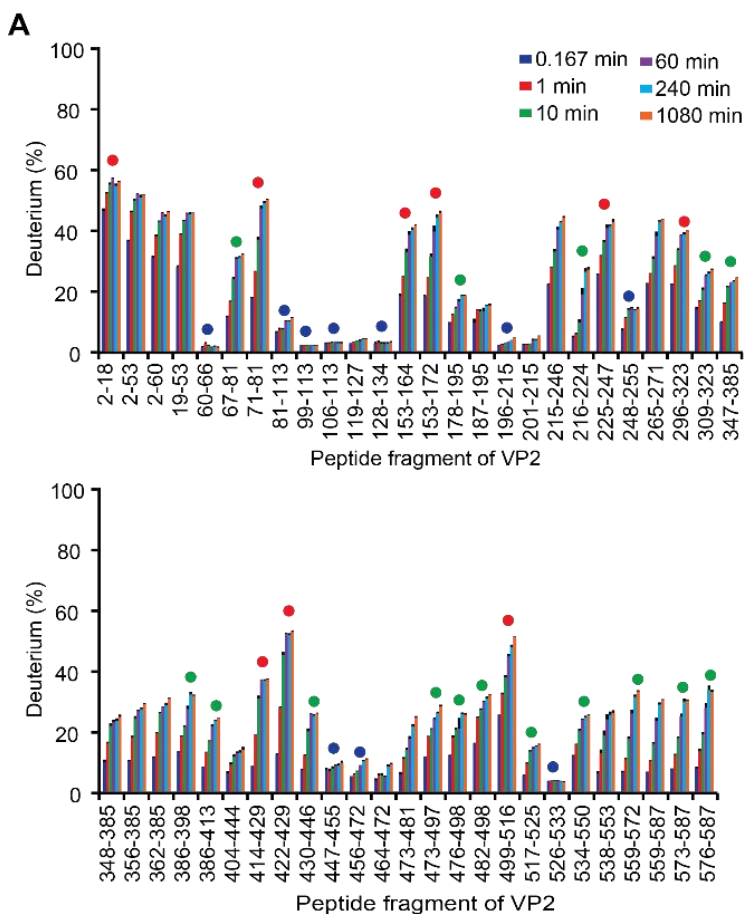
The general workflow of the temperature-dependent HDX experiments described in this paper is shown in [Figure 1D](#). It follows the procedure previously described by *Oyeyemi et al.*⁴⁸ and *Liang et al.*⁴⁹ to characterize temperature dependent changes in thermophilic enzymes. Overall the approach is similar to most other HDX experiments but includes additional sample preparation and data analysis steps. Prior to HDX analysis, we verified both the composition and stoichiometry of the purified VLPs using native mass spectrometry ([Figure 1C](#)). In these spectra a well-resolved series of charge states was detected around 30,000 m/z, which was assigned to a mass of 3883.0 ± 0.8 kDa, corresponding well with the expected mass of 60 copies of the monomeric VP2 protein: 3877.9 kDa. The mass of the VP2 monomer was determined by LC-MS under denaturing conditions ([Figure S1-B](#)). The oligomeric state was additionally confirmed using tandem MS experiments ([Figure S1-A](#)). Having verified the integrity of the VLPs, we performed HDX analysis ([Figure 1D](#)). Samples stored in protiated buffer were heated in parallel with a large volume of D₂O for 5 minutes. The solutions were subsequently mixed at a ratio that reached 98% deuterium content and continuously heated over different periods of time during which backbone amide hydrogens could exchange with deuterium from the buffer. After stopping the reaction with a quench solution, proteins were denatured and reduced and this mixture was loaded onto a HPLC system. The peptides that resulted from the digestion were separated and analyzed by the coupled mass spectrometer, after which the uptake time courses were measured.

Structural Elements Involved in Basal "Breathing" of the MVM Capsid

In previous structure-function studies, mutant MVM particles were compared with wild-type particles using spectrofluorometry, atomic force microscopy (AFM) and infectivity assays.^{21,26} Mutation of residues located around the base of the 5-fold axes pores abolished viral infectivity, impaired the transition observed by fluorometry, and showed a highly increased mechanical stiffness at the pore regions.^{21,26} Other studies showed that viral ssDNA segments bound to the capsid inner wall in the native MVM virion confer a higher resistance to thermal inactivation of its infectivity by increasing the mechanical stiffness of the capsid around the 2-fold and 3-fold axes (relative to mutant virions in which some of the capsid-DNA interactions had been removed).^{22-24,27} However, this biologically advantageous stabilization of the virion was achieved while specifically preserving the mechanical stiffness of the capsid around the 5-fold axis pores. Together, the above results indicated that the distribution of mechanical stiffness and conformational dynamics of the MVM virion and its capsid are essential for virus survival.

To directly investigate the equilibrium dynamics ('breathing') of different regions of the MVM capsid in its basal state, we performed HDX-MS experiments at 0°C without prior heating (Figure 2). Results provided a high-resolution map of the level of exposure to solvent of different capsid regions over time, revealing different kinetics in the regions represented by different peptides (Figure 2A). We classified the capsid peptides into three different groups according to their level of deuterium uptake after one hour: from 0 to 15% (blue dot), from 16% to 34% (green dot) and from 35 to 100% (red dot). Figure 2B shows the deuterium uptake level after one hour, color-coded on the crystal structure of the VLP (PDB ID 1Z14).¹⁸ The most dynamic capsid regions correspond to the Nt of the capsid protein subunits (located at the capsid interior and not visible in the crystal structure), some highly exposed loops at the tips of the 3-fold spikes and, interestingly, the structural elements forming the capsid pores at the 5-fold axis. These results provide direct proof for intense conformational fluctuations at equilibrium (breathing) in the capsid pore regions that are involved in translocation events during MVM infection.

Figure 2. Deuterium uptake by the MVM capsid at 0°C. a) Uptake of deuterium for a selection of peptides at different time points expressed as a fraction of the maximum uptake. Dots indicate the classification of the peptide after 1 hour of exchange with high uptake as red, medium uptake as green and low uptake as blue. b) Mapping of the peptide uptake levels after 1 hour on the capsid structure. For simplicity, only five subunits surrounding a capsid pore (center) are represented. The level of exposure from the highest to the lowest percentage is colored as red-white-blue, respectively. Capsid regions that could not be probed are shown in yellow. Squares indicate the most dynamic regions of the capsid.



Structural Dissection of Changes in MVM Capsid Dynamics during a Conformational Transition Associated to Biologically Relevant Translocation Events

A limitation of fluorescence spectroscopy is that it does not provide any detailed information about the structural elements and residues involved in the transition. In contrast, the peptide resolution offered by HDX-MS leads to a powerful approach to compare specific changes in the dynamics of different regions in the viral particle around the transition temperature. In this way structural elements involved in this transition could be identified. Purified VLPs aliquots were incubated between 10 seconds and 4 hours at 6 different temperatures (25, 37, 45, 50, 55 and 60 °C). An initial examination of the HDX time course plots at different temperatures revealed conspicuous differences between peptides that suggest region-dependent variations in dynamics. A representative set of these distinct behaviors is shown in [Figure 3A](#) (left column), where the time course plots of four different peptides are shown. Some peptides are characterized by a rapid exchange rate that was not dependent on temperature (i.e., 153-164), whereas others present increasing deuteration levels at increasing temperatures (i.e., 169-215, 178-195, and 248-255). Noticeably, for some peptides (i.e., 178-195 and 248-255) the deuteration level changes abruptly at temperatures close to the reported T_M of the capsid conformational change detected by fluorescence and associated to Nt externalization through the pores. To test whether these abrupt changes in dynamics could be associated to this transition, we fitted our HDX data to a unimolecular two-state transition in the same way that it had been done in fluorescence spectroscopy experiments.²⁰ Nicely, the T_M obtained by fluorescence ($47.2 \pm 0.3^\circ\text{C}$, [Figure 3B](#)) or by HDX-MS experiments ($\langle T_m \rangle 48 \pm 1^\circ\text{C}$, [Figure 3C](#)) were indistinguishable. Thus peptides with abrupt changes in dynamics around the T_M of the translocation-associated transition observed by fluorescence can be used as markers to identify capsid regions that are structurally altered during this transition, as described below.

To systematically analyze and quantify this conformational rearrangement in structural detail we carried out a thermodynamic analysis of the changes in dynamics of individual capsid peptides. Previous studies showed that it is possible to determine the energy barrier associated with the reversible internal motions of a small monomeric enzyme (tens of kDa) using HDX-MS as a function of temperature (see supplemental for theoretical background).^{48,49}

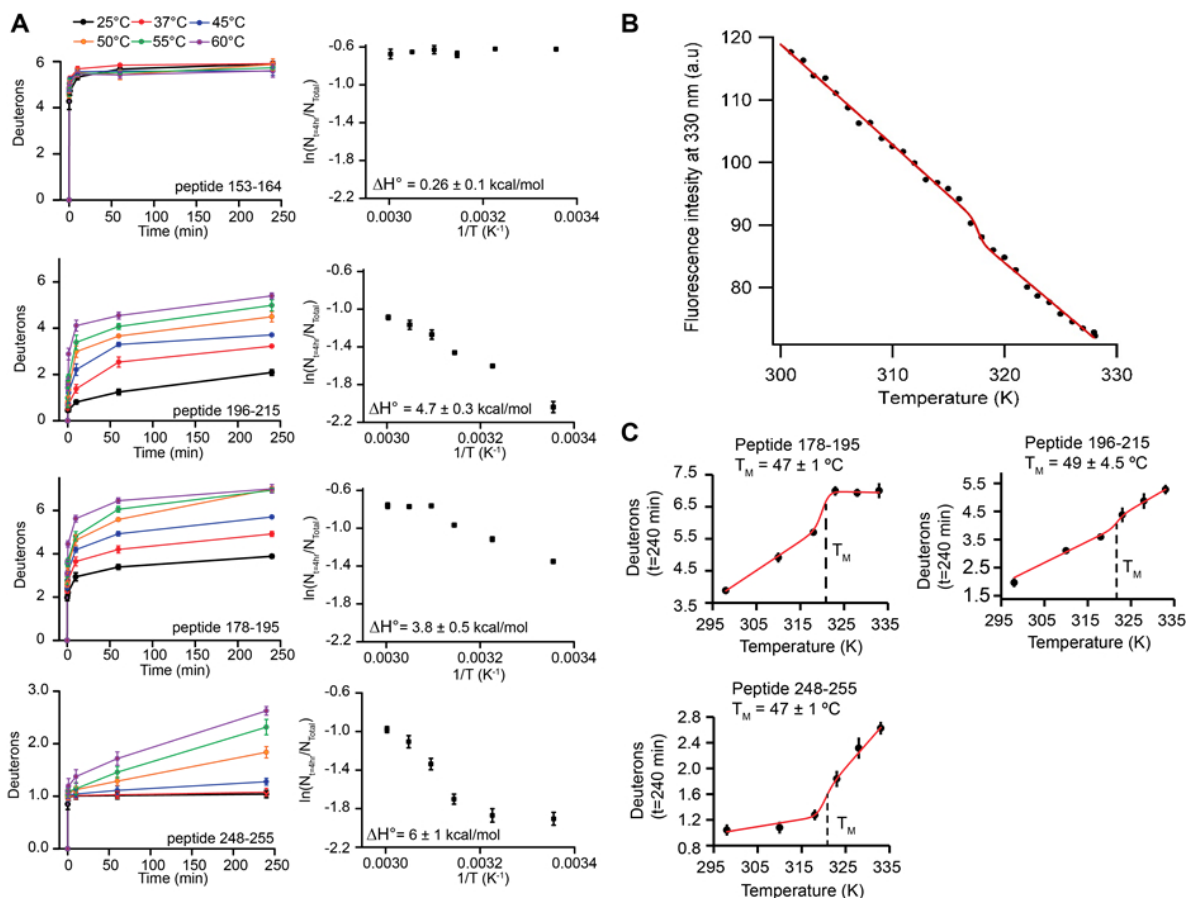


Figure 3. Probing the heat-induced transition of the MVM capsid by fluorescence and HDX-MS. (a) HDX time course plots of 4 representative peptides (left) and plots of $\ln\left(\frac{N_{t=4hr}}{N_{TOTAL}}\right)$ as a function of $\frac{1}{T}$ (right). From these plots the different average enthalpy (ΔH°) can be determined for that specific region. (b) Tryptophan-specific fluorescence of the MVM VLPs as a function of temperature. Data (dots) were fitted to a two-state transition (solid line). (c) HDX uptake plots of the number of deuterons exchanged at $t=4$ hours as a function of the temperature. Data (dots) were fitted to a two-state transition (solid line).

Plots of the log of the relative uptake after four hours, $\ln\left(\frac{N_{t=4hr}}{N_{TOTAL}}\right)$, against the inverse of the temperature ($1/T$) provide information about the average ΔH required to expose all the amide sites of each peptide (Figure 3A, right column). A peptide that exposes most of its amide sites at low temperature will present a single plateau and its average ΔH would be almost negligible (for example, 153-164). In contrast, a peptide whose amide hydrogen are protected at low temperature but become exposed at higher temperatures would reach different plateaus

and present higher ΔH values (i.e., peptide 169-215, 178-195 and 248-255). In principle, the observed increase in amide exposure of these more protected regions could be a fingerprint of higher dynamics, but it could also arise as a consequence of a loss of capsid integrity at higher temperatures. To verify that the capsids would not fall apart during heating in the HDX buffer, we acquired native MS spectra of MVM capsids under identical conditions. Even over an extended period of time (>5h) at 60 °C, the spectrum does not appear different from the spectrum acquired at basal temperature. This corroborates that the integrity of the particles were maintained even at the highest temperatures tested (Figure S1-C). It was also important to ascertain that the conformational transition probed was reversible. Fluorescence assays showed that after heating and cooling the sample from 27°C to 61°C (while waiting 30 min at the highest temperature), particles not only maintained their integrity but also kept their ability to undergo the temperature-induced conformational change (results not shown), which corroborates the reversibility of the process.

To identify which regions undergo the most abrupt changes in deuterium incorporation after the transition, we plotted the average ΔH from 25°C to 45°C ($\Delta H_{25^{\circ}\text{C}-45^{\circ}\text{C}}^{\circ}$) versus the average ΔH from 50°C to 60°C ($\Delta H_{50^{\circ}\text{C}-60^{\circ}\text{C}}^{\circ}$) (Figures 4A and S2). With this approach, peptides showing a similar uptake before and after the transition would fall in a region represented by a line of slope $m=1$ (region 2); peptides showing an increase in dynamics after the transition fall above this line (region 1); and peptides showing a reduced dynamics after the transition fall below the same line (region 3). Region 4 contains peptides presenting a faster exchange (red), with an average ΔH that was mostly negligible. Any transition-associated increase in equilibrium dynamics of these peptides, which include the disordered Nts within the capsid and the five long β -hairpins that delimit each capsid pore, was beyond the range of our experiments, as exchange was nearly complete even at the shortest times that could be reliably tested. Peptides 414-429 and 422-429 also belong to this fast-exchange group and deserve some mention. They correspond to an exposed loop situated close to the tip of each 3-fold spike, and present a 10-fold higher average ΔH before than after the transition. However, two-state fittings for these two peptides suggest that the abrupt increase in HD exchange occurs before the transition temperature. Indeed, peptide 422-429 had exchanged 80% of their N-H sites at 45°C, a value that remained constant at increasing temperatures, indicating that a structural change in this loop is not associated with the global transition.

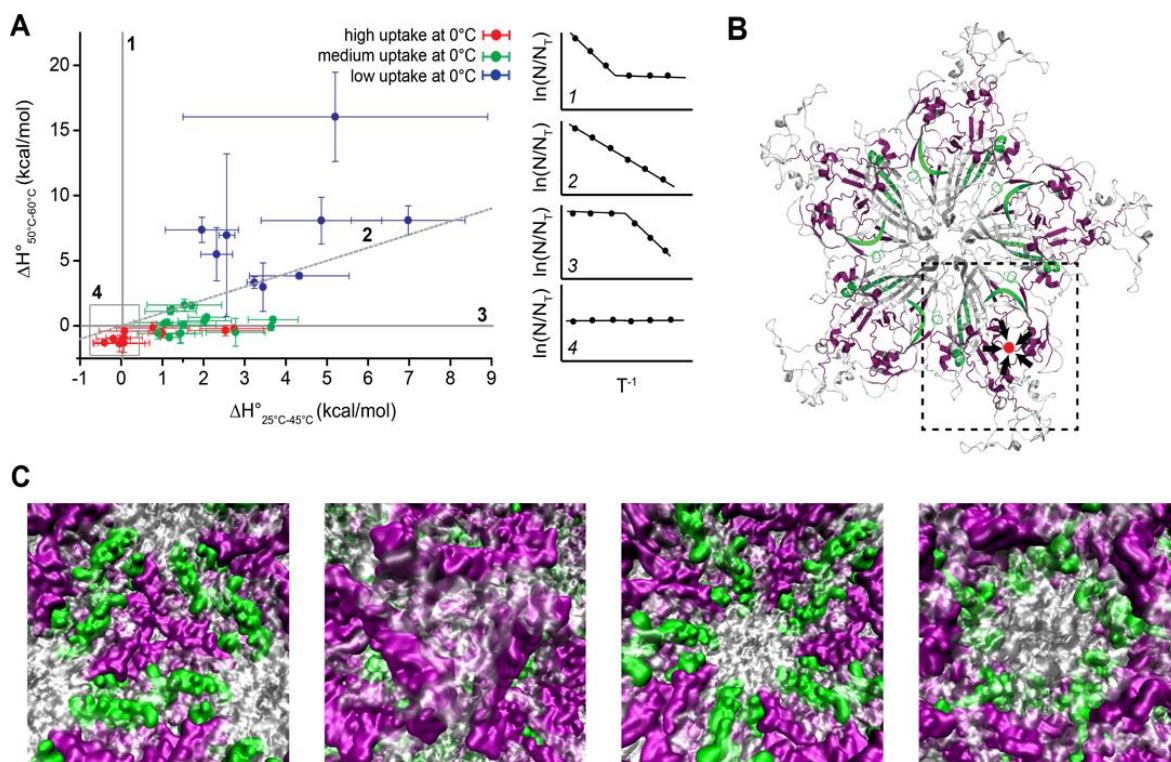


Figure 4. Peptides that present an abrupt change in dynamics around the heat-induced conformational transition of the MVM capsid. (a) Plot showing the average enthalpy change of each peptide before ($\Delta H^{\circ}_{25^{\circ}\text{C}-45^{\circ}\text{C}}$) and after ($\Delta H^{\circ}_{50^{\circ}\text{C}-60^{\circ}\text{C}}$) the transition (defined by the transition temperature T_M). Four regions were identified: increased deuteration after T_M (region 1), decreased deuteration after T_M (region 3) and no change in deuteration after T_M (region 2 and 4). The color indicate the dynamics of the peptides in the basal state ($T=0^{\circ}\text{C}$). (b) Peptides presenting an abrupt change in deuterium uptake are mapped in the MVM capsid structure. For simplicity, only five capsid subunits surrounding a pore are represented. In green are shown peptides that expose more residues after the transition (region 1) and, in purple, peptides that stop the incorporation (region 3). The inset square delimits a region of a capsid subunit close to the 3-fold axes where there is a substantial reduction in dynamics after T_M . Peptides 178-195 and 347-385, which present the most significant changes, are located in the inner core of this cavity. (c) Detailed view of a 3- and 5-fold symmetry axis. The inner part of the capsid (left of each symmetry) and outer part of the capsid (right of each symmetry). The peptides that become more exposed after T_M (green) are located in the inner part of the capsid.

Peptides presenting the most significant differences in dynamics associated with the transition (either increased dynamics, region 1, or decreased dynamics, region 3) were sorted and are listed in [Table S1](#) (see [Figure S2](#) for the criteria followed). Mapping of these selected peptides in the capsid structure (Figures 4b and 4c) revealed local conformational changes in multiple capsid regions that can be collectively described as follows:

i) Capsid regions with transition-associated conformational rearrangements leading to abruptly increased local dynamics during the global transition. They include three β -strands and two very short α -helices of each capsid subunit. With the exception of one of these strands (which is buried along the spike wall), these secondary structure elements form a part of the β -sandwich fold of each capsid protein subunit from which long peptides protrude to form the capsid spikes. Region 1 peptides defining these regular secondary structure elements involve about one-tenth of the capsid amino acid residues.

ii) Capsid regions with transition-associated conformational rearrangements leading to abruptly decreased local dynamics during the global transition. They include substantial portions of several long, convoluted loops of each capsid subunit that generally define parts of the thick walls of the spikes centered at the capsid 3-fold axes, away from the pores at the capsid 5-fold axes. Region 3 peptides defining these structural elements with abruptly decreased dynamics involve as many as one-fourth of the capsid amino acid residues.

To summarize, the structural transition associated with translocation events through capsid pores required for MVM infectivity is not limited to the vicinity of the pores. It involves a global conformational rearrangement of the capsid that substantially alters its equilibrium dynamics in a complex, region-dependent way.

Conclusions

In this work we have used HDX-MS to identify, with high spatial resolution, structural changes in the MVM capsid that are required for viral infection. Transition-associated, abrupt changes in local dynamics of peptide segments in the capsid served as markers to identify structural elements that modified their conformation during the transition. The results revealed that translocation events through capsid pores, that occur during the infection cycle, involve a global structural rearrangement of the capsid. Many of the elements showing altered conformations were located far from the pores, and included loops with abruptly decreased dynamics as well as regular secondary structure elements that showed marked increase in dynamics. This study provides a novel demonstration of the potential of HDX-

MS to structurally dissect functionally relevant, temperature-dependent structural transitions in viruses and other large macromolecular protein assemblies. Being able to probe structural dynamics of quite specific regions in virus particles may also facilitate the development of novel antiviral drugs aimed at impairing conformational transitions required for viral infection.

References

- 1 *Structural Virology*. (RSC Publishing, 2011).
- 2 *Viral Molecular Machines. Advances in Experimental Medicine and Biology*. Vol. 726 (Springer, 2012).
- 3 *Structure and Physics of Viruses*. (Springer, 2013).
- 4 Bothner, B. & Hilmer, J. K. in *Structural Virology* (eds M. Agbandje-McKenna & R. McKenna) 41-61 (RSC Publishing, 2011).
- 5 Johnson, J. E. Virus particle dynamics. *Adv Protein Chem* 64, (2003).
- 6 Johnson, J. E. Virus particle maturation: insights into elegantly programmed nanomachines. *Curr Opin Struc Biol* 20, 210-216, (2010).
- 7 Veesler, D. & Johnson, J. E. Virus Maturation. *Annu Rev Biophys* 41, 473-496, (2012).
- 8 Agbandje-McKenna, M., Llamas-Saiz, A. L., Wang, F., Tattersall, P. & Rossmann, M. G. Functional implications of the structure of the murine parvovirus, minute virus of mice. *Struct Fold Des* 6, 1369-1381, (1998).
- 9 Cotmore, S. F., D'Abramo, A. M., Ticknor, C. M. & Tattersall, P. Controlled conformational transitions in the MVM virion expose the VP1 N-terminus and viral genome without particle disassembly. *Virology* 254, 169-181, (1999).
- 10 Lombardo, E., Ramirez, J. C., Garcia, J. & Almendral, J. M. Complementary roles of multiple nuclear targeting signals in the capsid proteins of the parvovirus minute virus of mice during assembly and onset of infection. *J Virol* 76, 7049-7059, (2002).
- 11 Maroto, B., Valle, N., Saffrich, R. & Almendral, J. M. Nuclear export of the nonenveloped parvovirus virion is directed by an unordered protein signal exposed on the capsid surface. *J Virol* 78, 10685-10694, (2004).
- 12 Valle, N., Riolobos, L. & Almendral, J. M. In *Parvoviruses* (Edward Arnold, 2006).
- 13 Cotmore, S. F. & Tattersall, P. Parvoviral host range and cell entry mechanisms. *Adv Virus Res* 70, 183-232, (2007).
- 14 Cotmore, S. F. & Tattersall, P. Mutations at the Base of the Icosahedral Five-Fold Cylinders of Minute Virus of Mice Induce 3'-to-5' Genome Uncoating and Critically Impair Entry Functions. *J Virol* 86, 69-80, (2012).
- 15 Sanchez-Martinez, C., Grueso, E., Carroll, M., Rommelaere, J. & Almendral, J. M. Essential role of the unordered VP2 n-terminal domain of the parvovirus MVM capsid in nuclear assembly and endosomal enlargement of the virion fivefold channel for cell entry. *Virology* 432, 45-56, (2012).
- 16 Cotmore, S. F., Hafenstein, S. & Tattersall, P. Depletion of Virion-Associated Divalent Cations Induces Parvovirus Minute Virus of Mice To Eject Its Genome in a 3'-to-5' Direction from an Otherwise Intact Viral Particle. *J Virol* 84, 1945-1956, (2010).
- 17 Plevka, P. *et al.* Structure of a Packaging-Defective Mutant of Minute Virus of Mice Indicates that the Genome Is Packaged via a Pore at a 5-Fold Axis. *J Virol* 85, 4822-4827, (2011).

- 18 Kontou, M. *et al.* Structural determinants of tissue tropism and in vivo pathogenicity for the parvovirus minute virus of mice. *J Virol* 79, 10931-10943, (2005).
- 19 Hernando, E. *et al.* Biochemical and physical characterization of parvovirus minute virus of mice virus-like particles. *Virology* 267, 299-309, (2000).
- 20 Carreira, A., Menendez, M., Reguera, J., Almendral, J. M. & Mateu, M. G. In vitro disassembly of a parvovirus capsid and effect on capsid stability of heterologous peptide insertions in surface loops. *J Biol Chem* 279, 6517-6525, (2004).
- 21 Reguera, J., Carreira, A., Riobos, L., Almendral, J. M. & Mateu, M. G. Role of interfacial amino acid residues in assembly, stability, and conformation of a spherical virus capsid. *P Natl Acad Sci USA* 101, 2724-2729, (2004).
- 22 Reguera, J. *et al.* Functional relevance of amino acid residues involved in interactions with ordered nucleic acid in a spherical virus. *J Biol Chem* 280, 17969-17977, (2005).
- 23 Carrasco, C. *et al.* DNA-mediated anisotropic mechanical reinforcement of a virus. *P Natl Acad Sci USA* 103, 13706-13711, (2006).
- 24 Carrasco, C., Castellanos, M., de Pablo, P. J. & Mateu, M. G. Manipulation of the mechanical properties of a virus by protein engineering. *P Natl Acad Sci USA* 105, 4150-4155, (2008).
- 25 Castellanos, M., Perez, R., Carrillo, P. J. P., de Pablo, P. J. & Mateu, M. G. Mechanical Disassembly of Single Virus Particles Reveals Kinetic Intermediates Predicted by Theory. *Biophys J* 102, 2615-2624, (2012).
- 26 Castellanos, M. *et al.* Mechanical elasticity as a physical signature of conformational dynamics in a virus particle. *Proceedings of the National Academy of Sciences of the United States of America* 109, 12028-12033, (2012).
- 27 Castellanos, M., Carrillo, P. J. P. & Mateu, M. G. Quantitatively probing propensity for structural transitions in engineered virus nanoparticles by single-molecule mechanical analysis. *Nanoscale* 7, 5654-5664, (2015).
- 28 Zhang, Z. & Smith, D. L. Determination of amide hydrogen exchange by mass spectrometry: a new tool for protein structure elucidation. *Protein science : a publication of the Protein Society* 2, 522-531, (1993).
- 29 Konermann, L., Pan, J. & Liu, Y.-H. Hydrogen exchange mass spectrometry for studying protein structure and dynamics. *Chemical Society reviews* 40, 1224-1234, (2011).
- 30 Hamuro, Y. *et al.* Rapid analysis of protein structure and dynamics by hydrogen/deuterium exchange mass spectrometry. *Journal of biomolecular techniques : JBT* 14, 171-182, (2003).
- 31 Englander, S. W. & Kallenbach, N. R. Hydrogen exchange and structural dynamics of proteins and nucleic acids. *Quarterly reviews of biophysics* 16, 521-655, (1983).
- 32 Englander, J. J. *et al.* Protein structure change studied by hydrogen-deuterium exchange, functional labeling, and mass spectrometry. *P Natl Acad Sci USA* 100, 7057-7062, (2003).
- 33 Engen, J. R. Analysis of protein conformation and dynamics by hydrogen/deuterium exchange MS. *Analytical chemistry* 81, 7870-7875, (2009).

- 34 Bruning, J. B. *et al.* Partial agonists activate PPAR γ using a helix 12 independent mechanism. *Structure (London, England : 1993)* 15, 1258–1271, (2007).
- 35 Chung, K. Y. *et al.* Conformational changes in the G protein Gs induced by the beta2 adrenergic receptor. *Nature* 477, 611–615, (2011).
- 36 Gupta, S. *et al.* Local and global structural drivers for the photoactivation of the orange carotenoid protein. *P Natl Acad Sci USA*, (2015).
- 37 Houde, D., Peng, Y., Berkowitz, S. A. & Engen, J. R. Post-translational modifications differentially affect IgG1 conformation and receptor binding. *Molecular & cellular proteomics : MCP* 9, 1716–1728, (2010).
- 38 Lewis, H. A. *et al.* Structure and dynamics of NBD1 from CFTR characterized using crystallography and hydrogen/deuterium exchange mass spectrometry. *Journal of molecular biology* 396, 406–430, (2010).
- 39 Maegawa, G. H. B. *et al.* Identification and characterization of ambroxol as an enzyme enhancement agent for Gaucher disease. *The Journal of biological chemistry* 284, 23502–23516, (2009).
- 40 Shukla, A. K. *et al.* Visualization of arrestin recruitment by a G-protein-coupled receptor. *Nature* 512, 218–222, (2014).
- 41 Domitrovic, T. *et al.* Virus assembly and maturation: auto-regulation through allosteric molecular switches. *Journal of molecular biology* 425, 1488–1496, (2013).
- 42 Gertsman, I. *et al.* An unexpected twist in viral capsid maturation. *Nature* 458, 646–650, (2009).
- 43 Monroe, E. B., Kang, S., Kyere, S. K., Li, R. & Prevelige, P. E. Hydrogen/deuterium exchange analysis of HIV-1 capsid assembly and maturation. *Structure (London, England : 1993)* 18, 1483–1491, (2010).
- 44 Morton, V. L. *et al.* RNA-induced conformational changes in a viral coat protein studied by hydrogen/deuterium exchange mass spectrometry. *Physical chemistry chemical physics : PCCP* 12, 13468–13475, (2010).
- 45 Miranker, A., Robinson, C. V., Radford, S. E., Aplin, R. T. & Dobson, C. M. Detection of transient protein folding populations by mass spectrometry. *Science (New York, N.Y.)* 262, 896–900, (1993).
- 46 van den Heuvel, R. H. H. *et al.* Improving the performance of a quadrupole time-of-flight instrument for macromolecular mass spectrometry. *Analytical Chemistry* 78, 7473–7483, (2006).
- 47 Tahallah, N., Pinkse, M., Maier, C. S. & Heck, A. J. R. The effect of the source pressure on the abundance of ions of noncovalent protein assemblies in an electrospray ionization orthogonal time-of-flight instrument. *Rapid Commun Mass Sp* 15, 596–601, (2001).
- 48 Oyeyemi, O. A. *et al.* Temperature dependence of protein motions in a thermophilic dihydrofolate reductase and its relationship to catalytic efficiency. *P Natl Acad Sci USA* 107, 10074–10079, (2010).
- 49 Liang, Z. X., Lee, T., Resing, K. A., Ahn, N. G. & Klinman, J. P. Thermal-activated protein mobility and its correlation with catalysis in thermophilic alcohol dehydrogenase. *P Natl Acad Sci USA* 101, 9556–9561, (2004).

**Future Outlook and General Conclusions, Summarized Conclusions,
List of Publications & Acknowledgements**

General Conclusions and Future Outlook

Protein complexes are intricate. The work presented in this thesis focuses on the dynamics and mechanical properties of four protein complexes that represent interesting structures in nanotechnology because of the possibility of modifying their structure at will, besides their role in biology. The specificity of protein-protein interaction in a capsid is, in many instances, sufficient to govern the mechanical properties or dictate the organization of the shell. Understanding how the mechanical properties and dynamics are derived and how they change as a function of the environment or presence of cargo can direct the design on new protein-based nanodevices.

In **chapter 2** we showed that the mechanical properties of vault particles, similar in size to many virus capsids, are capable of recovering from fractures produced with only a few tens of piconewtons. These forces, in comparison with the breaking forces of most of virus shells,¹ are almost one order of magnitude lower. In addition, we found that the barrel of the structure governed the mechanical strength of the particles, and that continuum elastic theory represented an appropriate framework to interpret the stiffness and recovery times displayed by the particles. The particular set of mechanical properties of vaults might be the consequence of their labile and highly dynamic structure, which could be a requirement for their role in cellular transportation.² Interestingly, the other nanostructures that are known to display similar mechanical properties (at least to my knowledge) are microtubules. *Shcaap et al.*³ showed that indentations performed on microtubules presented hysteresis when the tip was retract while not trace of damage was observed in the subsequent images. Despite in their experiments there was no visual evidence of recuperation, the authors hypothesized that the phenomenon could be caused by a self-healing mechanism. A recent *in silico* AFM study performed on microtubules has captured the existence of this self-healing mechanism and showed that it consists of the reversible dissociation of lateral bonds between tubulins.⁴ This description of microtubule disruption presents a scenario similar to our findings of vaults, where we showed that fractures occurred along the lateral contacts of neighboring MVP subunits. The distribution of tubulin protofilaments conforming microtubules⁵ reassembles that of MVP monomers in the barrel zone, both structures bundling parallel to one another forming a cylinder. This finding suggests that there is a link between the protein structure and the self-healing ability of the shell, which might be related to their role in biology. In

the same way that the high dynamics of microtubules is associated with their need to polymerize and de-polymerize inside the cell,⁶ with the reversibility of lateral bonds been suggested to serve as means of inhibiting de-polymerization,⁷ the ability of vaults' barrel to self-repair might play a role in their function as nanocarriers. How vault particles are able to transport material inside or between cells remains a mystery, but their implication in processes of cellular transport suggests that a labile and highly dynamic structure might represent a biological advantage. On the technology front, these findings could inspire the design of similar *de novo* structure that would be expected to have mechanical properties suitable to exhibit high level of dynamics.

In **chapter 3** we explored the dynamic of vault particles as a function of pH, which might be a mechanism whereby releasing the cargo during cellular uptake through endocytosis. To do so we set up an experiment to monitor the pH-dependent dynamics of vault particles in real time. Although real-time AFM experiments to track protein dynamics is a well-established procedure, which started with the pioneered work by Müller *et al.* in 1999,⁸ it keeps surprising me why the possibility that AFM offers in this regard has not been exploited more often to study dynamic process of protein nanocages. A possible explanation might rely on the fact that the soft nature of these large nanostructure requires a tight control of the imaging force. However, many interesting biological problems could be addressed by observing in real-time and at a single particle level the structural dynamics triggered by changes in the physiological conditions that mimic biologically relevant processes, such as pH or molecular crowding. In chapter 2 we demonstrated that vault opening was not a pH-dependent process, as it was published before in literature,^{9,10} but that lowering the pH induced the weakening of lateral inter-monomeric contacts that promoted the formation of cracks in the barrel zone. Despite the formation of cracks, the quaternary structure of vaults was maintained if the pH was kept above 5.7, but lower values of pH led to protein aggregation. In the light of these results, we proposed a mechanism based on the crystallographic structure whereby vault would disassembly as a function of pH. Our model contemplates the disruption of four histidine-mediated polar bonds across lateral MVP-MVP contacts in the barrel and shoulder of the cage, with His534 participating in a histidine- α -helix charge-dipole interaction with the cap α -helix N-terminus of the neighboring MVP playing a crucial role among them. Overall, our findings shed some light on vault dynamics and might serve as means of designing strategies

to control payload delivery upon cell endocytosis, where the acidic nature of the endosomal microcompartment would represent the perfect environment.

In **chapter 4** we investigated the role that pH and ion chelation had on the stability of Tomato Busy Stunt Virus (TBSV). We found that at pH 8.5 and in the presence of a chelation agent (when calcium ions are removed from the structure and the particles present the expanded form) viruses collapsed upon adsorption. This result indicated that the expanded form was less stable than the native form, which we related to the increase in electrostatic repulsion between subunits.¹¹ A similar RNA viruses that also undergoes a pH-dependent swelling and whose mechanical properties has been extensively studied with AFM is CCMV.¹² *Klug et al* showed that after increasing the pH from 5 to 6 the capsids of CCMV softened.¹³ Because CCMV expands around pH 7 and the morphology of both shells at pH 5 and 6 cannot be distinguished, this change in stiffness had to be associated with a pre-transitional softening of the shell. Indeed, in a recent work by *Wilts et al.*¹⁴ a salt-stable mutant that precludes the expansion was used to show that the softening was not strictly coupled to the swelling of the protein shell. This result probed that the mere expansion was not the responsible for the shell softening, but that changes in capsid bonds and/or interactions with the packed RNA had to be implicated in the process. Supporting these results, our results in calcium-free TBSV nanoparticles indicated that the mere sequestration of calcium ions from the inter-capsomeric domains was sufficient to reduce capsid resilience and rigidity. Analogous decrease in the mechanical strength could be also induced by deforming the capsid with an AFM tip, which produced permanent deformation of the shell without removing capsomers. From those results we concluded that, (1) the chelation of ions introduced defects in the capsid shell that affected the overall mechanical properties of the capsid and, (2) the resistance of TBSV nanoparticle to lose capsomers was likely related to the stabilizing effect of the ssRNA molecule, which by interacting with the inner capsid tails would avoid the dissociation of the particle. The ability of RNA viruses to spontaneously self-assemble in the presence of the genome, in contrast to bacteriophages where the DNA has to be encapsulated via ATP hydrolysis and/or complexation with nucleic acid folding proteins,¹⁵ also indicates the important stabilizing effect of the genome in RNA viruses. From the technological viewpoint, the development of stable protein cages for payload transportation at the nanoscale might draw inspiration from the high resistance of TBSV nanoparticle (and other ssRNA plant

viruses) to lose capsomers and avoiding cargo release through tight pH-dependent cargo-shell interactions.

In **chapter 5** we used AFM and cryo-EM to study the effect that cargo-cargo and cargo-shell interactions have on the mechanical stability of virus-like particles derived from bacteriophage P22. To study the contribution of cargo-cargo interaction P22 VLPs were loaded with two different proteins (EGFP and CelB, which forms tetramers after shell encapsidation) The contribution of cargo-shell interaction was investigated through a capsid transition that mimicked the maturation pathway of P22 bacteriophages. Procapsids were transitioned to expanded capsids and the contacts between the cargo and the shell, mediated by the scaffolding proteins, were eliminated. Our results indicated that the cargo stiffened the cages via two different means. In the case of procapsids, when the cargo was linked to the shell, the capsid was reinforced structurally. In contrast, for expanded capsids the increase in rigidity was due to steric interaction. The different concentration of osmolyte between the inside of the shell and the surroundings created an osmotic pressure inside the shells of 30 atm. This value is of the order of the DNA-induced pressures found in other bacteriophages,¹⁶⁻¹⁹ *although* in natural viruses pressure arises from the short-range repulsion acting between neighboring DNA chains.²⁰ In addition, we found that procapsids containing CelB were the most brittle structures. We speculated that the formation of CelB tetramers inside the shell, which would impose an extra geometrical constraint, reducing the distance at which capsid subunits could be separated from their equilibrium position, was the responsible for rendering particles more brittle. Overall, our results showed that the interplay that exists between the cargo and the shell contributes to the (des)stabilization of the capsid via different physical mechanisms. Understanding these mechanisms and their molecular determinants would permit enhance the stability of these cages for their development as protective shields.

In **chapter 6** we showed that the controlled, symmetrical introduction of defects into a viral cage led to a symmetry-dependent destabilization of the capsid. In addition, we showed that symmetry-dependent binding of an accessory protein at the regions responsible for the undermined stability was capable of restoring the mechanical properties. We found that this recovery was also symmetry-dependent, and had a major effect on the regions of the capsid most weakened after the introduction of defects. Complementing the AFM results, our light

scattering and TEM analysis showed that under 0.5% SDS conditions defected VLPs exhibited much lower stability than intact VLPs. Likewise, Dec binding had a greater stabilizing effect toward defected VLPs than toward intact VLPs. The agreement between our single-particle and bulk chemical techniques likely originated from similar structural elements of the capsid being interrupted. Due to the difficulty in observing chemical destabilization in a non-bulk, symmetry-specific manner there remains a gap in the understanding of this process. However, single-particle mechanical perturbation results may provide some insights in this regard. The analytical tools that are associated with a particular field, such as in this case TEM, AFM and light scattering, offer instrument-dependent perspective of the system. Great efforts should be done to put together information coming from different techniques and viewpoints in order to assess more accurate pictures of the system. Complementing this data might allow us to understand better the information extracted from our system and, in turn, contribute to its future technical development.

In chapter 6 we also showed that to fully understand the mechanical properties of a capsid interactions at the residue level had to be considered. I do not want to finish this thesis without briefly mentioning this point. Many theoretical models have been proposed to explain the mechanics of virus particles so far, many of them based on continuum elastic theory.^{13,21-25} Continuum elasticity framework might provide very valuable information. For instance, elasticity theory has permitted to identify the distribution of stresses in virus capsids, gathering relevant structural information of competing mechanism for viral shell failure.²¹ However, continuum modeling omits the discrete nature of the capsid structure and thus it must be considered as a rough first approximation of the problem. Consider only that one amino acid mutation in a capsid protein might change the rigidity of the overall structure twofold.^{14,22} A recent study by *Cieplak et al.*²³ showed in a molecular model of 35 viruses that changes in mechanical properties do not simply correlate with virus size or symmetry, but with the mean number of interaction to neighboring amino acids. All-atom and/or coarse-grained simulation that factors in the discrete nature of the capsid and, in some cases, consider the structure at the amino acid level are required and will allow for better comprehensions of the underlying mechanism responsible for the mechanical properties of nanocages.

In **chapter 7** we used HDX-MS to identify the breathing distribution of the capsids of MVM. Up to that point, we had mainly investigated how capsids responded to deformation of a few

nanometers and what determined the mechanical properties of these nanocages. We had applied to them macroscopic concepts from material science such as rigidity, brittleness, or material fatigue, and thought of them as an assembly of building blocks (proteins) bound with a given interacting energy. In chapter 7 we changed the viewpoint, and considered viruses as dynamic entities that constantly fluctuate around an average conformation as a result of thermal energy. These fluctuations are commonly termed ‘breathing’, involve distances of only a few Angstroms and might play a role in the infection process.²⁴

Our HDX-MS results showed that important regions for the infectivity of the virus, such as the N-terminus or the structural elements forming the capsid pores at the 5-fold symmetry axes, were among the most dynamic regions of the capsid. This provided proof of the intense breathing of regions involved during translocation events during MVM infection. And interestingly, arise question about the potential connection between breathing and mechanical properties. The 5-fold symmetry axes in MVM particles is known to preserve their stiffness upon DNA encapsidation.²⁵ Also, it has been shown that any mutation in the MVM capsid that increased the rigidity of the pore was found to decrease the infectivity of the virion.²² These findings suggested that the AFM-tested flexibility of the pore, which extends to deformation of a few nanometers, have to be preserved through evolution. Whether or not a mutant that precludes infectivity decrease their breathing around the pore needs still to be tested, but I further studies in this direction might shed some light in the intricate nature that determines the mechanics of virus capsids. MVM is an amazing system to keep working on. All mutations done so far has shown that (overall) either the rigidity was maintain or increase, suggesting that an evolutionary pressure might have kept the capsids at their minimum of ‘softness’. It still strikes me how a single amino acid change might increase twofold the overall mechanical response of the capsid tested with an AFM tip as big as the capsid. But why there is —if it is the case— an evolutionary pressure that preserves such mechanics fascinates me even more. Complementing HDX-MS studies with AFM results might pave new ways to respond to these questions.

References

- 1 Roos, W. H., Bruinsma, R. & Wuite, G. J. L. Physical virology. *Nat Phys* **6**, 733-743, (2010).
- 2 Rome, L. H. & Kickhoefer, V. A. Development of the Vault Particle as a Platform Technology. *Acc Nano* **7**, 889-902, (2013).
- 3 Schaap, I. A. T., Carrasco, C., de Pablo, P. J., MacKintosh, F. C. & Schmidt, C. F. Elastic response, buckling, and instability of microtubules under radial indentation. *Biophys J* **91**, (2006).
- 4 Kononova, O. *et al.* Tubulin Bond Energies and Microtubule Biomechanics Determined from Nanoindentation in Silico. *J Am Chem Soc* **136**, 17036-17045, (2014).
- 5 Nogales, E., Wolf, S. G. & Downing, K. H. Structure of the [alpha][beta] tubulin dimer by electron crystallography. *Nature* **391**, 199-203, (1998).
- 6 Nogales, E. Structural Insights into Microtubule Function. *Annual Review of Biochemistry* **69**, 277-302, (2000).
- 7 Kononova, O. *et al.* Tubulin bond energies and microtubule biomechanics determined from nanoindentation in silico. *J Am Chem Soc* **136**, 17036-17045, (2014).
- 8 Muller, D. J. & Engel, A. Voltage and pH-induced channel closure of porin OmpF visualized by atomic force microscopy. *J Mol Biol* **285**, 1347-1351, (1999).
- 9 Goldsmith, L. E., Yu, M., Rome, L. H. & Monbouquette, H. G. Vault nanocapsule dissociation into halves triggered at low pH. *Biochemistry-Us* **46**, 2865-2875, (2007).
- 10 Querol-Audi, J. *et al.* The mechanism of vault opening from the high resolution structure of the N-terminal repeats of MVP. *Embo J* **28**, 3450-3457, (2009).
- 11 Robinson, I. K. & Harrison, S. C. Structure of the expanded state of tomato bushy stunt virus. *Nature* **297**, 563-568, (1982).
- 12 Mateu, M. G. Mechanical properties of viruses analyzed by atomic force microscopy: A virological perspective. *Virus Res* **168**, 1-22, (2012).
- 13 Klug, W. S. *et al.* Failure of viral shells. *Phys Rev Lett* **97**, (2006).
- 14 Wilts, B. D. *et al.* Swelling and Softening of the CCMV Plant Virus Capsid in Response to pH Shifts. *Biophys J* **98**, 656a-656a, (2010).
- 15 Hagan, M. F. Modeling Viral Capsid Assembly. *Advances in chemical physics* **155**, 1-68, (2014).
- 16 Hernando-Perez, M. *et al.* Direct Measurement of Phage phi29 Stiffness Provides Evidence of Internal Pressure. *Small* **8**, 2366-2370, (2012).
- 17 Smith, D. E. *et al.* The bacteriophage phi 29 portal motor can package DNA against a large internal force. *Nature* **413**, 748-752, (2001).
- 18 Evilevitch, A., Lavelle, L., Knobler, C. M., Raspaud, E. & Gelbart, W. M. Osmotic pressure inhibition of DNA ejection from phage. *P Natl Acad Sci USA* **100**, 9292-9295, (2003).
- 19 Jin, Y. *et al.* Bacteriophage P22 ejects all of its internal proteins before its genome. *Virology* **485**, 128-134, (2015).

- 20 Tzlil, S., Kindt, J. T., Gelbart, W. M. & Ben-Shaul, A. Forces and pressures in DNA packaging and release from viral capsids. *Biophys J* **84**, 1616-1627, (2003).
- 21 Zandi, R. & Reguera, D. Mechanical properties of viral capsids. *Phys Rev E* **72**, (2005).
- 22 Castellanos, M. *et al.* Mechanical elasticity as a physical signature of conformational dynamics in a virus particle. *P Natl Acad Sci USA* **109**, 12028-12033, (2012).
- 23 Cieplak, M. & Robbins, M. O. Nanoindentation of 35 Virus Capsids in a Molecular Model: Relating Mechanical Properties to Structure. *Plos One* **8**, (2013).
- 24 Bothner, B. & Hilmer, J. K. in *Structural Virology* (eds M. Agbandje-McKenna & R. McKenna) 41-61 (RSC Publishing, 2011).
- 25 Carrasco, C. *et al.* DNA-mediated anisotropic mechanical reinforcement of a virus. *Proceedings of the National Academy of Sciences* **103**, 13706-13711, (2006).

Summarized conclusions

1– We characterized the mechanical properties of individual vaults by performing nanoindentation experiments on full reclining particles and half-vaults. We found that reclining particles were softer than half-vaults, and with a finite element model we rationalized the origin of this difference in stiffness. In addition, our results demonstrated that vault particles exhibited self-healing capabilities that enable them to recover from failure within times shorter than 1 second. Our AFM images showed that these ruptures occurred in the barrel, along the lateral contacts of two neighboring MVPs, and we could estimate the energies involved in the breakage of these bonds. Overall, our results provided new insights into the dynamics of these enigmatic particles, which might help to understand their role as cellular nanocontainers or inspire the design of new protein-based nanostructures with self-healing capacities.

2- We performed real-time AFM experiments to investigate the pH-dependent dynamics of vaults at single particle level. We found that pH lowering destabilized the interaction between adjacent MVP monomers resulting in the formation of cracks in the barrel or shoulder zones. Those cracks were observed in vault particles maintaining their quaternary if the pH was maintained above 5.7, but lower values of pH led to protein aggregation. In addition, based on the crystallographic structure we proposed a model whereby this pH-dependent disassociation might occur. Our results offer a new picture of the pH-dependent dynamics of vaults, which before was thought to trigger vault opening, and might serve as a means to design strategies for cargo delivery upon cell endocytosis, where the pH of the environment gradually decreases.

3- We studied the mechanical role that calcium ions inserted in the viral shell had on the stability of TBSV nanoparticles. We found that the sequestration of these ions reduced capsid resilience and rigidity, and that deformations of the native forms above the elastic limit led to analogous decrease in the mechanical properties. Both the sequestration of calcium ions and the squeezing of the shell yielded to a rearrangement of the capsid subunits that it was not accompanied by a loss of capsomers. Experiments performed with multiple loading cycles confirmed the

resistance of these structures to lose capsomers, which proved the high plasticity of the shells. We speculated that this high plasticity was caused by the stabilizing effect of RNA at interacting with the inner tails proteins of the capsid. In summary, our results provided the first experimental evidence of the impact that calcium ions have on the mechanical properties of a viral shell.

4- We analyzed the effects that an heterologous cargo had on the stability of P22 virus-like particles. To achieve this goal we encapsulated two types of proteinaceous payloads, which allowed us to study the effect of a different cargo-cargo interaction. We also studied the effect of a different cargo-shell interaction by expanding the procapsid shell into the mature form, which unanchored the cargo from the vicinity of the inner capsid wall. We found that while bound cargo to the inner capsid surface mechanically reinforced the capsid in a structural manner (procapsids), unbound cargo diffusing freely within the shell cavity pressurized the cages up to ~30 atm due to steric effects (expanded capsids). In addition, we found that a strong cargo-cargo interaction rendered particles more brittle by imposing extra geometrical constraints between capsid subunits.

5- We showed that the controlled, symmetrical introduction of defects into a viral cage led to a symmetry-dependent mechanical destabilization of the shell. In addition, we showed that binding of an accessory protein at the weakest regions of the capsid was capable of restoring locally the loss of mechanical stability. Our AFM results were complemented with biochemical destabilization assays studied with light scattering and TEM, which showed the same trend of stabilizing/destabilizing effects. The coupling of single molecule and bulk techniques permitted the in depth examination of contributing factors to these symmetry-specific phenomenon, allowing for the future examination of both infectious viral systems and synthesized nanomaterials.

6- We used HDX-MS to identify, with high spatial resolution, structural changes in the MVM capsid that are required for viral infection. Our results revealed that translocation events through capsid pores involved a global structural rearrangement of the capsid, involving elements around the three-fold symmetry axes, located far

from the pores. Overall, the study provided a novel demonstration of the potential of HDX-MS to structurally dissect functionally relevant, temperature-dependent structural transitions in virus particles and other large macromolecular protein assemblies.

Conclusiones resumidas

1 - Caracterizamos las propiedades mecánicas de partículas vaults mediante nanoindentaciones en partículas enteras (*full-vaults*), apoyadas sobre el barril, o mitades (*half-vaults*), adsorbidas a través de la sección central. Nuestros experimentos mostraron que las partículas apoyadas sobre el barril eran más blandas. Un modelo basado en elementos finitos nos permitió entender el origen de esta diferencia en rigidez. Además, nuestros experimentos demostraron la capacidad autoreparativa de estas nanoestructuras. Vimos que la deformación de partículas con la punta del AFM inducía fracturas con tiempos de vida medio inferior a un segundo. Imágenes de AFM de alta resolución nos permitieron evaluar estas efímeras fracturas y determinar que se producían en la zona del barril, a lo largo de los contactos laterales entre monómeros de proteína adyacentes. Para resumir, estos resultados pueden contribuir a desentrañar el papel biológico de estas enigmáticas partículas, así como ser fuente de inspiración para el desarrollo de nanoestructuras proteicas con capacidades autoreparativas.

2 - Diseñamos un experimento en el que visualizamos en tiempo real la dinámica de partículas vaults individuales en función del pH. Nuestros resultados mostraron que la bajada de pH, en vez de abrir las vaults en dos mitades, como se sugería en resultados previos, desestabilizaba las interacciones entre monómeros adyacentes de la zona del barril. Este debilitamiento de las interacciones inter-monoméricas se traducía en la formación de fracturas en la zona del barril y hombro de la estructura. Si el pH de la disolución se mantenía por encima de 5.7, la estructura cuaternaria de las vaults se preservaba, a pesar de la presencia de fracturas, pero valores de pH más bajos provocaban el colapso de la partícula. Basados en la estructura cristalográfica de la partícula propusimos un modelo que racionalizaba nuestros resultados.

3- Estudiamos el papel que los iones calcio jugaban en la estabilidad mecánica de la estructura del virus del tomate (TBSV). Nuestros resultados mostraron que el secuestro de esos iones, insertados en el interior de las cápsidas, disminuía la rigidez y resiliencia de las partículas. Además, observamos que nanoindentaciones que sobrepasaban el límite elástico en virus nativos (con iones) causaban resultados

mecánicos similares. Ambos casos, tanto la quelación de iones como la deformación de la estructura vírica con la punta del AFM, provocaban una reorganización de la estructura vírica que no se veía acompañada por la pérdida de capsómeros. Repetidas nanoindentaciones sobre la misma partícula confirmaron la resistencia de estas estructuras a perder capsómeros, demostrando así su gran plasticidad. Especulamos que la presencia de RNA, interactuando con los extremos N-terminales de la cápsida proteica, era el responsable de esta plasticidad.

4 - Analizamos la influencia que distintas interacciones carga-cápsida y carga-carga tenían en la estabilidad de nanoestructuras derivadas del bacteriófago P22. Nuestros resultados mostraron que mientras el reforzamiento observado en las precabezas era estructural, interacciones estéricas eran las responsables del incremento de rigidez observado en cápsidas expandidas. La diferente concentración de osmolito (CelB o EGFP) entre el interior y el exterior de la cápsida promovía un influjo de moléculas de agua que se traducían en aumentos de presión de las estructuras víricas de hasta 30 atmósferas. Además, vimos que las precabezas con CelB eran las estructuras más frágiles. Argumentamos que la formación de tetrámeros, reduciendo la movilidad de los capsómeros de la estructura, podía ser la causa de esta mayor fragilidad.

5- Vimos que la introducción simétrica de defectos en las cápsidas expandidas de P22 inducía una desestabilización “anisótropa” de las estructuras (los parámetros mecánicos que se veían afectados dependían del eje de simetría). Además, vimos que el anclaje de “proteínas accesorio” (Dec) en las zonas de mayor debilidad era capaz de restablecer la estabilidad de las partículas, también, anisotrópicamente. Los resultados de AFM fueron complementados por experimentos de inestabilidad bioquímica observados por TEM y dispersión de luz, los cuales mostraron los mismos patrones de estabilidad/inestabilidad. La complementariedad de los resultados sugirió que ambos procesos estaban gobernados por los mismos determinantes moleculares, y que su unión podía desentrañar la especificidad de experimentos bioquímicos de *bulk*, ofreciendo la posibilidad de estudiar con mayor detalle tanto sistemas víricos infecciosos como nuevos nanomateriales.

6- Usamos HDX-MS para identificar cambios estructurales en cápsidas de MVM necesarios durante su proceso de infección. Nuestros experimentos concluyeron que los procesos de translocación a través de los poros promovían una reorganización global de la cápsida, que involucraba zonas situadas alrededor del eje de simetría tres, alejadas de los poros. A nivel más genérico, nuestro estudio probó el potencial de HDX-MS para determinar cambios estructurales en macrocomplejos proteicos que pueden ser de difícil acceso para técnicas como la cristalografía de rayos X, la cryo-EM o el NMR.

List of Publications

1. **A. Llauro**, P. Guerra, N. Irigoyen, J. F. Rodríguez, N. Verdaguer, P. J. de Pablo. *Mechanical stability and reversible fracture of vault particles*. Biophys. J. (2014); 106:687-695.
2. P. Ares, C. Garcia-Doval, **A. Llauro**, J. Gómez-Herrero, M.J. van Raaij, Pedro J. de Pablo. *Interplay between the mechanical properties of bacteriophage fibers and the strength of virus-host links*. Phys. Rev. E (2014); 89, 052710.
3. **A. Llauro***, E. Coppari*, F. Imperatori, A. R. Bizzarri, J.R. Castón, L. Santi, S. Cannistraro, P. J. de Pablo. *Influence of calcium ions and swelling on the mechanical properties of Tomato Bushy Stunt Viruses*. Biophys. J. (2015); 109:390-7.
4. **A. Llauro**, D. Luque, E. Edwards, B. L. Trus, J. Avera, D. Reguera, T. Douglas, P. J. de Pablo, J. R. Castón. *Cargo-shell coupling governs the stability of individual virus-derived protein cages*. Submitted.
5. M. van de Waterbeemd*, **A. Llauro***, J. Snijder, A. Valbuena, A. Rodríguez-Huete, M. A. Fuertes, P. J. de Pablo, M. G. Mateu, A. J.R. Heck. *Monitoring a temperature-induced structural transition of a viral capsid by hydrogen-deuterium exchange*. Submitted.
6. **A. Llauro**, P. Guerra, R. Chaudhary, B. Bothner, N. Verdaguer, P. J. de Pablo. *Decrease in pH destabilizes individual vault nanocages by weakening the interprotein lateral interaction*. Submitted.
7. **A. Llauro***, B. Schwarz*, D. Reguera, P.J. de Pablo, T. Douglas, *Mechanical effects of symmetry specific destabilization and restabilization of the bacteriophage P22 virus-like particle*. In preparation.

8. R. Kant, **A. Llauro**, S. Qazi, P. J. de Pablo, T. Douglas, B. Bothner, *Understanding the stability, biomechanics and dynamics of P22 bacteriophage during maturation*. Submitted.

Acknowledgements

Gracias Pedro por confiar en mí. Gracias por dejarme andar mi propio camino, y gracias por tu entusiasmo y apoyo. Tienes dos máquinas estupendas, a quién debo esta tesis tanto como a ti; y no lo son de casualidad, el gran equipo que tienes alrededor, y del que formas parte desde hace tantos años, explica el éxito. Ha sido un honor, he aprendido mucho. Gracias por los síes, por las conferencias y colaboraciones, por los consejos; gracias por esa carta. Y gracias, sobre todo, por ser la persona que hay detrás del científico. Me llevo un amigo.

Gracias Álvaro por enseñarme a manejar el AFM, fuiste tú, Merche andaba por las Américas. Gracias por las discusiones, gracias por los favores, gracias por compartir ideas y dudas. Gracias por tu rigor y sentido común. Gracias Merche por ser insaciable, por tu optimismo, por el apoyo y receptividad. Gracias por estar siempre dispuesta a echar un cable, por tu curiosidad, por enseñarme tanto de AFM. Gracias por ser la persona que eres, sobre todo. Marina, Natalia y Manuel; gracias por esos pequeños favores que tanto se agradecen, mucha suerte en vuestras carreras.

Julio, Cristina, Willy, Pablo, ¡menuda ciencia la vuestra! Gracias Julio por tu cercanía, y por saber tanto; gracias Cris por inspirar; gracias Willy por ser tan inteligentemente estupendo; y gracias Pablo por las discusiones, consejos y favores, os tendré siempre un ojo puesto. Chema, Iván, Héctor, Ana, Bruno, Miguel, Antonio, Alba, Santiago, gracias a todos por dar a esto el aspecto de familia. Iván y Héctor, a vosotros en especial. Gracias Iván por tus consejos, inteligentes y perspicaces. Héctor, gracias por lo vivido, dentro y fuera del laboratorio.

Núria Verdaguer y Pablo Guerra, gracias por vuestro entusiasmo y enseñanzas, y por purificar esas partículas estupendas. Me lo he pasado muy bien jugando con ellas. Pepe Castón y Dani Luque, gracias por las discusiones, por el entusiasmo y por enseñarme lo poco que sé de cryo-EM. Mauricio García, Milagros Castellanos y Alex Valbuena, gracias por muchas cosas. Gracias Mila por preparar esas muestras de MVM, las primeras que medí. Gracias Alex por las discusiones y favores, por ser estupendo. Mauricio, gracias en especial a ti; gracias por confiar en mí, gracias por apostar por el proyecto de Holanda, gracias por tu

rigor científico (en mayúsculas) y tu saber hacer, gracias por tus consejos, gracias por tus correcciones y gracias por esa carta. Ha sido un honor aprender de ti.

Thanks Emilia Coppari, Salvatore Cannistraro and Luca Santi for all the work with TBSV. Emilia, tanks for being so kind and helpful. Thanks Trevor Douglas, Ethan Edwards and Benjamin Schwarz for all the work with P22. Trevor, especial thanks to you for being always so receptive and helpful, thanks for your support, for that letter, and for introducing me to your great science. It is inspiring. I hope our paths will cross again. Ethan, thanks for being always so willing to help. Benji, thanks for the discussions, for being so smart and helpful (our fun it's not yet over). Brian Bothner and Ravi Chaundry, thanks for being so receptive and helpful, for accepting without hesitation that new collaboration. Albert Heck, Michiel van de Waterbeemd and Joost Snijder many thanks here. Thanks Albert for giving me the opportunity to visit your great lab, for being so helpful and for your support. I learnt a lot during that period. Thanks Michiel for teaching me about HDX-MS, for being so patient and helpful, during my stay there and afterwards. It has been a pleasure working with you, you will be a great scientist. Joost, thanks for your help with the proposal, for trying so hard at making those vaults fly, thanks for your advice and help during my stay there, and most of all, thanks for taking that flight.

Alfonso, Gela e Inés, gracias por ser mi familia en Madrid. Siempre lo seréis. Tamara y Alex; Álvaro y Álvaro; Jan; Pablo, César y Flor, gracias por estos años. Paz, gracias por la buhardilla, y por ser amiga. Mercès estimades, Jesús, gràcies per les visites. Laura i Rosie, gràcies per ser qui sou, per tots aquests anys, per ensenyar-me què és l'amistat. Muntsa, gràcies per ser-hi. Mare, pare i Lluís, gràcies per tot, per ser pinya, aquesta tesis és vostra.

Appendix

Supporting Information to Chapter 2

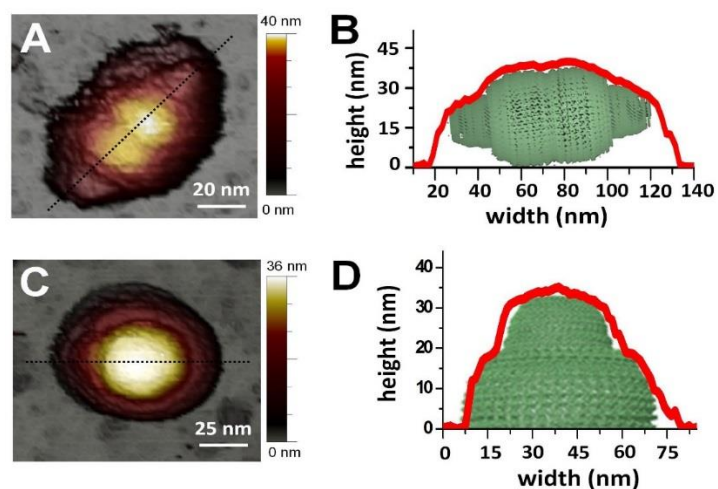


Figure S1. High-resolution AFM topographies of an entire reclining particle and a half-vault. (A) Topographical image of a reclining particle. (B) Longitudinal profile taken along the dotted black line in Fig. A. The height profile (*red line*) shows an excellent agreement with the X-Ray data of the vault structure. In this case, the vault is tilted about 5 degrees from the substrate. (C) AFM topography of a half vault with the cap facing up. (D) Profile taken along the dotted black line in Fig. C. Again, the dimensions agree with those obtained by X-Ray and EM.^[3]

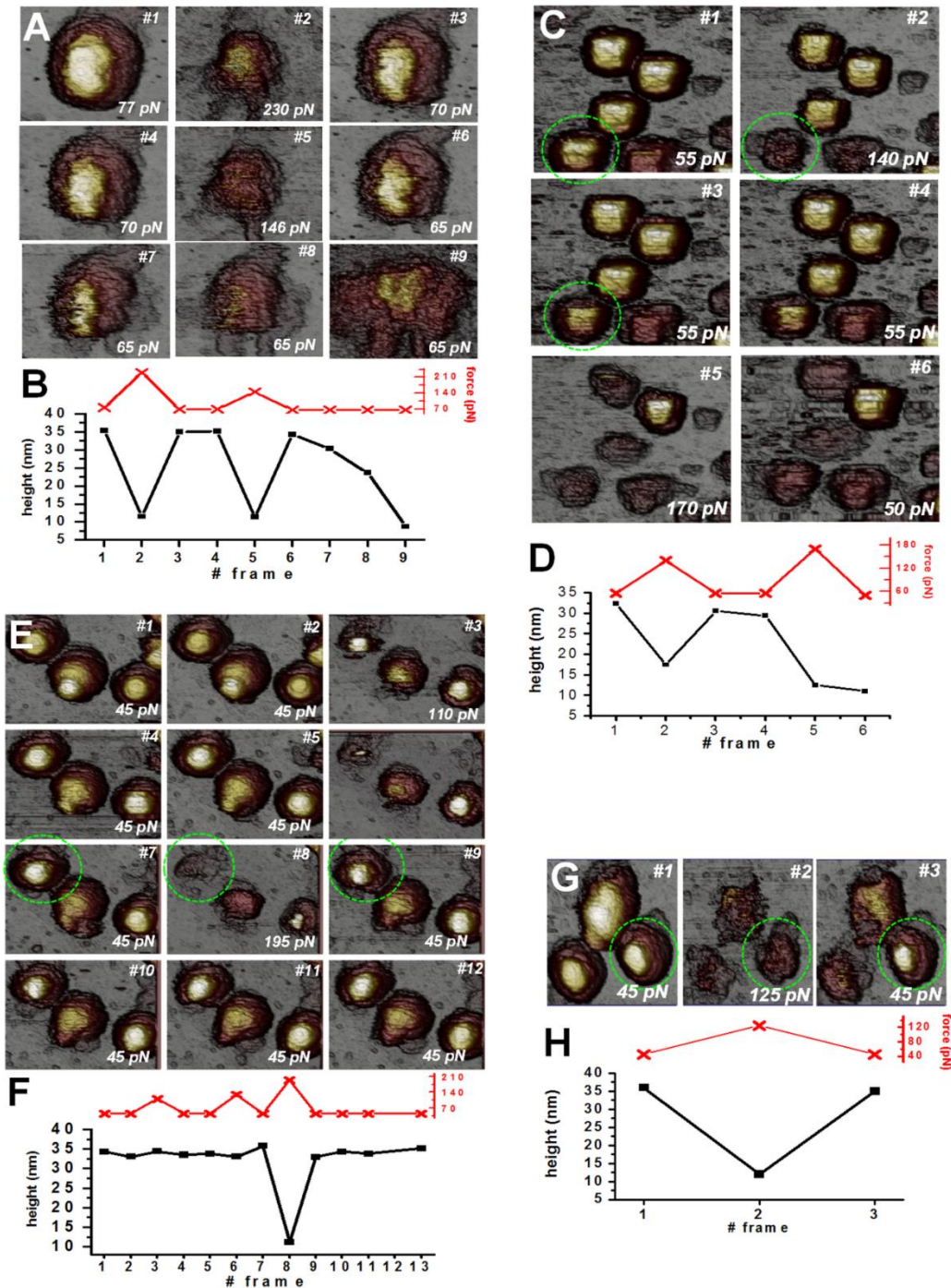


Figure S2. Half-vault deformation depending on force imaging. (A) Topographical images are time ordered and labeled with its corresponding imaging force. (B) (top) Imaging force evolution of Fig. S2 A. (bottom) Maximal height evolution of Fig. S2 A. (C-D), (E-F), and (G-H) correspond, respectively, to three more cases. The height evolution for these cases accounts for the half-vault circled with a green dotted line.

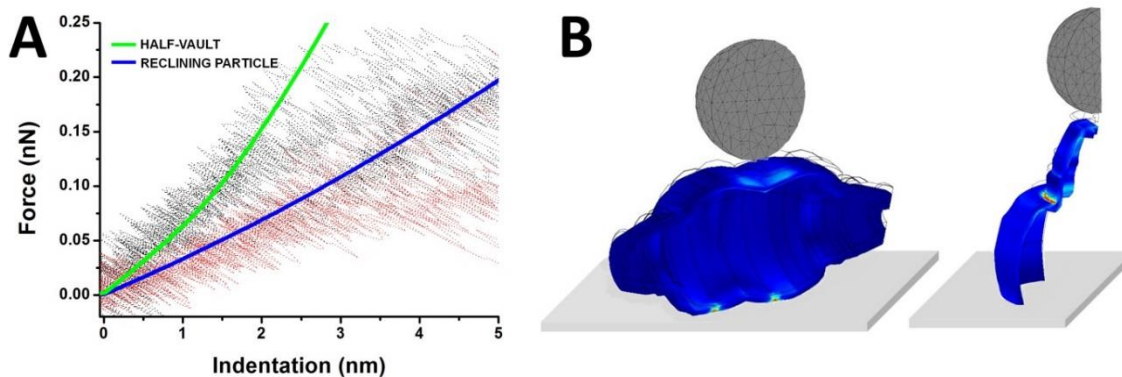


Figure S3. Finite Element Analysis. (A) FIC obtained in the Finite Element simulation for a half-vault (*green*) and a reclining particle (*blue*) when Young's modulus was set to $E=700$ MPa. On the background we have overlaid the experimental curves for 26 different half-vaults (black) and 13 different reclining particles (red). (B) (*left*) Image of a half segment of a reclining particle with a 6 nm indentation; again, the colors indicate the von Mises stress distribution. (*right*) Image of a quarter segment of a half-vault with a 6 nm indentation, the colors indicating the distribution of the von Mises stress.

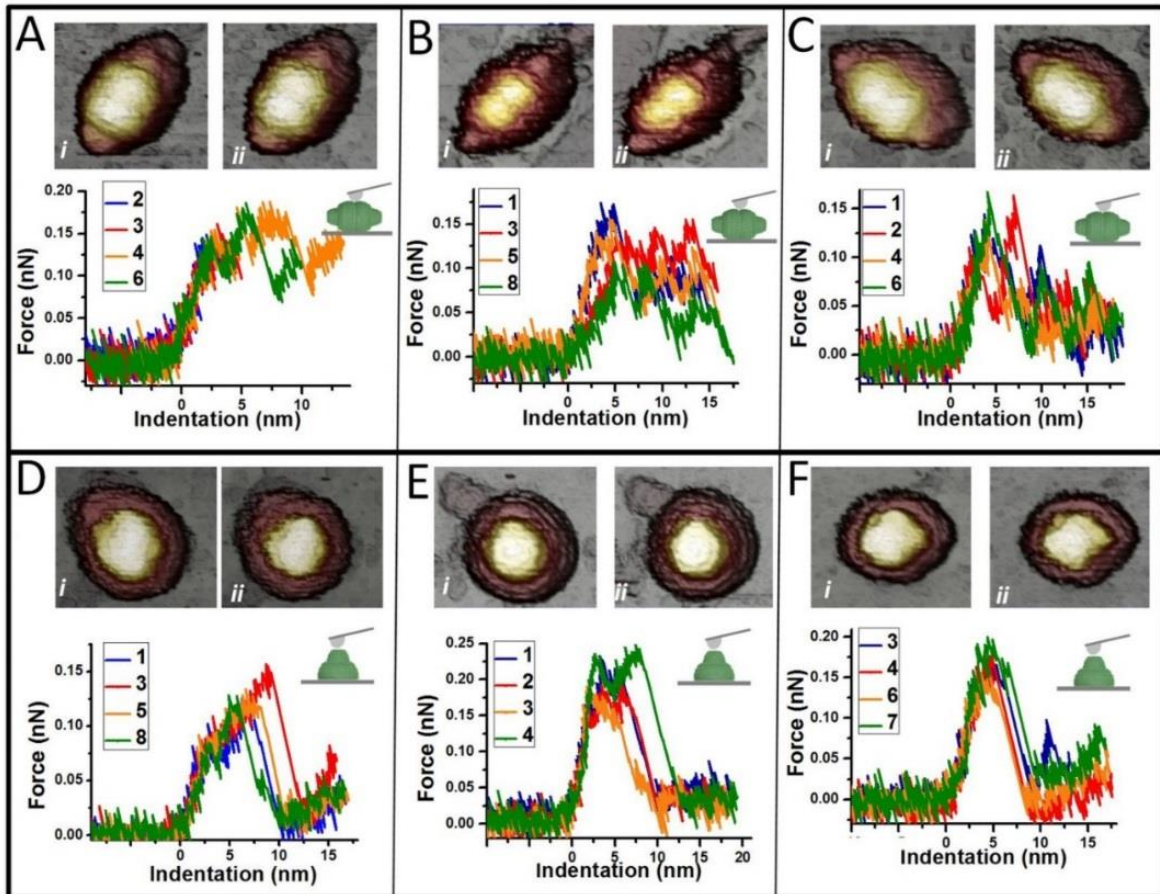


Figure S4. Cyclic loading. (A) Some of the FIC performed on top of the reclining particle shown in *i*. The numbers in the legend indicate the order of the curves. The image of the particle after the cyclic loading is represented in *ii*. (B, C) Two more examples, as in A. (D, E, F) Cycle loading experiments performed on half-vaults.

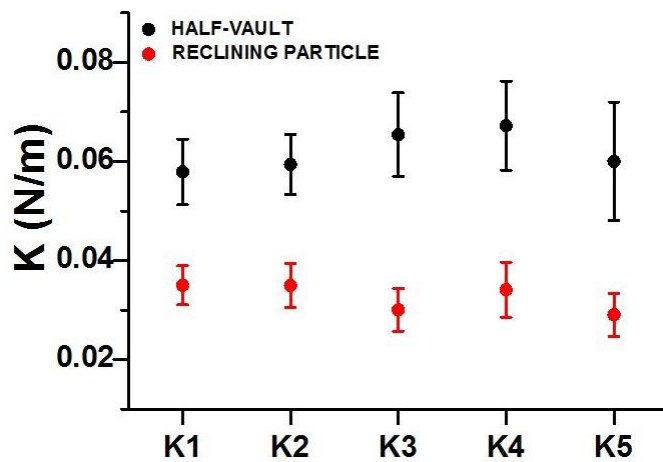


Figure S5. Evolution of the spring constant. The graph shows the evolution of the average spring constant value during the first indentation cycle (corresponding to 5 consecutive FICs). The values were obtained from 21 half-vaults and 13 reclining particles, respectively. Each FIC was performed beyond the breaking limit.

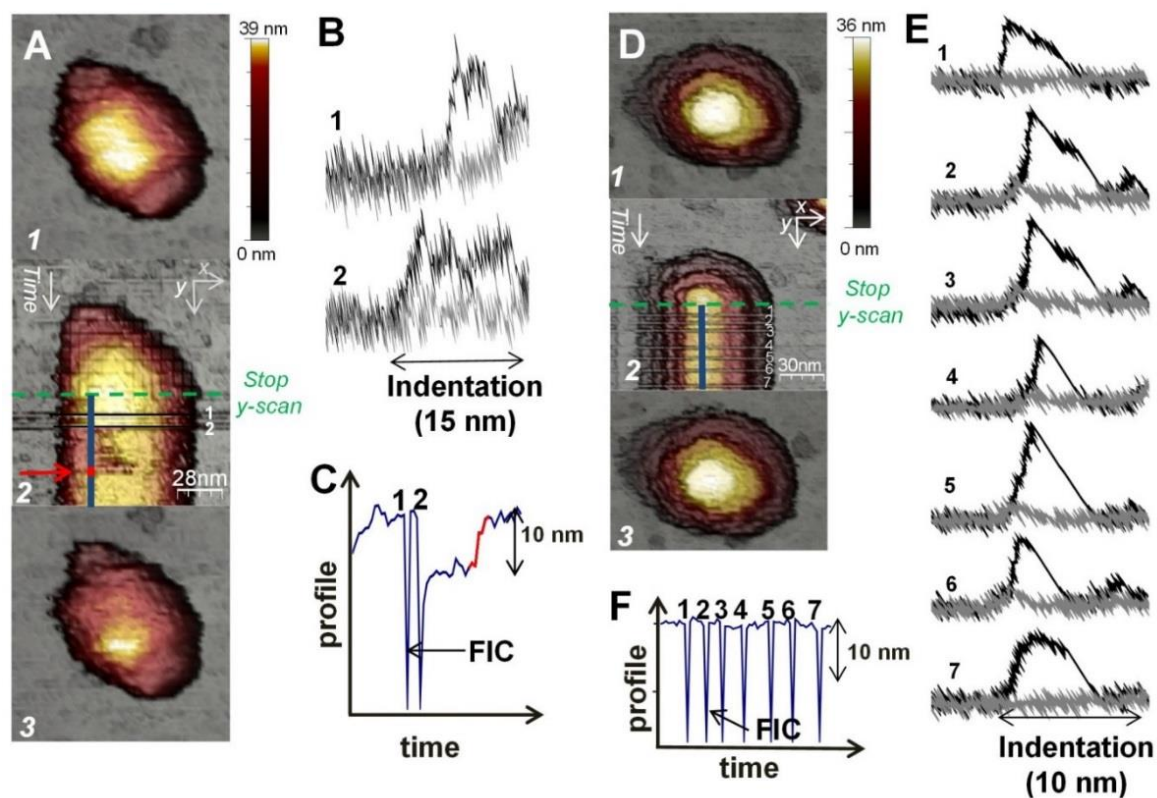


Figure S6. Monitoring of the topography in a stopped y-scan (A) Image of a reclining particle: (1) before the indentations, (2) during the indentations, and (3) after the indentations. All images were taken from top to bottom. In Figure A 2, the dashed green line indicates the place where the tip stopped scanning in the y-direction. Therefore, from this line, the tip was placed on top of the structure and FICs started. Each black line in figure A 2 corresponds to a different FIC. After the second indentation, the structure of the particle was damaged, as a partial loss in height was observed (darker zone on top of the structure). Further imaging of this profile showed a recovery of the structure (*red arrow*). (B) The indentations performed on the top of the structure, the number of each curve corresponding to the order in which they were performed. (C) Topographic profile corresponding to the solid blue line depicted in figure A 2. In this profile, each FIC is represented as a sharp decrease. After the second FIC, the structure lost 10 nm in height that was later recovered (*red line*). (D, E, F) The same experiment performed on a half-vault. In this case, the particle does not display any topographical changes. However, some backward curves present a recovery (2, 3, 4, 5, and 6) whereas others do not (1 and 7). These latter cases correspond to recoveries occurring during the non-contact part of the curve (flattened region), which we classified as medium recovery times ($650\text{ms} < RT < 2\text{s}$)

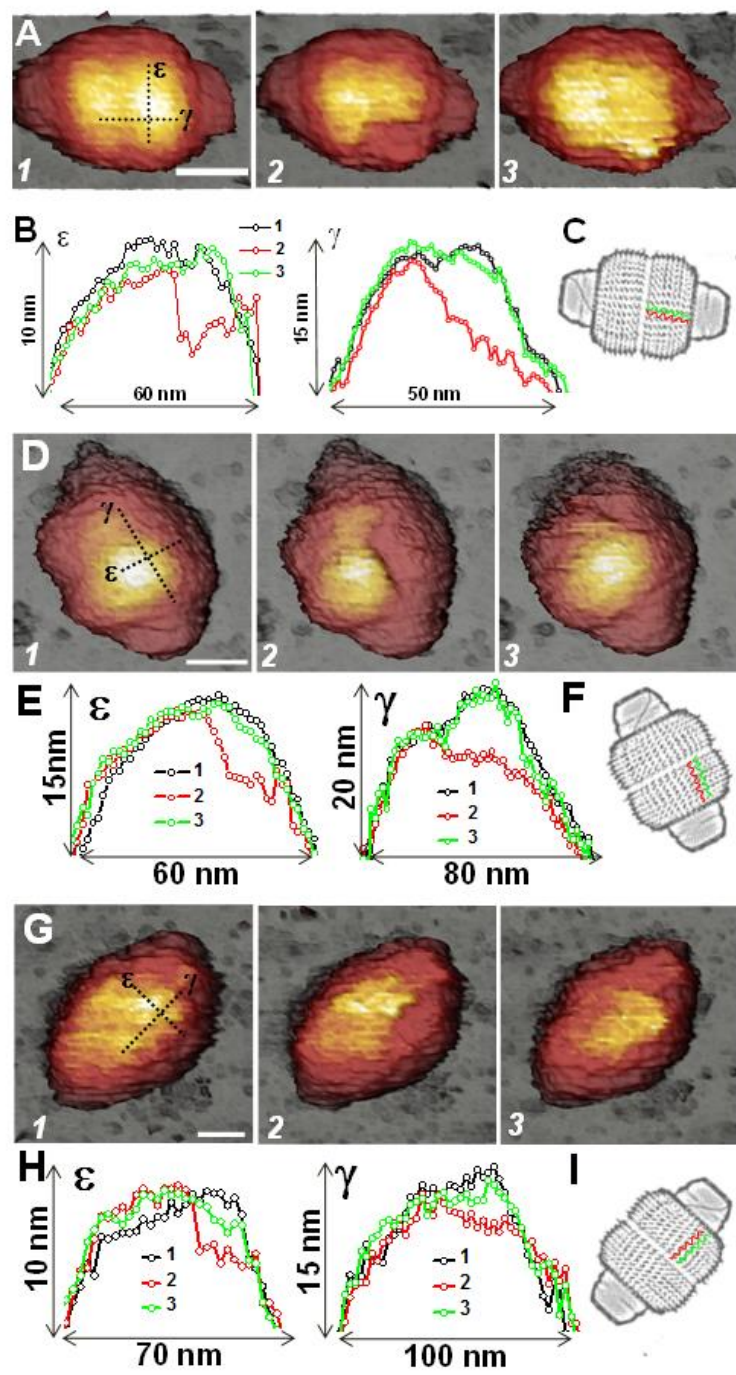


Figure S7. Reversible failure of vaults (A) Consecutive images of a reclining particle: (1) before the fracture, (2) just after the fracture, and (3) after the recovery. (B) Profiles ϵ and γ depicted with dotted black lines in Figure A1: before the fracture (*black*), after the fracture (*red*), and after the recovery (*green*). (C) Picture showing the line of fracture aligned between two neighboring MVPs (in *red*), with the depressed region highlighted in pink. (D, E, F) and (G, H, I) correspond, respectively, to two more cases of slow reversible fracture.

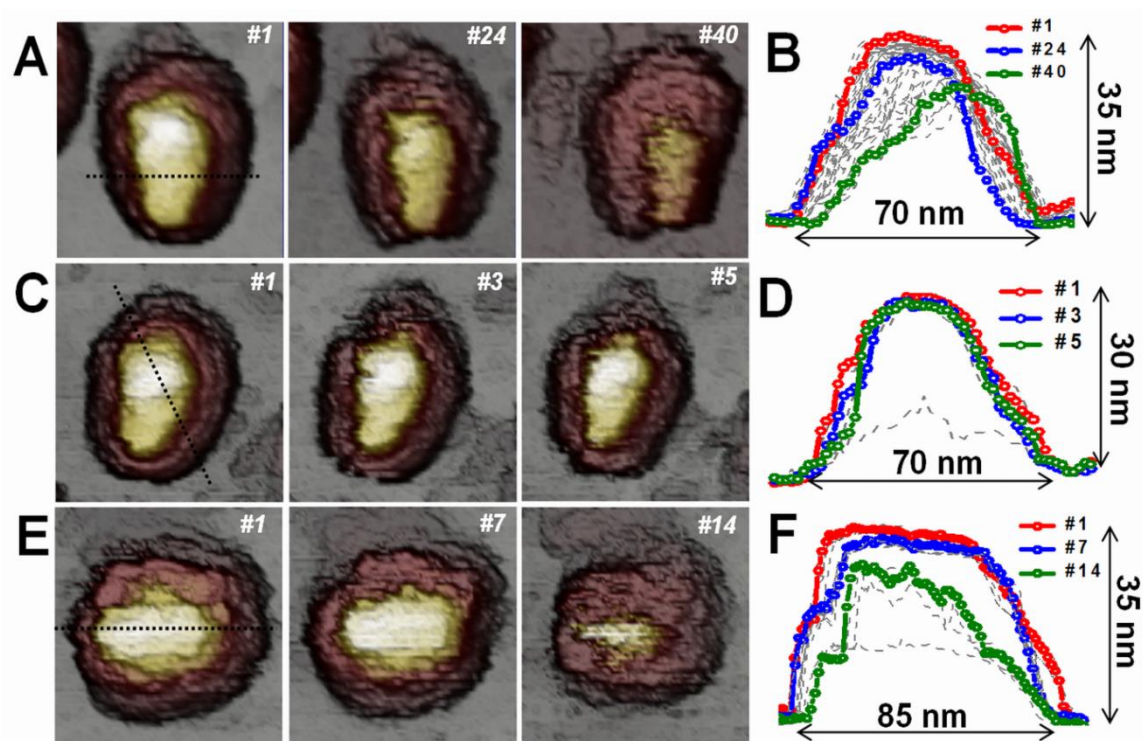


Figure S8. Three cases of fatigue experiments on half-vaults (A) Evolution of the topographical images of a half-vault imaged at 70 pN. Images are time ordered and labeled with the number of its corresponding frame. In this case, the particle was imaged 40 times, which corresponds to a time of 90 minutes. (B) Evolution of the profile taken along the dotted black line of Figure A-1. The profiles corresponding to frames 1, 24, and 40 are depicted in red, blue, and green, respectively. The rest of the profiles are depicted in grey. (C, D) and (E, F) correspond, respectively, to two more cases. The imaging force for these cases was about 75 pN.

Movie 1. Mechanical fatigue of a half-vault. This movie indicates the temporal evolution of figure 6. – it can be found online at <http://www.cell.com/action/showImagesData?pii=50006-3495%2814%2900009-5>.

Supporting Information to Chapter 3

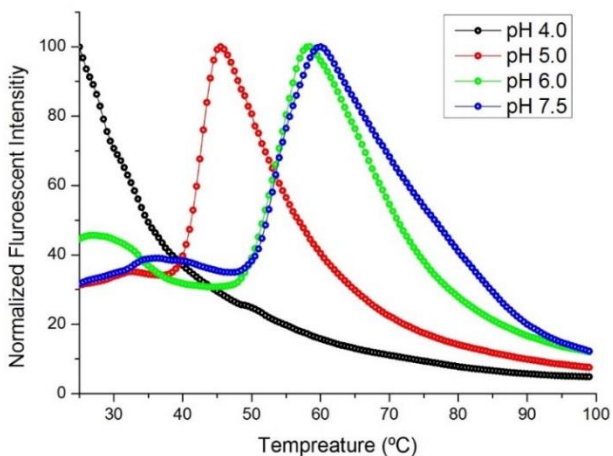


Figure S1. Differential scanning fluorescence at pH 7.5, 6.0, 5.0 and 4.0. The corresponding melting temperature are 60.5 ± 0.5 , 59 ± 0.5 and 46.0 ± 0.5 for pH 7.5, 6.0 and 5.4, respectively. Particles are not stable at pH 4.

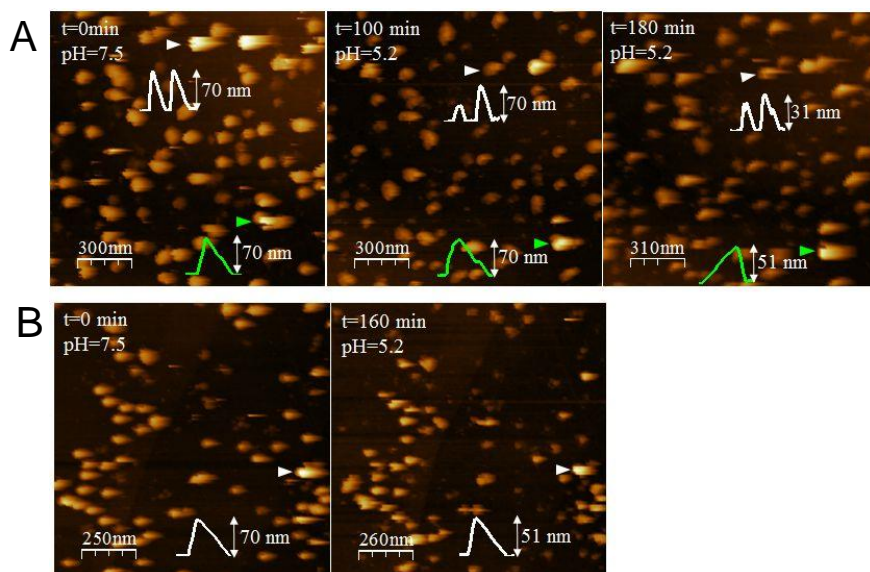


Figure S2. AFM topography evolution of single stand-up full-vault from pH 7.5 to 5.2. (A) AFM images of the same area before and after changing the pH from 7.5 to 5.2. At pH 5.2 some particles present a stand-up configuration, proving that lowering the pH not necessary open particles into halves (white and green arrows). (inset) Profiles of the particles. (B) AFM images of the same area before and after changing the pH from 7.5 to 5.2. (inset) Profile of the particle. Due to the pH lowering the height of the particle reduces likely as a consequence of an overall weakening. The height reduction does not account for an opening of vaults into halves. Color scale bar: white-golden-brown, from the highest to the substrate.

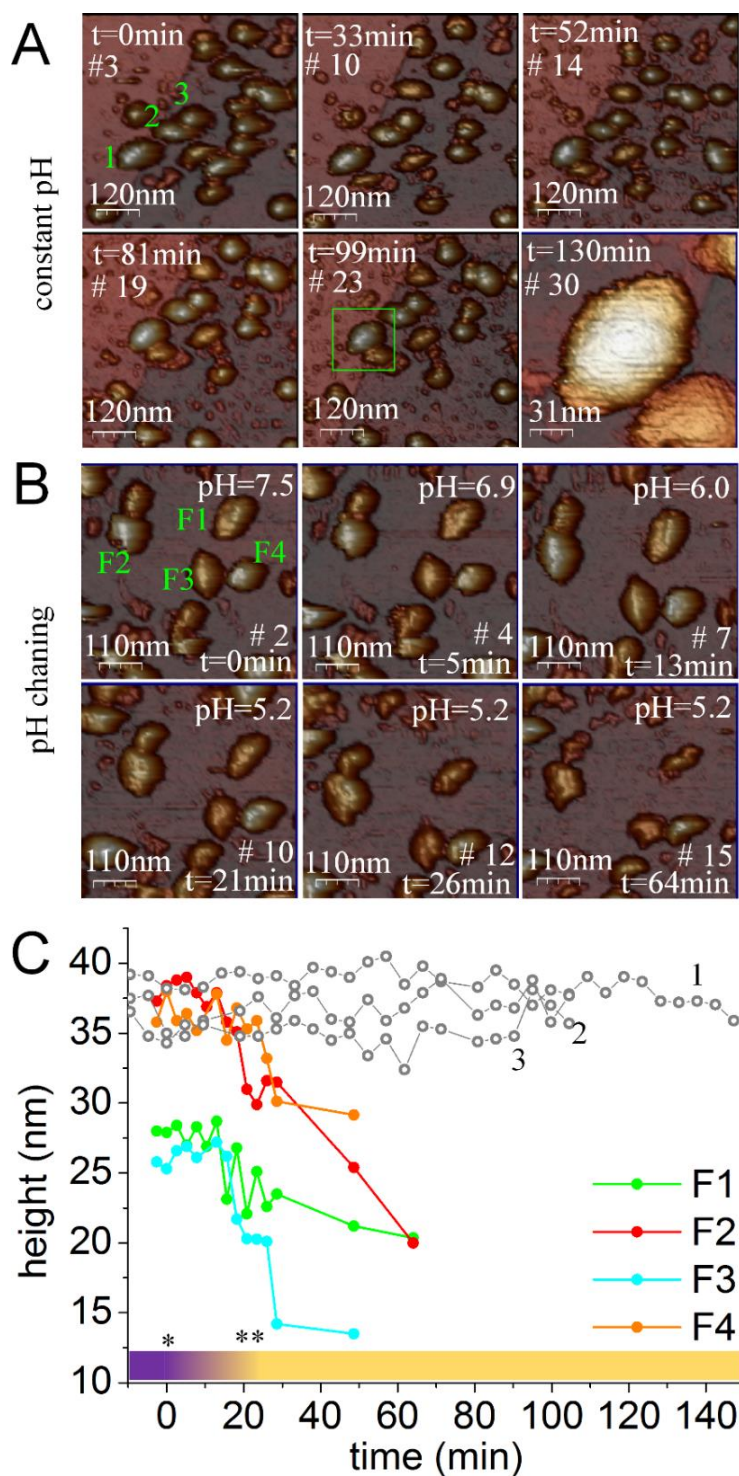


Figure S3. Control AFM experiments: evolution of the topography as a consequence of AFM imaging and pH exchange. (A) A region of vault particles ($600 \times 600 \text{ nm}^2$) imaged at constant pH for 105 minutes (24 frames). The figure shows different snapshots of the process, each frame is labeled with its corresponding time. Labels 1, 2 and 3 correspond to two reclining full-vaults and one half-vault, respectively. The evolution of their height is plotted in [Figure S3-C](#) (grey lines), which shows that it does not vary significantly as a consequence of AFM imaging. From time 103 minutes onwards consecutively higher-resolution images of full particle 1

←

(continued) were taken (green square, frame #23). Even at this higher-resolution ($200 \times 200 \text{ nm}^2$) the height of the particle was roughly maintained (grey line 1, [Figure S3-C](#)). (B) Evolution of the structural transition caused by lowering the pH at a faster exchange rate (in comparison with the experiments shown in [Figure 3](#)). Each frame is labeled with the time and the corresponding pH. Frame #1 ($t=0 \text{ min}$) shows the initial configuration, with the particles labeled from F1 to F4 (all the particles were full-vaults). Particles F1 and F3 were likely damaged from the beginning, which caused a lower initial height. (C) Evolution of the height for the experiments shown in [S3-A](#) and [S3-B](#). The color bar at the bottom indicates the pH exchange, from 7.5 (purple) to 5.2 (yellow). The asterisks indicate the pumping setting: onset of infusion (*) and complete pH exchanged (**). Particles collapsed after only ~60 minutes because pH 5.2 was reached faster. Color scale bar: white-golden-purple, from the highest to the substrate.

Supporting Information to Chapter 4

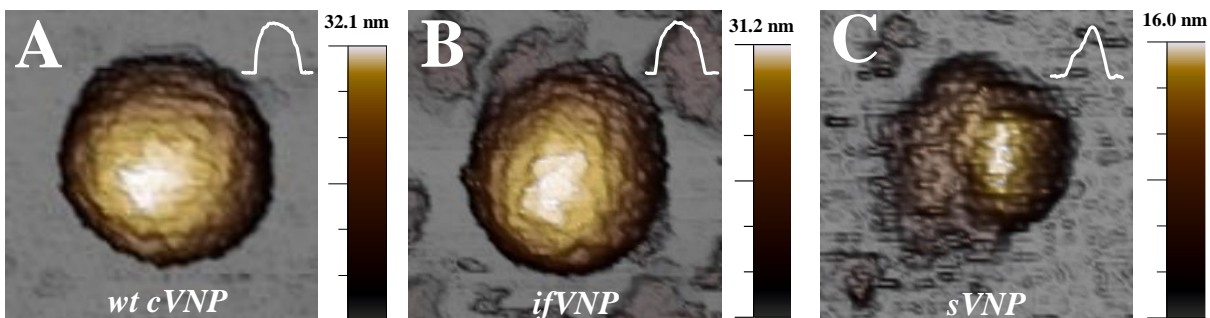


Figure S1. High-resolution JM-AFM topographies of the different forms of TBSV-NPs. (A, B, C) JM-AFM topography images acquired in liquid, of a *wt cVNP*, a *ifVNP* and a *sVNP*, respectively (insets). Profiles of the particles were taken along the central part. The image and profile of the *sVNP* show that the particle was collapsed upon absorption, as indicated by the lower height and the form of the structure.

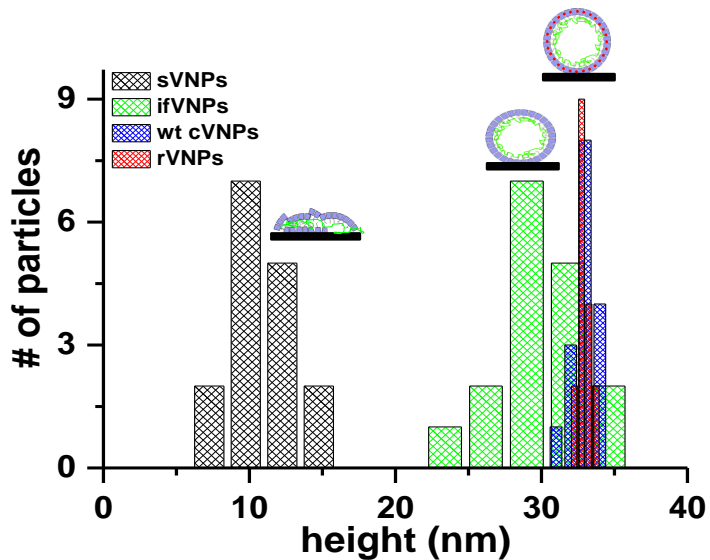


Figure S2. Height histogram of the different forms. *sVNs* and *ifVNs* present a higher dispersion in height than the native structure.

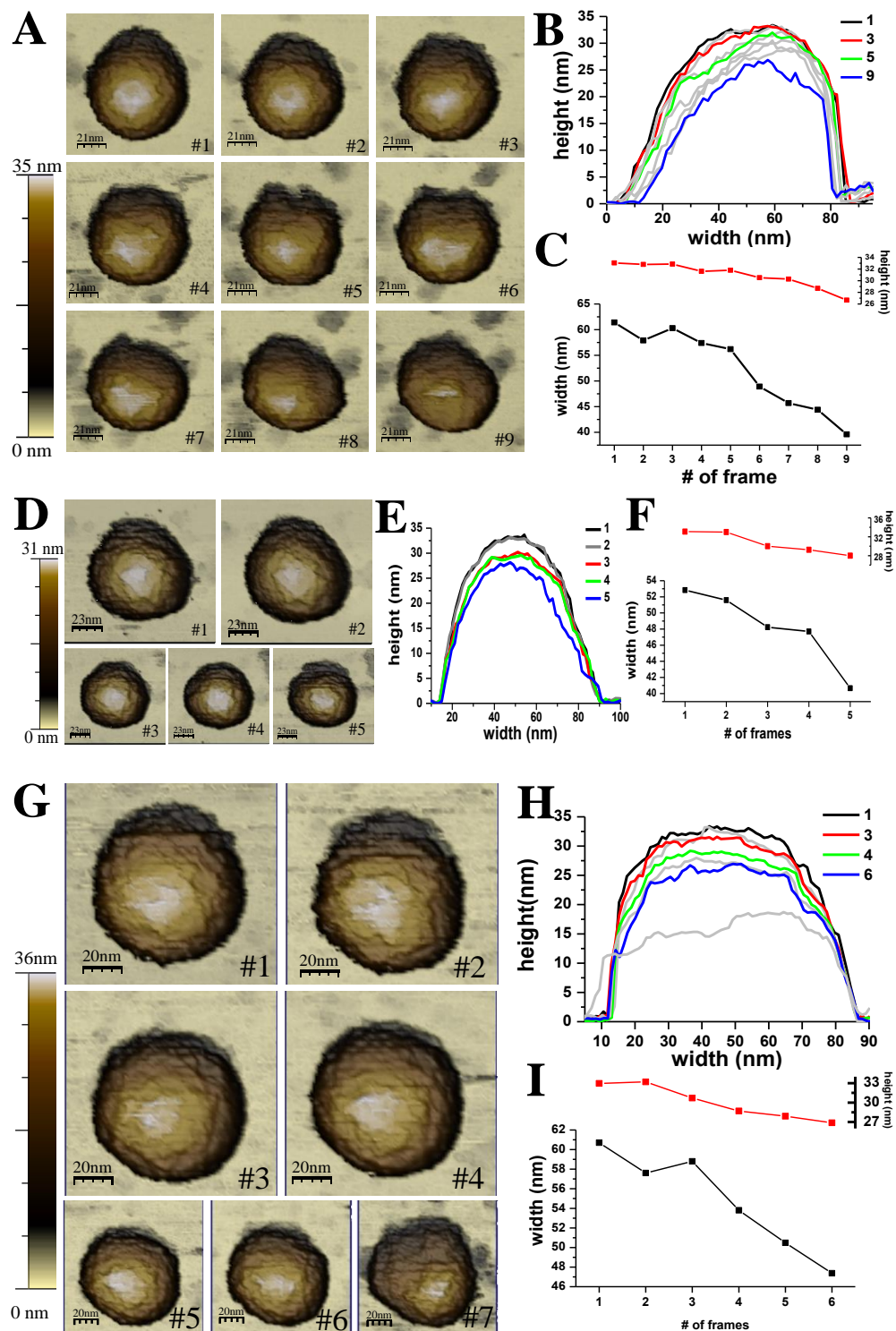


Figure S3. Evolution of wt cVNPs during an experiment of cyclic loading. (A) Evolution of JM-AFM topographical image of an individual wt cVNP during an experiment of cyclic loading. A single FIC was performed between consecutive images (B) Evolution of the profile of the wt cVNP taken along the central part of the structure. (D) Evolution of the width and height of the particle. The height corresponds to the maximum height of the profile and the width was measured at half of the height. (D, E, F and G, H, I) The same experiment performed on two others single wt cVNPs.

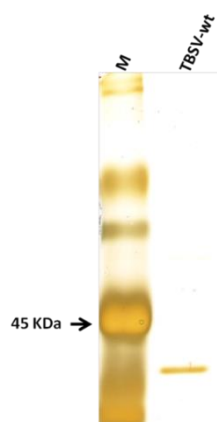


Figure S3. Evaluation of particles purification. Silver stained SDS-PAGE of purified TBSV-wt (1 μ g, lane 2). M, Standard molecular-weight size marker (lane 1).

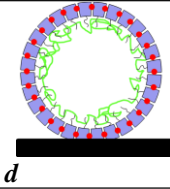
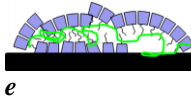
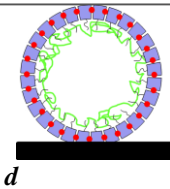
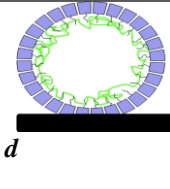
Acronym	Type of VNPs	Description	Height (nm)	Elastic constant ^a (N/m)		Elastic limit ^b (nN)		Sketch ^c
				FIC1	FIC2	FIC1	FIC2	
<i>wt cVNPs</i>	wild type Compact VNPs	Purified wt VNPs.	32.8±0.2	(0.72±0.09)	(0.51±0.07)	(3.20±0.25)	(1.75±0.20)	
<i>sVNPs</i>	Swollen VNPs	wt cVNPs put under swelling conditions by increasing the pH in the presence of EDTA, in order to induce the deprotonation of the Ca ²⁺ binding sites and the sequestration of these ions	Collapse into structures with an average height of 10±1	—	—	—	—	
<i>rVNPs</i>	Recompactd VNPs	The Ca ²⁺ binding sites of the sVNPs were protonated again by incubating the sVNPs by lowering the pH in a specific buffer containing a high concentration of Ca ²⁺ ions.	32.9±0.1	—	—	—	—	
<i>ifVNPs</i>	Ions free VNPs	sVNPs recompactd by lowering the pH but without supplying of Ca ²⁺ ions.	29.9±0.7	(0.55±0.07)	(0.36±0.03)	(1.90±0.15)	(1.7±0.1)	

Table 1. A brief description and some experimental results of the investigated viral nanoparticles (VNPs). All the values are given as (mean±SE); 11 wt cVNP and 16 ifVNPs were considered to determine the mechanical properties. ^a The elastic constants were obtained by linearly fitting the first part of the Force vs Indentation Curves (FICs); ^b the elastic limit is defined as the maximum force reached at the end of the linear deformation; ^c representations of the different VNPs forms: red dots are referred to the Ca²⁺ ions located at the specific binding sites ^d acidic buffer (NiCl₂ 5 mM, Na-acetate 50 mM, pH 5.3) and ^e swelling buffer (TRIS-HCl 0.1 M, pH 8.5, EDTA 50 mM). JM-AFM images were acquired under these buffer conditions.

Supporting Information to Chapter 5

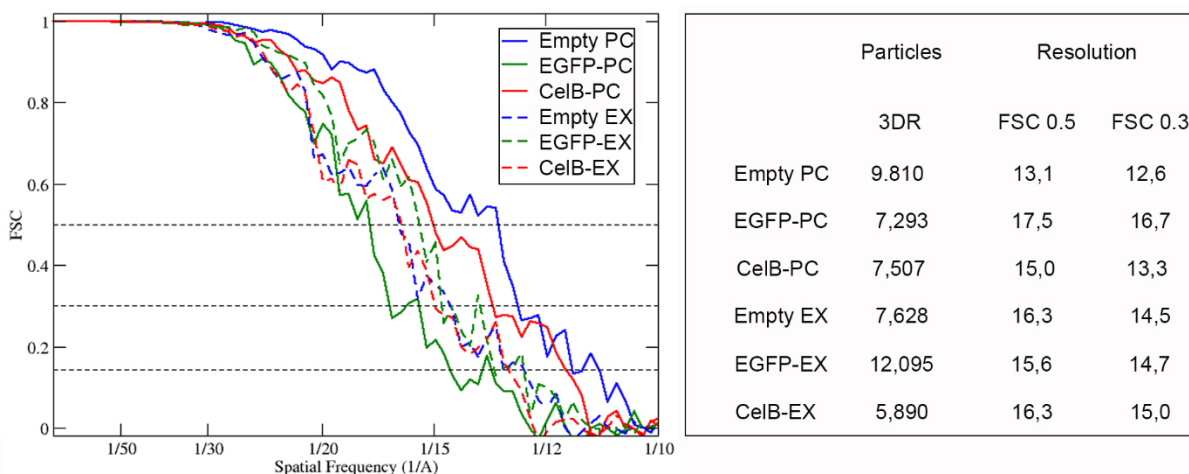


Figure S1. Resolution of empty procapsid (PC), EGFP- and CelB-PC, empty expanded particles (EX), EGFP- and CelB-EX. Fourier shell correlation (FSC) resolution curves were calculated for empty PC (blue), EGFP-PC (green), CelB-PC (red), empty EX (dashed blue), EGFP-EX (dashed green) and CelB-EX (dashed red). Number of particles included in the 3DR, and resolutions based on 0.5 and 0.3 criteria are indicated.

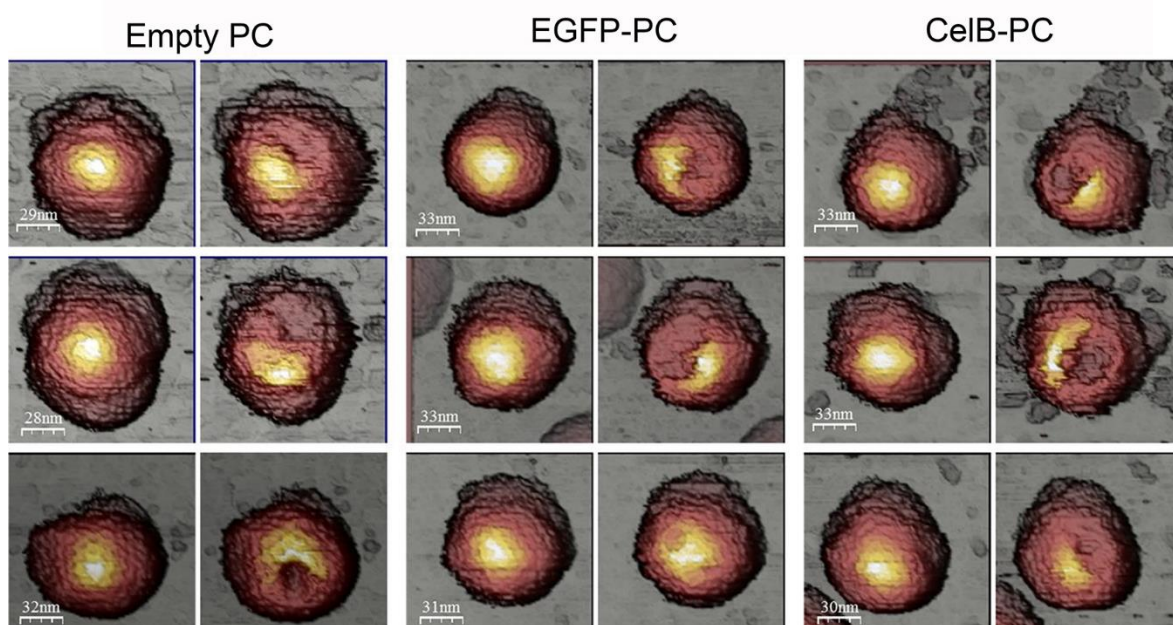
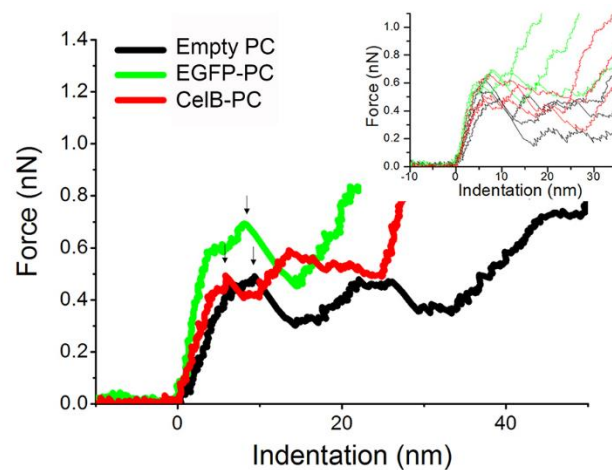


Figure S2. AFM nanoindentation on empty and loaded PC. (Top) Comparison of three typical nanoindentation curves for an empty PC (black), EGFP-PC (green) and CelB-PC (red). We observed a non-linear regime before particle breakage (arrows). (Inset) Other examples of PC FIC. (Bottom) AFM images of PC before (left) and after a single nanoindentation (right). Images show clear damage to the particle shell.

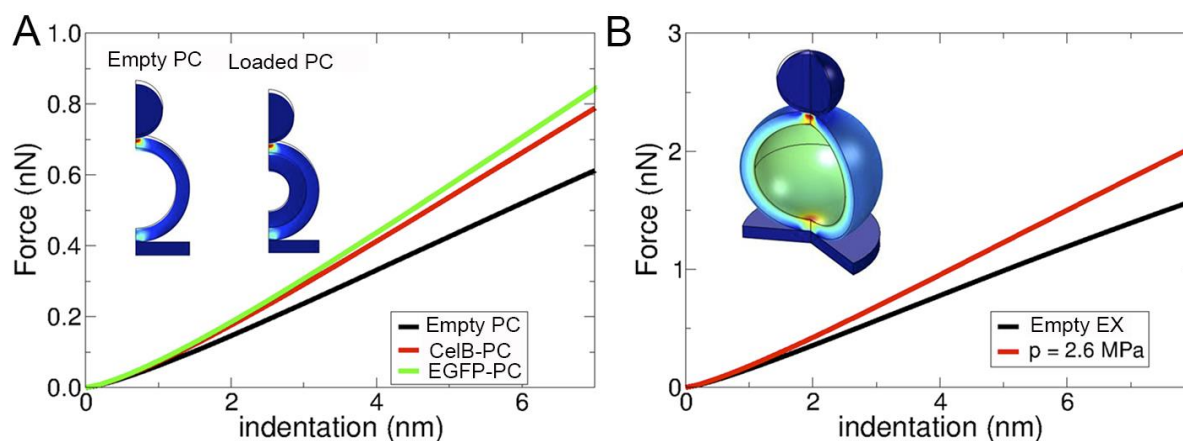


Figure S3. (A) Force-indentation curves obtained from Finite Element Simulations that mimic AFM experiments for PC. The empty PC is represented as a spherical shell with an external radius $R = 29.8$ nm and 7.5 nm thickness, indented on a hard substrate by a spherical tip with radius $R_{in} = 15$ nm. The Young modulus of the PC was $E = 58$ MPa, chosen to yield the same spring constant value as in experiments for empty PC. The cargo effect is modeled by addition of a second, 10-nm-thick layer (2D transverse sections, inset). The graph shows the values for the empty PC (black line); CelB-PC (red) and EGFP-PC (green) are shown with a second internal layer of $E = 6$ and $E = 8$ MPa, respectively. (B) Force-indentation curves obtained from Finite Element Simulations that mimic the AFM experiments for EX. The graph shows the values for an unpressurized empty EX (black line) and an EX (red) with an internal pressure of 2.6 MPa. The inset shows the model used for simulations, where EX is shown as a 6.6-nm-thick spherical shell with an external radius $R = 32.4$ nm, indented on a hard substrate by a spherical tip with a radius $R_{in} = 15$ nm. The Young modulus of the capsid was $E = 178$ MPa, chosen to yield the same spring constant value as in experiments for empty EX.

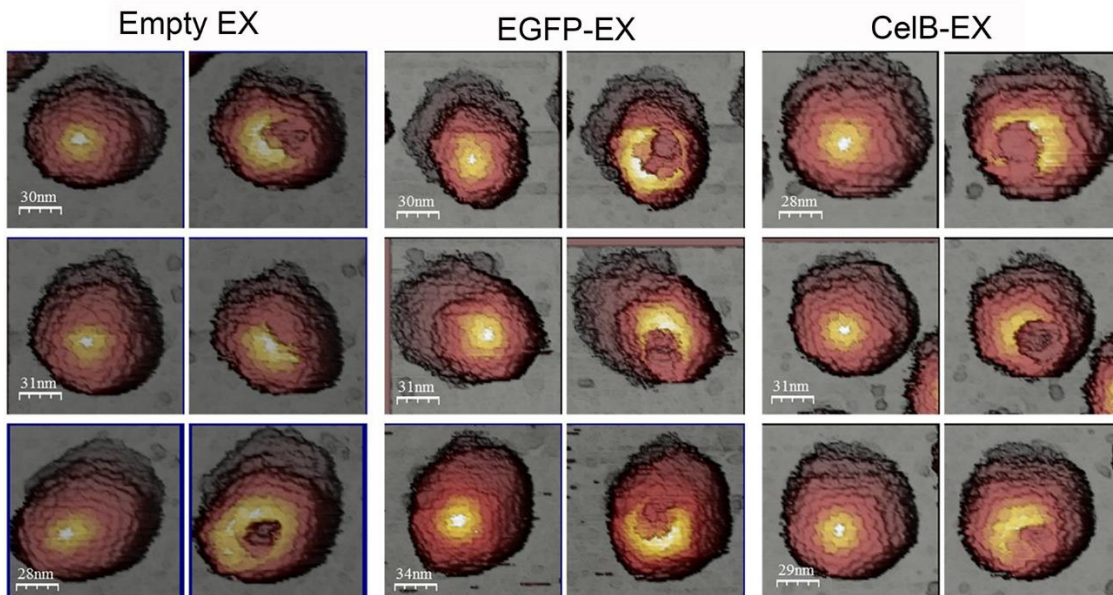
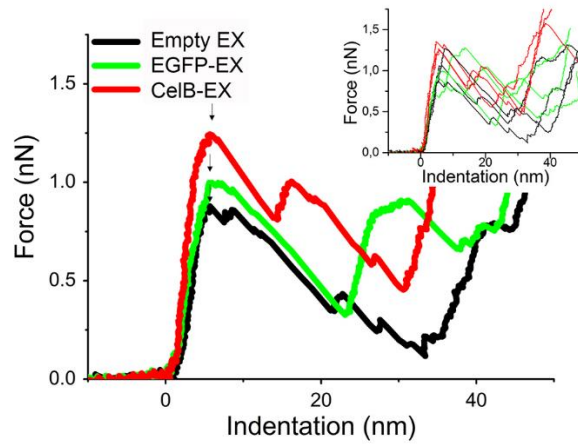


Figure S4. AFM nanoindentation on empty and loaded EX. (Top) Comparison of three typical nanoindentation curves for an empty EX (black), EGFP-EX (green) and CelB-EX (red). Particle breakage is indicated (arrows). (Inset) Other examples of EX FIC. (Bottom) AFM images of EX before (left) and after a single nanoindentation (right). Images show loss of some capsid subunits.

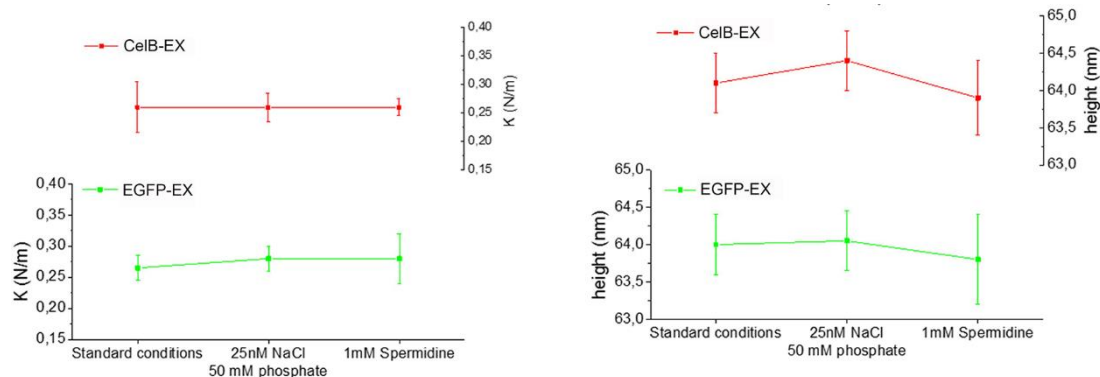


Figure S5. AFM indentations of CelB- and EGFP-EX in different buffers. We tested the effect of electrostatic interactions on cargo-loaded EX rigidity at low ionic strength (50 mM phosphate, 25 mM NaCl, pH 7) or in the presence of spermidine (100 mM phosphate, 50 mM NaCl, 1 mM spermidine, pH 7) compared to standard conditions (100 mM phosphate, 50 mM NaCl, pH 7). EGFP- and CelB-EX were tested similarly; each sample was incubated in standard buffer and its elastic constant measured by AFM, followed by buffer exchange first to lower ionic strength and then to spermidine buffer. No significant differences were found (Table S3). (A, B) Average elastic constant (A) and average height (B) of CelB-EX (red) and EGFP-EX (green) in different buffer conditions.

	Particles (n°)	Breaking force (nN)	K(N/m)	$\epsilon_{critical}$	Height (nm)	Relative deformation
Empty PC	32	0.56 ± 0.02	0.094 ± 0.006	0.18 ± 0.01	50 ± 1	0.84
EGFP-PC	35	0.68 ± 0.03	0.131 ± 0.005	0.17 ± 0.01	56.3 ± 0.5	0.94
CelB-PC	25	0.54 ± 0.03	0.12 ± 0.01	0.14 ± 0.01	56.5 ± 0.7	0.95
Empty shells ^a	12	0.53 ± 0.03	0.105 ± 0.004	0.17 ± 0.01	48 ± 1	0.81
Empty EX	24	1.02 ± 0.05	0.21 ± 0.01	0.13 ± 0.01	58 ± 1	0.90
CelB-EX	24	1.20 ± 0.07	0.27 ± 0.03	0.13 ± 0.01	63.3 ± 0.8	0.97
EGFP-EX	21	1.11 ± 0.05	0.27 ± 0.01	0.13 ± 0.01	62.7 ± 0.3	0.98

Table S1. Mechanical characterization of empty and loaded P22 PC and EX. The values show mean \pm SE of single particles. Breaking force is the maximum force reached before breakage. The elastic constant was determined by linear adjustment of the initial part of the FIC. Critical strain ($\epsilon_{critical}$) was calculated by dividing critical indentation by height. Particle height was determined from a profile of the center of its image. Relative deformation is the ratio of AFM height to nominal size from 3DR cryo-EM.

^acontrol experiment. Empty shells correspond to scaffolding-lacking procapsids.¹

	Volume ^a (nm ³)	Total cargo volume (nm ³)	Shell thickness (nm)	Net surface charge ^b (e)
PC	46,452 ^c		7.5	-
EX	71,936 ^d		6.6	-840 ^j
CelB (tetramer)	581 ^e		-	-37 ^k
EGFP	55 ^f		-	0 ^l
C _t helix-loop-helix	4.2		-	5 ^m
SP N _t linker	15.8 ^g		-	2 ⁿ
CelB & 4 SP	661	21,152 ^h	-	-288
EGFP & 1 SP	75	16,800 ⁱ	-	+1586

Table S2. Volume and charge of P22 PC, EX and their cargos

^aMeasurements were obtained by 3D cryo-EM analysis

^bNet surface charges were calculated as indicated in the VIPERdb server (<http://viperdbscripps.edu>); basically, net surface charge is calculated by adding the charges of the inner surface-exposed positive (Lys, Arg, His) and negative (Glu, Asp) residues.

^cVolume when a perfect sphere is assumed, PC inner radius = 223 Å (outer radius = 298 Å).

^dVolume when a perfect sphere is assumed, EX inner radius = 258 Å (outer radius = 324 Å).

^eCelB tetramer dimensions: 101 x 101 x 57 Å

^fEGFP monomer dimensions: 48 x 33 x 35 Å

^gVolume occupied by the SP segment 141-263

^hVolume for 32 CelB tetramers

ⁱVolume for 224 GFP monomers

^jThe EX asymmetric unit inner surface has a total charge of -14 e (39 Asp, 62 Glu, 23 Lys, 64 Arg).

^kThe CelB tetramer outer surface has 169 Asp, 283 Glu, 238 Lys, 92 Arg, and 85 His

^lThe GFP outer surface contains 12 Asp, 12 Glu, 16 Lys, 6 Arg and 2 His

^mThe SP C_t helix-loop-helix motif has 7 Asp, 1 Glu, 7 Lys and 3 Arg

ⁿThe SP N_t linker (residues 141-263) has 6 Asp, 10 Glu, 9 Lys, 8 Arg and 2 His

Buffer	CelB-EX			EGFP-EX		
	Particles (n°)	K (N/m)	Height (nm)	Particles (n°)	K (N/m)	Height (nm)
50 mM NaCl, 100 mM phosphate	9	0.26 ± 0.045	64.1 ± 0.4	4	0.27 ± 0.02	64 ± 0.4
25 mM NaCl, 50 mM phosphate	14	0.26 ± 0.025	64.4 ± 0.4	13	0.28 ± 0.02	64.05 ± 0.4
1 mM spermidine	17	0.26 ± 0.015	63.9 ± 0.5	7	0.28 ± 0.04	63.8 ± 0.6

Table S3. Elastic constant and height of CelB- and EGFP-EX in distinct ionic conditions

Finite element simulations of P22 PC and EX

Finite elements simulations of AFM indentation of P22 were performed using the COMSOL Multiphysics 4.3 program (Comsol, Stockholm, Sweden). In all cases, the capsid wall was considered to be made of a homogenous material, using Young Modulus E and Poisson ratio $\nu = 0.3$ (a standard value for protein-like materials). This model capsid was placed on a hard flat substrate and indented by a hard spherical object with radius $R_{in} = 15$ nm to mimic the AFM tip. The system was simulated using a 2D axisymmetric model meshed with over 3000-6000 triangular elements. Contacts were implemented between the shell and the tip as well as the supporting surface during indentation with a contact-penalty stiffness method according to manufacturer's protocols. A parametric, non-linear solver was used to simulate the stepwise lowering of the tip onto the capsid. The spring constant was derived from a linear fit of force v_s indentation for small indentations in the linear region between 2 and 6 nm.

The empty PC was modeled as a thick spherical shell with an external radius $R = 29.8$ nm and thickness $h = 7.5$ nm (Figure S2A, inset). The presence of cargo attached to the PC was modeled by adding a second layer beneath the capsid layer with a different Young's modulus and 10 nm thick (estimated from 3DR cryo-EM radial density profiles). The indentation curves obtained for the model PC with a $R_{in} = 15$ nm tip and Young modulus value $E = 58 \pm 4$ MPa, chosen to reproduce the experimental value of the empty PC spring constant (0.094 ± 0.006 N/m), is shown in Figure S2A. The indentation curves for two PC with the internal second (cargo) layer showed Young's modulus values of 6 MPa and 8 MPa, yielding spring constants of $k = 0.12$ and $k = 0.131$ N/m, identical to the experimental values measured for CelB-PC and EGFP-PC, respectively. The effective Young's modulus for the cargo is thus nearly 10 times smaller for CelB and 7 times smaller for EGFP than that of the PC shell.

The empty EX was modeled as a thick spherical shell with an external radius $R = 32.4$ nm and thickness $h = 6.6$ nm (Figure S2B, inset). Finite elements simulations were used to corroborate pressure estimates based on the Vela formula. Indentation curves for the model EX capsid with a $R_{in} = 15$ nm tip and a Young modulus value $E = 0.178 \pm 0.009$ GPa, chosen to reproduce the experimental spring constant value of empty EX (0.21 ± 0.01 N/m), are shown in Figure S2B. The indentation curve when EX internal pressure is 2.6 MPa, which yields a spring constant $k = 0.27$ N/m, is identical to the experimental value measured for the

cargo-loaded EX. The estimated pressure in finite element simulations is thus 2.6 ± 1.1 MPa, compatible with the value obtained from the Vela formula (Eq. 1, main text).²

Electrostatic contributions to osmotic pressure in EX

The cargo can be considered a solution of N effective charged spheres in an electrolyte with a Debye length given by the salt concentration of the buffer (100 mM phosphate, 50 mM NaCl, yielding $\kappa^{-1} = 0.796$ nm). Electrostatic repulsion between the cargo molecules is screened by the buffer salt and is described using the electrostatic repulsion part of the DLVO potential between two charged spheres; this allows calculation of the second virial coefficient B_2 , which quantifies the leading electrostatic contribution to the osmotic pressure. In the simplest approximation of treating the cargo as point charges,³

$$B_2 = \frac{z^2}{2\Sigma}$$

Where Σ is solvent ionic strength and z is the charge of cargo molecules, in elementary charge units. The resulting contribution to the osmotic pressure is

$$\Pi_{elect} = k_B T \rho^2 B_2$$

For CelB, with an estimated charge of 9 electrons ($Z = -9$; [Table S2](#)) per tetramer (which includes the SP charge),

$$p \approx k_B T \rho^2 B_2 = 180 Pa$$

For EGFP, with an estimated positive charge of 7 ([Table S2](#)),

$$p \approx k_B T \rho^2 B_2 = 5000 Pa$$

In both cases, this contribution is negligibly small and cannot explain the large pressure values derived in the nanoindentation experiments.

The electrostatic contribution to the osmotic pressure can also be estimated through the Donnan equilibrium, by which the chemical equilibrium between the capsid interior and exterior, with a fixed charge that cannot escape from the capsid, leads to a higher interior counterion concentration that is responsible for the osmotic pressure. The osmotic pressure here can be evaluated as described,⁴ to yield

$$\Delta\Pi = k_B T \left(\sqrt{n_0^2 - n_b^2} - 2n_b \right)$$

where n_0 is net charge density of the cargo and n_b is bulk salt density (~150 mM here).

The interior charge density can be estimated as $n_0 = \frac{zN}{V_{capsid} - V_{cargo}}$, where we subtract the volume occupied by the cargo. For CelB with $z = -9$ per tetramer:

$$\Delta\Pi = k_B T \left(\sqrt{n_0^2 - n_b^2} - 2n_b \right) = 370 \text{ Pa}$$

For EGFP with $z = 7$ per molecule:

$$\Delta\Pi = k_B T \left(\sqrt{n_0^2 - n_b^2} - 2n_b \right) = 9800 \text{ Pa}$$

In this case, the electrostatic contribution is thus also negligibly small.

To summarize, the osmotic pressure is dominated by packing effects, since the electrostatic contribution is negligible. This was confirmed by AFM nanoindentations, which showed no change in the elastic constants, independently of the presence of spermidine (which further screens electrostatic interactions) or when ionic strength was reduced.

References

- 1 Thuman-Commike, P. A. *et al.* Mechanism of scaffolding-directed virus assembly suggested by comparison of scaffolding-containing and scaffolding-lacking P22 procapsids. *Biophys J* **76**, 3267-3277, (1999).
- 2 Vella, D., Ajdari, A., Vaziri, A. & Boudaoud, A. The indentation of pressurized elastic shells: from polymeric capsules to yeast cells. *J R Soc Interface* **9**, 448-455, (2012).
- 3 Hill, T. L. *An introduction to statistical thermodynamics.* (Courier Corporation, 2012).
- 4 Cordova, A., Deserno, M., Gelbart, W. M. & Ben-Shaul, A. Osmotic shock and the strength of viral capsids. *Biophys J* **85**, 70-74, (2003).

Supporting Information to Chapter 6

	S5		S3/S2	
	# of particles	%	# of particles	%
EX	29	59	20	41
EX+Dec	37	70	16	30
WB	25	66	13	34
WB+Dec	34	68	16	32

Table S1. Adsorption frequency depending on symmetry. The number of single particles and its corresponding percentage are shown.

		S5			S3/S2		
		# of particles	mean	SE	# of particles	mean	SE
EX	Fbreaking (nN)	16	1,05	0,03	14	1,14	0,05
	K (N/m)	16	0,20	0,01	14	0,19	0,02
	$\delta_{critical}$ (nm)	16	9,5	0,8	14	11,4	1,2
	Height (nm)	16	57	1	14	50	1
	$\epsilon_{critical}$	16	0,16	0,02	14	0,23	0,02
	Energy ($K_B T$)	16	1257	138	14	1624	237
EX+DEC	Fbreaking (nN)	21	1,26	0,05	13	1,3	0,1
	K (N/m)	21	0,23	0,02	13	0,19	0,03
	$\delta_{critical}$ (nm)	21	11,5	0,9	13	11,5	1,5
	Height (nm)	21	56,8	0,6	13	52,1	1,0
	$\epsilon_{critical}$	21	0,20	0,02	13	0,22	0,03
	Energy ($K_B T$)	21	1799	213	13	1821	436
WB	Fbreaking (nN)	18	1,07	0,07	11	0,66	0,04
	K (N/m)	18	0,15	0,01	11	0,14	0,01
	$\delta_{critical}$ (nm)	18	10,9	1,3	11	8,69	0,92
	Height (nm)	18	52,84	0,57	11	46	1
	$\epsilon_{critical}$	18	0,21	0,01	11	0,19	0,02
	Energy ($K_B T$)	18	1457	266	11	716	120
WB+DEC	Fbreaking (nN)	21	1,12	0,04	9	0,96	0,09
	K (N/m)	21	0,14	0,01	9	0,13	0,01
	$\delta_{critical}$ (nm)	21	14,17	0,56	9	12	1
	Height (nm)	21	55,55	0,52	9	51	1
	$\epsilon_{critical}$	21	0,26	0,01	9	0,23	0,02
	Energy ($K_B T$)	21	1984	146	9	1421	273

Table S2. Mechanical characterization. Breaking force, elastic constant (k), critical indention ($\delta_{critical}$), height and critical strain ($\epsilon_{critical}$) for the different morphologies: EX, EX+Dec, WB and WB+Dec. SE: standard error.

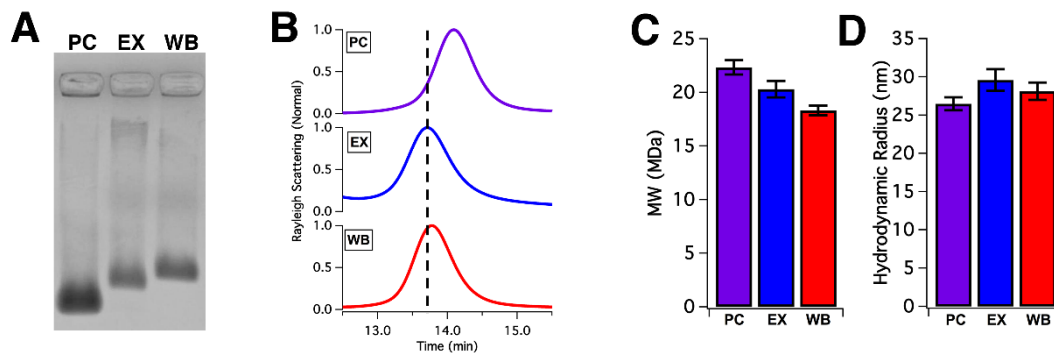


Figure S1. Characterization of capsids shows complete expansion of EX and subsequent penton loss in WB. (A) Non-denaturing agarose gel shift of PC, EX and WB capsid samples. (B) SEC chromatograms of PC, EX and WB displaying the Rayleigh scattering ratio. Dashed line marks the retention time of EX and WB. (C) Average hydrodynamic radius of PC, EX and WB measured across the peak width at half max of the SEC chromatograms. (D) Number average molecular weight of PC, EX and WB samples measured by multi-angle light scattering. Error bars represent the standard error on the mean.

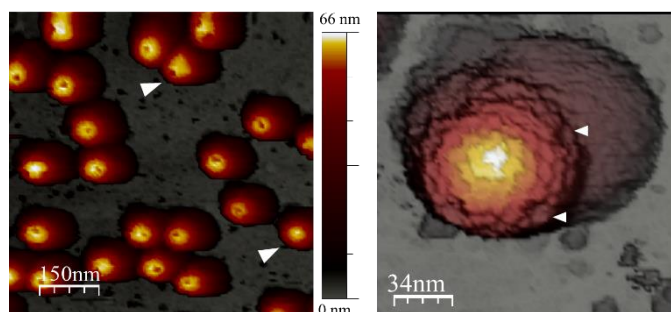


Figure S2. AFM images of WB presenting some of the pentons. (left) Large AFM view. The white arrowheads indicate a particles adsorbed along the 3- and 5-fold symmetry axes showing some pentons. (right) High-resolution of a WB with a penton on the top. The arrowheads indicate two penton vacancies.

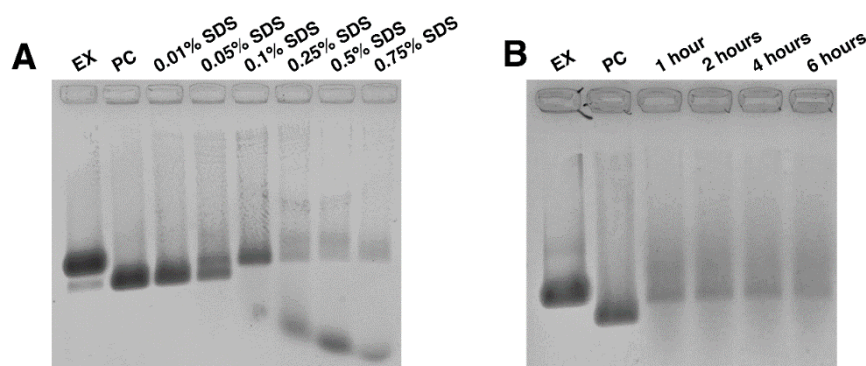


Figure S3. SDS expands and then degrades the P22 VLP. (A) PC VLP incubated in increasing concentrations of SDS for 15 minutes. (B) Extended incubation of PC in 0.1% SDS. In both gels a PC and heat-expanded EX control are included for reference.

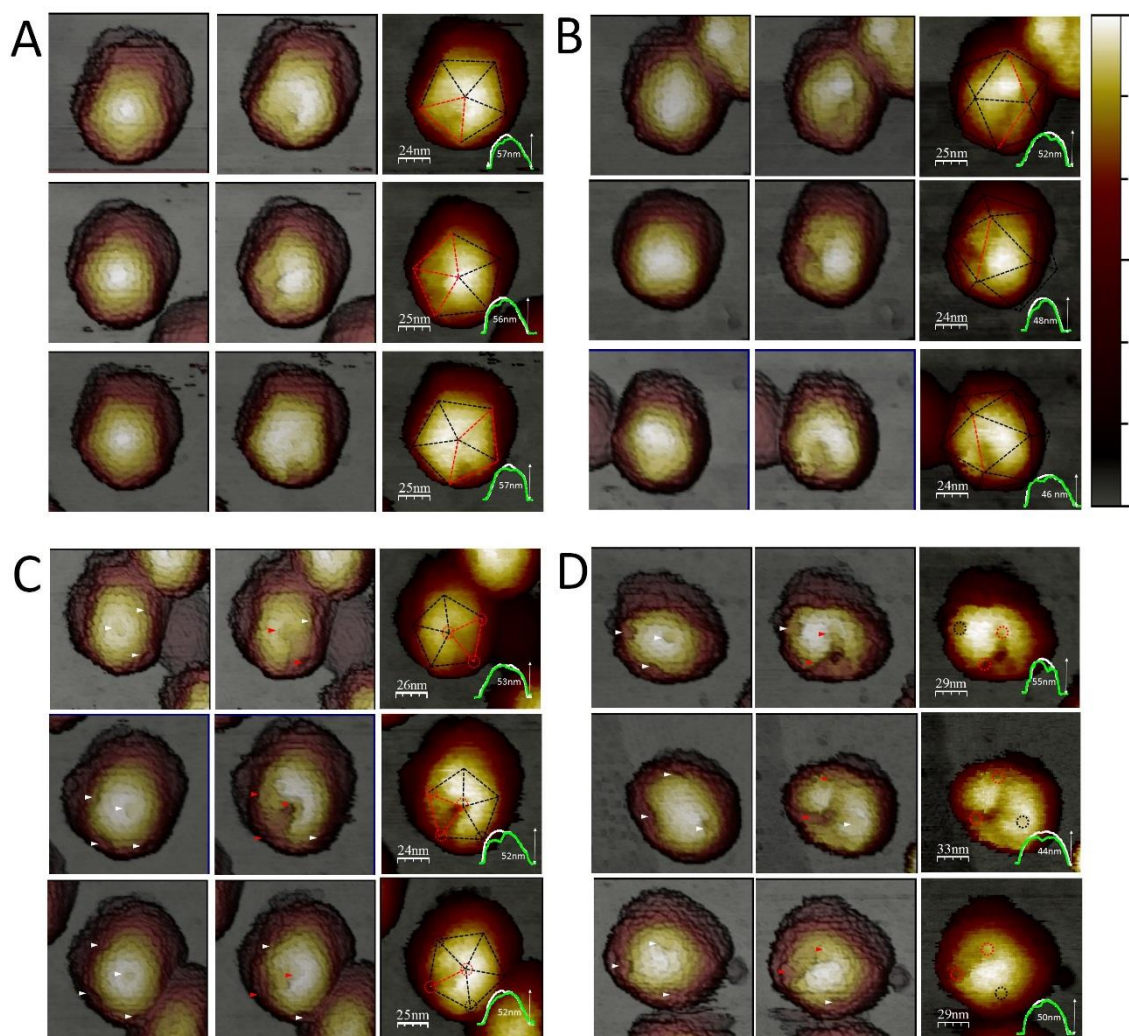


Figure S3. Pattern of breakage. (A) Each row: 3D AFM image of an EX capsid in the S5 axes before and after the nanoindentation (left and middle). The image on the right side shows a 2D representation of the particle after the breakage. A pentagon with its 5 faces is overlapped to the structure (dash lines). The red lines highlighted the parts of the particles that were clearly affected. (inset) Profile of the particle before (white) and after (green line) the damage. (B) As before but with three EX capsids along their S3 axes. In this case the 2D AFM images (right) shows an icosahedron along its 3- or 2-fold symmetry. (C) Each row: 3D AFM images of a WB along the S5 axes before and after the nanoindentation (left and middle). The arrows point the position of the missing pentons (in red are represented the sites involved during the breakage). The image on the right shows a 2D representation of the particle after the breakage. A pentagon with its 5 faces is overlapped to guide the eye (dash lines). In red are represented the regions affected by the damage. The insets show the profile of the capsids before and after the breakage. (D) As in (C) but with the WB along its 3-fold symmetry axes.

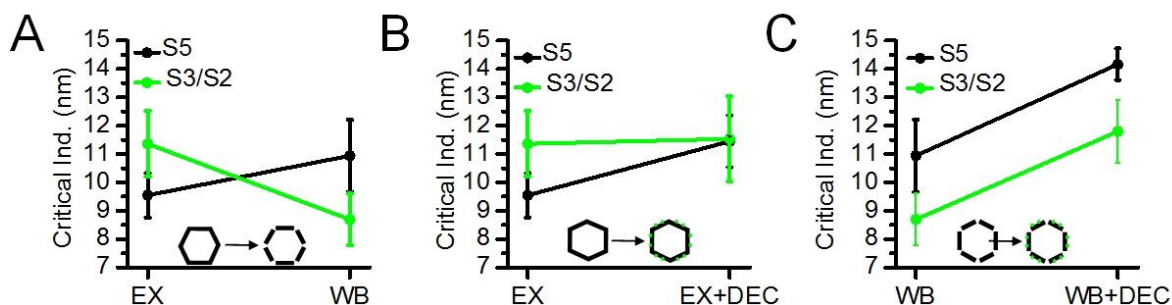


Figure S4. (A) Evolution of the critical indentation (δ_{critical}) along the EX \rightarrow WB transition. (B) Evolution of the critical indentation (δ_{critical}) along the EX \rightarrow EX+Dec transition. (C) Evolution of the critical indentation (δ_{critical}).

EX			WB		
Interface	Symmetry	Association Energy(kcal/mol)	Interface	Symmetry	Association Energy(kcal/mol)
F1-G1	Q-3	-14.8	C7-E1	Q-3	-28.7
B1-C10	Q-3	-14.2	B1-C10	Q-3	-24.6
C7-E1	Q-3	-13.9	D1-D7	I-3	-24.1
A1-G2	Q-3	-13.2	B1-E2	Q-3	-23.6
B1-E2	Q-3	-12.7	B1-C1	Q-6	-17.2
D7-E1	Q-2	-9.1	E1-F1	Q-6	-17.1
A1-F2	Q-3	-7.2	A1-B1	Q-6	-14.8
B1-F2	Q-2	-7.1	A1-F2	Q-3	-13.8
A1-G1	Q-2	-6.7	D1-E1	Q-6	-12.9
C1-C10	I-2	-6.5	C1-D1	Q-6	-12.0
D1-D7	I-3	-5.5	A1-F1	Q-6	-5.7
B1-C1	Q-6	-4.4			
A1-F1	Q-6	-1.7			
C1-D1	Q-6	-1.2			
E1-F1	Q-6	-0.5			

Table S3. Association energy between inter- and intra capsomeric subunits for EX and WB. The association energy was calculated based on the buried surface areas (information was extracted from ViperDB).¹ In black are represented interaction existing in both forms, in red and blue interfaces lost due to the transition, and in green interactions gained due to the transition. Note that red corresponds to interactions with the pentons (subunit G) and blue to interactions between hexamers. All the gained interactions were within an hexamer subunit (green) (see Figure X for position of the interfaces).

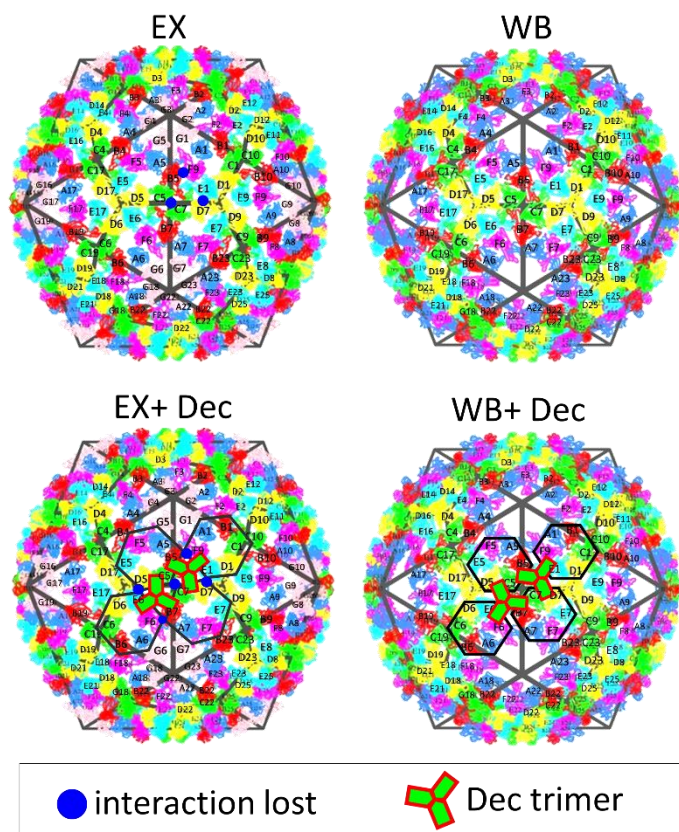


Figure S5. Interaction energy between subunits (based on table S3). Hexameric subunits (A-G) are colored in blue, red, green, yellow, cyan and pink, respectively. Pentameric subunits (G) are colored in pale pink. (*top*) Comparison of EX and WB forms (PDB: 3iyi and 3iyh)². Blue dots in EX represent the interfaces where the interactions were lost after the transition. (*bottom*) Comparison of EX+Dec and WB+Dec. The position of two Dec trimer are superimposed on the structures; each trimer lays between three hexamers (marked with a solid black line)^{3,4}. Note that the trimer reinforces the position where the interactions were lost after the transition.

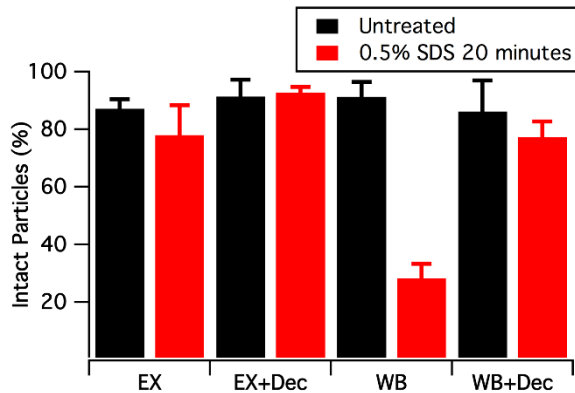


Figure S6. Percentage of undamaged structures observed by TEM.

References

- 1 Carrillo-Tripp, M. *et al.* VIPERdb2: an enhanced and web API enabled relational database for structural virology. *Nucleic Acids Res* **37**, D436-442, (2009).
- 2 Parent, K. N. *et al.* P22 Coat Protein Structures Reveal a Novel Mechanism for Capsid Maturation: Stability without Auxiliary Proteins or Chemical Crosslinks. *Structure* **18**, 390-401, (2010).
- 3 Parent, K. N. *et al.* Stepwise molecular display utilizing icosahedral and helical complexes of phage coat and decoration proteins in the development of robust nanoscale display vehicles. *Biomaterials* **33**, 5628-5637, (2012).
- 4 Tang, L., Gilcrease, E. B., Casjens, S. R. & Johnson, J. E. Highly discriminatory binding of capsid-cementing proteins in bacteriophage L. *Structure* **14**, 837-845, (2006).

Supporting Information to Chapter 7

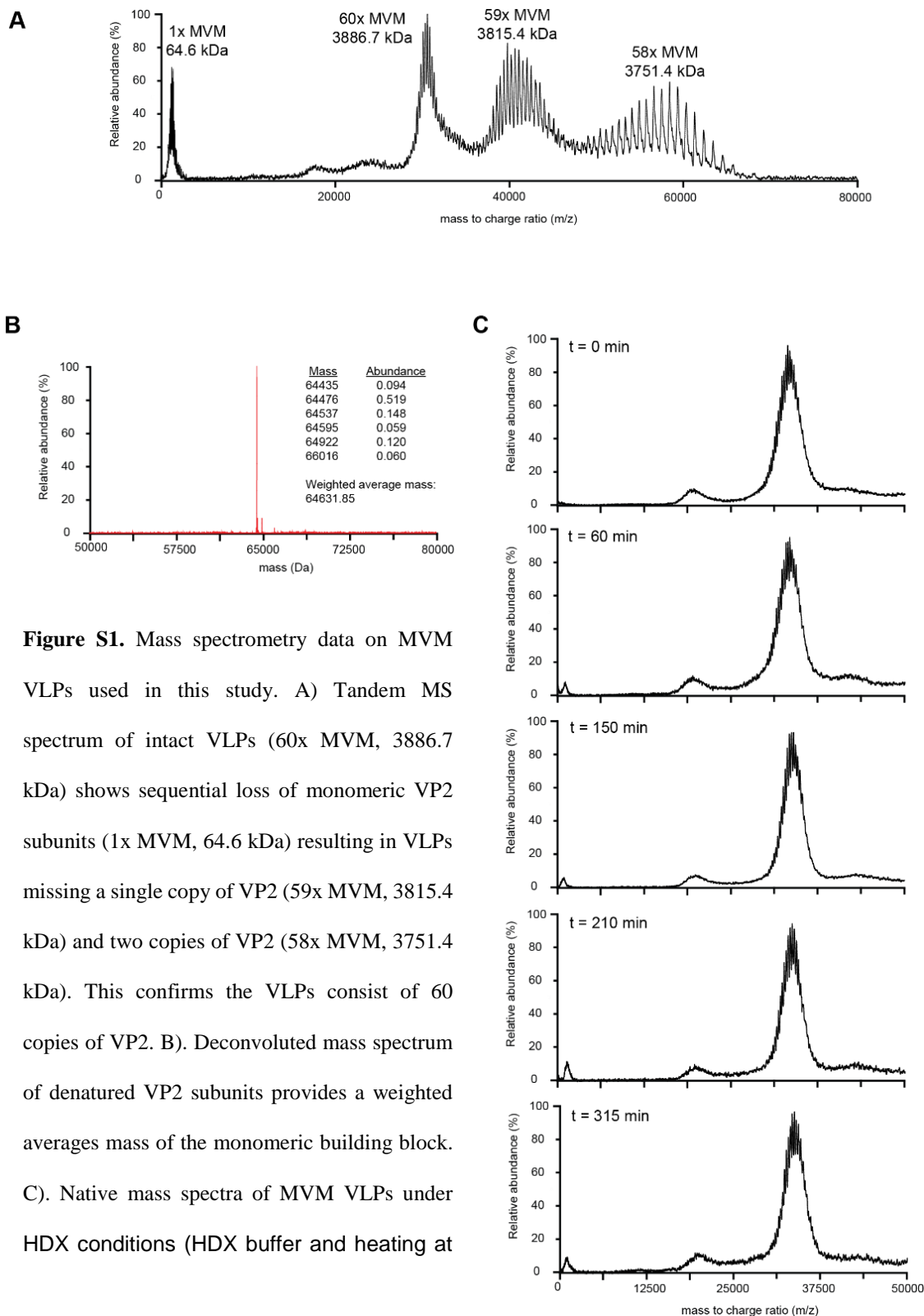


Figure S1. Mass spectrometry data on MVM VLPs used in this study. A) Tandem MS spectrum of intact VLPs (60x MVM, 3886.7 kDa) shows sequential loss of monomeric VP2 subunits (1x MVM, 64.6 kDa) resulting in VLPs missing a single copy of VP2 (59x MVM, 3815.4 kDa) and two copies of VP2 (58x MVM, 3751.4 kDa). This confirms the VLPs consist of 60 copies of VP2. B). Deconvoluted mass spectrum of denatured VP2 subunits provides a weighted averages mass of the monomeric building block. C). Native mass spectra of MVM VLPs under HDX conditions (HDX buffer and heating at

Peptide classification

Peptides whose error bar fell into the linear region (*line of slope $m=1$* , dashed line) were considered as not presenting a significant difference in deuterium uptake before and after the temperature transition, T_M . Likewise, peptides falling above or below the linear region were sorted as ‘increase in deuteration after the transition’ (in green, Figure 4) or ‘decrease in deuteration after the transition’ (in purple, Figure 4).

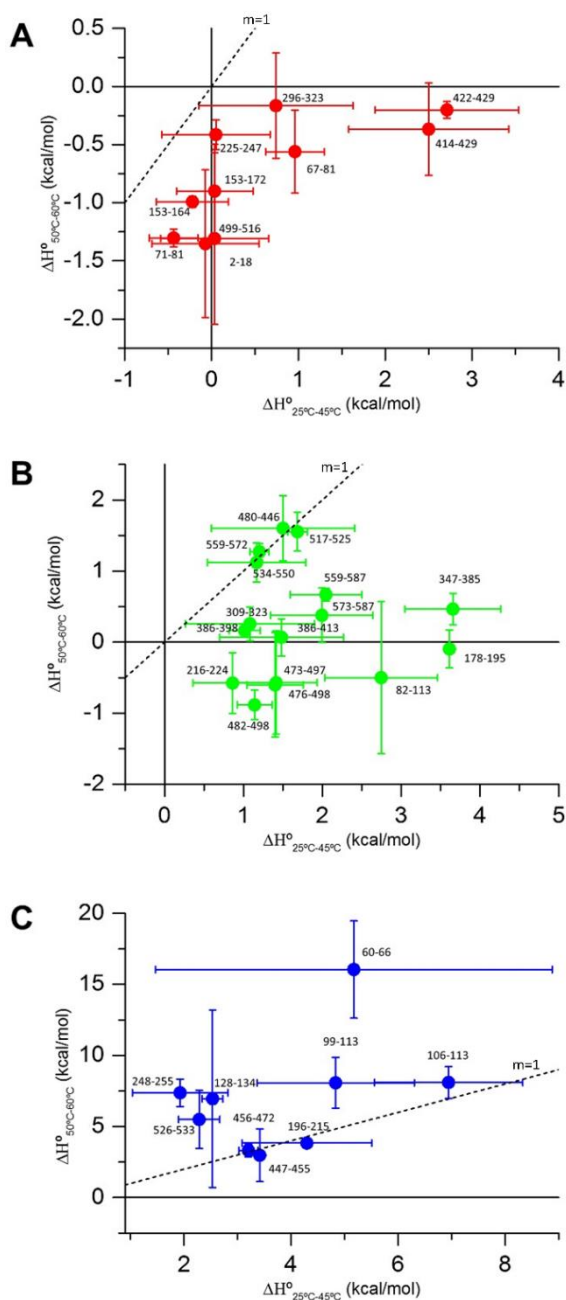


Figure S2. Average enthalpy before and after the temperature-induced transition. (a) Average enthalpy from 50°C to 60°C *versus* 25°C to 45°C for each peptide presenting a high basal uptake (35 to 100%). Dashed line corresponds to a line with a slope equal to the unit, where peptides presenting the same level of uptake before and after the transition should fall. (b, c) The same than before but for peptides presenting medium (16 to 34%, green) and low (0 to 15%) uptake at the basal state.

Red (35 to 100% basal uptake)	Flat región (region 4)	2-18, 67-81, 71-81, 153-164, 153-172, 225-247, 296-323, 499-516.
	Saturation (region 1)	414-429, 422-429
Green (16 to 34% basal uptake)	Linear increase (m=1) (region 2)	309-323, 430-446, 517-525, 534-550, 559-572
	Decrease deuteration after T _M (region 1)	82-113*, 178-195, 216-224, 347-385, 386-413, 386-398, 473-497, 476-498, 482-498, 573-587, 559-587
Blue (0 to 15% basal uptake)	Linear increase (m=1) (region 2)	106-113, 196-215, 447-455, 456-472,
	Increase deuteration After T _M (region 3)	60-66, 99-113*, 128-134, 248-255, 526-533

Table S1. Peptides classification according to deuterium uptake before and after the transition. *Because peptides 82-113 and 99-113 present overlapping sequence; we split their sequences in two (i.e., 82-100 and 101-113) to map them on the structure.

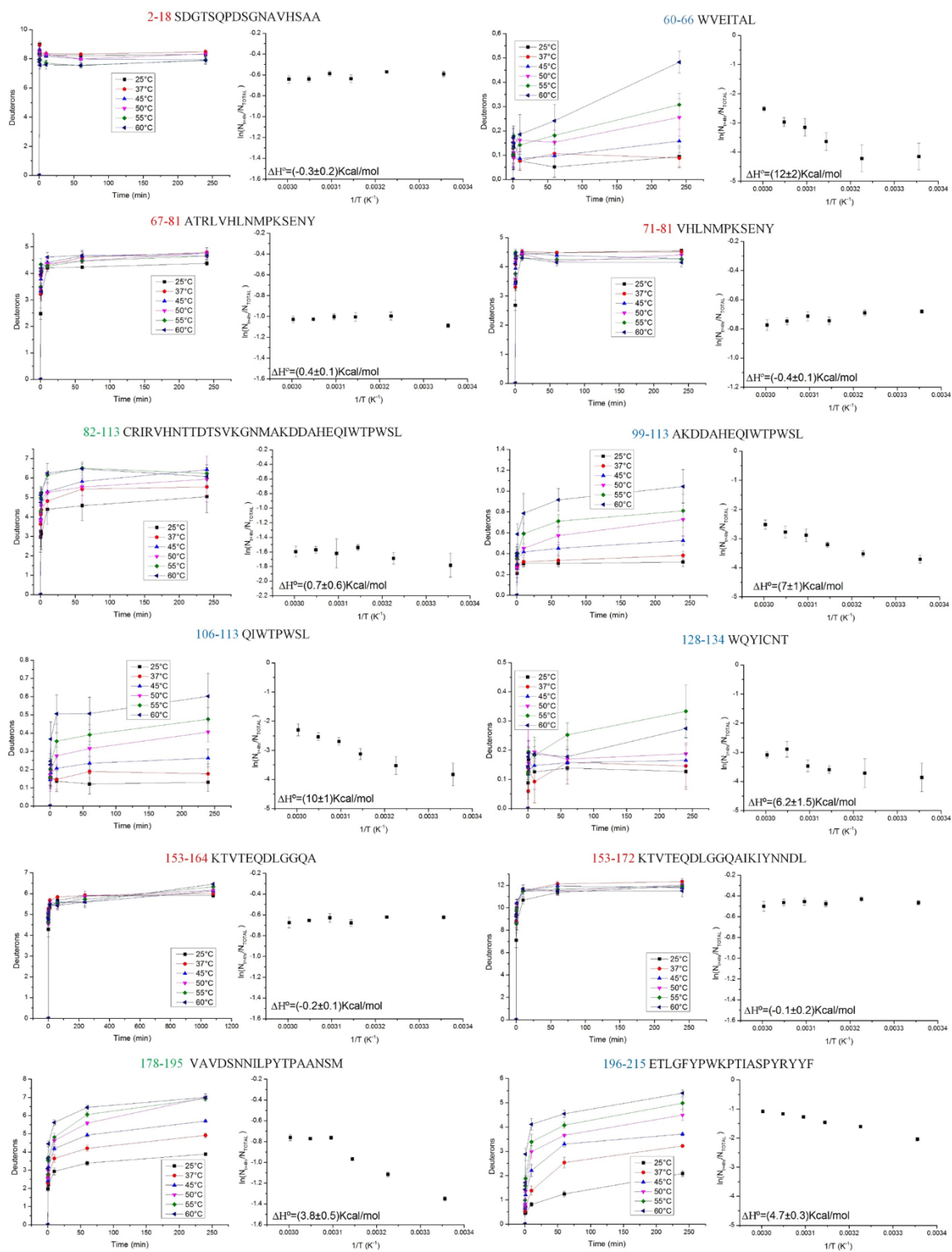


Figure S3. HDX time courses as a function of temperature are represented together with the corresponding Arrhenius plot. The peptide sequence is shown on top of each figure, with the color (red, green, and blue) indicating the level of uptake in the basal state.

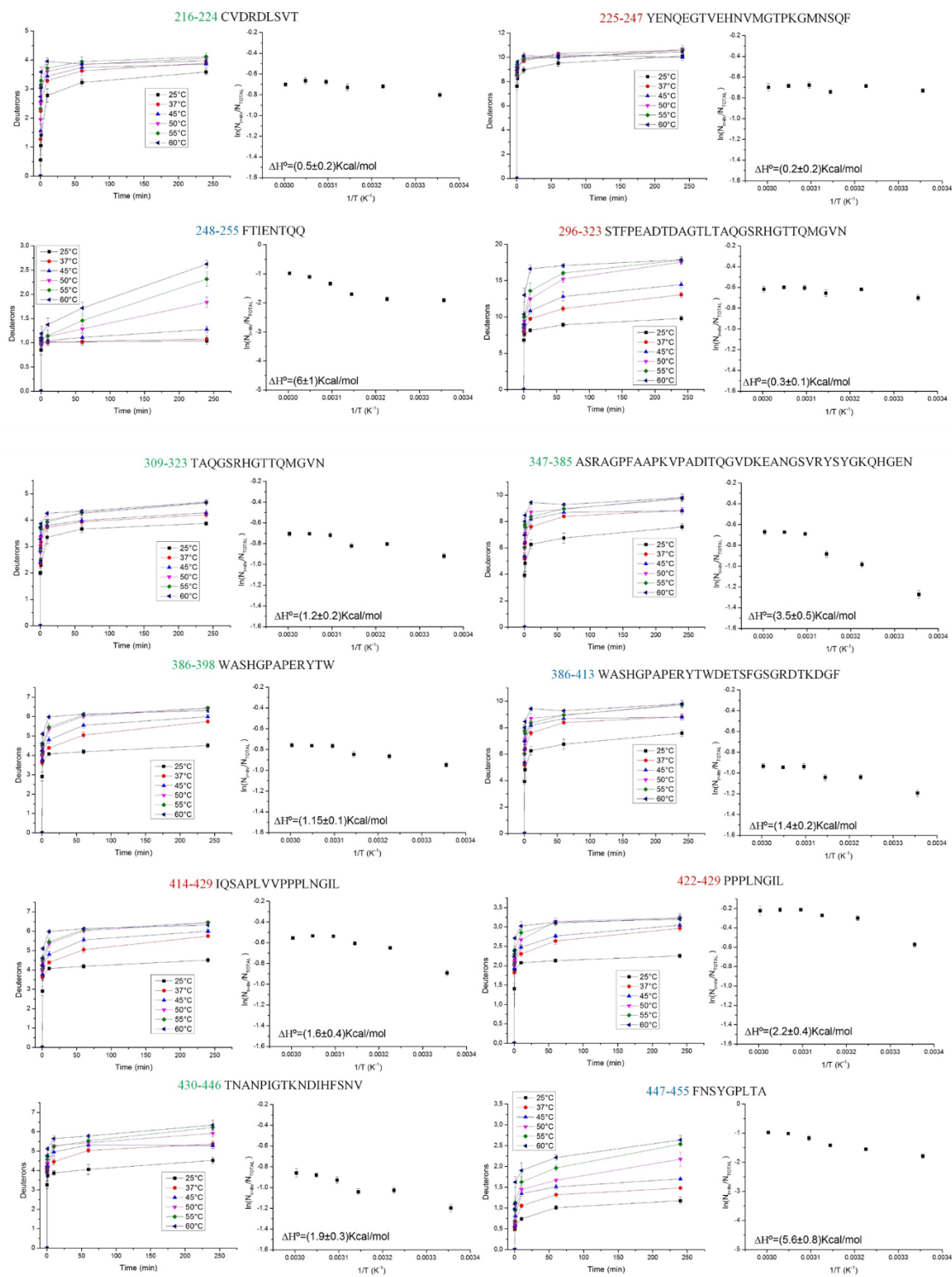


Figure S4. List of peptides identified in the temperature-dependent HDX-MS experiment. HDX time courses as a function of temperature are represented together with the corresponding Arrhenius energy plot. The peptide sequence is shown on top of each figure, with the color (red, green, and blue) indicating the level of uptake in the basal state.

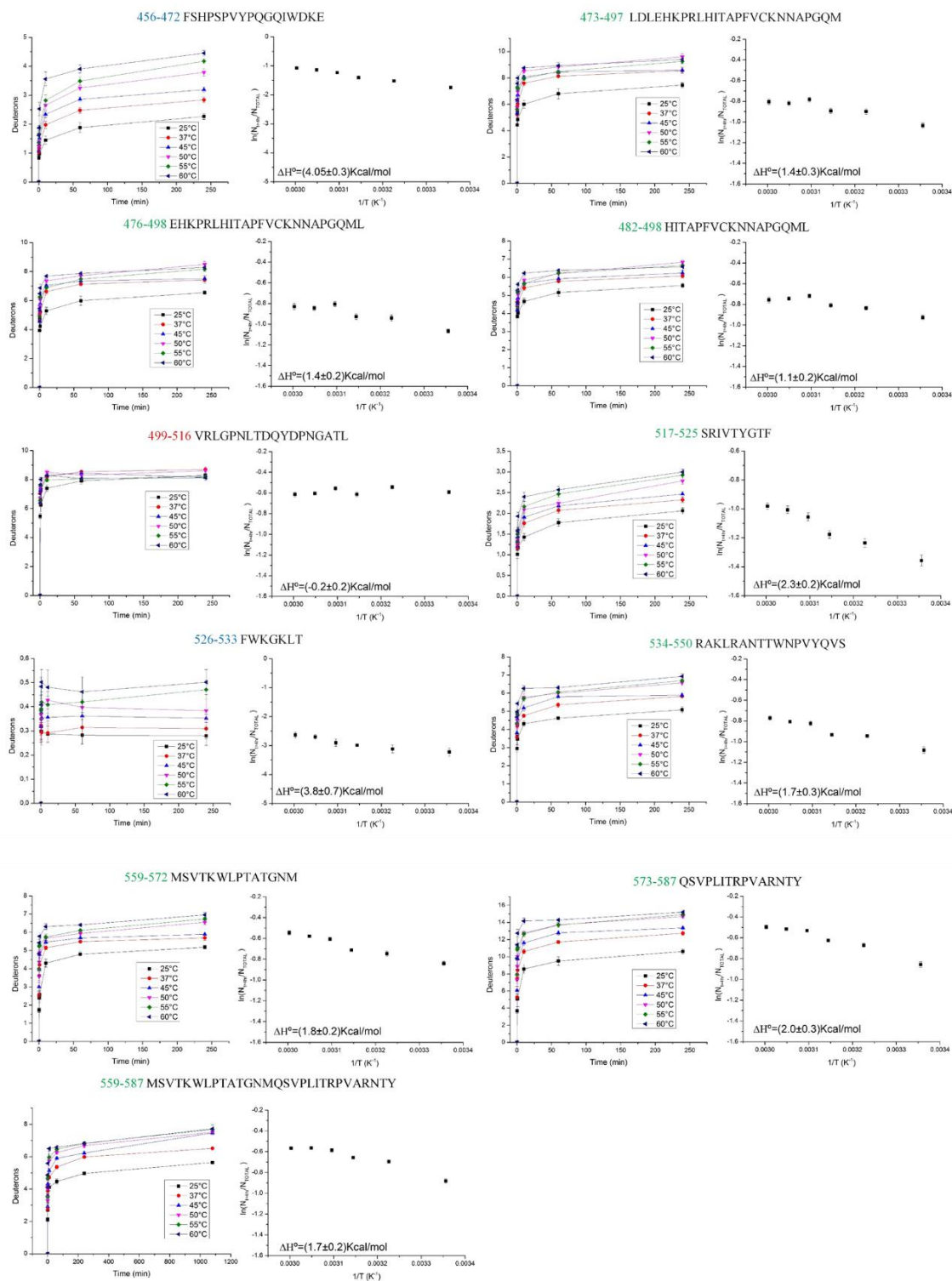


Figure S5. List of peptides identified in the temperature-dependent HDX-MS experiment. HDX time courses as a function of temperature are represented together with the corresponding Arrhenius plot. The peptide sequence is shown on top of each figure, with the color (red, green, and blue) indicating the level of uptake in the basal state.

Theoretical background

HDX experiments are characterized by an intrinsic chemical rate constant (k_{ch}) that determines the probability that a hydrogen from an amide group would be exchanged (N-H \rightarrow N-D). This conversion, however, is modulated by the conformational flexibility of the protein that regulates how many of the amide sites are accessible to solvent and/or are involved in hydrogen bonding at each specific time. Under EX2 limit conditions ($k_{close} \gg k_{ch}$), this dual contribution implies that the global kinetic rate measured in our HDX experiments is $K_{HDX} = K_{open}k_{ch}$, where $K_{open} = \frac{k_{open}}{k_{close}}$ represents the equilibrium constant of the opening reaction.



Although raising the temperature is expected to increase the values of both K_{open} and k_{ch} , it is important to mention that K_{open} is characteristic of a particular transient open state (E_{open}) that should be temperature independent. The fact that some of our time courses reach different levels of deuteration (i.e., plateaus) at different temperatures indicates that the nature of E_{open} varies and offers a means of evaluating the conformational flexibility of different regions in the viral particle. Each E_{open} state is characteristic of a particular conformational state of the virus, which is different from a simple transient fluctuation from closed to open but provides information about the grade of local conformational flexibility. As it has been previously shown by Oyeyemi *et al.*,¹ we can define an apparent enthalpy for this local conformational change that would represent the average property of the local enthalpy of each different amide within a peptide chain:

$$\Delta H_{avg}^o = \frac{\sum n_i \Delta H_i^o}{\sum n_i} \quad [2]$$

with n_i the hydrogen at amide i that exchanges. Assuming that the distribution of states as a function of temperature follows a Boltzmann distribution, $P = Ae^{\frac{-\Delta H_{avg}^o}{RT}}$, we can then determine this average enthalpy by plotting the $\ln\left(\frac{N_{t=4hr}}{N_{TOTAL}}\right)$ versus the inverse of the

temperature, $\frac{1}{T}$, where $N_{t=4hr}$ is the number of sites exchanged after 4 hours and N_{TOTAL} the total number of exchangeable sites.

References

- 1 Oyeyemi, O. A. *et al.* Temperature dependence of protein motions in a thermophilic dihydrofolate reductase and its relationship to catalytic efficiency. *P Natl Acad Sci USA* **107**, 10074-10079 (2010).